ON THE EXTENSION AND VERIFICATION OF THE BREE DIAGRAM

by

NG HEONG WAH

A thesis submitted in accordance with the requirements of the University of Liverpool for the degree of Doctor in Philosophy

Division of Applied Mechanics,
Department of Mechanical Engineering,
The University of Liverpool.

Liverpool

July, 1982

SUMMARY

The Bree Diagram, albeit in modified forms, has been used in the ASME III Codes for a number of years. Its purpose is to limit cyclic thermal and sustained pressure or mechanical loads in pressure vessel structures in order to prevent progressive cyclic deformation or ratchetting and alternating plasticity. A uniaxial beam model assuming elastic/perfectly-plastic stress-strain material properties subjected to cyclic thermal and a mechanical load was used to derive the original diagram.

The purpose of this work was threefold. Firstly, the uniaxial beam model with the same material properties was extended theoretically to three new sequences of cyclic loading in order to examine any changes in the structural behaviour. These alternative sequences were

(1) continuous or sustained thermal and cyclic pressure loads,

(2) in-phase cyclic thermal and pressure loads, and

(3) out-of-phase cyclic thermal and pressure loads.

It was found that the original Bree Diagram exhibited a response to loading which was more likely to cause ratchetting than the other sequences whereas sequences (2) and (3) were most likely to cause alternating plasticity. Sequence (1) resulted in the complete absence of both types of behaviour.

The second aim was the experimental determination of the Bree Diagram limits for ratchetting on three material/temperature combinations. These were mild steel at room temperature and Type 316 stainless steel at room temperature and 400°C. The experimental techniques utilized the equivalent to the uniaxial beam model by subjecting instead of a cyclic thermal load, a cyclic curvature bending load on

the beam whilst applying a continuous axial mechanical load. Having proven the technique, an experimental rig was developed to subject the test material to an axial load and cyclic bending at either ambient or elevated temperature. A practical method was developed to measure the ratchet strains. The limit for ratchetting was found to be in good agreement with the Bree Diagram for mild steel but was not so for stainless steel. Consequently, the ASME III Code appears to have defined an excessively large design stress. A test at 400°C accumulated less strain in less cycles than an identical room temperature test.

Finally, a detailed analysis by computation was undertaken to understand the mechanism for ratchetting for this steel. A number of computer programs were written to calculate ratchet strains in the beam model using various material models. Comparison with experimental results showed that classical models of kinematic hardening greatly underestimated the ratchet strains. Computations incorporating cyclic properties indicated that the beam was highly responsive to a form of cyclic relaxation. Satisfactory agreement was obtained with the magnitude and ratchetting rate at larger cycles.

It was concluded that a knowledge of the cyclic behaviour of this steel is essential for accurate prediction of ratchet strain.

ACKNOWLEDGMENTS

I am particularly grateful to my supervisor, Dr. D. N. Moreton, for his immense enthusiasm and encouragement throughout the duration of this work. During the numerous discussions, he has given me invaluable guidance and many helpful suggestions as well as much well founded criticisms.

Others who have assisted me over the years are too numerous to mention. In particular I am thankful for the assistance given to me by Mr. F. Cummins, of the Drawing Office, for the detailed design of the test rigs, Mr. R. Porter for the manufacture of the rigs and Mr. S. Dobbins for the commissioning of the rigs as well as helping in countless other tasks around the laboratory.

This work would not have been possible without the financial support of a Postgraduate Research Studentship given to me by the University of Liverpool and a research grant from the National Nuclear Corporation Limited. For these, I am indebted and wish to express my gratitude.

In the preparation of this thesis, I wish also to express my sincere appreciation to Mrs. J. McIntosh for her careful typing and to Mrs. A. Green for tracing some of the figures.

CONTENTS

CHAPTER PAGE

NOTATION

D	Mean Diameter of Cylinder
E	Young's Modulus
N	Number of Cycles to Failure
R	Mean Radius of Cylinder
T	Mean Temperature
W	Axial Load
X	Ratio of Pressure Stress to Yield Stress
Y	Ratio of Thermal Stress to Yield Stress
a,b,c	Co-ordinates of Elastic-Plastic Interfaces Measured for Wall/Beam Midsurface
d	Width of Wall/Beam that Yields Plastically at Two Successive Half Cycles
e	Distance of the Origin to the Centre of the Translated Yield Locus
K	Gradient of Stress Distribution in Wall/Beam
n	Number of Half Cycles
p	Internal Pressure of Can
r	Radius of Curvature
t	Wall or Beam Thickness
z	Hysteresis Loop Width
x	Co-ordinate Measured Outward for Wall/Beam Midsurface
w	Beam Width
a_n, $a_{(n+1)}$	Co-ordinate of Elastic-Plastic Interface at two Successive Half Cycles

Greek Alphabet

ΔT	Temperature Difference Across Wall/Beam
$\Delta T'$	Temperature Difference Accounting for Biaxial Temperature Gradient
$\Delta\varepsilon$	Strain Range
α	Thermal Coeffient of Linear Expansion
γ	Poisson's Ratio
δ	Ratchet Strain/Cycle
ε	General Strains
μ	Microstrain
σ	General Stresses
$\sigma(x)$	Stress Distribution as a Function of x (Distance Measured from the Midsurface of Wall/Beam)
ε_1	Longitudinal Strain
ε_2	Transverse Strain
ε_n	Inner/Upper Surface Strain of Wall/Beam at n^{th} Half Cycle
ε_p, ε^p	Plastic Strain
ε_T	Total Strain
ε_y	Yield Strain
ε_a	First Cycle Axial Strain due to Axial Load only
σ_1	Longitudinal Stress
σ_2	Transverse Stress
$\sigma_{0.1}$	0.1% Proof Stress
$\sigma_{0.2}$	0.2% Proof Stress
σ_a	Axial Stress
σ_b	Stress Due to Curvature Bending

σ_p	Pressure Stress
σ_{pE}	Effective Prestress
σ_t	Thermal Stress
σ_x	Constant Elastic Stress through Wall/Beam Thickness
σ_Y, σ_y	Yield Stress (First Departure from Linearity)
σ_z	Axial Stress in Cylinder
σ_θ	Hoop Stress in Cylinder
σ'_Y	Yield Stress (Linear Kinematic Hardening Idealization)

CHAPTER 1

INTRODUCTION

The problem of progressive distortion and cyclic plasticity of structural components subjected to a combination of a constant and a cyclic load have been investigated over many years. Progressive distortion, also commonly known as incremental collapse or ratchetting, is the accumulation of cyclic and permanent deformation on any structural component which leads to functional tolerances being exceeded and in extreme cases, rupture. Cyclic plasticity occurs without any progressive growth but causes parts of a structure to undergo alternating inelastic deformation. Although tolerances are not affected, prolonged cycling may cause low cycle fatigue failure. The condition of loads that cause these problems are often cyclic variations of stress which exceed the maximum elastic range of the material with usually the inclusion of a continuous "follow on" load. These load conditions are common in engineering and the problems are solved by designing on the basis of shakedown concepts.

At present however most of these design procedures are applicable only to structures and loadings which have been idealized as simple, easy to analyse configurations. More complicated structures are still designed on the basis of elastic limits which is wasteful of materials. Economic incentives and sometimes structural design requirements demand better and more efficient designs which in their turn create the need for research and development to study the response of structures subjected to these loads in greater detail.

The introduction of the fast breeder reactor has created a major impetus of research into these problems on a world wide basis. The fast

reactors, many of which are still working prototypes in various parts of the world, are more efficient than the existing generation of thermal reactors. This increased efficiency has been obtained by operating at higher temperatures and lower pressures than previously. This has meant that the dominating consideration for thermal reactors in design, excepting a few specialized components, has been to demonstrate the structural integrity of pressure loading only. Fast reactors, in particular the Liquid Metal Fast Breeder Reactors (LMFBRs) operate with liquid sodium as the high conductivity heat transfer medium in the heat exchanger circuits, causing higher thermal gradients on containment components. These gradients are known to vary rapidly as a result of frequent changes imposed on the reactor by the demands of the grid and by infrequent shutdowns and emergency procedures. These fluctuating thermal gradients, combined with the continuous pressure load are conditions which are ideal for ratchetting and cyclic plasticity.

It is significant to note that, in the high temperature and radioactive environment of the reactor core and primary heat exchanger circuit, matters are complicated by time dependent degradation of material due to creep and irradiation. Therefore designers must take into account not only the loading conditions but also the time dependent nature of the materials in order to optimize the design in the higher temperature regions of the reactor.

Although the novel problems presented by the fast reactor have just been briefly described, the work to be presented in this thesis is specifically concerned with only the aspect of cyclic loading on a structure without time dependent creep and irradiation damage of the material.

A structure which has received considerable attention because of

its geometrical simplicity is the cylinder under constant internal pressure with a cyclic thermal gradient across the wall thickness. The behaviour of the cylinder was first considered by Miller (1) in 1959 for linear and parabolic temperature gradients. The solutions for the two cases are in the form of load limits which separate the ratchetting and non-ratchetting behaviour. Bree (2) in 1967 considerably extended the analysis of the behaviour of this structure when he analysed the behaviour of nuclear reactor fuel cans. In the fast reactor core, heat is generated by fission reactions in mixed uranium-plutonium oxide fuel rods which are cladded with Type 316 stainless steel sheaths. About 200 of these rods are assembled together with boron carbide control rods into a fuel assembly through which liquid sodium is circulated to extract the heat. The problem which Bree considered was the purely mechanical strain behaviour of the cladding under the combined effects of internal pressure due to the fission byproducts and the intermittent high heat fluxes caused by start-up and shutdown of the reactor. In his work Bree studied a hollow thin wall cylinder subjected to an internal pressure. The cylinder wall was subjected to a heat flux through the wall. Using the idealization of elastic/perfectly-plastic material, the magnitudes of the pressure load were defined as hoop stress divided by the yield stress and the thermal load as the elastically calculated maximum thermal stress divided by the yield stress. The result of the analysis, shown in Fig. 1.1, was a 'map' of the response of the can where the loadings form the x and y axes of the plot. For loadings which are in the area E, the response is purely elastic. In region P, the inner and outer fibres experience alternating compressive and tensile plastic strain of equal magnitude. In this region there is no overall growth of the wall but with continued cycling fatigue failure may

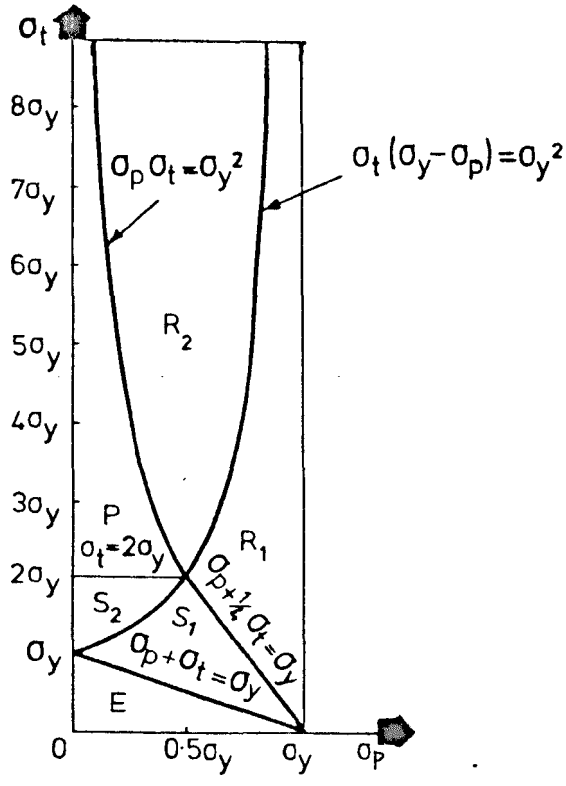

STRESS REGIME	CAN BEHAVIOUR
R_1 and R_2	RATCHETTING
S_1 and S_2	SHAKEDOWN AFTER FIRST HALF CYCLE
P	PLASTIC CYCLING
E	ELASTIC

Fig. 1.1. The Bree Diagram

result. In region S1 and S2 the can shakes down after the first load cycle with no further plastic deformation and the response is then fully elastic. The distinction between S1 and S2 lies in the occurrence of yielding on one surface for the former case and yielding on both surfaces for the latter case during the first load cycle. The region R shows the ratchetting regime which is again divided into R1 and R2 based on the same distinction as in the region S. The diagram has become known as the Bree Diagram.

The model of Bree consists of a uniaxial element under a constant tensile stress equal to the hoop stress and a thermal gradient modified by a Poisson's ratio factor across the thickness. This model has come into popular use, and has been employed by many investigators who applied various material models (e.g. kinematic hardening) and time dependent properties (e.g. creep) in their studies. It is also worthy of note that Miller's criteria for ratchetting has been incorporated in the ASME III Code (3) and a later development on Bree's analysis by O'Donnell and Porowski (4) to account for creep in addition to ratchetting has resulted in a design rule which was incorporated in the ASME III Code Case 1592 (5) in 1974. This code case was later reissued as the ASME III Code Case N-47-12 (6) in 1977. It may be added that the code cases as distinct from the ASME III Code which is the main part, are additions made from time to time in order to clarify requirements existing at the time and when the code interpretations are unclear. It is interesting to note that despite the fact that the ASME III Code rules for preventing ratchetting in thermal cyclic loading problems arose partly from Bree's work on fuel can claddings, ASME III excludes from its consideration tubes or other forms of sheathing used for cladding nuclear fuel. This anomaly is due to the classification of

'Class 1' (or Nuclear Power Plant) components only as pressure retaining or reactor core support and pressure retaining barriers for containing or channelling fluid. This would broadly include vessels, storage tanks, piping, pumps, valves, core support structures and so on.

The assumptions and hence the implications to the limits at which the resulting analysis can be applied are well known. Nevertheless to establish the grounding for the next topic, it is re-examined briefly. Bree considered the fluctuating thermal gradient as a quasi-static thermal loading, consisting of the application and removal of a linear temperature gradient and a uniaxial approximation of the pressure stress in the hoop direction acting on a uniaxial element. The elastic/perfectly-plastic material model predicted a constant rate of ratchet, at any location within the R1 or R2 regimes of the Bree Diagram. The materials chosen for reactor components which experience high temperature and irradiation are required to have superior high temperature properties and resistance to damage by irradiation. These are chosen by most of the nuclear power organizations to be an austenitic stainless steel of Type 316 which has a very pronounced strain-hardening. The strain-hardening affects the strain accumulation rates by the progressive reduction of the incremental strain with cycles. The creep strains are a very important concern at high temperature and recent experimental evidence suggests that at low temperatures, it can occur at rates which cannot be ignored.

The Bree Diagram has, with a little modification, been incorporated into the ASME III Code and Code Case N47. The ASME III Code, which is applicable to stainless steel components at temperatures below 427°C (800°F), has required that for the Bree Diagram, the yield stress be defined as 1.35 times the 0.2% proof stress of the material. This is

approximately 3.5 times the yield stress based on the first yielding of the material (i.e. for Type 316 stainless steel). The selection of the high yield stress value is speculated by the author to be an attempt to account for the benefits provided by strain and cyclic hardening. Such a proof stress is also much easier to identify than first yield. Code Case N47 governs above 427°C, the temperature defined as the average through the wall thickness during the hot part of the cycle. The ratchetting boundary is based on a modified yield stress of 0.9 times the 0.2% proof stress at temperature. The above numerical values have been derived from the wide data base accumulated over many years from research and operating experience of nuclear power plants. A survey of the literature has revealed a small number of experimental investigations on the Bree cylinder or model. These exploratory experiments examined specific conditions of loads which yielded results basically in accord with Bree but these were not of sufficient quantity to be comprehensive. Of greater significance is the total lack of experiments on Type 316 stainless steel. The reasons for this is probably the difficulty of creating thermal stresses of sufficient magnitude and the problems of strain measurement at high temperatures. By solving these problems, it is now possible to conduct a comprehensive experimental programme to reveal the experimental Bree Diagram for Type 316 stainless steel. This task forms some of the experimental content of this thesis.

The experiments consisted of three sets of tests. Two sets were conducted at temperatures of 400 and 20°C using a Type 316 stainless steel. The third set is a room temperature (20°C) test on mild steel to specially verify the Bree Diagram for an elastic/perfectly-plastic material.

Bree gives a comparison between the state of stress in the uniaxial

element and that in a beam element which is subjected to a steady axial load together with a cyclic deformation to a prescribed radius of curvature. The analogy between the stress states of such a beam element and the uniaxial element of Bree is easily demonstrated. The axial stress in the beam element is analogous with the hoop stress (or pressure stress) of the uniaxial element whilst the bending stress is analogous to the thermal stress. The thermal stress in the uniaxial element is caused by the thermal gradient whilst in the beam element this is provided by bending to a constant curvature. Hence in actual experimentation, a thermal gradient is no longer necessary. The problems of creating the thermal gradient across the beam are so intractable that, to the author's knowledge, this method has never been attempted. Some workers decide that it is much easier to carry out pipe ratchetting experiments on a real pipe which actually carries liquid sodium. Others prefer to conduct experiments on other simple geometries where thermal cycling can be applied with less practical problems. The literature survey contains a description and discussion of these experiments. Whilst pipe ratchetting experiments utilizing liquid sodium are the best method of carrying out experiments, they are very expensive and require the technical expertise of large organizations. Furthermore, because of the cost, very few experiments are conducted and the very well conducted ones become "Benchmark experiments". Benchmark experiments are experiments chosen to provide experimental data on which to verify and qualify inelastic analysis calculations. Experiments on simple geometries or idealizations are better suited to study these problems because large numbers of tests provide more data for analysis.

Based on the analogy of bending, experiments have been performed on

long thin strips of steel as test specimens and cyclically deforming these to a prescribed radius of curvature whilst applying a steady axial load. A test rig was developed for subjecting the strips to the loading described. This, in essence, consists of a wheel of fixed radius which is driven by a motor through a crank, rack and pinion train to oscillate through an angular range. The specimen strip was wound over half the circumference of the wheel and subjected to dead weight forces at the ends via a chain and pulley system. The deformation of the specimen is measured by displacement transducers. By the variation of the wheel size and the weight, a wide range of load combinations have been investigated. For elevated temperature tests, a heating system comprising of a hot insulated enclosure and other modifications are added to the rig. The insulated enclosure encloses the wheel and the specimen completely, raising the temperature of the contents to the required test temperature. A microcomputer was employed to sample the experimental data and control the temperature of the hot enclosure.

The Bree uniaxial element has enabled the prediction of the strain behaviour of the cylinder under cyclic thermal and steady pressure loading. The accuracy of the prediction is dependent on a number of factors. The first is the realism of the material model employed in the analysis and secondly the method of representing the loadings. Finally there is the closeness to which the physical geometry of the structure is related to the analytical model. Attempts to improve the material model involve a great increase in analytic complexity and particularly time dependent behaviour such as creep have only been resolved by the use of "approximate methods". Due to the aforementioned reasons, most of the continuing efforts in structural analysis in general are employing computer inelastic analysis. With the powerful computers now available, computer programs

can employ increasingly more complex and realistic time dependent material models on more sophisticated structures and loadings. However these programs are prohibitively expensive to develop and support and are not in widespread use. The main function of these programs has been to validate final design of critical components. The use of computer programs on simplified problems are much less expensive and make less demands on the programmer's skill. Programs of this type are increasingly in common use for initial design analysis.

Computer analyses of the latter category have been conducted by the author on the University's mainframe computer. The aims of the analyses are firstly to solve the Bree problem using more realistic material behaviour and hence obtain more realistic prediction of the deformation to compare against experimental data. The numerical investigation shows that reasonable correlation to experimental results requires unconventional models based on material effects seen in special material testing techniques. Some of these material effects are discussed in the literature survey. Secondly, there is a need to compare the various solutions obtained based on different conventional models of elastic/perfect-plasticity, linear kinematic and non-linear kinematic hardening and less conventional models of cyclic hardening/softening and stress relaxation. The sensitivity of the ratchetting behaviour to these models has been assessed. The description of all the above models are discussed in chapter 5.

The third aim for conducting computer studies is to assess the effect of variation in the sequence of loading. As the loading in the Bree model is quasi-static (i.e. temperature gradients and pressure load assume stepped values), only four types of cyclic sequences are possible. Variation of the phase relation of axial and thermal loads have given

three new alternatives to the Bree Diagram. These diagrams have important practical implications. In the environment of the power plant (both nuclear and conventional), thermal loading and pressure occurs in sequences which are dependent on the function and operational variables of each component. With few exceptions, the Bree Diagram has been indiscriminately used in many situations which are not of the sequence of Bree. Some situations (e.g. in heat exchanger circuits) are in fact of the in-phase cyclic thermal and pressure type or are close approximations to it. With the immense complexity of power plant internals, it is conceivable that there are many situations where the alternative sequences apply. The sensitivity of ratchetting rates and limits for the sequences when considered shows that close attention to detailed aspects of loading can facilitate better design and eliminate potential ratchetting problems by reconsidering the design of the control systems and operating procedures.

These computer analyses have been restricted to constitutive models without time dependency. Effects such as creep and dwell times are not considered although in one of the models discussed earlier, a relaxation effect has been included. The effect of time is indirectly implied because stress relaxation occurs through the conversion of elastic strains to creep strains. The degree of relaxation can be controlled and is presently based on experimental data. Computer studies of creep, fatigue and damage caused by these effects on the Bree model have been covered by researchers elsewhere (see literature survey) and it was considered unnecessary to expend the considerable time and effort on developing a program to perform nearly similar tasks. In addition, the programs have been designed to predict the results of experiments which are performed at fast cycle times whereby the effect of creep (at room

or elevated temperature) are reduced. By improving the programs to their present state of complexity, an optimum degree of compromise has been reached between the realism of the model and computational complexity. Analytical solutions have also been obtained for the three alternatives to the Bree Diagram. These solutions were sought to provide an alternative solution method to the computer solutions. They were shown to be exactly in accord with the computer calculations both in the boundaries separating the regimes of behaviour and the ratchetting strain rates. Expressions governing the boundaries and the ratchetting strain rates were derived. In the same chapter, the solutions for the Bree Diagram have been obtained in entirety as it was noted that Bree did not present all the calculations in detail in his paper (2). The crux of the analytical method rested on the assumption that a steady cyclic stress state exists in a structure after a few cycles of loading. This assumption was proven by Frederick and Armstrong (20) and shown also to exist in the computer solutions. For each alternative in the loading sequence, a discussion was given on the implications on the structural behaviour.

Throughout this thesis, the thermal and pressure analogy is adopted. Hence all figures and text will always refer to thermal and pressure stresses for convenience although it is realised that it is not always the case.

Finally in this thesis, an account of experimentation on the shakedown and ratchetting of T-section beams is reported. Although this has only a slight relevance to the main work in the geometry and the loading of the structure concerned, the experiments were initially conceived to investigate the ability of commercial elevated temperature strain gauges to perform reliably for long durations at 400°C in the cyclic loading of T-section beams. If the reliability of the strain

gauges prove acceptable, a programme of experimentation would have been planned to investigate more thoroughly, the variation of maximum shakedown loads on T-section beams at a range of temperatures. The techniques of strain gauging which would by then have been acquired could have been used for investigating shakedown at elevated temperatures of pressure vessels. These objectives were only partially achieved because the strain gauges proved to be unreliable at the period of time which was crucial for detecting shakedown. This work is reported here not only for completeness but also for its role in leading the way to the present work.

CHAPTER 2

LITERATURE SURVEY

2.1 Introduction

A great deal of theoretical and experimental work has been published on the subject of progressive deformation in simple and complex structures under cyclic loading. The Bree model which is one of simple geometry has received intensive investigation. Other models such as the two-bar model and that of the axially loaded tube under cyclic torsion have also been studied. Complex structural tests have been conducted in smaller numbers but considerable efforts on the theoretical aspects have been in evidence. Many of these studies have been carried out under the auspices of nuclear power organizations or by their contractors. This is because the problem of ratchetting at elevated temperatures among the many others faced by these organizations is an important one. The survey of the literature is presented in six sections. Section two is a brief discussion of the nuclear power systems in operation and under development with emphasis on the areas where the conditions leading to cyclic thermal loading might occur. Section three details the relevant sections of the ASME and the British Standard Codes where these apply to the problem. The definitions of design stresses and the allowable limits applicable to these loadings are discussed. The fourth section is concerned with the theoretical investigations based on the Bree model while section five deals with the experimental investigations. Section six completes the surveys of section four and five by combining the theoretical and experimental investigations of the cyclic deformation behaviour of other structural geometries. The final section considers the classical constitutive models of material behaviour and some of the

reported works which study the more subtle aspects of material behaviour of stainless steels which are not accounted for by classical constitutive models.

2.2 An Overview of the Problem Background

In chapter 1, it was seen that the advent of fast reactor technology has created the conditions for rapid thermal cycling which may cause ratchetting. Also, fast reactors operate at temperatures beyond 1000°F (540°C) which is within the creep range of austenitic stainless steels. The reactor core and the surroundings are subjected to irradiation of neutron flux which affects creep and other mechanical properties in a number of ways. These effects greatly affect the structural behaviour of reactor components and have to be accounted for in design.

The construction of a typical LMFBR reactor core and its immediate surroundings is now examined. In North America and Europe most LMFBR designs are similar in a wide sense due to the international co-operation that exists between the countries. Therefore the typical LMFBR being discussed contains all the basic elements common to all LMFBR designs. As the name suggests, the LMFBR utilizes a liquid metal coolant (sodium) to transfer heat from the reactor core. Since the sodium becomes radioactive, an intermediate heat transfer loop of liquid sodium is employed between the reactor coolant system and the turbine water-steam system to eliminate any possible radioactive leakage. These loops are called the primary and secondary circuits respectively. The temperature varies from about 350-700°C at the core to about 20-450°C (shutdown and running temperatures respectively) at the steam generator heat exchanger end. Austenitic stainless steels (Type 316 and 304), high nickel based alloys (e.g. H800) and $2\frac{1}{4}$Cr-1Mo steel are used in the steam generator heat exchanger and turbine system. The piping throughout the reactor is mainly of Type 316 or 304 stainless steels. The core of a 1000MW LMFBR can contain about 10^5 Type 316 stainless

steel cladded mixed uranium-plutonium oxide fuel rods of approximate 6mm diameter by 2.8m long. Reactor control is by boron carbide control rods which are cladded in Type 316 stainless steel. Fuel rods and control rods are assembled in groups to form a fuel assembly which is surrounded by a hexagonal container called the duct. The duct provides support to the rods and the upper and lower hardware for directing sodium flow. The ducts are assembled in hexagonal arrangements inside a pressure vessel with openings for inflow and outflow of sodium and other support and controlling mechanisms. This pressure vessel, called the core barrel, is further contained by an outer pressure vessel which contains the sodium 'pool' and main piping inlets and outlets for the primary circuit. The duct, core barrel and outer pressure vessel are of Type 316 stainless steel.

The types of problems presented in nuclear engineering vary widely in scale and severity. These are due to the effects, separately or in combination of elevated temperature, irradiation and sodium environment. Some characteristics of elevated temperature problems are due to heat generation from within the material due either to irradiation or to nuclear reactions in the instance of the fuel rods. This is superimposed on the heat flow due to thermal gradients in reactor structures. The structures so affected are reactor core pressure vessels and piping in the primary circuits. The fuel rods and the sheathing are affected by volumetric changes due to swelling and thermal stresses. Increases in the heat output rate can increase thermal stresses due to uneven temperatures causing fuel cracking. The fuel sheathing when subjected to thermal cycling exhibits the deformation which has been described by Bree. Structures such as heat exchangers, both of the primary and secondary circuits, are not highly irradiated but are susceptible to

Bree-type behaviour by virtue of their function which involves thermal cycling. Elevated temperature acting by itself presents problems which are time dependent. Prolonged operation in an elevated temperature environment leads to thermal ageing, a process involving void formation, grain growth and growth of precipitates in the material which influences the structural behaviour by the initiation and growth of fatigue cracks. Also yield strength of steels are reduced by operating in an elevated temperature environment. Thermal creep which is time, temperature and stress dependent relaxes deformation controlled stresses arising from thermal gradients by converting elastic to creep strains. This may lead to creep ratchetting occurring at conditions where shake-down would otherwise have taken place in a thermal cyclic loading situation.

In addition to the problems of operating in an elevated temperature environment, LMFBR components are subject to fast neutron irradiation which introduces major changes in the response of structural material both mechanically and microstructurally. Fast neutron irradiation introduce a process like cold working i.e. increase in strength and decrease in ductility of the material, called helium embrittlement. While the increase in strength is beneficial, the decrease in ductility is detrimental in that it makes normally ductile alloys more susceptible to brittle fracture and offsets the beneficial increase in strength. In essence, strength and ductility like many other material properties subjected to irradiation become fluence dependent. Fluence is a measure of irradiation effects and is the neutron flux integrated over the exposure time. The response of the material to a given transient therefore becomes dependent on the accumulated fluence at the time of the event.

The effect of irradiation on stainless steels is irradiation induced swelling through void formation. Tolerances have to be provided to accommodate the increased volume due to swelling without loss of function. When swelling is constrained, swelling induced stress will develop and should be taken into account in the analysis. Stainless steel Type 316 has superseded Type 304 in LMFBR components because of its better resistance to swelling and better high temperature properties.

Irradiation also affects creep by enhancing it. The increased fraction known as irradiation creep is present at low temperatures where thermal creep is negligible and in the form of increased rates of deformation at temperatures where thermal creep is present. The total creep rate is dominated by irradiation creep processes at low temperatures and is eventually swamped by normal thermal creep at high temperatures. Like thermal creep, irradiation creep relaxes deformation controlled stresses, e.g. thermal stress, swelling induced stresses and peak stresses.

The effects of sodium on austenitic stainless steels are twofold. Firstly sodium preferentially leaches out chromium and nickel from the steels and secondly carbon is either added (carburization) or taken away (de-carburization) to the steel depending on the temperature and carbon activity of the sodium. The effects can influence the mechanical properties of stainless steel, but so far indications are that these effects are of minor significance to structural integrity.

The above are some of the problems encountered in LMFBR reactor design. It is seen that the real operating environment and conditions are vastly more complicated than the idealised assumptions which conservatively account for the effects described. A large information base has been accumulated by researchers in this field. The information that

has been presented in this section has been gathered from two sources, (7) and (8). The former contains extensive reference lists which for reasons of expediency are not quoted.

2.3 The ASME and B.S. Codes

The aim of this section is to introduce the ASME and the B.S. Codes within the limits of applicability to nuclear power plant components operating at temperatures below and above the creep range. The definitions of allowable design stresses and allowable deformation limits are described whenever applicable to the cyclic thermal loading problem. This section is considered necessary because the codes have been very closely linked to the development of nuclear and conventional power plants. The continual reference to the codes in many of the publications on the subject requires one to be familiar with the details of those parts of the codes mentioned. The rules and recommendations of the codes are also constantly evolving as a result of continued research for better reactor safety.

The section of the ASME Code that deals with the design of major nuclear components is known as the American Society of Mechanical Engineers (ASME) Boiler and Pressure Vessel Code, Section III, Nuclear Power Components, Division 1, Class 1 (3), or ASME III in short. (Division 1 and Class 1 respectively mean that the code is concerned with metal components at the highest level of assurance of structural integrity). According to Section III, nuclear power plant components are classified as components which are designed to provide a pressure containing barrier or to act as a pressure retaining barrier or to support reactor core structures in the nuclear power system. This broadly includes vessel storage tanks, piping, pumps, valves and core support structures. ASME III was established during the development of thermal reactors when temperatures were in the subcreep regime and coolant pressures were high. The limits of applicability of the temperature in ASME III are set at 427°C for austenitic steels and 370°C for

ferritic steels. The introduction of the Code Case N47 (6) (formerly Code Case 1592 (5)) was mainly a response to the need created by the development of high temperature nuclear reactors such as the LMFBR. Code Case N47 extends the allowable temperature into the creep regime.

BS5500, 'Specification for Unfired Fusion Welded Pressure Vessels' (9) is a British Standard Code which covers the design of pressure vessels for conventional power plant use. It does not however specifically cater for nuclear reactor pressure vessels. These are covered by BS3915 (Carbon and Low Alloy Steel Pressure Vessels for Primary Circuits of Nuclear Reactors, 1965) for thermal reactors. In the U.K. the parties concerned with the design, use and manufacture of nuclear pressure vessels may agree between themselves to use BS5500 or ASME Codes where applicable in place of other British Standards. For this reason only BS5500 is considered in the discussion. Unlike the ASME Codes, BS5500 has no temperature distinction. The design stress specifications are such that the code covers all temperatures.

2.3.1 ASME III and Code Case N47 ((3) and (6))

To ensure that the codes can be applied discriminately to the various structures under different loading conditions, stresses are classified into five categories based on the assumption that different classes of stress have different and unique identities. These are as follows:-

P_m - Primary Membrane Stress averaged across a solid section due to mechanical load only and excluding discontinuities and concentrations.

P_L - Primary Local Membrane Stress averaged across a solid section due to mechanical load only and including discontinuities but not concentrations.

P_B - Primary Bending Stress which is a component of the Primary Stress proportional to the distance from the centroid of solid section and produced by mechanical load only. Also discontinuities and concentrations are excluded.

Q - Secondary Membrane plus Bending Stress which is self equilibrating in order to satisfy continuity of structure (e.g. that which occurs at structural discontinuities). This is caused by mechanical load or differential thermal expansion and excludes local stress concentrations.

F - Peak stresses are certain thermal stresses which may cause fatigue but not distortion of vessel shape. Also these stresses are the increment added to the primary or secondary stresses caused by a concentration (notch).

Tables in the Code provide aids in the classification of stresses that are present in some typical vessel and piping locations under different loading. The Code then limits the stress categories above by means of stress restrictions. Since these are similar in both ASME and BS5500 Codes, they are given below only once:

$$P_m \leq S_m$$

$$P_L \leq 1.5\ S_m$$

$$P_L + P_B \leq 1.5\ S_m$$

$$\Delta(P_L + P_B + Q) < 3.0\ S_m$$

The righthand side of the inequalities are the stress restrictions.

S_m is the design stress and Δ indicates range of variation of the stresses. For a secondary stress (Q) which is caused by a temperature excursion at the point at which the stresses are being analysed, the value of S_m is taken as the average of the S_m for the highest and lowest temperature of the metal during the transient. When part or all the secondary stress is due to mechanical load, the value of S_m is taken as the S_m value for the highest temperature during the transient. S_m is a modified form of the mechanical properties scaled by a numerical factor. The material properties and the scaling factor used are dependent on the temperature range and the type of material (e.g. ferritic or austenitic steels).

According to the ASME III Code (less than 427°C which is for austenitic steels), S_m is chosen as the lowest of the following quantities:-

Ferritic Steels	Austenitic Steels
a. $\frac{1}{3}$(tensile strength at temperature)	a. $\frac{1}{3}$(tensile strength at temperature)
b. $\frac{2}{3}$(yield strength at temperature at the 0.2% proof strain)	b. $\frac{2}{3}$(yield strength at room temperature at 0.2% proof strain)
	c. 0.9(yield strength at temperature at 0.2% proof strain)

Because of the assumption of time independence (i.e. negligible creep and relaxation) the ASME III Code guards against only time independent failure modes. These are as follows:-

1. ductile rupture
2. gross distortion due to buckling and incremental collapse
3. fatigue

The ASME III Code itself (i.e. the main part) does not place any restrictions on deformation of the components.

In the Code Case N47 (greater than 427°C for austenitic steels), creep effects are significant and failure modes to be accounted for are as follows:-

1. ductile rupture for short term loadings
2. creep rupture from long term loadings
3. creep/fatigue failure
4. gross distortion due to incremental collapse or ratchetting

In addition to the above restriction on failure modes, the Code Case N47 imposes the following strain limits on the maximum accumulated inelastic strain:

1. strain averaged through the thickness of 1%
2. strain at the surface, due to an equivalent linear distribution of strain through the thickness of 2%
3. local strains at any point of 5%

The above limits apply to computed strains accumulated over the expected lifetime of the structural element under consideration. Creep/fatigue failure is accounted for by the restriction on creep and fatigue damage. One of the recommended methods is the linear damage summation rule which assesses separately the damage due to fatigue and creep and combines them in a linear manner.

Code Case N47 also allows a designer to use inelastic computer analysis to demonstrate that a component is satisfactory. This is

necessary in determining the ratchetting strains when the shakedown limit is exceeded. Material data charts for a restricted range of steels, showing minimum rupture stresses and average isochrones of strains against stresses are provided. These charts are used for calculating creep strain limits or design stresses related to rupture stresses based on an elastic basis over the expected lifetime. The material data provided are for Type 304 and 316 stainless steels, alloy 800H and $2\frac{1}{4}$Cr-1Mo steel which are commonly used in the power plant industry.

2.3.2 BS5500 Code (9)

The philosophy of BS5500 is essentially similar to the ASME Code as far as the stress classification and restrictions are concerned. For time dependent material behaviour, both codes limit all the calculated stresses to a value below the shakedown limit for cyclic load and below the limit load for steady load. Thus, in the absence of creep, design can proceed knowing the shakedown limit and the limit load in conjunction with a suitably defined material yield stress. When the design temperatures are high enough for creep to become an important feature in the design, the design stresses are redefined using rupture stress data. The BS5500 design stresses are the lower of the following:-

Ferritic Steels (carbon, carbon manganese and low alloy steels	Austenitic Steels
(I) Up to and including 50°C	
a. $\frac{2}{3}$(yield strength at room temperature at 0.2% proof strain)	a. $\frac{2}{3}$(yield strength at room temperature at 1% proof strain)
or	or
b. $\frac{1}{2.35}$(tensile strength at room temperature)	b. $\frac{1}{2.5}$(tensile strength at room temperature)
(II) Between 150°C and above	
c. $\frac{2}{3}$(yield strength at temperature at 0.2% proof strain	c. $\frac{1}{1.35}$(yield strength at temperature at 1% proof strain
or	or
d. $\frac{1}{2.35}$(tensile strength at room temperature)	d. $\frac{1}{2.5}$(tensile strength at room temperature
(III) Time dependent design strength (for both Ferritic and Austenitic steels)	
e. $\frac{1}{1.3}$ (Mean value of stress required to produce rupture in 100,000 hrs at temperature)	

Similar to the ASME III Code but unlike the N47 Code, BS5500 places no formal restrictions on the deformation of the components under consideration. It is also seen that BS5500 does not at present contain any provision for limiting thermal cycling ratchet behaviour. There is however the requirement that shakedown to elastic action should occur during the first few cycles thus limiting the deformation implicitly. The design stresses are based on creep rupture data under constant load which are more suitable for steadily loaded structures.

2.3.3 Code Rules on Thermal Stress Ratchetting

Both ASME III and Code Case N47 have provisions for preventing the occurrence of thermal stress ratchetting. In ASME III, the solution of Miller (1) has been used. The solutions are in the form of primary and secondary stress restrictions on the cases of parabolic and linear cyclic thermal gradients on a portion of an axisymmetric shell loaded by steady internal pressure. In order to prevent cyclic growth in diameter, the stress conditions are as follows:-

Case I — Linear variation of temperature through the wall

For $0 < x < 0.5$, $y = 1/x$

For $0.5 < x < 1.0$, $y = 4(1-x)$

Case II — Parabolic constantly increasing or decreasing variation of temperature through the wall

For $.615 < x < 1.0$, $y = 5.2(1-x)$

For $x < 0.615$, the following applies

Approximately	$x = 0.3$,	$y = 4.65$
	$x = 0.4$,	$y = 3.55$
	$x = 0.5$	$y = 2.70$

where y = maximum allowable range of thermal stress computed on an elastic basis divided by the yield strength.

x = maximum general membrane stress due to pressure divided by the yield strength.

The yield strength value is taken to be $1.5\ S_m$.

In Code Case N47, the solutions of O'Donnell and Porowski (4) are used to bound the creep strains in Case I. The primary stress intensity

is generalised to include the effect of bending of the shell while the secondary stress remains the same. The expressions for x and y are as follows:

$$x = (P_L + P_B/K_t)\ \max/SY$$

$$y = (Q_R)\ \max/Sy$$

where K_t is the bending adjustment factor and Sy is the wall averaged temperature yield strength which is taken to be the 0.2% proof stress. The method of determining the creep strain is to be described in the section 2.4 in this chapter.

2.3.4 Creep-Fatigue Evaluation

For loadings where creep and fatigue are dominant features, Code Case N47 limits the total damage by a linear summation of the individual damage by creep and fatigue using the following expression:

$$\sum_{j=1}^{j=p} \left(\frac{n}{N_d}\right)_j + \sum_{K=1}^{K=q} \left(\frac{\Delta t}{T_d}\right)_K \leqslant D$$

where D = total creep-fatigue damage

n = numbers of applied cycles of loading condition j

N_d = number of design allowable cycles of loading condition j from one of the design fatigue curves corresponding to the maximum metal temperature during the cycle

q = number of time intervals of time duration Δt needed to represent the specified elevated temperature service life at the point of interest for the creep damage calculations

T_d = allowable time duration determined from stress to rupture curves for a given stress and the maximum temperature at the point of interest and occurring during the time interval K

2.4 Theoretical Investigation Utilizing the Bree Model

In this section, the theoretical work which has utilized the Bree Model is examined. By the Bree Model, it is emphasized that only investigations utilizing the uniaxial idealization of Bree (2) are considered.

The early literature in this field is mainly confined to studies in cyclic loading of structures made of elastic/perfectly-plastic materials with time independent properties. Studies on such structures have the advantage of simplicity when time dependence is avoided. Therefore the states from one load cycle to the next can be assumed to be quasi static, thus load controlled deformation or thermal strains assume stepped values. The occurrence of ratchetting effects due to the interaction of elastic and plastic strains have been noted and simple analytical examples have been given by Prager (10), Gill (11), Ruiz (12) and Hill (13). More examples of greater complexity and practical value are works carried out by Miller (1), Edmunds and Beer (14), Bree (?) and Burgreen (15). The approach used by these authors were basically the same and each have obtained suitable solutions to simplified versions of their own specific problems. The approach used was later modified and improved by others to include the effects due to time dependence such as creep, fatigue and rapid transient type loading.

It is firstly necessary to define the terms used in this work. The word ratchetting is defined as that cyclic inelastic deformation that is due solely to time independent plasticity effects. When time dependent inelastic deformations are included, such as due to creep, the deformation is termed creep ratchetting.

From this point, the discussion will centre on the model by which Miller (1) analysed the reactor fuel can and the further detailed analyses conducted by others. Miller's model (1) is one of the elements

of the tube or fuel can of radius R, thickness d and subjected to pressure p. The problem was reduced to one in which an element of tube was subjected to an axial stress σ_z = pR/2d and a circumferential stress σ_θ= pR/d with a linear or parabolic temperature distribution through the thickness. This idealization gives rise to a uniaxial beam model which is subjected to a primary stress of pR/d and a secondary stress due to the temperature difference ΔT. From this model, Miller was able to obtain solutions for the loadings which give rise to shakedown or ratchetting. He also initially obtained the solution for the three-bar structure which will be described in section 2.6. Fig. 2.1 shows the solutions for three-bar structure and the fuel can when subjected to parabolic and linear temperature gradients. These solutions now form the basis of the ASME III (3) restrictions on primary stress in the presence of thermal loadings of this type.

Burgreen (15) firstly studied the problem by considering the behaviour of a two-bar structure under thermal loading. The structure consisted of two bars of equal lengths rigidly attached together at the ends and subjected to a constant axial load with one of the bars subjected to variations in temperature. Analytical formulae were obtained to calculate ratchetting strains with the relative area of the two bars being variables. The analysis was later extended in a subsequent publication (17) in which a multi-element assembly was proposed to study the same problem. Such an assembly, containing a large number of elements, is analogous to the two-bar model. However, each bar experiences a slightly different temperature from its nearest counterpart. By having a large number of elements, a homogenous structural state was approached and by subjecting the structure to a temperature variation across its width, a solution similar to Miller's was obtained.

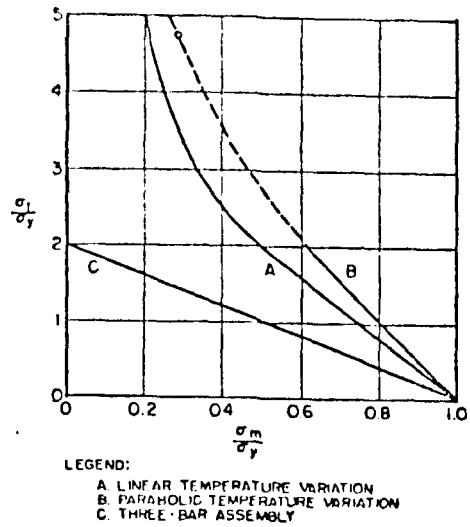

Fig. 2.1. Thermal Stress Beyond Which Cyclic Growth Occurs
Miller [1]

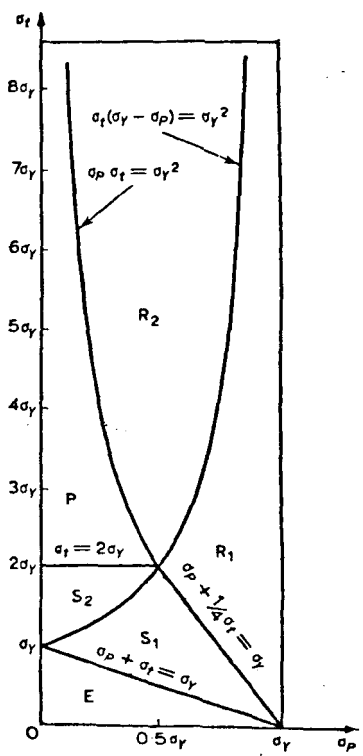

Stress régime	Can behaviour
R_1 and R_2	Ratchetting
S_1 and S_2	Shakedown after first half-cycle
P	Plastic cycling
E	Elastic

Fig. 2.2. Bree Diagram. Bree [2]

Bree (2) extended Miller's analysis by using the uniaxial beam model and extended the $\frac{\sigma_t}{\sigma_y}$ vs. $\frac{\sigma_p}{\sigma_y}$ plot shown in Fig. 2.2 to include the by now familiar categories of structural response which are referred to as R1, R2, P, S1, S2 and E regimes of behaviour for an elastic/perfectly-plastic material with time independent material properties. In the R1 region, the ratchet strains/cycle are given by:-

$$\delta = \frac{2\sigma_t}{E} \left(1 - 2\sqrt{(\sigma_y - \sigma_p)/\sigma_t} \right)$$

and in the R2 region

$$\delta = \frac{2\sigma_t}{E} \left(\frac{\sigma_p}{\sigma_y} - \frac{\sigma_y}{\sigma_t} \right)$$

It is later shown that a small incursion into the R1 and R2 regions can cause large deformation by ratchetting after a few cycles. Incursion into the P region indicates alternating plasticity which may ultimately lead to failure by low cycle fatigue. By using the relationship derived by Coffin (18), the number of cycles to failure can be predicted. Bree also calculated the effect on the diagram if there is a complete relaxation of residual stresses by creep during the hot part of the cycle. Residual stresses are set up by plastic deformation and are beneficial in that the elastic range of stresses are increased and consequently an opportunity for shakedown exists. As a consequence of creep, residual strains are converted to creep strains and without the beneficial residual stress distribution, ratchetting will occur in regions where shakedown would have otherwise taken place. When relaxation is complete, the S1-R1 and P-R2 boundaries fall to the elastic boundary as seen in Fig. 2.3. Next, Bree assessed the effect when the yield stress is temperature dependent by assuming a higher yield stress

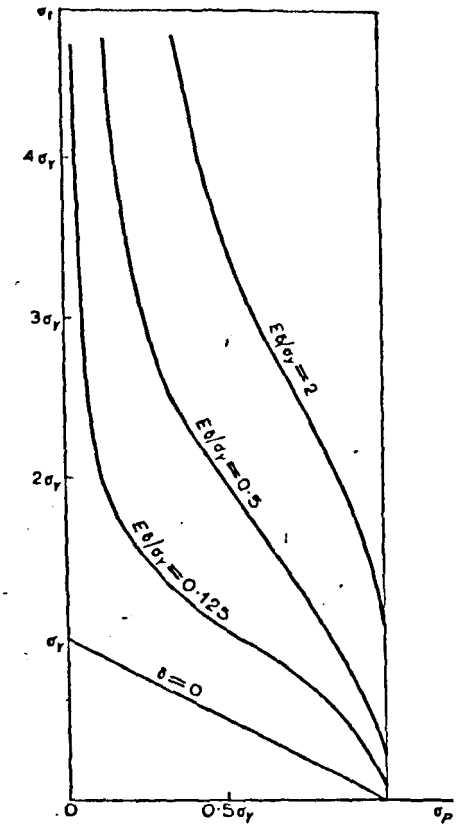

Fig. 2.3. Lines of Constant Ratchet Strain per Cycle When Creep Causes the Stress to Relax Completely to the Pressure Stress While the Reactor is at Power. Bree [2]

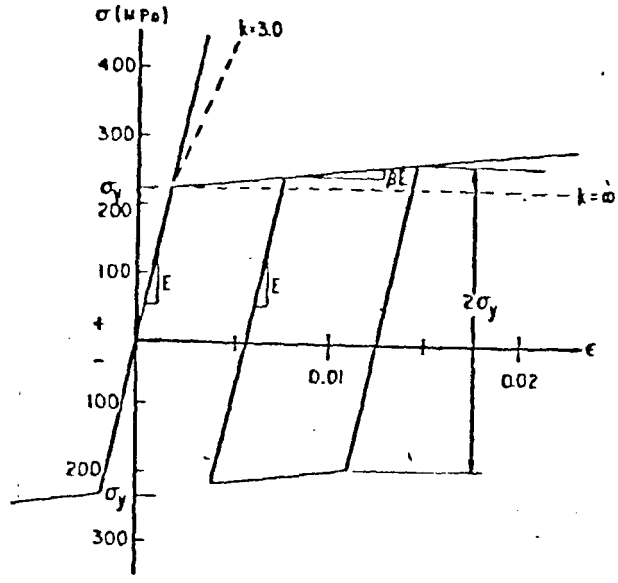

Fig. 2.4. Uniaxial Stress-Strain Curve for Linear Kinematic Strain Hardening Material Drawn for σ_y = 231 Mpa, E = 131,000 MPa and K = 44.5, 3.0 and Infinity. Mulcahy [21]

σ'_y for the low temperature part of the cycle and a uniform lower value σ_y for the linear temperature distribution. It was shown that the effect is not significant when compared with a Bree diagram calculated using a yield stress equal to $\frac{\sigma'_y + \sigma_y}{2}$. Although this averaging gives an indication of the effect of temperature, it should be noted that the real situation is one of varying absolute temperature during each half cycle. When work hardening is considered, it is found that the ratchetting criterion is not greatly affected. However, work-hardening causes the increment of strain per cycle to decrease asymptotically to zero after an infinite number of cycles. Thus, the constant strain accumulation per cycle predicted by an elastic/perfectly-plastic material model (see Fig. 2.22) greatly overestimates that predicted by the isotropic strain-hardening model for given mechanical and thermal loads. Work-hardening is defined in this context as the increase in the stress in the plastic range with increasing plastic strain without the Bauschinger effect otherwise known as isotropic hardening.

On the basis of the assumption of complete relaxation of residual stresses due to creep, the ratchet strain per cycle is increased greatly compared to the case without creep. This assumption was seen to be unduly pessimistic and was later reconsidered. Bree in the second publication (19) extended his work to the case where creep causes only partial relaxation of internal stresses and evaluated the ratchet strains. Creep was considered to occur only in the high temperature excursion and in accordance with a secondary creep law of the form $\dot{\eta} = A\sigma^n$ where $\dot{\eta}$ is the creep rate, σ the applied stress and A and n are constants for the material. An additional time parameter was introduced to account for the on power (high temperature) duration of the cycle during which creep occurs. The solution was based on the construction of a steady state

stress cycle for the uniaxial model which enabled the ultimate behaviour of the can to be determined without tracing the detailed history of its deformation. This procedure is based on the theorem by Frederick and Armstrong (20) which states that two bodies differing only in their initial patterns of internal stress will develop identical stress patterns in regions of creep and plasticity if they are subjected to the same variations of temperature and load. The total strain increment is considered to be a sum of two components, δ_1 and δ_2, δ_1 being the plastic ratchet strain and δ_2 the increase in creep strain due to the steady stress state. As the on power duration increases, the incremental strains tends to an upper limit corresponding to complete relaxation of internal stress. When the on power duration is small, creep is insignificant and on the incremental growth criterion becomes that of the Bree Diagram without creep. It was noted that the creep law described was of a simple form which took no account of the effect of temperature. Because of the complexity of the results, it was impossible to present them in the simple form of a Bree Diagram.

Mulcahy (21) extended the analysis of Bree by assuming for the material properties an idealized Bauschinger effect. The material model was different from the work-hardening model described by Bree (2) which was of linear isotropic hardening while Mulcahy's model was one of linear kinematic hardening (Fig. 2.4). The result was presented as a Bree Diagram with the contours of upper limit accumulated ratchet strains. The hardening coefficient was chosen at the value K = 4.62 which corresponds to a hardening coefficient fitted to Type 316 stainless steel in the annealed state at room temperature. Fig. 2.5 shows that the contour of zero accumulated strain approximated very closely to the elastic/perfect-plasticity line. Therefore, the material response

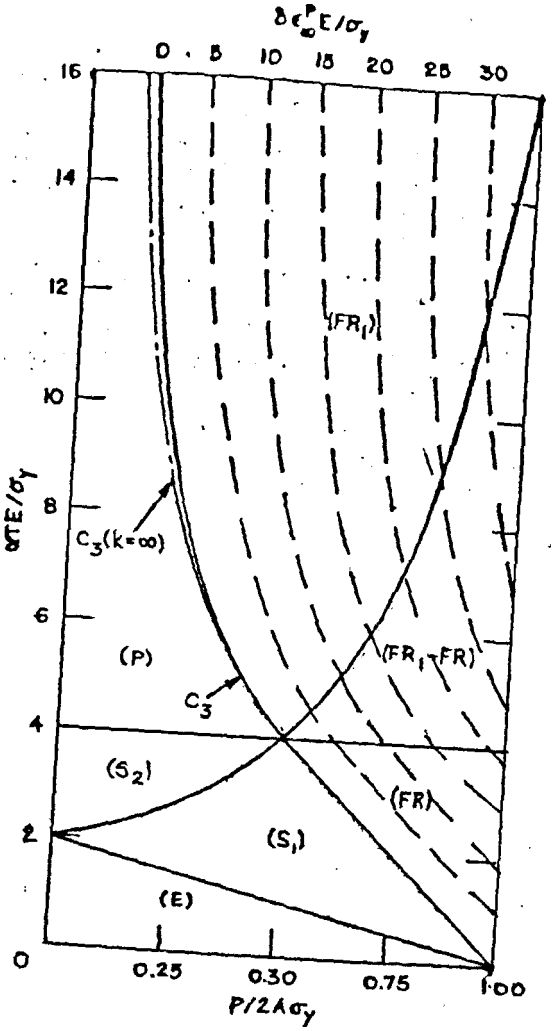

Fig. 2.5. Regions of Bree Type Behaviour and Constant Strain Accumulation Contours for K = 46.2. Mulcahy [21]

typical of reactor operating conditions, the ratchetting loads and temperature variations were very nearly the same as those of an elastic/perfectly plastic material. However, the amount of strain accumulation was found to be a most sensitive function, nearly inversely proportional, to the strain-hardening coefficient. The rate of strain accumulation per cycle was found to be a decreasing function with increasing cycle numbers. For a given strain-hardening coefficient, it was found that the maximum rate of strain accumulation occurred for the largest value of the temperature and was relatively insensitive to the pressure load. It was expected that 90% of the strain accumulation for an infinite number of cycles would occur within the first 25 cycles. The material model used by Mulcahy did not include creep effects because of the complexity of the analysis.

The material assumption of non-linear kinematic hardening has been investigated by Moreton and Ng (22). The uniaxial stress-strain curve was modelled by an Osgood-Ramberg (23) power law, using the uniaxial stress-strain data of a Type 316 stainless steel tested at room temperature. A computer program was written to calculate the accumulated strain, cycle by cycle. The results obtained showed the cycle numbers necessary to reach asymptotic strain accumulation is dependent on the thermal and pressure stress. These range from 5 to 20 cycles for a thermal stress range from $\frac{\sigma_t}{\sigma_y} = 3.0$ to $\frac{\sigma_t}{\sigma_y} = 4.5$. The results of Mulcahy (21) using the linear kinematic hardening material model shows that greater than 27 cycles are required. The smaller number of cycles required by a non-linear kinematic model is thought to be due to the conservatism of the linear model.

At present, no work has been published which investigates the effect of cyclic hardening or softening on the Bree beam model. There is

however a broad knowledge base of uniaxial cyclic stress/strain experiments and theoretical models. Ng and Moreton (24) have attempted to simulate the cyclic hardening effect by using a cyclic hardening model proposed by Jhansale (25) and preliminary results indicated that cyclic hardening had little effect except in a small reduction in the total accumulated strains over that of the non-cyclic hardening model.

At this juncture, it is useful to review the work of O'Donnell and Porowski (4) since it uses a simple approximate method to estimate creep and plastic strains. The generic name for these methods is simplified inelastic analysis methods. These methods are very useful in initial design studies since they provide an approximate evaluation of structural behaviour without expensive detailed computer inelastic analysis. A review by Leckie (26) introduces and discusses some of these methods used today. O'Donnell and Porowski's approach in bounding creep strain offer an alternative to Bree's partial relaxation method (19). They also considered the case of the thin tube as in the Bree analysis and used the same assumptions employed by Bree including the stress distribution he devised when the cylinder reaches a steady cyclic state. The method applies if the stresses are within the S1, S2 or P regions of the elastic/perfectly-plastic Bree Diagram and uses the maximum stress that occurs at any point in the shell wall which remain below the yield strength to bound the creep strains. The maximum stress value, called the creep stress σ_c was used to obtain the maximum creep strain that could be accumulated during the expected lifetime of the components. It can also be associated with the stress to give the required creep strain or some other allowable limit for the design lifetime and temperature of the component. The maximum creep strain or upper bound creep strain is obtained from creep properties of the material or from isochronous stress strain curves. The contours of stresses, denoted by σ_c/Sy shown in

Fig. 2.6 is to be used in obtaining upper bound strains. It should be emphasized that the bounds of O'Donnell and Porowski, bound only the uniform creep strain which accumulates during the elevated temperature part of the cycle. In order to evaluate the total inelastic strain (creep plus plastic) the plastic ratchet strain from Bree's analysis is added to the upper bound creep strain obtained by O'Donnell and Porowski. This additive operation may be questionable due to the possible microstructural interaction of plastic strain cycling on subsequent creep behaviour. This is principally of concern in region P where the outer fibres are subjected to plastic strain cycling as well as creep. However, due to the lack of information regarding this complex situation and the probability that the amount of material affected is small, the assumption was not regarded as unreasonable. The procedures have been tested and verified against the results of a series of detailed inelastic analysis (27) and is now being incorporated into the ASME Code Case N-47-12 (6).

The simplified methods for bounding creep strain was extended by O'Donnell et al. (28) to include biaxial stresses in shells. The method considers the simultaneous asymmetric loading on a shell of revolution where an overall expansion and thermal shock result in any combination of biaxial thermal stress components which are superimposed on the biaxial membrane stresses. A biaxial model was developed around a biaxially stressed element using the assumption of elastic/perfect-plasticity and the Tresca yield condition. The two orthogonal faces of the element were subjected to membrane stresses of the same or opposite signs and thermal stresses of positive or negative gradients through the thickness. Three different load situations were investigated. The analyses which are omitted here involved finding the elastic core stresses σ_{c1}, and σ_{c2} in the two principle directions at the shell midwall.

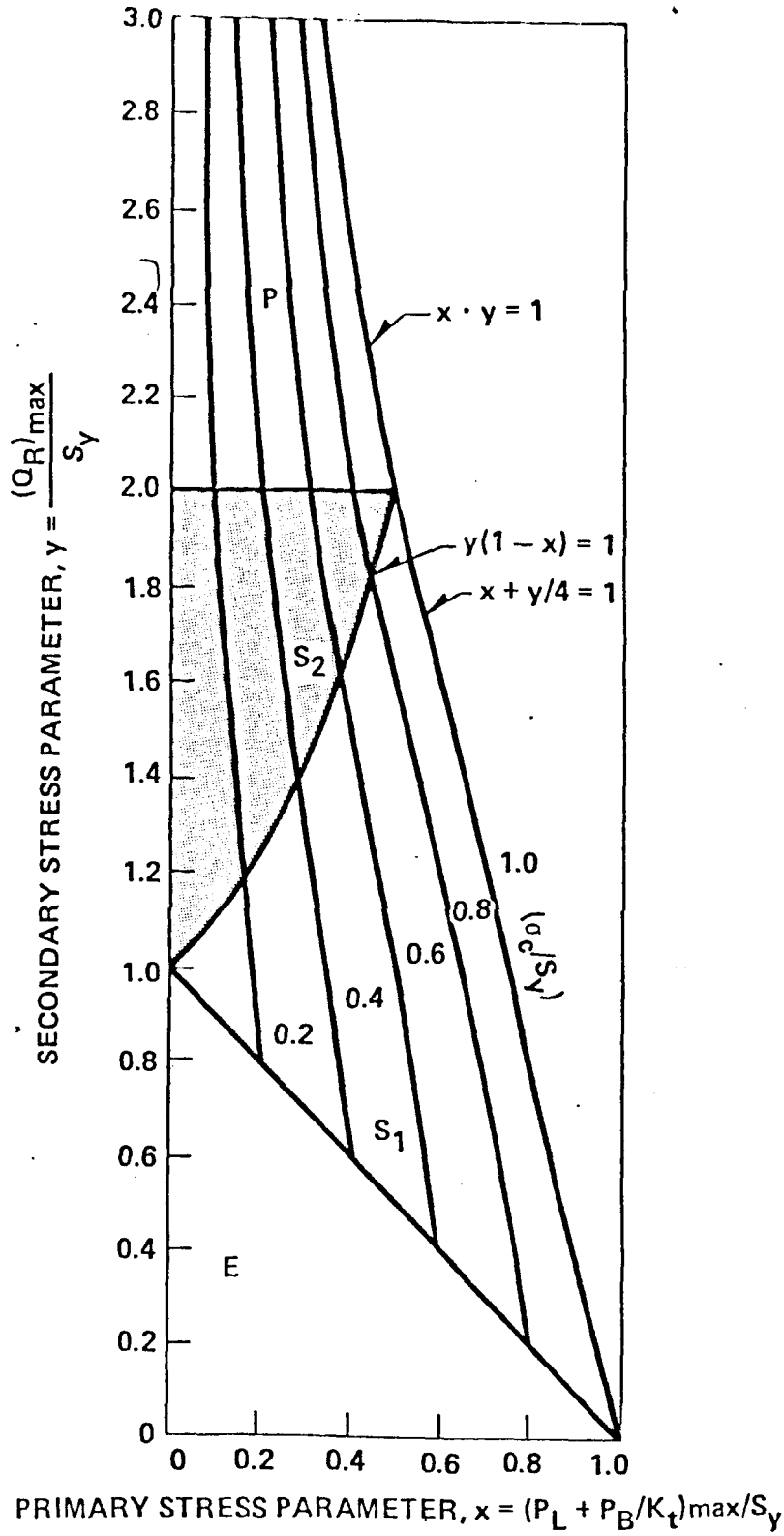

Fig. 2.6. Effective Creep Stress Loci, Based on O'Donnell and Porowski Upper Bounds. O'Donnell and Porowski [4]

From these two stresses, the effective stress $\bar{\sigma}$ was determined. The effective stress is related to the effective core strain for creep by the isochronous curves of the ASME Code Case N47 within the specified component lifetime. The separation of the effective core creep strain into its components in the principal directions was achieved by means of the Prandtl-Reuss flow relations. As a comparison the biaxial and the uniaxial model were used to bound creep strains in the case of the pressurized cylinder. Assuming a constant effective core stress, the maximum of the strain components calculated was 15% less than that given by the bounds of the uniaxial model. For the case of a pressurized sphere the value was 50%. These values indicated that the uniaxial model is conservative for pressurized spheres and cylinders and that the bounds can be improved by a biaxial model. For its simplicity, the uniaxial model can be advantageously used in shells where the biaxial membrane stresses are of the same signs and the biaxial thermal stresses on one face are both higher than on the other.

One of the major problems encountered in inelastic analysis is that of thermal transients in Fast Breeder Reactor Cores. These transients are caused by the rapid changes in temperature within the structures during shutdown or startup either in emergencies or in normal operation. The review up to this point has been concerned with steady cycling where the steady state temperature distribution is assumed to be allowed to develop. The effects of rapid thermal transients give rise to non-linear temperature distribution leading to more complex behaviour of the Bree beam model. Goodman (29) analysed the effects of these transient loadings on the Bree problem and used the same assumptions that Bree adopted, i.e. elastic/perfectly-plastic material and temperature independent yield stress without creep. He considered the effect of two forms of non-linear temperature distribution on the Bree Diagram and therefore illustrates

the types of problems to which the Bree Diagram cannot be applied directly. Two cases are considered, the first considers the effect of a thermal downshock (a rapid drop in temperature) on only one surface (Case 1) and the second, (Case 2), considers the effect on both surfaces simultaneously. To quantify the properties of a transient, two non-dimensional parameters were introduced, the Biot number B and the Fourier number F. The Biot number B is defined by $B = \frac{hd}{k}$ where h = heat transfer coefficient of fluid/surface interface, d = thickness of plate and k = thermal conductivity. This quantity defines the relative ability of the interface and the plate thickness to transmit the same amount of heat across a unit area. The Fourier number is defined by:

$$F = \frac{\tau}{\bar{\tau}} \qquad \text{where} \qquad \bar{\tau} = \frac{pcd^2}{K}$$

p = density and c = thermal capacitance. $\bar{\tau}$ is the characteristic time and it measures the rate of decay of temperature in a transient. F is therefore a measure of the relative value of τ(the ramp time) and $\bar{\tau}$ (the characteristic decay time). The ramp time is the duration taken by the drop or rise in temperature from the normal to reach the minimum or maximum temperature respectively in a transient. From these two dimensionless groups, a large B means a high heat transfer rate to the surface and vice versa and a large F means a very slow change in temperature and vice versa. The results calculated numerically by a computer program showed that for case 1 where the downshock is on a single side, there is a considerable reduction in allowable thermal loading for small primary loading but the effect is less significant for case 2. For the largest values of F (nearly quasi-static) and B, the ratchet strain per cycle coincides with the quasi-static case and is hence in accord with Bree's quasi-static model. Another important result comes from the study of plate thickness in the case of the double sided downshock. For a

prescribed value of the primary and secondary loading, the ratchetting strain per cycle decrease with the plate thickness, therefore there exists a critical plate thickness at which ratchetting will not occur. It has to be noted that although these results show that transients do have a severe effect upon ratchetting, the assumptions have however ignored the important effects of creep and the variation in yield stress due to temperature.

A theoretical analysis given by Phillips (30) extended the work of Goodman by considering the accumulation of creep and fatigue damage on the Bree plate. Creep damage can be caused by steady or cyclic primary load, by the relaxation of the thermal stress or both in combination. In the Bree type problems, the latter effect is the most important due to the high stresses that are regenerated at every cycle and sustained by hold time. Fatigue is caused by the repeated plastic strain cycling on the structure. The combined effect of creep and fatigue is assessed via the linear damage summation method recommended in ASME Code Case N47. The calculations examine the dependence of creep and fatigue damage on such factors as the applied loads, the degree of hardening of the material, the length of the creep dwell periods and the severity of the transient thermal loadings as measured by the Fourier and Biot numbers. The procedure for calculating the stress and stress distribution as well as the ratchet strain is similar to that of Goodman (29). The assumptions used for the material properties were that of kinematic hardening, and included creep. The creep law used represented the creep behaviour by

$$\dot{\varepsilon} = A_1 \left(\frac{\sigma}{\sigma_y}\right)^n e^{-Q/RT}$$

where A_1, σ_y, n, Q and R are constants.

The creep rupture lifetime t_r is represented by the equation

$$\left[\frac{|\sigma|}{\sigma_y}\right]^m t_r = A_2 e^{Q/RT}$$

where A_2 and m are constants

The values of the constants are chosen to represent as well as possible the behaviour of Type 316 stainless steel at 600°C. The creep damage is accumulated according to the rule of Robinson (31) given by

$$D_c(t_2) - D_c(t_1) = \int_{t_1}^{t_2} \frac{dt}{t_r(\sigma(t), T(t))}$$

where $\sigma(t)$ and $T(t)$ are the stress and temperature histories of the material under consideration. The fatigue damage is accumulated according to the rule of Miner (32) given by

$$D_f(N_2) - D_f(N_1) = \sum_{r=N_1}^{r=N_2} \left[\frac{\Delta\varepsilon_{p.r}}{A_3}\right]^{\frac{1}{\beta}}$$

where N_2 and N_1 are the cycle numbers, $\Delta\varepsilon_p$ is the plastic strain range and A_3 and β are material constants taken from low strain-rate fatigue data for Type 316 stainless steel at 600°C. The results of this analysis show that for an elastic-plastic material, creep and fatigue damage accumulates rapidly under large compressive stresses at the hot surface which leads to local failure of the surface fibres of the plate. For a hardening material, the strain and creep damage accumulation becomes very rapidly decelerated.

Creep damage accumulation was shown to increase with increase in dwell time. The effect was most significant on the hot surface but as the damage front takes a large number of cycles to propagate across the cross-section it may be that although the surface of the material has

nominally failed, the structural strength is still maintained. However, a larger dwell time meant a lesser degree of fatigue damage accumulation in the same period since the cycle per unit time is proportionally decreased. The realistic values of F and B in problems of this type are in the range of 0.01 to 1.0 for the former and large (>>1) for the latter. When $B \gg 1$, creep damage accumulation was found to be affected less compared with fatigue damage accumulation under variation of F. Fatigue damage was therefore significantly related to large B values. The overall deformation of the beam was increased by introducing rapid transient loadings as opposed to quasi-static thermal loadings and this occurred more significantly near the ratchetting boundary on the Bree Diagram. The assumption of kinematic hardening led to reduced accumulation in both deformation and damage when compared to an elastic/perfectly-plastic material. Again, it is necessary to note that simple models have been used in this study to obtain the above results.

Abo-El-Ata (33) had adapted the methods of Bree and O'Donnell and Porowski to account for irradiation induced creep and swelling of the structural material. The adaptation centred around the development of the maximum swelling induced stress model using certain simplifying assumptions concerning the irradiation effects. This stress model was then considered as an additional primary stress to be included in the constant pressure stress parameter of the Bree or O'Donnell and Porowski methods. In order to assess the justification of his method, it is necessary to follow his analysis in more detail. The analysis was limited to two irradiation related effects i.e. that of irradiation induced swelling and creep which are of importancein the fast reactor core area. Irradiation induced swelling is caused by void formation inside the grains and the rate at which this occurs was considered in the

analysis as constant with fluence (fast neutron flux integrated with time) but to increase with the temperature to a maximum (at about 500-600°C) beyond which it decreases. This temperature is significantly within the range (350-700°C) over which the fast reactor components are expected to operate. When swelling is restrained either by adjacent components or by differential swelling, swelling induced stresses will develop and become an additional loading mechanism to be accounted for in subsequent analysis. Analysis considering the induced stress on an elastic basis related to the swelling strain would be regarded as excessively conservative due to the stress relaxation of irradiation induced creep. Irradiation induced creep is the name given to that part of time dependent deformation under a given load and temperature condition attributed to neutron irradiation. In the simplest form used in the analysis irradiation creep strain at a given temperature depends linearly on stress and fluence.

Taking a material point on the Bree structure which is subjected to constant fluence and temperature, the consequences of swelling and creep occurring were considered. While the swelling induced stress was building up, irradiation creep tends to reduce these stresses since irradiation creep rate increases linearly with the stress. After an initial rise with fluence, the swelling induced stress is expected to reach a plateau and remain constant at that maximum value. Since the material never experiences a swelling induced stress higher than this value, elastically calculated swelling induced stress is therefore overly conservative. Swelling induced stresses do not disappear upon removal of the temperature gradient in the Bree element and hence may be considered as a primary stress. In using the methods of Bree (the solution based on complete relaxation of stress) and O'Donnell and Porowski (for calculating the upper bound creep strains), the effect of thermal creep

and stress are also included. The thermal stresses which are due to the temperature gradient can be relaxed by thermal and irradiation creep. The Bree complete relaxation method and the O'Donnell and Porowski upper bound method may be used conservatively to evaluate the strain accumulation after including the maximum swelling induced stress in the primary stress calculations. In summary the author recommended the following procedure for evaluating plastic and thermal creep strains:

1. When thermal creep is insignificant, secondary stresses will be relaxed by irradiation creep such that shakedown occurs only in the E region of the Bree Diagram. The plastic ratchet strains may, therefore, be conservatively estimated by Bree's complete relaxation method.

2. When thermal creep is significant, secondary stress relaxation will occur due to both thermal and irradiation creep. In this case, the plastic ratchet may still be evaluated using Bree's complete relaxation method while the uniform thermal creep deformation may be evaluated using O'Donnell and Porowski's upper bounds.

By using the methods proposed, it is implied that the assumptions inherent in the Bree's and O'Donnell and Porowski's analyses are used. Furthermore, the assumptions of negligible irradiation creep and swelling during the lower temperature part of the cycle are unrealistic because these effects are strongly fluence and not temperature dependent. However, it is noted that the analysis used experimental evidence based on Type 316 stainless steel at 500°C.

Owais and Otter (34) examined the solutions of the reference stress method proposed by Ainsworth and Goodall ((35) and 36)) in which the reference stress was obtained from the limit or shakedown analysis of the Bree structural model and the upper bound creep solutions of the ASME

Code Case N47. A full finite element inelastic study of the Bree model was also made to investigate the creep and creep damage using as material data, that of Type 316 stainless steel. The object was to assess the validity and conservatism of the different methods. The need for simplified methods of inelastic analysis has already been recognised as a useful tool for performing initial screening of designs without incurring the expense of full finite element analysis.

The load cycle characteristic was however dissimilar to that of Bree where the mechanical load was maintained constant. The authors considered the load cycle which was more like the conditions present in the reactor situations. Here the mechanical load was cycled such that it was applied just before applying the thermal load and removed after the thermal load had been removed. Therefore the mechanical load was always present during the application of the thermal load. Assuming temperature independence, the effect of cycling the pressure load on the Bree Diagram is shown in Fig. 2.7. It is observed that although the ratchetting boundary remained the same, the boundary between shakedown and alternating plasticity decreased meaning that some region of shakedown behaviour had become that of alternating plasticity. The finite element computation simulates the cyclic conditions as follows: the low and high temperature (wall averaged) are 370 and 600°C respectively. No creep occurred at low temperature while at high temperature, a hold period of 1000 hours was allowed for creep to develop. Pressure cycling had a zero base value. The material was modelled as elastic/perfectly-plastic and had a creep strain rate dependent on stress and temperature (based on secondary creep law). Comparison between the results are for a primary stress level of 0.44 and various secondary stress levels ranging from 1.0 to 1.5 which all lie within the shakedown limit. Neglecting all the calculations

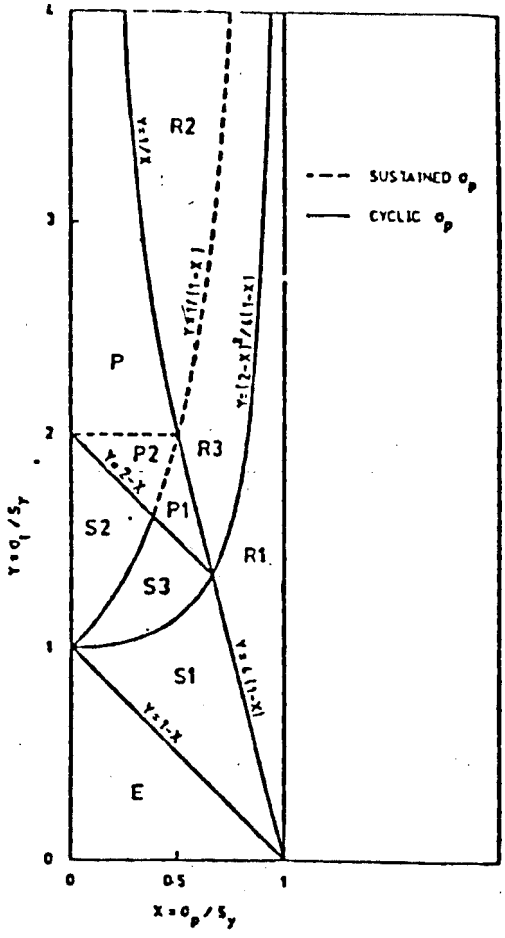

Fig. 2.7. Stress Regimes for Sustained and Cyclic Primary Stresses Compared. Owais and Otter [34]

for the simplified methods, the results of the comparison showed that for the maximum accumulated creep strain at the end of cycling, the degree of conservatism relative to the finite element results, in increasing order were as follows: N47, Shakedown and the lower bound shakedown methods. Both N47 and the shakedown method showed increasing conservatism with increasing secondary stress level. As for creep damage prediction, the increasing order of conservativeness were, shakedown, lower bound shakedown and N47. The outcome of this study showed that although computer inelastic analysis was least conservative, the simplified methods showed varying degrees of spread; for creep strains, there is an order of magnitude of variation and for creep damage, that order is two.

2.5 Experimental Investigations on the Bree Model

The ratchetting phenomenon had been observed and reported by many workers often as the results of investigations into pressure vessel behaviour. Weil and Rapasky (37) while investigating pressure vessels subjected to repeated thermal stresses observed progressive distortion. Coffin (38) in his work on fatigue under repeated straining of uniaxial specimens also observed incremental growth under combined steady and cyclic loads. Moreton and Moffat (39) among others reported persistent cyclic strain increments in stainless steel pressure vessel components when the repeated pressure load exceeded the shakedown pressure. The work by Parkes (40) which involved a study on the problem of incremental collapse of an aircraft wing with aerodynamic skin heating superimposed on the normal wing loading was perhaps the first to seriously study the subject.

As for experimental studies of the Bree beam problem, the first tests were performed by Goodall and Cook (41) on En58J stainless steel (18 Cr:8 Ni:Mo) beam specimens in the annealed condition at 600°C. The experimental procedure used a mechanical loading technique consisting of two hydraulic rams which were independently controlled to exert axial and bending load on a beam type specimen. In these tests the cycle time was 4 cycles/min. which was assumed to be short enough for creep to be neglected. Three tests were conducted under varying axial loads each with a fixed bending load of $\frac{\sigma_t}{\sigma_y} \simeq 4$, which therefore lie in the R2 region of the Bree Diagram. The ratchet strains were plotted against cycle number for both theory and experiment. The theoretical ratchet strains were calculated on the elastic/perfectly-plastic model of Bree, the yield stress of 200 MN/m^2 was selected from an elastic/perfectly-plastic fit to the stress strain curve of the test material and this was approximately

10% higher than the 0.2% proof stress. It was seen that the results accorded very well with the theory for the initial cycles. The accumulated strain thereafter decreased as would be expected of a strain-hardening material and was about half the value theoretically predicted after 5 cycles. About 10 cycles of loading were applied to each specimen.

The series of tests were carried out by Anderson (42) using an experimental set-up which was described in a previous publication (43). The loading method used to simulate the thermal loading was again by bending a specimen to a fixed curvature. In the test procedure, the specimens were subjected to constant axial stress and to represent the thermal strains were bent alternatively around two mandrels of opposite curvature at a temperature of 649°C. It is noted that the tests simulated a particular type of loading where the temperature gradient alternates in the sign of its slope every other cycle. Such a case had not been considered in Bree's analysis where the gradient is only of one sign. The tests which were conducted on Type 304 stainless steel, were 20 in number and the number of cycles applied varied from 10 to 16. A number of testing points were selected on the Bree Diagram. The experimental results again showed that the first few cycles of accumulated strain correlated very well with the prediction of Bree. However, agreement was not achieved for these cases where ratchetting was not predicted. The ratchetting boundary was calculated using a design yield stress of 1.5 S_m where S_m according to the ASME III Code is 0.9 the 0.2% proof stress at above 427°C. Several specimens which were within the non-ratchetting boundary acquired deformation exceeding 1%. The value of 1% is the deformation limit set by the ASME Code Case N47. These cases would however all lie within the ratchetting regime if it was calculated based on 1.0 S_m as the design yield stress. The tests were all completed within 24 hours but because the

temperature was so high, the magnitude of the creep strain contribution to the total accumulated strain was uncertain.

A series of tests were carried out by the author (22) using an experimental rig which is to be described in greater detail in chapter 4. The material used was mild steel and the tests conducted at room temperature. Mild steel was selected for its near elastic/perfectly-plastic characteristic. This material was thus ideally suited for verifying the Bree Diagram. The experimental results showed that like the results of Goodall and Cook (41) and Anderson (43), the point of onset of ratchetting, is in good agreement with Bree, the rate of strain accumulation, however, was not in agreement with Bree.

Another series of tests have been conducted by Yamamoto, Kano and Yoshitoshi (44). Tests were conducted on hot rolled Type 304 stainless steel pipes in a solution treated condition by passing through it alternatively hot and cold sodium. This alternate flow of sodium subjected the inside of the pipe to an alternate increase and decrease of temperature varying from 550 to 250°C in one of the tests. The pipes were each subjected to increments of axial load and a total of 5000 thermal cycles; 140 thermal cycles were applied at each increment of axial load. The temperature difference (between hot and cold sodium) was maintained constant all the time and the cycle time was about 10 mins. A ratchetting boundary on the Bree Diagram was plotted based on the experimental results and is shown in Fig. 2.8. By calculating backwards, this boundary was found to coincide with theoretical prediction if the yield stress was 20% higher than the 0.2% proof stress. Also, it was calculated that the accumulated strain can be more closely evaluated by including linear work hardening. This test was carried out without interruption except for the increase in the axial load after every 140 cycles of thermal cycling. It

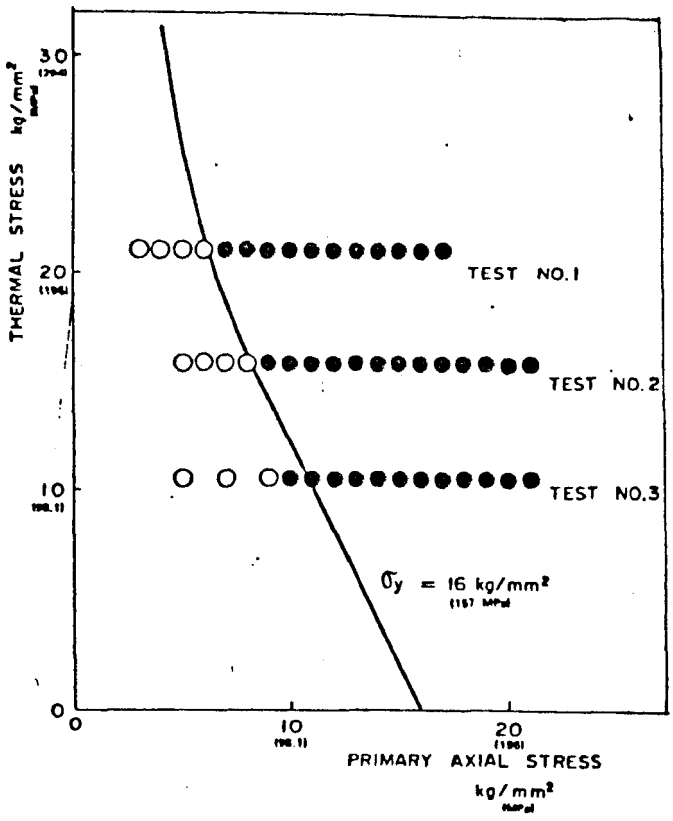

Fig. 2.8. Test Conditions and Limiting Boundary of Ratchetting in Stress Region R. Open and Solid Circles Represent Shakedown and Ratchetting Respectively. Yamamoto et al. [44]

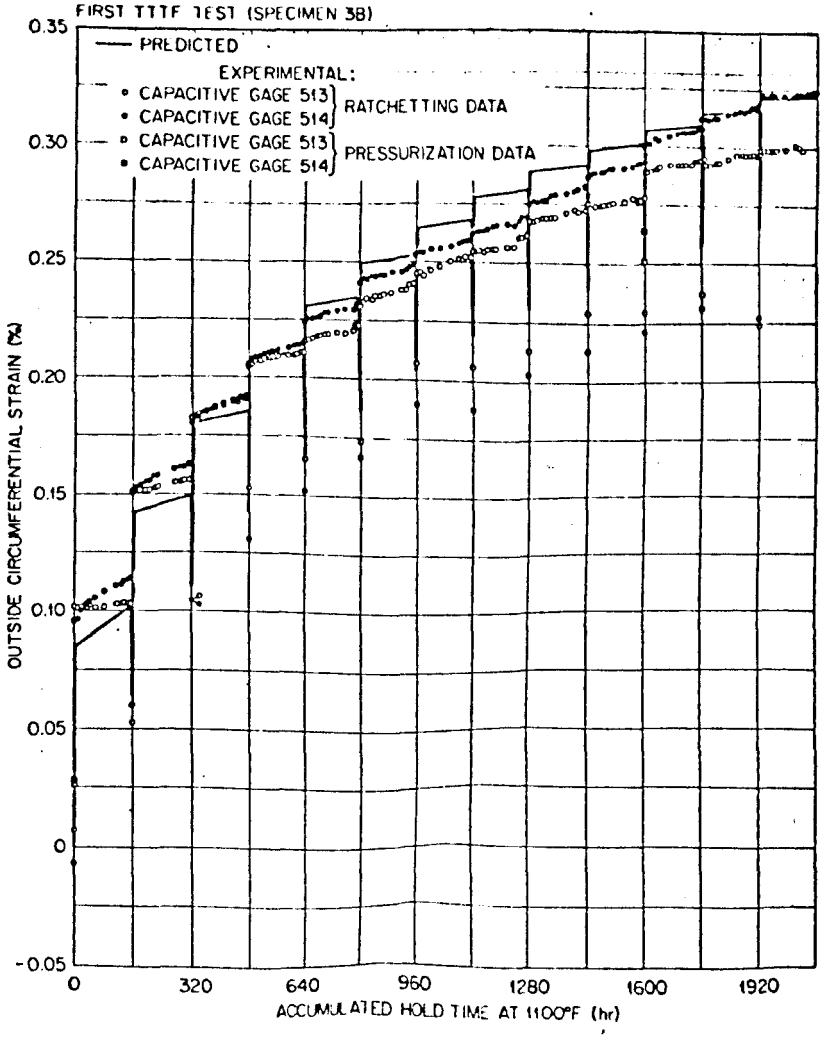

Fig. 2.9. Comparisons of Measured and Predicted Circumferential Ratchetting Strains at the Outside Surface of the First Pipe. Clinard et al. [47]

was found that at the initial 5 increments of load (low values of axial load), no strain was accumulated indicating shakedown or alternating plasticity behaviour. At the 6th increment, the strain was seen to accumulate over the first few cycles and gradually drop to a rate which appeared to be constant. The comparison between the predicted ratchet strain increments per cycle using Bree's equation for non-workhardening and the experimental results shows that Bree may be over conservative.

Corum et al. (45) conducted two pipe ratchetting experiments at elevated temperatures as part of a programme of research at Oak Ridge National Laboratories (ORNL) to provide experimental data for benchmark problem calculations. These experiments have already been referred to in the introductory chapter in connection to their use in verifying the author's program in this thesis. The tests have been very well conducted and yielded very interesting results. Firstly, the experiments will be explained, followed by the results.

The pipes used were similar geometrically and were made from a well documented heat of Type 304 stainless steel. The properties of the steel had been thoroughly analysed and are reported by Corum (46). The data were intended for use by analysts and designers for testing their programs and included the following; elastic constants and stress strain curves from 800 to 1100°F (427 to 593°C) and at room temperature and uniaxial constant-stress creep data for 1100°F plus other physical properties. Each pipe test specimen was 30 in. in length at the test section, having an external diameter of 8.44 in. with wall thickness of 0.375 in. The first test subjected the pipe to a nominal sodium temperature and pressure of 1100°F and 700 psi respectively during the long term hold periods. The thermal transient occurred first from 1100°F to 800°F at a rate of 30°F/s. When the temperature reached 800°F, the internal pressure was removed completely

and instantly reapplied. When the pressure steadied at 700 psi, the temperature was returned to 1100°F at a lower rate of 50°F/hr. A hold period was applied for 160 hrs before the next transient initiated. For this specimen 13 cycles were applied. The second specimen was subjected to 23 cycles of which the first 5 cycles consist of a thermal transient from 1100 to 800°F at a rate of 22.8°F/s and at the nominal pressure of 400 psi. Following this, 13 more severe cycles similar to that first specimen test were then applied to be followed by 5 more cycles at the original conditions.

The test approach utilized a one way flow of sodium which was heated and controlled by a network consisting of a pipe nest and tanks. The sodium was stored at 800°F and heated when required by the pipe nest to 1100°F before entering the specimen pipe, on exit it drained into a storage tank. Argon gas was used for the pressurization system. The specimen pipes were lagged and surrounded by a zone controlled oven for maintaining the uniform temperature against heat loss. They were fully instrumented for measurement of through thickness and spacial temperature distribution. Strains are measured by capacitance type strain gauges and by extensometers.

On the first transient, the through thickness temperature distribution against time was measured and compared against predicted thermal response. The good agreement showed that the authors have verified the correct thermal loading.

The measured response of the first specimen shown in Fig. 2.9 indicated substantial ratchetting in the early cycles but the increments of growth/cycle decreased continually with the increasing number of cycles. The second specimen exhibited an initial increment of growth during the first 5 cycles and little thereafter. This is shown in Fig. 2.10. It is seen

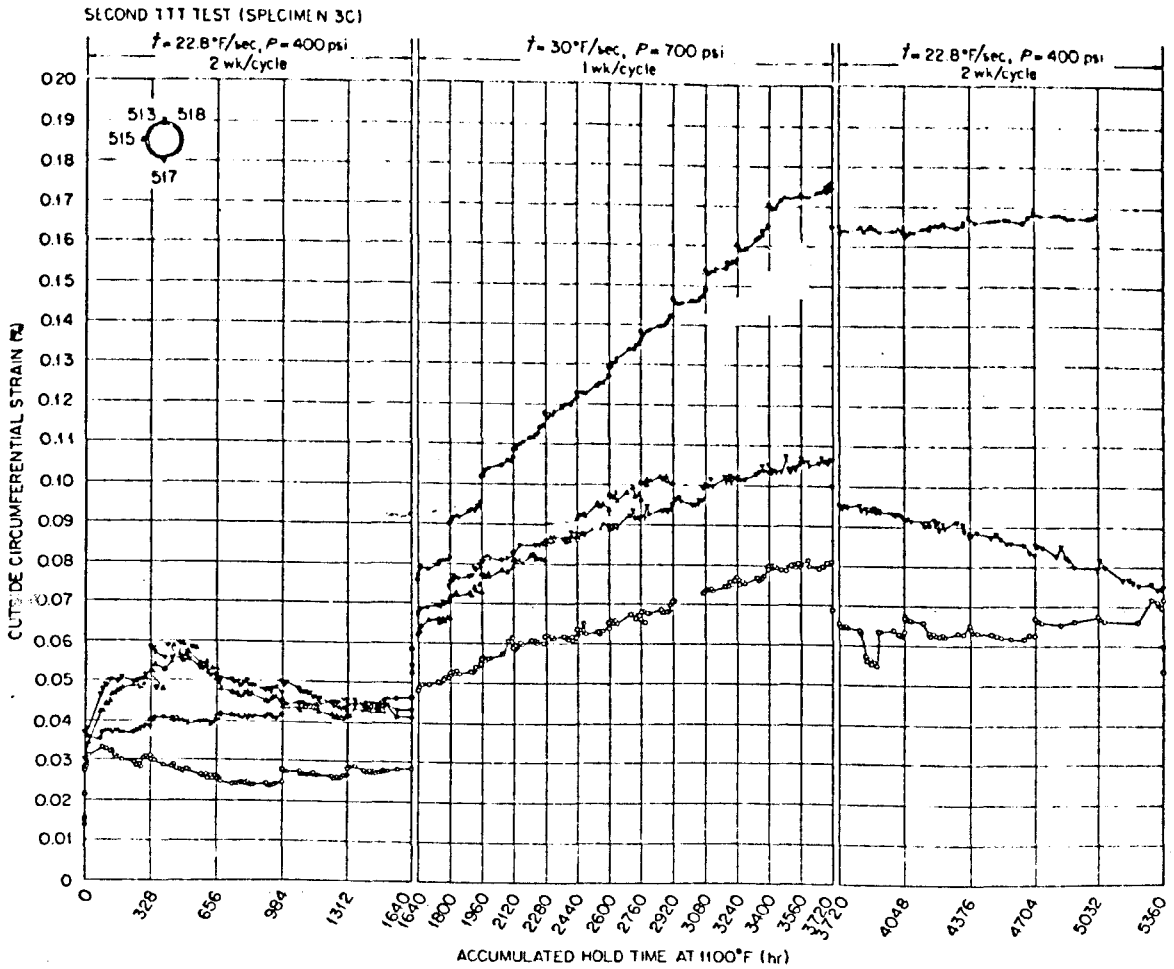

Fig. 2.10. Measured Circumferential Ratchetting Strains on the Outer Surface of the Second Pipe. Corum et al. [45]

that on applying the more severe load, the ratchetting is increased greatly but this is not as much as in the first specimen. On removing the severe load, ratchetting ceased completely. This behaviour shows that the initial severe cycles have overloaded and work-hardened the specimen such that the ratchetting response is decreased. The creep strains accumulated during the hold periods as seen in the Figures 2.9 and 2.10, are small when compared to the ratchet strains at each transient during the initial cycles but become of similar magnitude in the latter cycles.

It is noticed that because the pipe specimens were lagged and heated to maintain constant through-thickness pipe temperature, the temperature gradient was of an approximately parabolic form but existed only for a short duration (about 32s) during the drop in temperature of the sodium. The peak temperature difference was measured at 175°F (97°C). During the rest of the hold period, the through-thickness temperature and hence the stress distribution became uniform. It is during the transient period that the thermal gradient assumed by Bree is applicable. This difference has significant implications. The loading prescribed by Bree is one where a continuous thermal gradient is present during the on-power phase due to the continuous heat transfer from inside to outside the wall. If sufficient time is allowed for stress relaxation effects to take their course on the non-uniform through thickness stress distribution, a different response will be seen. Furthermore his analysis is not applicable due to the cyclic pressure loading. An inphase cyclic thermal and pressure loading in a quasi-static approximation is more appropriate for representing this Bree type behaviour.

The experimental data provided by this benchmark problem have been utilized by Clinard et al. (47) for verifying their finite element computation and by Ainsworth and Goodall (36) who applied a bounding theorem

above the short term shakedown limit on Bree's uniaxial model. Both solutions were only applied to the loading of the first test. The organisation of the finite element method of Clinard et al. will not be described here but it appeared that the predictions of the strain accumulation were almost exact as shown in Fig. 2.9. The solution of Ainsworth and Goodall involved the work and deformation bounds which apply to the steady cyclic state conditions. Again omitting any reference to the highly involved analysis, the upper bound predictions when compared to the experimental data overestimated the accumulated strains which peaked to a maximum of 20% above the strain value at the 13th cycle. This deviation considering the assumptions made was regarded as good agreement. It was noted that the upper bound and the finite element methods have no allowance for the effect on material properties of any creep-plastic interaction since they both employed the material data provided by Corum (46). It was suggested by Ainsworth and Goodall that since the agreement has been good, any creep-plastic interaction has negligible effect on the overall deformation at least as far as the present case was concerned.

2.6 Studies on Other Structural Geometries

In this section, the theoretical and experimental response of other structures which are subjected to constant primary and cyclic secondary loads are examined. These structures are under much investigation because they exhibit many of the real features of structural behaviour such as plastic cycling, shakedown and ratchetting. These responses are similar to that of the Bree uniaxial model and can therefore be called Bree-like. From a general survey, three main categories of structures have been identified. They are: (a) the two-bar structures, (b) axially loaded and cyclically twisted cylinders or tubes and (c) axially loaded tubes with travelling axial temperature gradient. These categories are surveyed in that order. The aim of this section is to encompass all these studies together under the general heading of Bree-like problems and examine the similarities and differences between the various types of structures and the applicability to real problems.

2.6.1 The Two-Bar Structure

The geometry of the structure is shown in Fig. 2.11. As can be seen the deformation is constrained to be in the axial direction when subjected to a steady load P in addition to the cyclic temperature history during which the temperature of bar II is cycled between T_o and $T_o + T$. The temperature of bar I remains constant at T_o. In the figure, the lengths and cross sectional areas are unequal and the relative ratios are represented by η and γ respectively and thus the relative volumes of the material undergoing deformation are varied. The calculations are relatively easy to perform on such structures when based on elastic/perfect-plasticity.

The two-bar structure was examined firstly by Parkes (48) who, in a series of publications, examined the problem of thermal cycling of

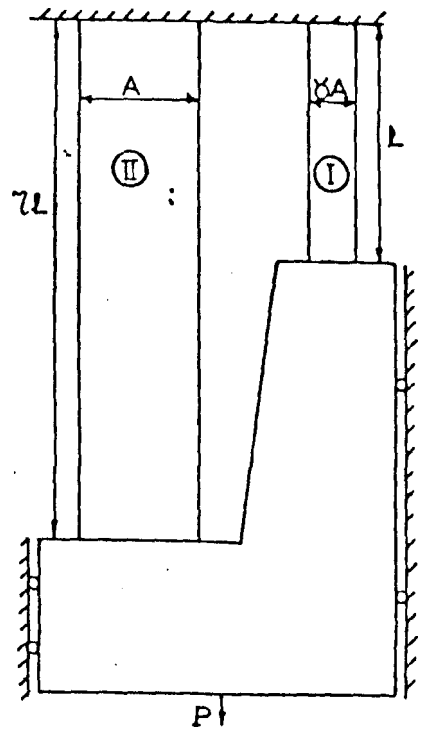

Fig. 2.11. The Two-Bar Assembly. Megahed [51]

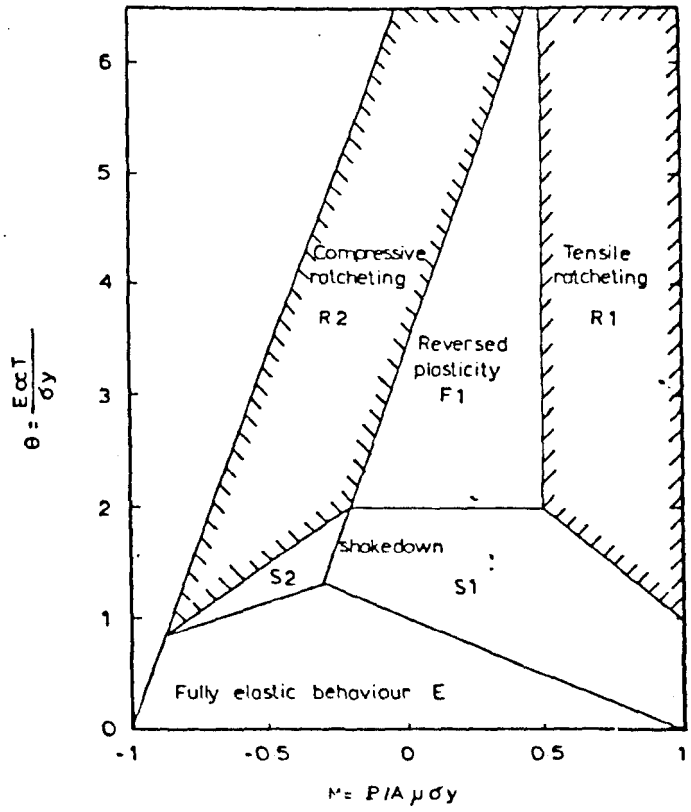

Fig. 2.12. Modes of Behaviour for a Two-Bar Assembly for $\eta = 2$, $\gamma = 0.5$ and the Temperature Dependent Parameter $\rho = 0.15\theta$. Megahed [51]

high speed aircraft wings subjected to aerodynamic friction heating on the skin combined with the normal wing loads. The wing was simulated as a two-bar structure. The heated bar represented the skin and the constant temperature bar represented the web between the skins. The effects of the essential parameters on the behaviour of the wing were demonstrated by the model. Miller (1) discussed the mechanism of thermal ratchetting on the two-bar structure and showed that material strain-hardening reduces the ratchet strains considerably. Burgreen (17) investigated the modes of response of the two-bar structure for elastic/perfectly-plastic material like those before him but accounted for unequal length and cross-sectional areas of the bars. Brunsvold et al. (49) extended the analysis for kinematic material behaviour to account for the Bauschinger effect and also included the parameter for variable material properties for the bars. Mulcahy (50) analysed and compared the kinematic hardening, elastic/perfectly-plastic and isotropic hardening material for a two-bar structure with equal areas and length ratios. Finally, in the most recent publication, Megahed (51) improved on the work of Mulcahy by accounting for unequal area and length ratios. Ainsworth (52) used the method of reference stresses and temperatures to obtain approximate solutions for creep in two-bar structures. Because of the uniaxial conditions that exist in a two-bar structure, the reference parameters were easily obtained from uniaxial creep data.

Briefly, the elastic solution to this problem is as follows: when the axial force P is applied before thermal cycling, the elastic stresses due to P from equilibrium and compatibility considerations are,

for bar I, $\sigma_I^P = P/\mu A$, for bar II, $\sigma_{II}^P = P/\mu\eta A$

where $\mu = (1 + \gamma\eta)/\eta$

When the thermal loads are applied in the first half cycle to bar II, the thermal stresses are given as,

$$\sigma_I^t = E\alpha T/\mu \qquad \text{and} \qquad \sigma_{II}^t = -\gamma E\alpha T/\mu$$

where T is the maximum temperature difference between bars I and II

α,E the coefficient of linear expansion and modulus of elasticity respectively

Hence, the stresses in the bars will oscillate between σ_I^P and $\sigma_I^P + \sigma_I^t$ for bar I and σ_{II}^P and $\sigma_{II}^P + \sigma_{II}^t$ for bar II on thermal cycling.

For the purpose of classifying the two types of loading, the primary or mechanical load is characterized by

$$M = P/A.\sigma_y.\mu$$

and the secondary or thermal load by

$$\theta = E\alpha T/\sigma_y$$

where σ_y is the yield stress. The two normalized parameters form the axis of a Bree-type diagram showing the various deformation behaviour of the structure. Solutions are obtained analytically by solving successively the problem to determine the states of stress and strains satisfying the condition of equilibrium, compatibility and current stress strain relations.

The Bree-type diagram for an elastic/perfectly-plastic material with temperature dependent yield stress was obtained by Megahed (51) and is shown in Fig. 2.12. It is seen that the modes of behaviour are similar to that of Bree. Here, in the elastic (E) region there is

fully elastic behaviour in both bars. In the shakedown (S1 and S2) regions, a limited amount of plastic strain has occurred in one of the bars in the first half cycle. In the reversed plasticity (F1) region, alternating plastic cycling has occurred in one of the bars. In the ratchetting region (R1 and R2), an equal amount of plastic strain increment has occurred in both bars. The mechanism of ratchetting is described as the alternative cyclic plastic straining of the two bars where plastic strain incurred in bar I during the heating half cycle is followed by the same in bar II during the subsequent cooling half cycle.

The effect of altering the area ratio is to vary the relative volumes of the material that are undergoing thermal cycling while varying the length ratio would represent the effect of a stress concentration within a real structure. These simulations are conceptually useful for studying structural behaviour where there is a high cyclic local stress acting on one part while the rest remains at a relatively low stress. This high local stress may be caused by mechanical or thermal loads. Two-bar structures can be used to predict structural behaviour provided the correct physical relation is found between the model and the structure in question.

One of the greatest attractions of the two-bar model is its ability to translate from model to experiment without great difficulty. The two-bar model has the experimental advantage that the thermal load can be imposed on one bar without greatly affecting the other. While the model consists of two bars, experimentally three bars are often required so that no lateral restraints are needed to keep the bars straight during the temperature changes on either the centre or the two side bars. Experiments have been conducted by a number of workers

for different test temperatures, material and bar cross sectional shapes.

Gatewood et al. (53) reported experiments on a three-bar assembly under "equivalent" thermal cycling. By "equivalent", it was meant that a compression stress equal to the thermal stress on the centre "heated" bar was induced by heating the connecting link between the bar and the rigid support thus inducing the thermal stress. This compression stress experienced by the centre bar was "equivalent" to the thermal stress. This was done to eliminate the temperature effect on the test material, the three bars remained at room temperature. The conditions for ratchetting and shakedown were studied but no attempt was made to compare the experimental results with the theoretical estimates of ratchetting strains. Swaroop and McEvily (54) tested tubular specimens of Type 1020 steel arranged in a three-bar assembly. The centre bar was cycled within the temperature range 159 to 620°C. The axial load was varied at four values. The ratchetting strains calculated according to the Miller-Burgreen approach were found to agree well with the experiment. Uga (55) reported an experimental study of thermal ratchetting in the three-bar specimen made from Type 304 stainless steel. Uga used a plate-shaped specimen with two symmetrical air gaps in the centre portion and load chucks at the ends. The side bars were heated to 405°C and the centre bar to 180°C in one half cycle and all the bars were at 50°C at the next half cycle. The tests (5 in number and lasting 21 cycles each) showed incremental strain growth which decreased with the cumulative strain growth. Megahed (56) used the experimental results of Uga to verify the results of his analyses. By firstly modifying the theoretical thermal cycle to the one used by Uga, satisfactory agreement was obtained between the linear isotropic and kinematic hardening models within the 21 cycles tested. The number of cycles in these tests were

too low for steady state strain accumulation to be reached. The hardening rules were seen to give a better prediction of cyclic growth at low cycles but would overestimate the growth if the experimental results were extrapolated to larger numbers of cycles. The elastic/perfectly-plastic model consistently predicted a much larger strain accumulation.

Ainsworth (57) conducted tests using Type 316 stainless steel in the usual three-bar assembly at a common temperature of 600°C while the centre bar was cycled between 600 and 700°C. The results of the 6 tests which were all carried out at a constant primary load but at various hot dwell times and total cycle times were compared with theoretical predictions based on the approximate reference stress and temperature solution of reference (52). The conclusions were that the cyclic temperature tests supported the predictions that cycle times have a small effect on behaviour in the cyclic stationary state. The cyclic stationary state as proposed by Frederick and Armstrong (20) is a state of periodic stress distribution in the structure when operating in the creep range and subjected to periodic load and temperature. The predictions of the average displacement rates have been conservative and were supported experimentally by the constancy of the displacement rates seen during the periods when temperature and mechanical loading were constant.

2.6.2 Axially Loaded and Cyclically Twisted Cylinder or Tube

These tests are performed on either thin walled tubes or solid cylinders under constant axial load P and reversed cyclic torsion between two shear strain limits of range $\Delta\gamma$. The shear stress range calculated on an elastic basis is ΔQ equal to $2.G.\Delta\gamma$, where G is the shear modulus.

The primary stress is defined as P/A, where A is the cross-sectional area and the secondary stress is the shear stress amplitude which is $\Delta Q/2$. The deformations are measured in the axial direction.

The above assumptions that the axial stress is equivalent to the primary stress and the shear stress amplitude to that of the secondary stress that occur in real structures subjected to thermal cycling (e.g. tubes and plates) is so far not well substantiated. The primary and secondary stresses as defined in the codes are based on a stress system which is dissimilar to the stress system used in these tests. Some researchers have already assumed that these stress definitions are applicable to design and certain correlations in experimental results seem to support these claims. This is because the test results are representative of that produced by stress systems in practice although they arise from a different cause. These correlations are described later in this section. Firstly the experiments undertaken for this class of loading are given.

The early tests were carried out by Inoue et al. (58) on copper rods at room temperature from 400 to 1900 cycles. Nozue et al. (59) conducted tests on Type 304 stainless steel tubular specimens at room temperature at various axial loads against constant shear strain limits for about 600 to 800 cycles. Some relatively recent tests were performed by Lebey et al. (60) and their co-workers at the Centre d'Etudes Nucleaires (CEA) at Saclay in France. These tests were performed at room temperature for Type 304 stainless steel and at room temperature, 300°C and 600°C for Type 316 stainless steel using tubular specimens. The test results are shown in Fig. 2.13 for both steels at 10 and 500 cycles. It can be observed that these are similar to the Bree Diagram, in that for low secondary stresses, small changes in primary stress

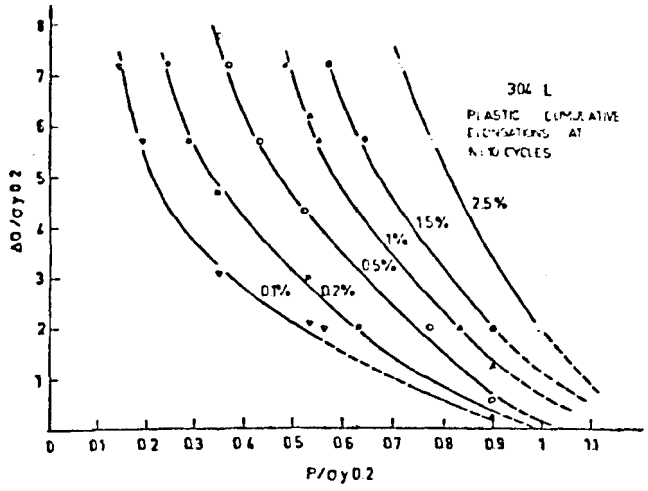

304 L steel. Plastic cumulative elongations at N = 10 cycles

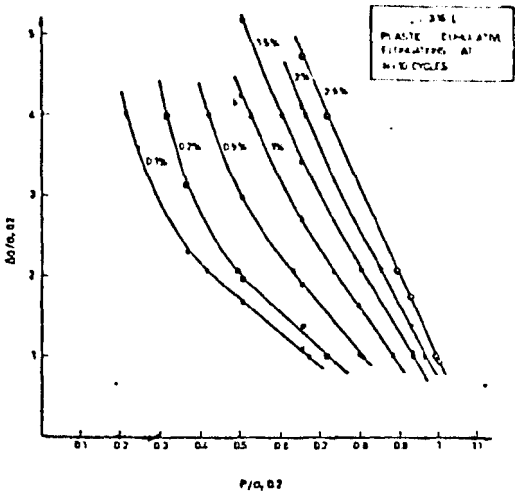

316 L steel. Plastic cumulative elongations at N = 10 cycles

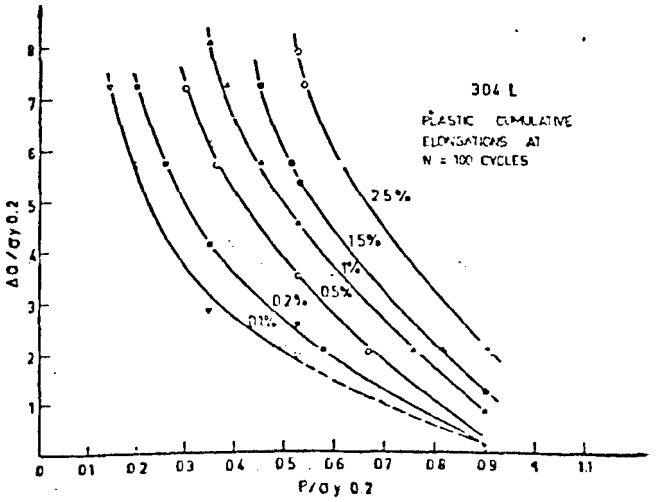

304 L steel. Plastic cumulative elongations at N = 100 cycles

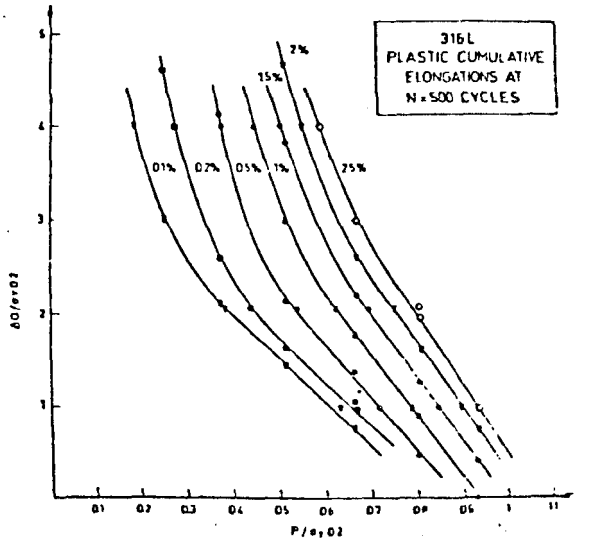

316 L steel. Plastic cumulative elongations at N = 500 cycles

Fig. 2.13. Contours of Constant Accumulated Strain After Various Numbers of Cycles for Type 304 and 316 Stainless Steel. Lebey et al. [60]

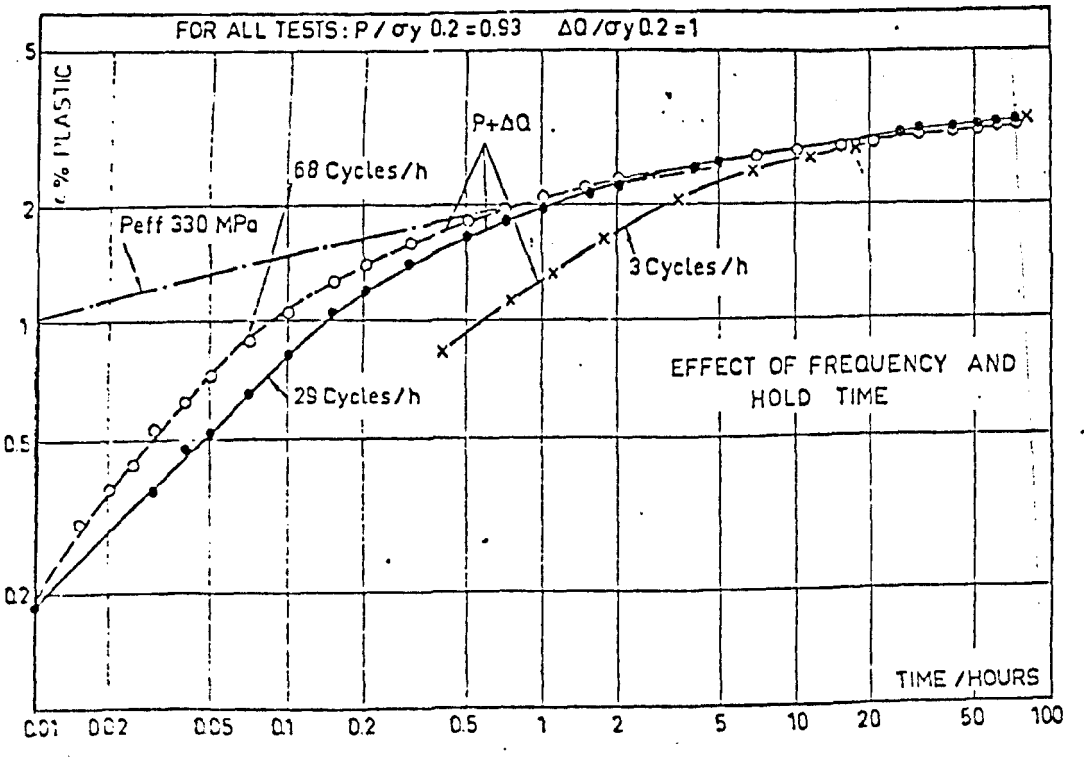

Fig. 2.14. The Effect of Frequency of Cyclic Tests Compared with the Creep Curve at a P_{eff} Stress for Type 316 Stainless Steel at Room Temperature. Cousseran et al. [61]

cause large strain accumulation while the reverse occurs for large secondary stresses. Cousseran et al. (61) later reported tests where the cycle time of the tests were varied. The results shown in Fig. 2.14 is a plot of plastic strain accumulation against total time. It is seen that the effect of frequency vanishes after a short time and the accumulated strain of all the tests tends toward a same asymptotic value after a period of time. Also plotted is the cold creep strain of a test at stress equal to 330 MPa. Because of the coincidence of the maximum accumulated strains of the various tests to the creep strain, this stress is called the "effective stress" or P_{eff}. The significance of this stress value will now be explained.

Lebey et al. (60) described a method of correlating the results of ratchetting experiments conducted by other workers on other structural geometries such as the Bree beam tests and two-bar structure tests. The method was based on finding the "effective primary stress" P_{eff} which was defined as the fictitious primary stress which when applied alone without the secondary stress would cause the same amount of deformation as that in a test with both the actual primary and secondary stress applied together at the same temperature and within the same time of the actual test. P_{eff} was determined from a known test deformation against either the instantaneous tensile curve or creep curve of the same material.

Two further parameters are defined, the secondary stress index, SR as $SR = \Delta Q/(P + \Delta Q)$ and the efficiency index V as $V = P/P_{eff}$. The plotting of V against SR^2 of any test data gives the so called efficiency diagram. The sources of experimental data that were used and the corresponding efficiency diagram is shown in Fig. 2.15. It is seen that if the experimental points were made to lie consistently to one side of

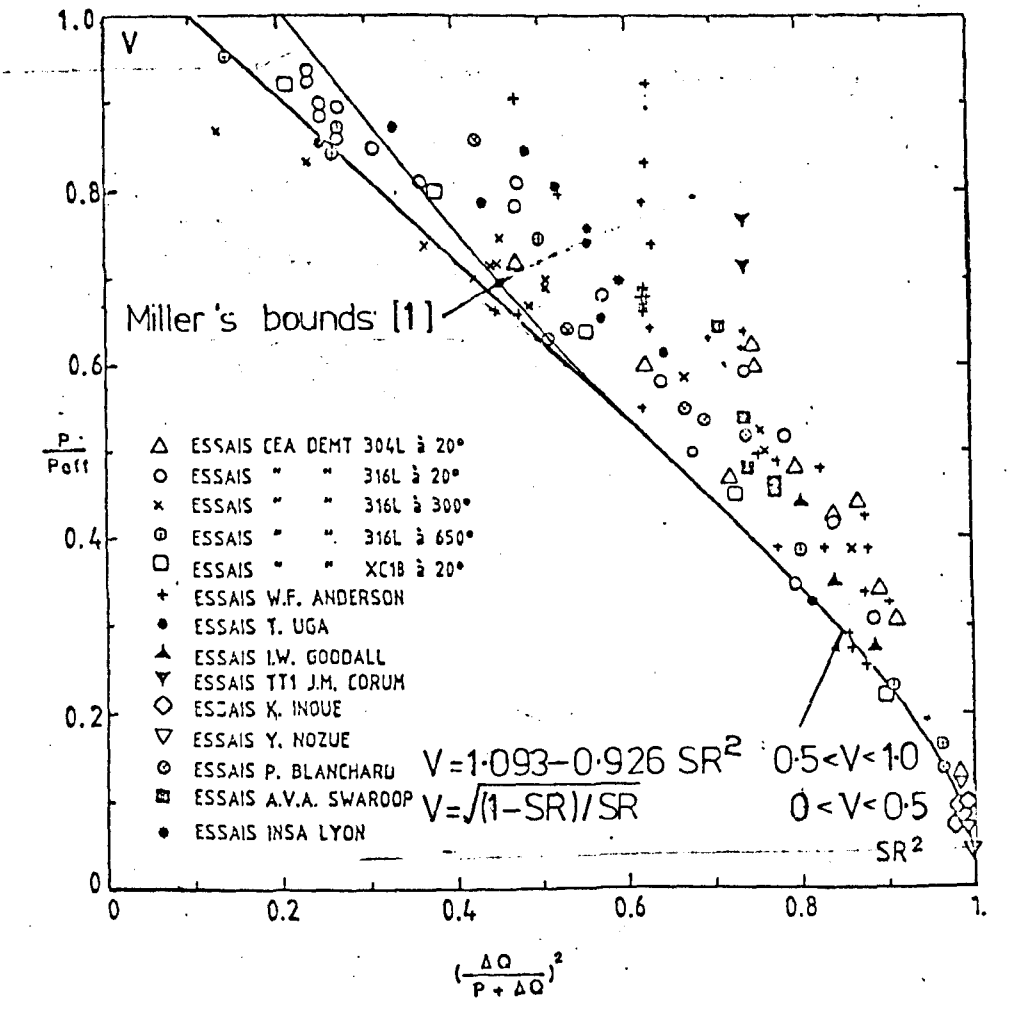

Fig. 2.15. The Result of Plotting the Experimental Data of Various Sources on the Efficiency Diagram. The Bounds are Plotted According to Miller's Criterion for Thermal Stress Ratchetting and on an Empirical Basis. Roche and Moulin [62] (Modified)

a curve, then the condition for conservatively bounding the non-ratchetting region on the left side of the curve may be determined. Roche and Moulin (62) have described the curve by the expression:

$$1.0 > V \geq 0.5, \qquad V = 1.093 - 0.926\ SR^2$$

$$0.5 > V > 0, \qquad V = ((1-SR)/SR)^{\frac{1}{2}}$$

Based on this curve, it would be possible to extract the value of P_{eff} when the values of P and ΔQ are known. The strain accumulation can thus be obtained under a prescribed cycle number of a total time of operation.

The authors proposed that the value of P_{eff} should be limited to the allowable values of the primary stress intensity (Pm) in the ASME III Code. This means that P_{eff} equals P_m which is limited to 1.5 S_m. The code limits the design stress Sy to Pm in the bound for thermal ratchetting. In order to see how the curve as expressed by Roche and Moulin (62) will compare with Miller's ratchetting criterion on which the ASME III Code bounds for thermal ratchetting were based, a simple calculation is made. For a linear temperature gradient, the bounds are:

$$\text{for} \quad 0 < x < 0.5, \qquad y = 1/x$$

$$\text{for} \quad 0.5 < x < 1.0, \qquad y = 4(1-x)$$

where x is the primary stress parameter and y is the secondary stress parameter each normalized to the design stress Sy. Assuming that the yield stress is now P_{eff} instead of Sy and the primary stress is P and the secondary stress is ΔQ, it is now required that x and y are converted to SR and V.

Hence, $x = P/P_{eff}$ and $y = \Delta Q/P_{eff}$

Also $V = P/P_{eff}$ and $SR = \Delta Q/(P+\Delta Q)$ as defined by Lebey et al.(60)

therefore $x = V$

for $0 < x < 0.5$, or $0 < V < 0.5$ on the efficiency diagram

$$y = 1/V \qquad (2.1)$$

Since $SR = \Delta Q/(P + \Delta Q)$

dividing throughout by P_{eff} and inverting gives

$$\frac{1}{SR} = \left(\frac{P}{P_{eff}} + \frac{\Delta Q}{P_{eff}}\right)/\frac{\Delta Q}{P_{eff}}$$

$$\frac{1}{SR} = (V + y)/y \qquad (2.2)$$

Using Eqn. (2.1) in Eqn. (2.2) gives

$$\frac{1}{SR} = V^2 + 1$$

$$\therefore \quad SR = \frac{1}{(V^2 + 1)}$$

For $0.5 < x < 1.0$, or $0.5 < V < 1.0$

$$y = 4(1 - V) \qquad (2.3)$$

Using Eqn. (2.2) and Eqn. (2.3) gives

$$\frac{1}{SR} = (V + 4(1-V))/4(1-V)$$

$$= (1 - \tfrac{3}{4}V)/(1 - V)$$

$$\therefore \quad SR = \frac{1 - V}{1 - \frac{3}{4}V}$$

The result of plotting the above derivations on the efficiency diagram is already shown in Fig. 2.15. The diagram shows that Miller's criterion is less conservative than the empirical curve of Roche and Moulin (62) at $v > 0.5$. The good correlation obtained through the efficiency diagram gives support to the present philosophy of classifying the stresses in this class of loading in terms of primary and secondary stress categories. It is also of great interest to note that in view of the widely differing sources of experimental data used and the various different techniques and test conditions, such a good correlation can still be achieved.

2.6.3 Axially Loaded Pipe with Travelling Axial Temperature Gradient

This is a class of thermal loading on pipes which cannot be properly assessed by the Bree model because the stress system consists of mutually perpendicular thermal and axial stresses. This loading condition arises from the situation in LMFBR's where the flow of liquid sodium having uneven axial temperature distribution flow in piping under pressure. This causes an axial temperature front which travels down the length of the pipe having temperature gradients in the axial and radial directions. The gradients are dependent on the difference between the pipe and the sodium temperature and the velocity of the thermal front. Large temperature gradients and repeated traversing of these thermal fronts are capable of causing the pipe to ratchet within the traversed length in both axial and hoop directions.

Various studies were made on the problem and most of these have been discussed by Kraus (63) in a report published in conjunction with an international benchmark project study on 'Simplified Methods for Elevated Temperature Design and Analysis'. The project considered two specially

chosen benchmark experiments. Problem I being the Oak Ridge Pipe Ratchetting Experiment which was described in 2.4 and problem II was the Saclay Fluctuating Sodium Level Experiment. The latter experiment was intended to simulate the type of loading which has just been introduced. In the experiment sodium was made to repeatedly rise rapidly up a vertical axially loaded pipe to create the thermal load. The theoretical analyses that were made to support the experiment data were carried out by a number of workers using various techniques. The finite element type solutions were provided by Chern (63) and Goodier et al. (63) and approximate analyses were made by Goodman (63), O'Donnell and Porowski (63) and Casier and Zarka (63). The report of Kraus briefly discusses the methods employed by the above workers to predict the magnitude of deformation in the pipe problem. There was however no direct comparisons between predictions and experiment in the report due to the unavailability of the experimental results at the time of preparation of the report. The results of the comparison of the various predictions were however examined. The conclusions were that for the approximate analyses methods there were much better mutual agreement compared with that of finite element techniques. The report briefly discussed the reasons for some of the variability in the results and the overall conclusions were that each method used material property assumptions and testing conditions models which differed from each other. In this section, the detailed examination of the above techniques both finite element and approximate types with the exception of one, will not be attempted because of the length and complexity.

In order to better appreciate the problem and the differing behaviour compared to the other structural configurations discussed so far, the theoretical analysis of Goodman (64) is described. Goodman

gave the only externally published report of the solutions in the benchmark project and this work presented the approximate analysis of the problem based on an elastic/perfectly-plastic material. The temperature or thermal front was idealized as a step change in temperature in the axial direction. The stress and strain history were assessed in terms of simple formulae established from thin shell solutions. Fig. 2.16 shows the temperature, deformation and elastic bending moment and force resultant profiles. The problem analysis was considered to be of three distinct categories, i.e. that of stationary axial thermal gradient and long and short traverses. In the stationary axial thermal gradient category, the thermal front was immobile and imposed at a circumference of the tube and removed. In the long traverse analysis, the thermal gradient swept through the length of the tube such that most of the vessels were free from the local residual bending stresses remaining at the extreme positions of travel. The distance of the traverse over the axial distance where the residual bending ceased to have any effect was governed by a cylinder geometry parameter. Without the effect of residual bending which tends to reduce the thermal stresses, the long travelling thermal front will subject every point on the tube to the more severe thermal stress. For the case of short traverse, the residual bending stress can exist within the short length of the tube and this increased the elastic stress range. Another difference between the categories is that in the stationary case the variation of maximum thermal stress is σ_t which is equal to $E\alpha\Delta T/2$ (ΔT being the temperature difference, E and α denote the usual quantities) while for the two other cases, the variation is $2\sigma_t$. This is due to the reversal of sign of the thermal stress when the front passes through the material point. This difference will be seen to significantly affect shakedown ability.

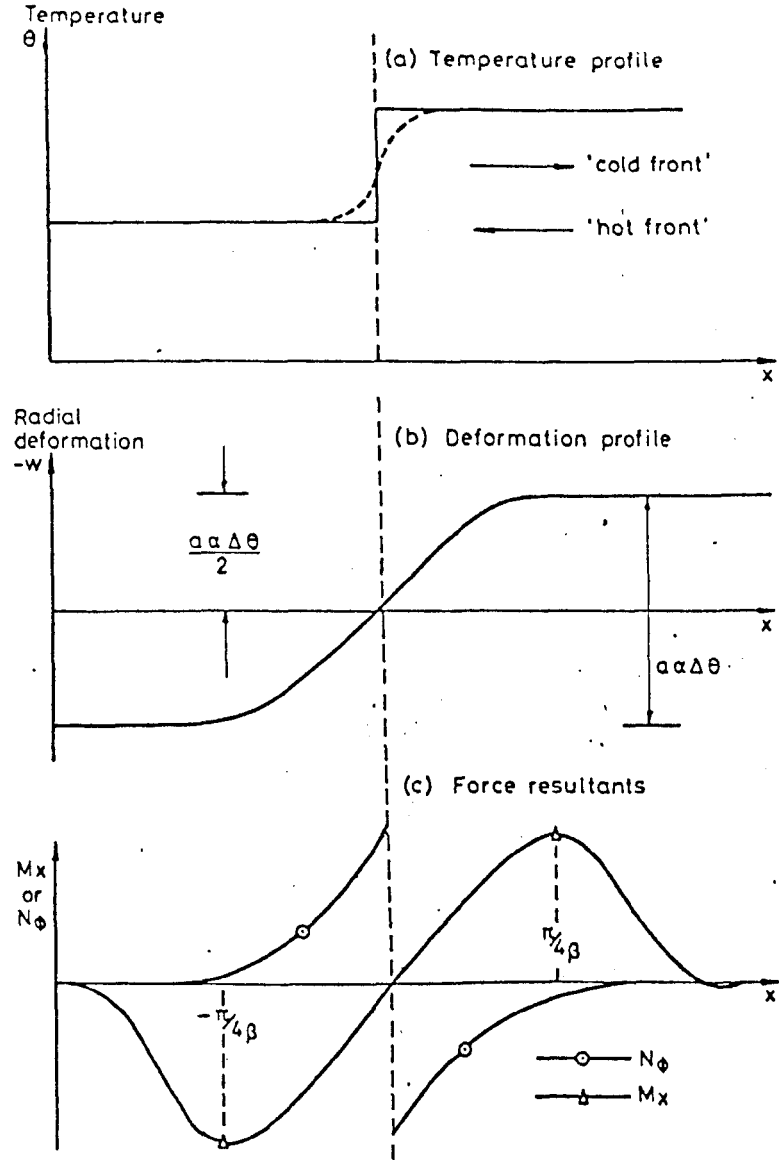

Fig. 2.16. Temperature, Deformation, Elastic Bending Moment and Force Resultant Profiles. Goodman [64]

The shakedown limit to the problem was calculated and plotted in a Bree-type Diagram shown in Fig. 2.17. The primary stress parameter $\bar{P}$ is the axial stress normalized to the hot yield stress, while the secondary load $\bar{\theta}$ is σ_t normalized to the same yield stress. Shakedown limits for various temperature dependent yield stress are shown for the short traverse case. In the long traverse case, the shakedown and the first yield load coincide. The shakedown limit for the stationary thermal gradient case was included by Ponter (65) in the analysis of the problem as part of an interpretive survey on ratchetting in simple structural geometries. The chosen operating point of the benchmark study was at $\bar{P} = 0.27$ and $\bar{\theta} = 1.8$ taking the yield value of 150 MN/m^2. The solution for this test point was obtained and found to be in agreement with the finite element result of Goodier et al. (63).

A realistic pipe problem lies in between that of the long and short traverse cases and the thermal gradient would be less severe than a step change considered in the analysis. This would imply that the shakedown limit lies between those of the two cases considered and the ratchetting is reduced. Further, case 1 is extremely unrealistic because it is practically impossible to impose a step thermal gradient without any movement of the front. Any movement of the front which is greater than the thermal zone will move it closer to the short traverse case and the possibility of ratchetting. In the short traverse case, continued circumferential ratchetting is restrained by the region immediately outside the traversed region and if the axial ratchet continues, a progressive thinning of the section is expected. This effect is not expected in the long traverse case where there are no such restraints. It is also seen that in the Bree-type Diagram, ratchetting is expected at zero axial load.

There are two experimental studies which have recently been conducted

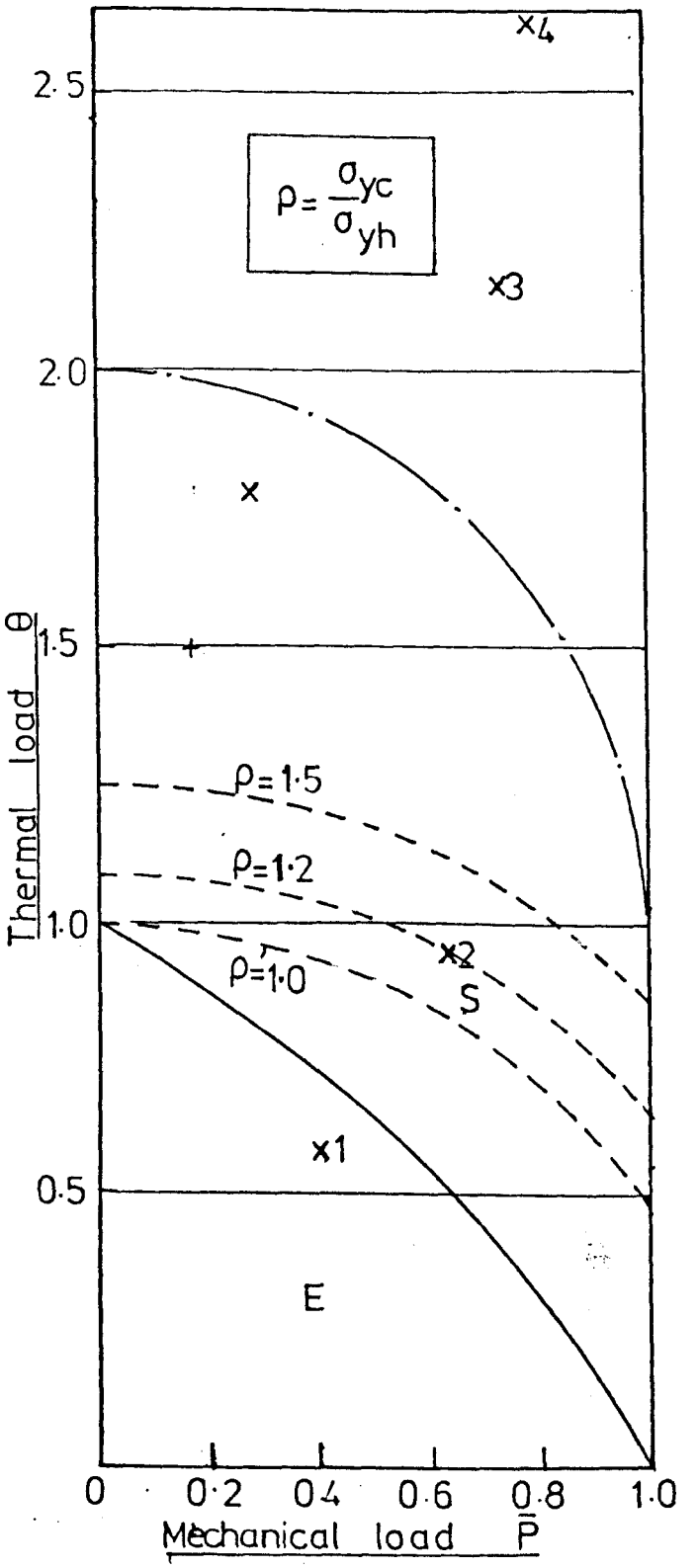

Fig. 2.17. Bree-Type Diagram for Different Categories of Loading and Test Points of Experiments and Benchmark Study. Adapted from Goodman [64] and Ponter [65]

The following legend apply:—·—Shakedown limit for stationary thermal gradient [65] ------ Shakedown limit for short travels and ——— Shakedown limit and first yield for long travels [64]

(+) test point of Saclay Sodium Level Expt [66]
(x) Benchmark Study Operating Point [63]
(x1, x2, x3, x4) test points of Cousin et al. [67]

to simulate the problem. The first was the variable sodium level experiment by Rivolet and Moulin (66) and the second by Cousin et al. (67). The Variable Sodium Level experimental rig consisted of two concentric cylindrical shells. The outer shell was the experimental shell and the inner shell was used to reduce the volume of sodium required. The annular space between the shells was filled with sodium which rose and fell between the inlet and outlet ports set 200 mm vertically apart. The tested shell was made of ICL 167F steel and was 1.202m in outside diameter and 1.45 mm thick. It was made from rolled sheets which were longitudinally welded. The outer shell was instrumented with several types of displacement gauges and thermocouples on the inside and outside surfaces measured the temperature distribution. An axial load equivalent to an axial stress of 40 MPa was applied to the cylindrical shell via two rings of "elastic loading devices" which were attached to the top and bottom rims of the shell. An hydraulic jack at the bottom rim reduced the stress by 10 MPa so that the axial stress cycled between 30 and 40 MPa where the latter value corresponded with the higher sodium level. The temperature of the sodium was maintained constant at 350°C and the inert argon gas above the sodium surface at 75°C. A typical cycle is shown in Fig. 2.18 where the sodium level was raised within 68s, maintained at high level for 63s and lowered to low level within 14s approximately. The axial stress was applied and removed outside the thermal loading. It was noted that the first cycle in a test suffered more severe thermal shock than the subsequent cycles due to the lower initial temperature of the shell. If the cycle times were sufficiently long, then the shell temperature would have sufficient time to cool before the next elevation of sodium leading to more consistent thermal loading. In the case of short cycle

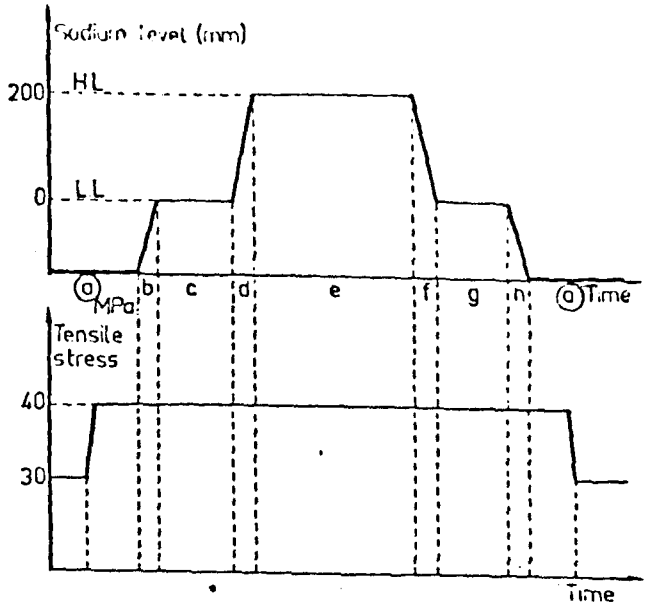

Fig. 2.18. Loading Cycle of Fluctuating Sodium Level Test. Rivolet and Moulin [66]

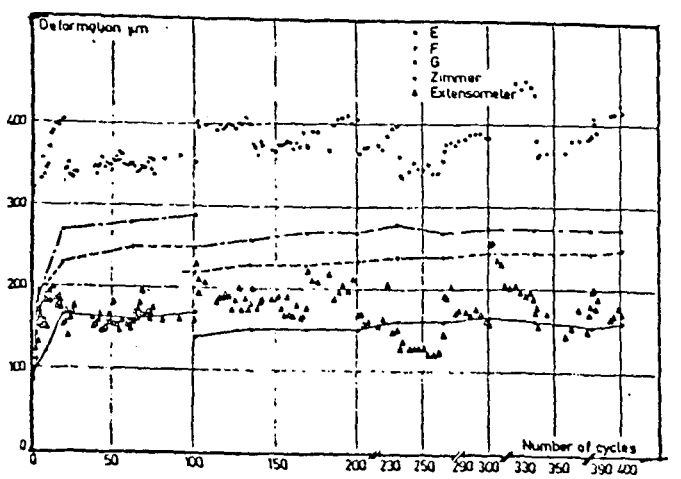

Fig. 2.19. Axial Inelastic Displacement Measured at Different Position of Shell and by Two Extensometers. Rivolet and Moulin [66]

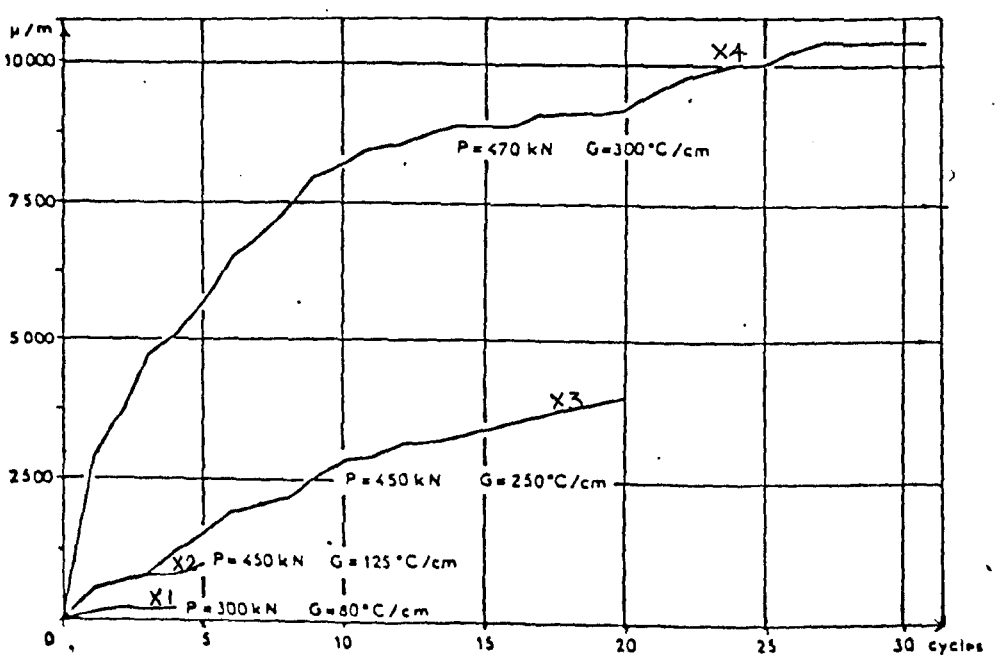

Fig. 2.20. Accumulated Axial Displacements at Different Loading Against cycle Number. Cousin et al. [67]

times, the first cycle was designated as type 1 while the subsequent cycles were designated type 2. Type 1 cycles had a measured axial temperature step of 250°C and type 2 of 210°C. Radial temperature gradients were less than 5°C through the shell thickness. Based on tensile stress-strain data provided the loading conditions will correspond to $\bar{P} \triangleq 0.17$ and $\bar{\theta} \triangleq 1.49$ for type 1 cycles and $\bar{\theta} \triangleq 1.25$ for type 2 cycles if the yield stress is 235 MN/m^2 (0.2% proof stress) at 350°C and for a maximum axial stress of 40 MPa. This differs considerably from the operating point in the benchmark study. The cycle tests were performed at the same loading conditions for 400 cycles. The results are shown in Fig. 2.19. This shows that most of the axial strain was accumulated during the first 18 cycles and amounted to 0.143% and the circumferential strain at the same number of cycles was 0.265%. After 100 cycles, shakedown was definitely identified and the total strain accumulation was approximately 0.145 and 0.278% for axial and circumferential direction respectively. The next 300 cycles showed no accumulation of strains.

This second experiment by Cousin et al. (67) although not specifically stated, appeared to be directed towards simulating the stationary temperature gradient case. The experimental rig consisted of a cylindrical shell made of ICL 167 SPH steel (a variant of Type 316 stainless steel) of 400 mm diameter, 2mm thick and 1 m in height. The temperature on the upper half of the cylinder was maintained at 800°C by the circulation of hot combustion gases which were deflected from ring shaped nozzles located around the mid height. The lower portion of the cylinder was cooled by a series of water jets which focus water at and below the mid height. The measured axial gradient was 300°C/cm at the maximum. A constant axial load was applied at the lower edge of

the cylinder throughout each test. The cylinder was instrumented for measurement of temperature gradients along the axial direction and displacements axially and radially were measured by LVDTs. Four tests were conducted at different axial stresses and thermal gradients and for cycle numbers which varied from 4 to 81. Tensile tests were also conducted to determine the 0.2% yield stresses at 20°C and at 100 to 500°C in steps of a 100°C each. When based on the 0.2% yield stress at the mean temperature at the thermal front, the normalized primary $\bar{P}$ and secondary stress $\bar{\theta}$ parameters were for each test; (0.4, 0.56), (0.63, 0.93), (0.73, 2.14) and (0.79, 2.64) where the numbers in the brackets are $\bar{P}$ and $\bar{\theta}$ respectively. These test points are marked in Fig. 2.17. The thermal gradient was applied for 3 hours and the entire load cycle lasted 12 hours.

The experimental results are shown in Fig. 2.20. The first two tests achieved shakedown within 5 cycles and the third and fourth tests accumulated about 0.35% at the 20th cycle and 1% at the 30th cycle respectively before shaking down. Considering that the Bree-type Diagram of Goodman (64) were employing elastic/perfectly-plastic properties, the experimental results are seen to be largely in agreement with the expected behaviour by virtue of the locations of the test points on the diagram.

The numerical solutions of Arnaudeau et al. (68) for thin circular cylinders under axisymmetrical thermal and mechanical loading applies to both the cases of stationary axial and traversing thermal gradients. For the former case, values of the ratchet strain per cycle were rigorously computed for a limited range of primary and secondary load parameters and tabulated. Based on these values, one can calculate the constant ratchet strain/cycle under known axial and thermal loads. The

possible application for predicting the initial strain accumulation of the tests of Cousin et al. (67) were examined. Although the analysis was applicable to the tests, comparisons cannot be made because the magnitude of the applied loads lie outside the given values and reasonable extrapolation could not be made. For the traversing axial thermal gradient type of loading, the axial and circumferential strain/cycle were given for different traverse distances for constant axial and thermal loads. Comparison of these values with that of the stationary thermal case indicates ratchet rates are increased for the former.

The test results described in this section have all tended to shakedown with low cycle numbers when ratchetting was expected except in the tests of Cousin et al. (67). These exceptions are labelled X3 and X4 in fig. 2.17. However, the effects of hardening on this type of structure are still significant.

2.7 Constitutive Relationships and Material Behaviour

In conjunction with the experiments conducted during this research programme, deformation data on Type 316 stainless and mild steel material has been obtained. Computer studies were undertaken to analyse the behaviour of the Bree uniaxial model using several constitutive relations that were suitable for these materials. Firstly, comparisons were made of the results of the computations using different constitutive relationships and secondly these results were compared with the experimental ratchet data. Attempts to predict the deformation behaviour show that the experimental ratchet data can only be predicted reasonably closely provided empirically derived constitutive relations are used. In this section a review is made of the literature to examine the existing commonly used constitutive relations and their capability in representing real material behaviour. As more realistic constitutive relations would provide a more accurate prediction of ratchetting, it is also necessary to examine the results of some material tests from which other constitutive relations have been based. From the survey, two facts emerged, firstly there are many constitutive relations being proposed with different capabilities and complexities. Secondly there is relatively little experimental material test data on Type 316 stainless steel. The survey concentrates firstly in section 2.7.1 on the common material models which are based on the so-called classical plasticity theory. In the section 2.7.2, a survey is made of the material data information base that has been published in the open literature with an emphasis on material tests on Type 316 stainless steel. At present, it is known that the coverage on material data required to satisfy data needs for LMFBR design is incomplete in certain areas and effort and expense has been made to remedy the situation (Wood (69)).

In this section, the data are selectively examined to enable only a qualitative understanding of the complex material response in relation to shakedown and ratchetting behaviour under cyclic loading at elevated temperature.

2.7.1 Material Models

If the stress-strain-time or constitutive relationship for a material is known, it is theoretically possible to combine this with the conditions of compatibility and equilibrium to calculate the history of stress and strain occurring in a load bearing component. In practice, however, the formulation of these complex relations require such large quantities of complex, expensive and long term testing, that these are rarely conducted unless justified by extreme need. Designers have relied upon approximations of the complex response of the material obtained from a limited number of tests and combined it with the use of design methods based on shakedown and limit load concepts. This has proved mostly adequate for currently used conventional and some nuclear pressure vessel designs under constant and varying loads at low temperatures and at constant loads at elevated temperatures. The ASME III (3) and other codes such as BS 5500 (9) are based primarily on the material model of elastic/perfect-plasticity. Structural concepts of limit load and shakedown are functions of this model although the design yield stress may take the values of rupture stress or stress required to achieve a design strain limit at the end of a certain lifetime for applications where creep is significant. Approximate methods such as the representative reference deformation stress or reference stress methods in short are also based on the elastic/perfectly-plastic design yield stress concept (Leckie (70)). The latter methods are used for

constant load and distributed temperature creep deformation. The above methods are widely used in structural analysis for predicting the load capacity of a structure where the stresses and operating temperature do not vary appreciably during the operating lifetime of that structure. It has already been mentioned that the operation of an LMFBR power plant involves rapid changes in thermal and mechanical loadings followed by long periods of sustained operation at constant mechanical and thermal loads. They therefore involved periods of cyclic loadings and of constant loading called hold or dwell periods. As far as the deformation behaviour at ratchetting and alternating plasticity conditions are concerned interaction with creep during hold times causes increased deformation such that history dependence of the materials plays a prominent role. It is important therefore that a realistic constitutive relation must incorporate some form of cyclic and creep dependency such that accurate cycle by cycle computer analysis capable of reproducing actual component behaviour may be made possible. This is at present a difficult problem. Approximate methods to find reference stress and temperature have been proposed by Ponter and Leckie (71) and Ainsworth (72) which give a measure of the deformation of the components. With the class of structures which are subjected to temperature and cyclic loading, greater care has to be taken when using modified shakedown solutions in the selection of appropriate yield stresses and the input of the important features of material behaviour under the perceived loading conditions. This also applies to finite element analysis. Code Case N47-12 (6) in the ASME Code has specifically recommended the use of non-linear, incremental time stepping inelastic finite element analysis for important or critical components. Although the analysis by this method is expensive and often time consuming to develop, the most

important question concerns the qualification of computer programs by comparison to experimental results. Notwithstanding, the superiority of the finite element method over the approximate methods described above in the former's ability to account for complex geometrical details, the formulation of constitutive relations in the computer programs have not really caught up with the accuracy of the numerical calculations. This is because implementation of complex constitutive relations have been difficult both theoretically and practically. There are continuing developments of constitutive models with increasing realism but because these are often expressed in complex mathematical statements, they are seen to be rarely used in practice. For the present purpose, most structural analysis work is based upon constitutive relations using linear kinematic, isotropic or non-linear strain-hardening as the hardening rules plus a linear creep law.

For most strain-hardening materials, the model which predicts the behaviour most accurately is that of Mroz ((73) and (74)). The Mroz model employs the concept of a field of surfaces of constant workhardening moduli. Each nodal stress value in the piecewise linear uniaxial stress strain curve is represented in the stress space by a surface geometrically similar to the initial yield surface but of a different size. This is shown in Fig. 2.21(a). The yield surface is assumed to translate within this field, contacting and then pushing each surface along with it as each is encountered as in Fig. 2.21(b). Associated with each surface is that value of the workhardening modulus characteristic of the piecewise linear segment immediately following the nodal stress value. The amount of hardening is a function of some scalar parameter such as the equivalent uniaxial plastic strain or the total plastic work. The Mroz model is also applicable to cyclic behaviour. For biaxial stresses, there is agreement over the use of the initial and subsequent yield condition

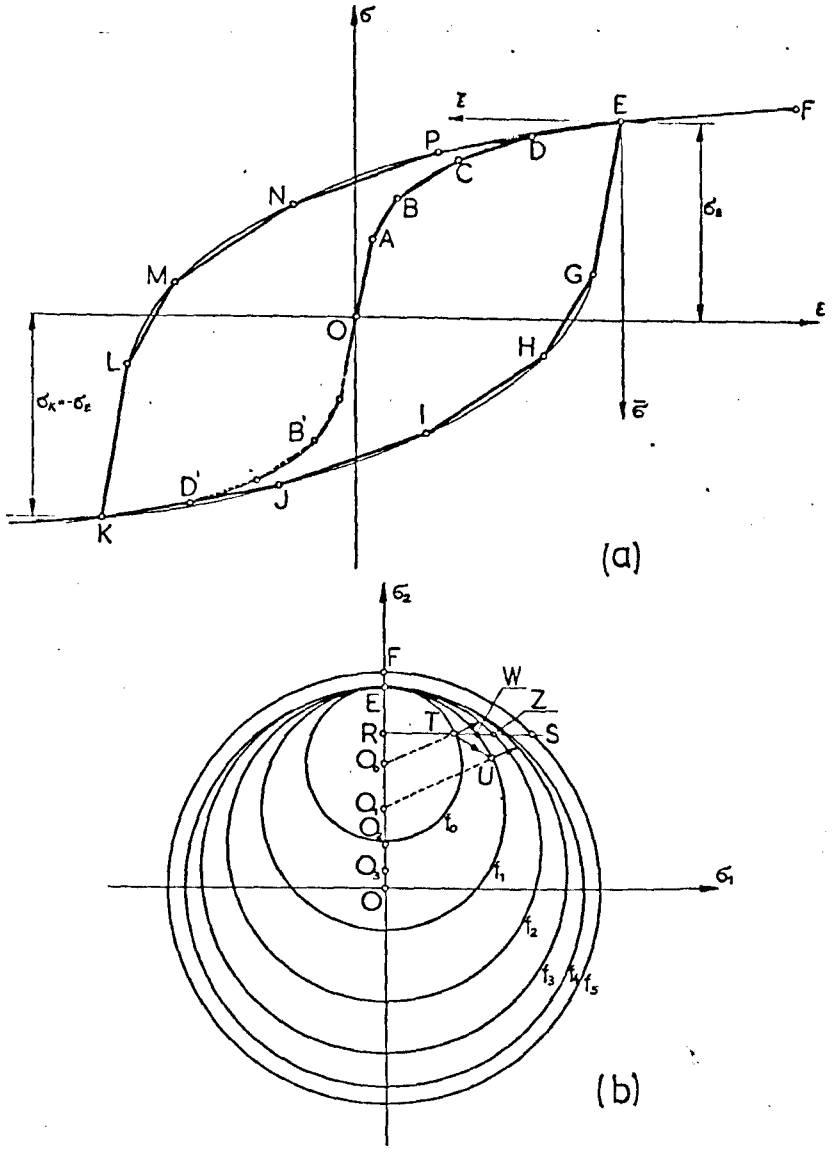

Fig. 2.21. Approximation of the Stress Strain Curve by Portions of Piecewise Linear Curve (a) and the Representation in the Stress Space by Yield Surfaces f_n (b). Mroz [74]

(the von Mises Criterion) and the flow rule (the normality condition). The von Mises Criterion has been proven to best represent actual material and is now accepted widely. The normality condition which is the most generally accepted flow rule states that as the stress state of the material comes into contact with and pierces the material yield surface, the resulting plastic strain increment is along the outward normal to the yield surface at the point of penetration.

Isotropic hardening postulates that the yield surface expands uniformly about the origin of stress space during plastic deformation. In its simplest form, the von Mises yield condition is assumed. In contrast to isotropic hardening, kinematic hardening proposes that the yield surface retains its shape, initial size and orientation with respect to the origin of stress space but translates as a rigid body during plastic deformation. The concept was first proposed by Prager (75) and in the present form called the Prager Ziegler model (76), the yield surface translates in the direction of the vector connecting the centre of the yield surface and the current stress state.

The aforementioned have considered the monotonic behaviour of the models. Cyclic behaviour based on the models under symmetric strain controlled cycling beyond yield show differences which vary considerably. For the elastic/perfectly-plastic model, the stress oscillates between $\pm$ the yield stress. The isotropic model will after a number of cycles achieve fully elastic behaviour where the stress oscillates between $\pm E\varepsilon$ where E,ε are Young's modulus and strain amplitude respectively. The linear kinematic hardening and the Mroz models each reach cyclic behaviour within one cycle where the maximum stress reached equals the stress at the maximum strain on the monotonic stress strain curve. These characteristics are shown in Fig. 2.22. The actual

behaviour of an arbitrary material is shown in Fig. 2.23. These figures show that the ideal material behaves quite differently from real materials. This is due to the ability of a real material to cyclically harden or soften leading to either maximum or minimum stresses which become greater or less than the monotonic stress at the controlled strain amplitude. Fig. 2.22 (a, b, c, d) shows the response of the models of perfect plasticity, isotropic, and kinematic hardening and the Mroz model when subjected to various strain and stress controlled histories. The behaviour of the models for strain controlled cycling about a mean strain (Fig. 2.22 (b)) is similar to that at a zero mean strain, excepting the isotropic model which behaves fully elastically after a few cycles, the responses of other models are that of hysteresis type behaviour. The Mroz and kinematic models attain a maximum stress which is unchanged with cycles. The actual behaviour of most materials is that of cyclic relaxation of the maximum stress until the mean stress approaches zero (Fig. 2.23 (c)). In the condition of stress controlled cycling about zero mean stress, the models give cyclic plasticity or fully elastic behaviour (Fig. 2.22 (c)). These responses are somewhat similar to actual material behaviour. The final type of loading conditions is that of stress cycles at a fixed non zero mean stress during which the models predict essentially the same response for the perfectly plastic and isotropic hardening models. Strain is accumulated at the first cycle and behaviour becomes fully elastic afterwards. The other models demonstrate hysteresis behaviour. In actual behaviour, for sufficiently large strains, the material may suffer from incremental growth or ratchetting (Fig. 2.23 (d)). It is to be noted that Fig. 2.22 is drawn for arbitrary magnitudes of strain and stress loads. For less extreme loadings, most of the hysteresis behaviour is replaced by fully elastic behaviour.

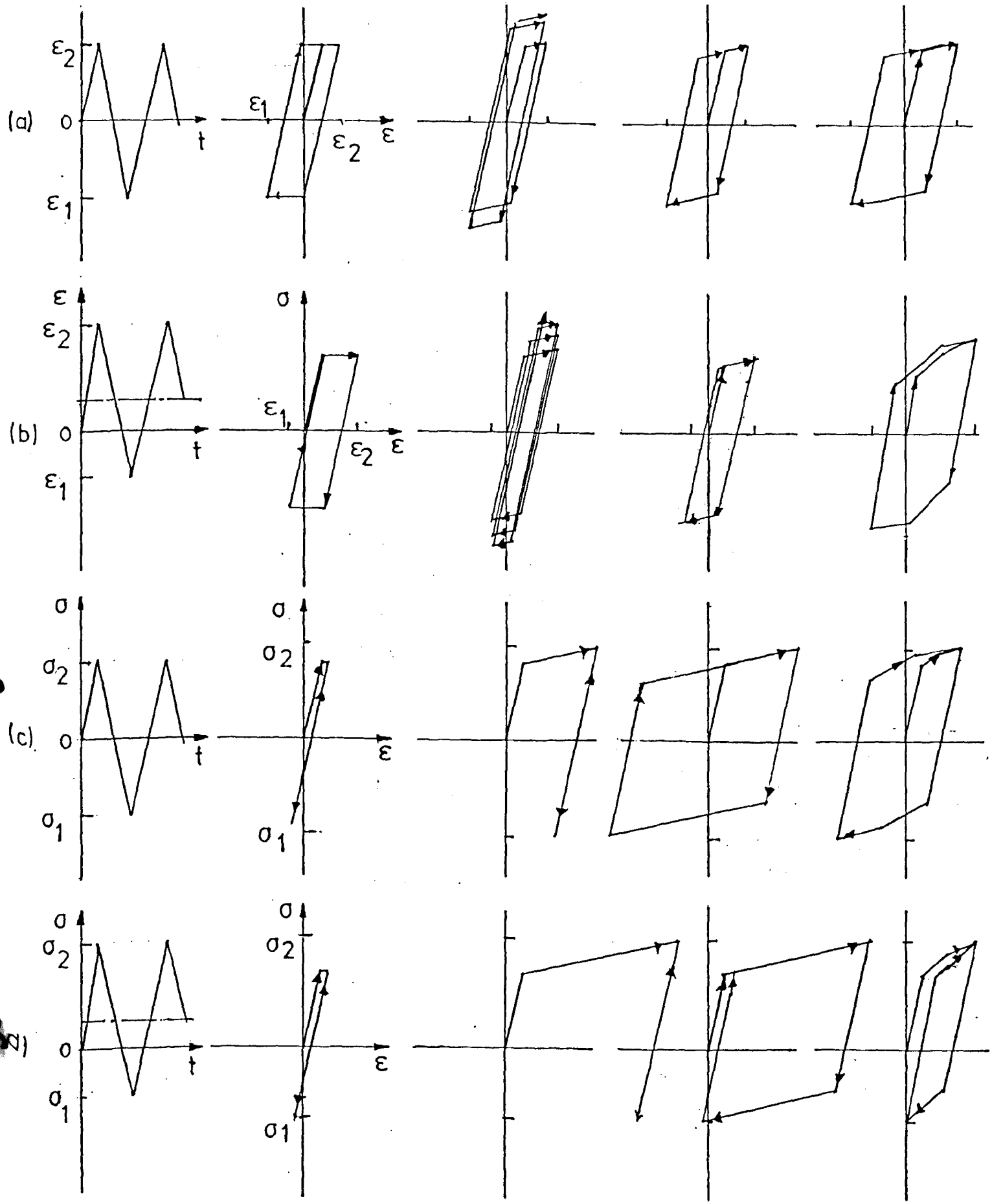

Fig. 2.22. Schematic Illustration of the Response of Various Material Models

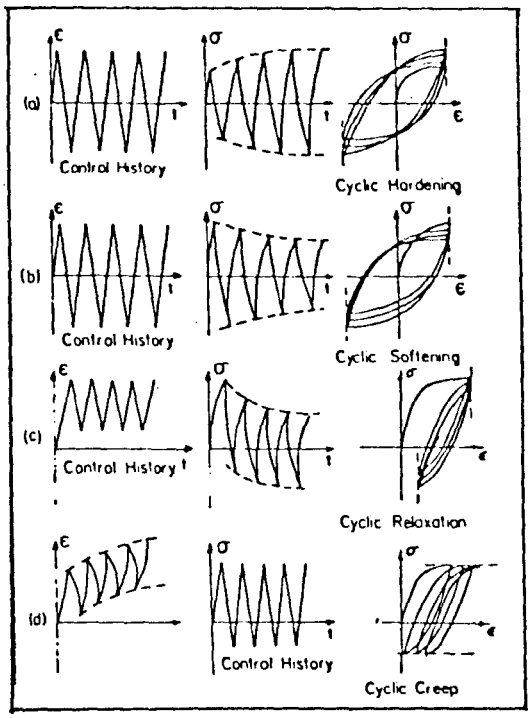

Fig. 2.23. Schematic Illustration of Cyclic Transient Phenomena. Jhansale [25]

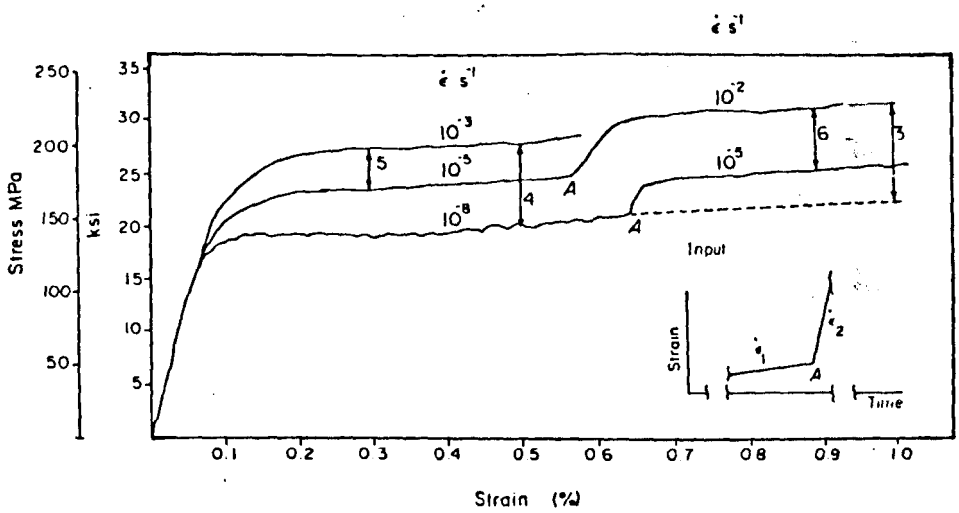

Fig. 2.24. Stress-Strain Diagrams at Different Strain-Rates. At Points A, the Strain-Rate is Instantaneously Changed. Annealed AISI Type 304 Stainless Steel. Krempl [78]

2.7.2 Experimentally Determined Material Behaviour

Experimental tests to obtain information on the behaviour of stainless steels particularly that of Type 316 are an important part of nuclear engineering research. As Type 316 stainless steel is used in many of the reactor core components as well as in the primary circuits of a typical LMFBR, it is essential that relevant materials data are provided for the reliable design of these components. An important parameter in common with these components is that of reversed strain cycling with dwell time at temperatures in the creep range. This can lead to damage of the material by combined creep and fatigue. The creep damage is caused by the relaxation of stresses when the elastic strains are converted into creep strains during the dwell time, while the fatigue damage is due to the repeated cycling of strain due to thermal loading. It is based on this delineation, i.e. that creep and fatigue are phenomenalogically separate, that the linear damage summation rule was proposed in Code Case N47. On this assumption creep does not interact with fatigue. Creep and fatigue tests can therefore be performed separately. This assumption is now being questioned and it is considered that creep-fatigue tests have to be performed at the same time on one specimen (Wood (69)). Fatigue-creep tests are long term tests and an evaluation of the variables such as temperature and microstructure caused by cast to cast variations involve prohibitive testing times. These tests are often performed by the power generating organizations to provide data suitable for the operational characteristics for the lifetime of the plant. This in the U.K. is approximately 500 major temperature cycles in 20 to 30 years of service while the hold time per cycle is likely to be of the order of 500 hours (Wood (69)). Extrapolation techniques are used to reduce the number of tests and the

testing times from 100,000 to 10,000 hours. While some tests are long-term and highly comprehensive, others are of shorter duration. These tests are concerned with low and elevated temperature deformation, stress relaxation and low cycle creep and fatigue testing. These tests are required for providing information on the material properties in the operating conditions at the plant. In this section, unless otherwise specified, the material behaviour of Type 316 stainless steel only will be examined. This section is aimed at examining the material behaviour of this steel so that an understanding is gained of the effects on the thermal ratchetting behaviour of the Bree uniaxial model. The format of this section is that each material property is examined separately using data from the literature -

1) Strain rate sensitivity

In monotonic loading, the stress strain response is affected by strain rate sensitivity at room temperature. Results of strain rate tests on Type 304 stainless steel at 20°C obtained by Krempl (78) is shown in Fig. 2.24. The material is more resistant to deformation at the higher rates. Wood and Williamson (79) conducted strain rate sensitivity tests on Type 316 stainless steel at a rate of 3×10^{-5}/s (corresponding to BS3688 for standard tensile testing) and at a slower rate of 1×10^{-7}/s. The result surprisingly too showed that the slower strain rate test had a higher stress strain curve. This finding is further supported by Jaske et al. (80) who tested the same steel at strain rates of 4×10^{-3} s^{-1} and 4×10^{-5} s^{-1} at two temperatures of 566 and 649°C. Wood and Williamson suggested that this could be due to carbon and nitrogen content of the steel being more effective in restricting dislocation movement at the lower strain rate.

2) Room temperature creep

Room temperature creep or cold creep have been reported by a number of workers, e.g. Moreton and Moffat (39) and Ellis et al. (81). Lebey et al. (60) measured cold creep strains for Type 316 stainless steel, shown in Fig. 2.25 and indicated that about 2% strain was accumulated after 290 hours at 0.8 $\sigma_{0.2}$ in one test and in another, greater than 1% strain was accumulated within 130 hours at 0.9$\sigma_{0.2}$. Although the stress values were close to that of first departure from linearity, the large amount of creep is highly significant and may have important consequences in the measurement of room temperature structural ratchetting strains. From the author's experience, cold creep strains were measured in a uniaxial tensile test and found to be much less. It is suggested that material variability may have caused this difference.

3) Elevated temperature creep

Elevated temperature creep data is supplied by Code Case N47 in the form of isochronous stress vs. total strain (i.e. creep plus plastic strain) for four types of metals including Type 316 stainless steel. The curves in the code were derived by Blackburn (82) from creep data of up to 10,000 hrs and extrapolated to 300,000 hrs. Pure creep strain data is difficult to obtain because of the difficulty of separating the creep strain from the total strain. The plastic strains form a large part of the total strain and can cause a significant error when improperly separated.

4) Stress relaxation

Stress relaxation data may be indirectly obtained from creep deformation or be obtained from stress relaxation tests. Wood and Williamson

	$P_{0.3}(0.2)$			
	0·80	0·93	1	1·07
Plastic elongation	0·2 %	1·05 %	2 %	3·25 %
Duration of test	290 h	130 h	145 h	250 h

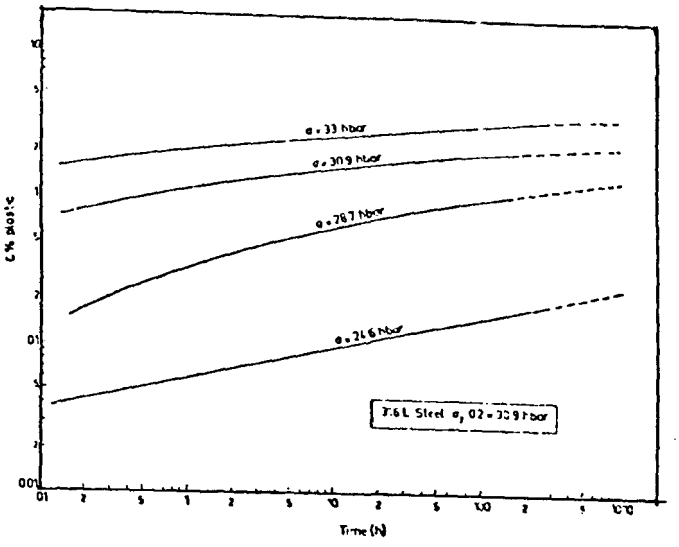

Fig. 2 Cold-creep curves—316 L steel

Fig. 2.25. Cold-Creep Curves on Type 316L Stainless Steel at Room Temperature. Lebey et al. [60]

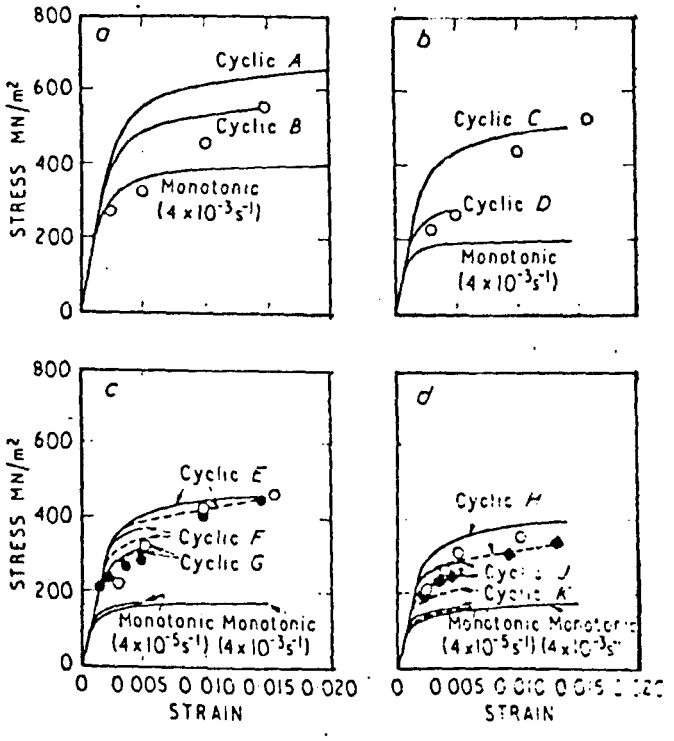

Fig. 2.26. Comparison of Monotonic and Cyclic Stress-Strain Curves for Type 316 Stainless Steel. Jaske et al. [80]

(a) At 21°C.
(b) At 427°C.
(c) At 566°C.
(d) At 649°C.

Incremental Step — Annealed; ····· Aged 1000 h at test temperature

Constant Amplitude, Continuous Cycling — Annealed; • Aged 1000 h at 566°C; • Aged 1000 h at 649°C

	$\dot{\varepsilon}$, s⁻¹	$\frac{\Delta\varepsilon}{2}$		$\dot{\varepsilon}$, s⁻¹	$\frac{\Delta\varepsilon}{2}$
Cyclic *A*	4 x 10⁻³	±0·0289	Cyclic *F*	4 x 10⁻⁵	±0·005
Cyclic *B*	4 x 10⁻³	±0·0145	Cyclic *G*	4 x 10⁻³	±0·005
Cyclic *C*	4 x 10⁻³	±0·0146	Cyclic *H*	4 x 10⁻³	±0·0145
Cyclic *D*	4 x 10⁻³	±0·005	Cyclic *J*	4 x 10⁻³	±0·005
Cyclic *E*	4 x 10⁻³	±0·0145	Cyclic *K*	4 x 10⁻⁵	±0·005

(79) have conducted monotonic incremental strain tests at 400°C. In these tests the specimens were initially strained to 0.05% and held constant for 2 hrs while the changing stresses were measured. Thereafter strain increments of 0.02% were applied and again held constant for 2 hrs before the next increment. A total of 37 increments were applied which accumulated 0.77% strain by the end of the test. It was found that stress relaxation is virtually complete within about 10 mins and the maximum stress relaxation was found to be within 10% of the maximum stress.

5) Elevated temperature stress strain curves

Monotonic stress-strain curves were obtained at 21, 427, 566 and 649°C by Jaske et al. (80). These curves follow the usual pattern of decreasing stress at the same strain with the increase in temperature Fig. 2.26. There are to the author's knowledge, no investigations where the temperature is varied during the same uniaxial test. Such tests would represent the real situation in structures which are subjected to thermal transients where the temperature varies within each cycle at a material point in the structure.

6) Strain controlled cycling at a zero mean strain

Strain controlled cyclic tests are usually carried out in order to obtain fatigue data whilst tests with hold time incorporated, at the extreme or maximum strain part of the cycle, are for obtaining creep-fatigue data. Strain cycling under fully reversed (i.e. with reverse yielding) and zero mean strain conditions cyclically hardens or softens the material until a stable cyclic state is reached after which no hardening or softening occurs. Cyclic tests are usually presented by

plotting together the stabilized maximum stresses against the strain amplitudes at which they are obtained. Fig. 2.26 shows the results obtained by Jaske et al. (80) for temperatures of 21, 427, 566 and 649°C at strain rates of 4×10^{-3} s^{-1} and for strain amplitudes up to 2.89% (i.e. low cycle). Cyclic hardening is seen at all temperatures. It was also found that the degree of hardening varies with temperature and the prior heat treatment (annealing or ageing). Ageing, (a process whereby a specimen is exposed for prolonged periods at a test temperature) for 1000 hrs produced only a slight decrease in cyclic hardening at 566°C and a large decrease at 649°C. Constant strain amplitude cyclic tests (where a specimen is used once for one strain amplitude) gives less cyclic hardening than incremental strain amplitude cyclic tests (where a specimen is used for a range of strain amplitudes applied in increasing order of magnitude) at all temperatures. This difference is reduced with larger strain amplitudes. The reason for the above behaviour is due to the effect of prior hardening received at each strain increment in the incremental strain amplitude cyclic tests. Jaske and Frey (83) later conducted more cyclic tests on long life fatigue of Type 316 stainless steel. These tests had smaller strain amplitudes and were designed to supplement long life fatigue data in the elevated temperature range greater than 427°C (800°F)) and extending the 10^6 cycles now currently available. The test temperatures were 21, 427, 538 and 593°C. Fig. 2.27 shows the extent of cyclic hardening by plotting the maximum stress range exhibited against cycles for each of the test temperatures. At 21°C there is some noticeable cyclic softening at strain ranges below 0.45% which stabilized at about 10^3 cycles. At all other temperatures there is consistent cyclic hardening at all strain ranges which do not seem to stabilize even after 10^5 cycles or more in most cases. This

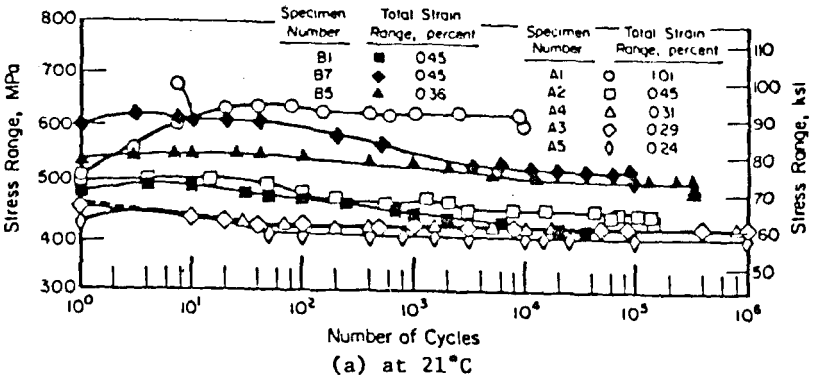

(a) at 21°C

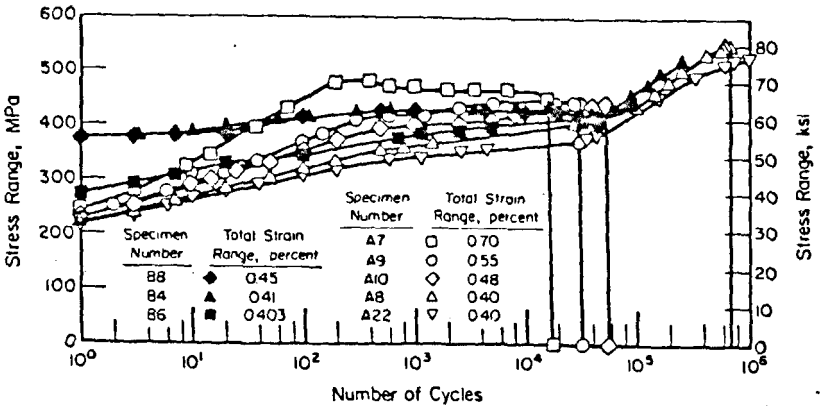

(b) at 427°C

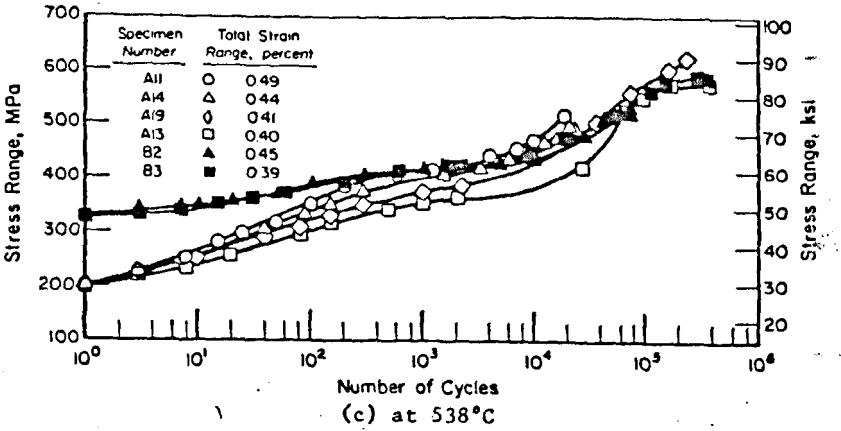

(c) at 538°C

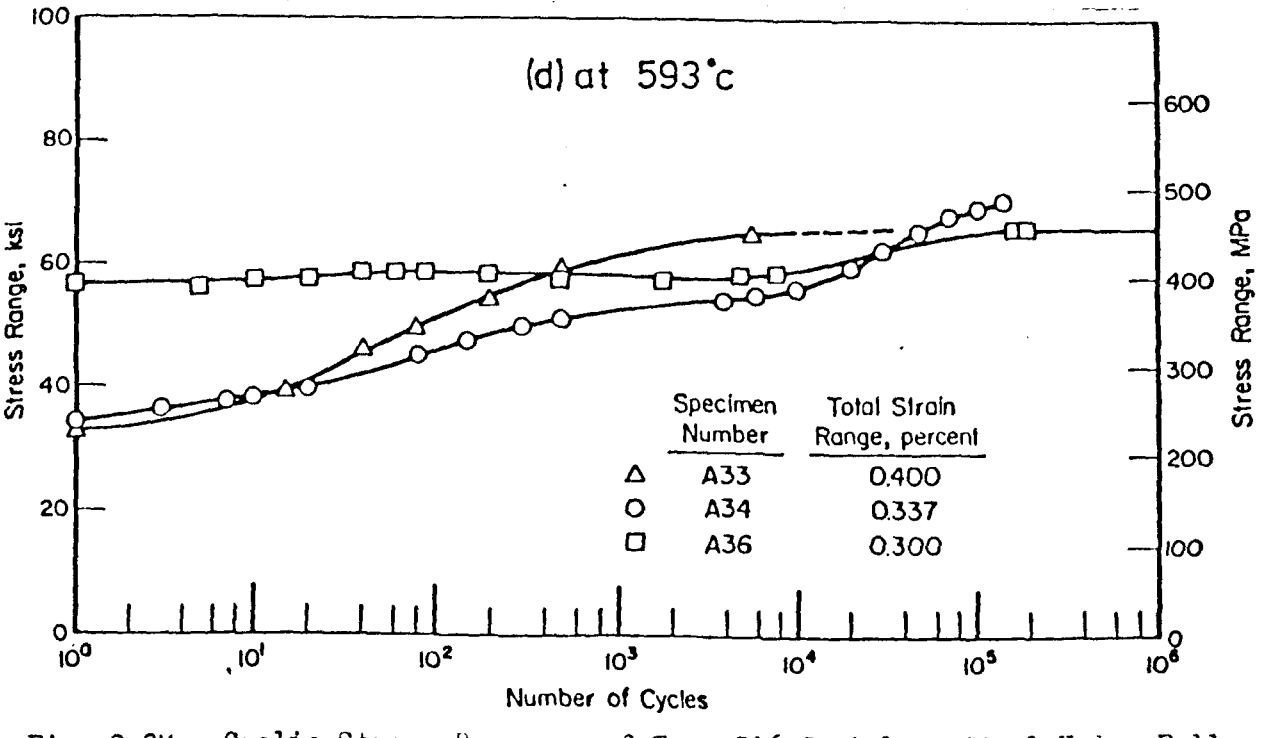

Fig. 2.27. Cyclic-Stress Response of Type 316 Stainless Steel Under Fully Reversed Strain Cycling in Air. Jaske and Frey [83]

observation of continous cyclic hardening was suggested to be caused by the high frequency (0.5 to 0.6 Hz) of the tests giving higher strain rates ($0.004s^{-1}$) which was considered necessary in order to reduce testing times.

7) Stress controlled cycling at zero mean stress

The cyclic strain response under stress controlled cycling was studied by Jaske and Frey (83) to compare with strain controlled cyclic results. Fig. 2.28 shows the strain range response plotted against cycle number at four stress amplitudes at 0.5 to 1.0 Hz frequency in air at 427°C. It is seen that cyclic hardening initially reduced the strain range response to stable ranges in cases of low stress amplitudes. For the cases of high stress amplitude, the strain range began to increase after approximately 100 cycles by cyclic softening which led to eventual failure.

8) Strain controlled cycling at non-zero mean strain

Goodall et al. (84) reported tests to study the influence of a strain offset on the cyclic stress response at 600°C. The tests involved applying an 0.5% offset after the material had stabilized after cyclic hardening at ± 0.25% strain amplitude. Cycling at the same strain amplitude was continued. When the offset was applied, the plastic hardening modulus decreased rapidly and during the subsequent cycles, the material showed cyclic relaxation such that the mean stress developed during the imposition of the offset disappeared after 90 additional cycles. Cyclic relaxation suggests a mechanism for memory decay, which is not described by conventional hardening models and which could weaken the ability of hardening to halt ratchetting.

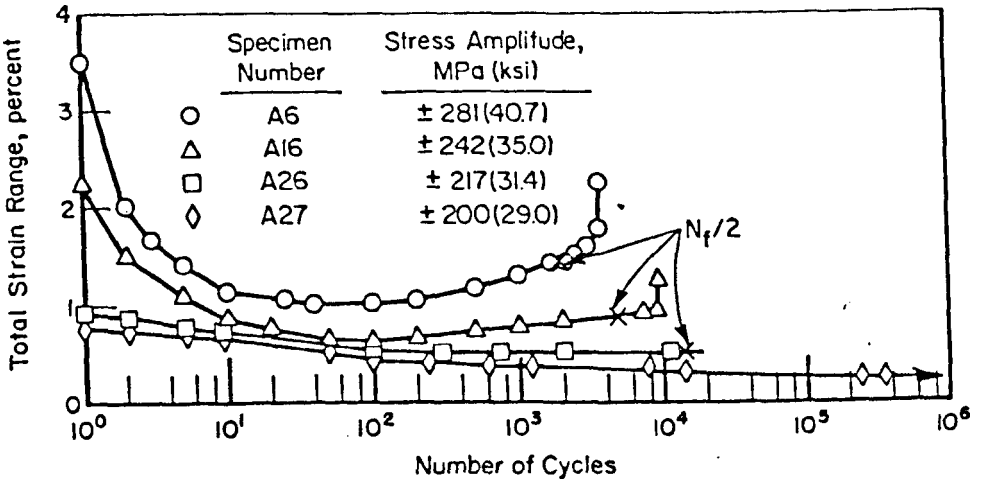

Fig. 2.28. Cyclic-Strain Response of Type 316 Stainless Steel Under Load Cycling at About 0.5 to 1.0 Hz and in Air at 427°C (800°F). Jaske and Frey [83]

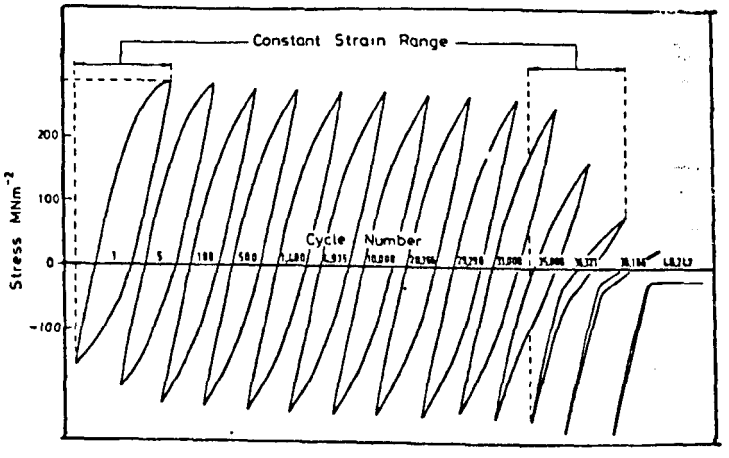

Fig. 2.29. Hysteresis Loops Obtained at ± 0.2% Strain Range After 1% Prestrain (0.2 min/cycle) on Type 316 Stainless Steel at Room Temperature. Goodall [86]

In another test reported by Goodall (86), a specimen was initially prestrained to 1.0% in tension and then cycled about that strain at an amplitude of $\pm$ 0.2%. Initially the hysteresis loop was symmetric to the mean stress created by the initial monotonic prestrain. During the subsequent cyclic straining, the mean stress decreases to zero whilst the peak to peak stress increased slightly. This behaviour, shown in Fig. 2.29, is again an effect of cyclic relaxation of stresses which is caused by the hardening of the material.

9) Strain controlled cycling followed by imposed cyclic strain increment

In a strain controlled cyclic test conducted by Goodall et al. (85), the test specimen was subjected to three cyclic modes. It was initially stabilized by strain controlled cycling of $\pm$ 0.25% strain amplitude and zero mean strain for 400 cycles. A positive strain increment of 0.025% per cycle was then imposed for 44 cycles on the mean strain value thus causing the value to accumulate 1.1% on the 44th cycle. Finally strain controlled cycling was reimposed at the original strain amplitude of $\pm$ 0.25% but at the mean strain of 1.1%. The results are shown in Fig. 2.30 (a and b). The hatched area covers the strain control cycling history up to 700 cycles while the pair of curves represent the locus of maximum and minimum stresses during the test. Fig. 2.30(b) shows an expanded plot of Fig. 2.30(a) during the imposed ratchetting phase starting from cycle number 400 to 444. From both figures it is seen that only a small kinematic increase in stress response is evident during the initial few cycles of the enforced ratchetting after which the stresses tend to remain steady. On the return to strain controlled cycling without the imposed ratchet, cyclic stress

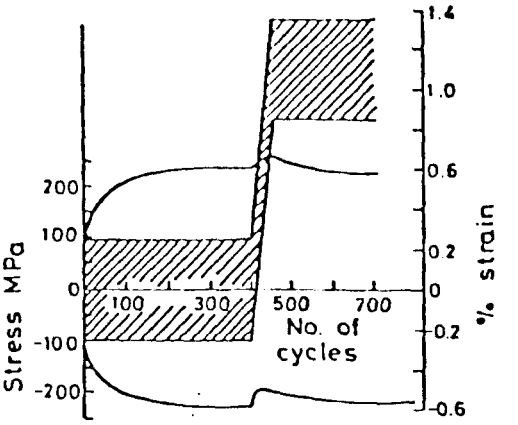

(a) Strain range ± 0.25 with 10 min. Tension dwell and 0.025% strain off-set each cycle.

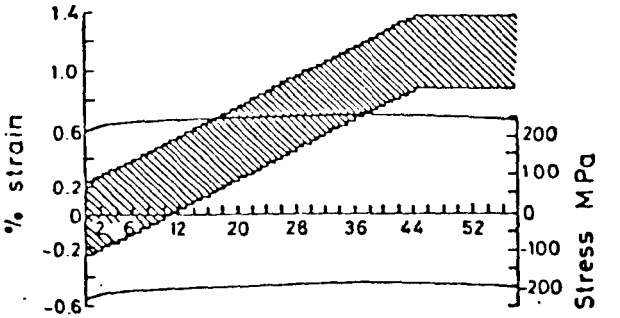

(b) Detail of plastic strain cycles 400-450

Fig. 2.30. Strain Controlled Cycling with Imposed Ratchetting on Type 316 Stainless Steel at 600°C. Goodall et al. [85]

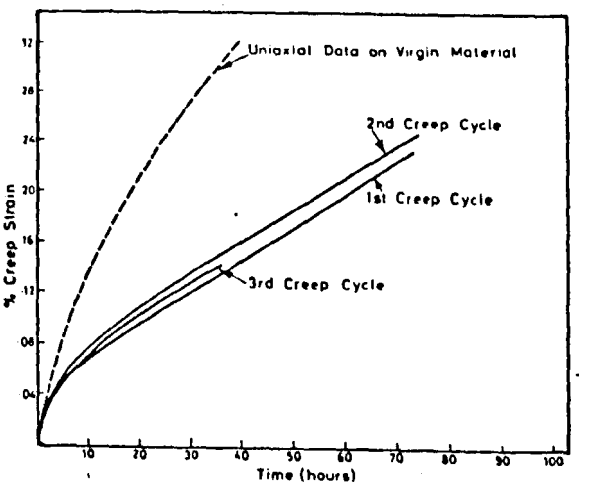

Fig. 2.31. Variation of Creep Strain with Time at 185 MN/m^2 After Precycling at ± 0.25% Strain Range on Type 316 Stainless Steel. Goodall [86]

relaxation is immediately seen (Fig. 2.30(a)) and this persists for the remaining cycles. The cyclic relaxation reduces the mean stress of the stress response to zero while the stress range remains similar to the stabilized stress range before the imposition of the enforced ratchet.

10) Strain controlled cycling followed by creep

Cyclic-plasticity and creep interactions are an important consideration in structures subjected to cyclic loads and temperatures above the creep range. The tests to assess the effect of prior plastic strain cycling on subsequent creep behaviour were conducted by Goodall (86) where cyclic strain controlled tests $\pm$ 0.25% strain were followed by constant stress creep at 600°C. The results shown in Fig. 2.31 show that prior cycling eliminated the primary creep strain rate of the virgin material. The result is seen to imply that the magnitude of creep deformation has been reduced because prior strain cycling has increased the creep resistance.

Chapter 3

Theoretical Considerations

3.1 Introduction

The theory of the Bree diagram has been given by Bree (2). He did not however show the analysis and derivations for certain aspects of the theory and has only given the relevant end results. Examples of these are the derivations of the equations for the boundaries differentiating the various regimes of structural behaviour in the diagram and the illustration of stress and strain calculations for regimes other than ratchetting (R1) and alternating plasticity (P1). The object of sections 2 and 3 is to cover these aspects in greater detail. Section 2 firstly describes the background theory in brief and then shows how the various types of structural behaviour can be achieved by use of a diagrammatic approach. This approach depends on cycle by cycle calculations of the stresses and the various components of strains which are then plotted to scale in a schematic format. The aim of showing this approach in such a form is to enable one to see in visual terms, how various regimes of structural behaviour come into being, in particular that of ratchetting. Section 3 gives in detail the analysis to obtain the boundaries (or hereafter known as bounds) of the Bree diagram which are determined from equilibrium conditions and wall surface yielding behaviour or criteria. The section further shows the analogy between the thermal stress and bending approach to the problem. By using classical elasto-plastic beam bending theory, it is shown that similar results are obtained although the total strain behaviour will be different.

The other main aim of this chapter is to show in the fourth section the analyses for finding the structural responses of three other

sequences of loading of the thermal and pressure loads on the Bree uni-axial model. These sequences are: (1) Continuous thermal and cyclic pressure loading, (2) Out-of-phase cyclic thermal and pressure loading, and (3) In-phase cyclic thermal and pressure loading. Where ratchetting is present, the expressions for ratchet strain per cycle are obtained. The analysis utilised the same method as that of section 3 on the 'Bree' sequence of loading and relies on the assumption that a steady cyclic stress state exists in the structure after a few cycles of loading. This latter assumption has been proved by Frederick and Armstrong (20) and numerical studies by computer finite element program by the author on all the above sequences have shown the existence of these states. The numerical studies which are described in Chapter 5 are in accord with the analytical results. A discussion and comparison of the behaviour of the various sequences follows at the end of the section.

3.2 A Diagrammatic Approach to Understanding the Bree Problem

In this section, the opportunity to describe the analysis of Bree in greater detail is firstly taken. This is followed by the main objective which is to describe the diagrammatic approach.

For a thin walled cylinder subjected to a constant internal pressure and cyclic through wall thermal gradient Bree obtained a closed form solution for the strain behaviour for any combination of pressure and thermal gradient. This solution was presented as a plot of σ_t/σ_Y against σ_p/σ_Y, where σ_t is the maximum fictitious elastic thermal stress and σ_p the pressure stress. This plot depicted zones of elastic, shakedown, alternating plasticity and ratcheting strain behaviour and has become known as the Bree diagram.

At the core of a fast-nuclear-reactor the fuel is contained within thin-walled cylinders - the fuel cans. During the life of the reactor the fuel is burnt up and produces both a change in volume of the fuel and some gaseous products. The effect of this is to subject the fuel cans to an internal pressure, which may be considered constant throughout the life of the can. In addition, at start-up and shut-down of the reactor, the fuel cans experience a high thermal gradient across the can wall. The effect of the pressure is to produce a constant bi-axial elastic stress whilst the temperature gradient causes a temporary thermal stress sufficient to cause plastic deformation. Since start-up and shut-down operations are likely to be cyclic, then the thermal stress will be cyclical in nature.

3.2.1 Elastic Analysis

(a) Pressure Stresses. From equilibrium for a thin wall cylinder subjected to an internal pressure we have in polar form

$$\int_{-t/2}^{+t/2} \sigma_\theta \, dx = 2 \int_{-t/2}^{+t/2} \sigma_z \, dx = \frac{pd}{2t} \qquad (3.1)$$

Where p is the pressure, σ_θ the hoop stress, σ_z the axial stress, t the thickness and x the radial co-ordinate measured +VE outwards from the mid-wall of the cylinder.

Assuming that σ_θ and σ_z have mean values σ_p and $\sigma_p/2$ respectively we have

$$\sigma_p = \frac{pd}{2t} \qquad (3.2)$$

(b) Thermal Stresses. The temperature distribution measured relative to the can mid-wall is given by

$$T = -\Delta T x/t \qquad (3.3)$$

If an element of the can is considered as a flat plate which is prevented from bending in both the axial and hoop directions then the temperature gradient gives rise to thermal stresses

$$\sigma_t = E\alpha\Delta T/2(1-\gamma) \qquad (3.4)$$

in both the axial and hoop directions. This stress is minimum ($= -\sigma_t$) at the inside surface and maximum ($= +\sigma_t$) at the outside surface.

Thus the total elastic stresses are:

$$\sigma_\theta = \sigma_p + \frac{2x\sigma_t}{t}$$

$$\sigma_z = \frac{\sigma_p}{2} + \frac{2x\sigma_t}{t} \qquad (3.5)$$

It should be noted that these are elastic stresses and may thus be fictitious since a yield criterion has yet to be introduced.

3.2.2 The Uniaxial Model

An elastic/plastic analysis of the stresses given by (3.5) can only be achieved by a numerical method. Bree, therefore, attempted to simplify the analysis by considering only the stresses in the hoop direction (which are the dominant stresses).

By assuming that

$$\Delta T' = \Delta T/(1-\gamma) \tag{3.6}$$

where $\Delta T'$ denotes the temperature difference for the uniaxial model, the hoop stress could be written as

$$\sigma = \sigma_p + \frac{2x\sigma_t}{t} \tag{3.7}$$

Consequently the model contains all the physical features of the biaxial stress system but yields simpler analytical solutions. Thus, Bree argued, a better qualitative understanding of the problem could be gained than from a detailed numerical solution.

3.2.3 Statement of the Simplified Problem

Now considering the deformation of an element of the can which is subjected to a steady hoop stress, σ_p, together with an alternating thermal stress due to the alternating temperature distribution

$$T = -\frac{\Delta T'x}{t} \rightarrow \text{constant} \rightarrow -\frac{\Delta T'x}{t} \rightarrow \ldots \tag{3.8}$$

the element being restrained from bending due to the temperature gradient.

If the total strain in the hoop direction is denoted by ε_T then the condition that bending is prevented can be written as

$$\varepsilon_T = \text{constant} \tag{3.9}$$

and from equilibrium.

and from equilibrium,

$$\int_{-t/2}^{+t/2} \sigma \, dx = \sigma_p t \qquad (3.10)$$

The yield condition may be written

$$\begin{aligned} |\sigma| &= \sigma_Y \text{ (in plastic regions)} \\ |\sigma| &< \sigma_Y \text{ (in elastic regions)} \end{aligned} \qquad (3.11)$$

where σ_y is the yield stress, and finally the uniaxial stress/strain relationship may be written as

$$\varepsilon_T = \frac{\sigma}{E} + \varepsilon_p + \alpha T \qquad (3.12)$$

where ε_p is the plastic strain, and αT is the thermal strain.

1st Half Cycle: During this period the can is subjected to the pressure loading together with the temperature gradient. On substituting for αT in Eqn. (3.12) the stress strain relationship becomes

$$\varepsilon_T = \frac{\sigma}{E} + \frac{2x\sigma_t}{Et} + \varepsilon_p \qquad (3.13)$$

2nd Half Cycle: During this period the can is subjected to the pressure loading only hence Eqn. (3.12) becomes

$$\varepsilon_T = \frac{\sigma}{E} + \varepsilon_p \qquad (3.14)$$

It is therefore required to solve Eqns. (3.13) and (3.14) subject to the restraints of Eqns. (3.9), (3.10) and (3.11).

It can be noted that for both the 1st and 2nd half cycles, ε_T must be constant through the thickness of the can wall. Hence from Eqn. (3.13), i.e. for the first half of the cycle $(\frac{\sigma}{E} + \varepsilon_p)$ must be linear in x with slope $\frac{2\sigma_t}{Et}$

i.e.

$$(\frac{\sigma}{E} + \varepsilon_p) = \frac{-2\sigma_t}{Et} x + \varepsilon_T \qquad (3.15)$$

Thus in regions of the can where ε_p is constant $\frac{\sigma}{E}$ has slope $\frac{2\sigma_t}{Et}$.

For the second half of each cycle, Equation (3.14) applies and since ε_T is constant $\frac{\sigma}{E} + \varepsilon_p$ is uniform across the can wall. Thus $\frac{\sigma}{E}$ and ε_p have equal and opposite slopes at each point in the can.

3.2.4 The Condition of Ratchetting

Consider firstly Fig. 3.1(a). This shows the stress distribution through the wall of the cylinder due to the pressure and the thermal stress. The pressure stress alone will always be less than the yield stress and to this is added the thermal stress. However, this summation then violates both of Equations (3.10) and (3.11). In order to satisfy (3.10) and (3.11) the stress distribution must take the form of Fig. 3.1(b) and the value of x = a may be found from the equilibrium condition - i.e. Equation (3.10), and results in

$$x = a = -\frac{1}{2}\cdot\frac{t}{E}\left[1 - 2\sqrt{(\sigma_Y - \sigma_p)/\sigma_t}\right] \qquad (3.16)$$

3.2.5 The Diagrammatic Approach

The methodology of the approach can best be illustrated by selecting an operating point $(\sigma_p/\sigma_Y, \sigma_t/\sigma_Y)$ on the Bree diagram and working through the Fig. 3.2(a). The point chosen in this case lies in the type R1 ratchetting regime.

Referring to Fig. 3.2(a) A, B and C show the contributions to the total strain D for the first half cycle. It is known that the total strain must be uniform through the can wall and the summation of $(\sigma/E) + \varepsilon_p + \alpha T$ shows this to be so. Thus the left hand column of Fig. 3.2(a) shows the contributions to the total strain for the first half cycle - i.e. pressure load + thermal gradient.

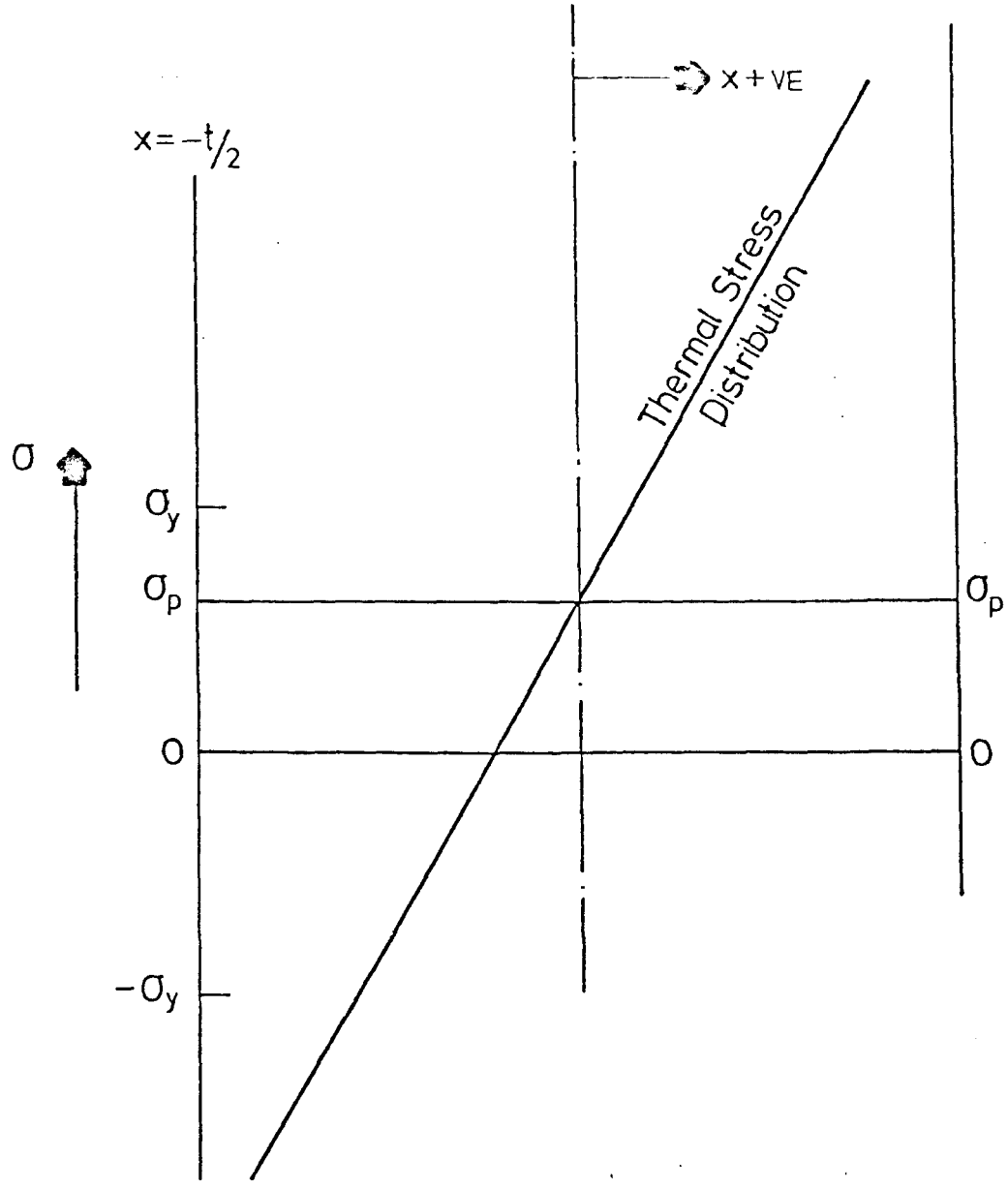

FIG. 3.1(a) Stress Distribution During 1st Half Cycle

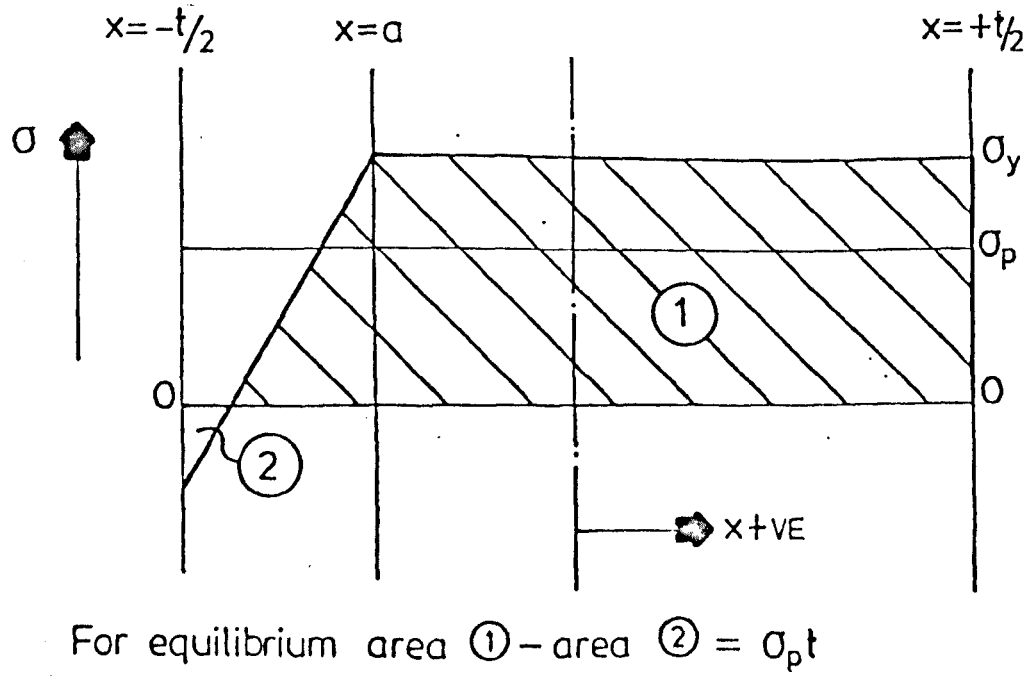

For equilibrium area ① − area ② = $\sigma_p t$

FIG. 3.1(b) Summation of Stresses During the First Half Cycle but Violating the Conditions of Equilibrium & Yield

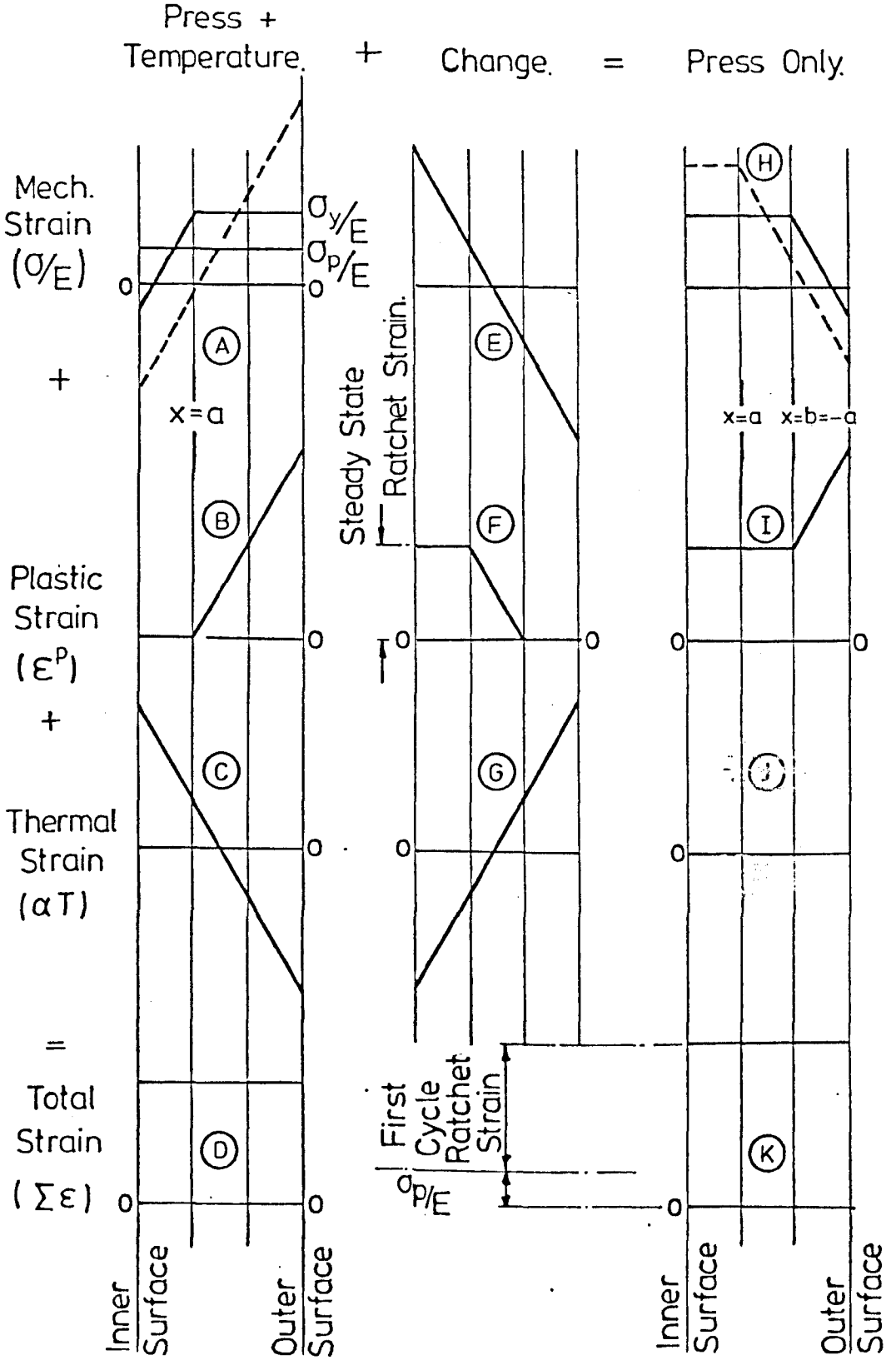

FIG. 3.2(a) Ratchetting Regime R1 at Operating Point σ_p/σ_y = 0.55, σ_t/σ_y = 2.0

The centre column of Fig. 3.2(a) shows the strain changes required to reach the second half cycle, i.e. pressure only. The strains at this stage are shown in the right hand column of Fig. 3.2(a).

Working across the top row of Fig. 3.2(a) E shows the fictitious elastic stresses to be added to A to remove the thermal stress. This results in H (dotted) which again violates (3.10) and (3.11). In order to satisfy (3.10) and (3.11) the full line H is required. This incurs no additional plastic strain in the zone x = b to x = +t/2, but in the zone x = -t/2 to x = b the additional plastic strain of F is incurred. The total plastic strain is then I which is B + F. The thermal strains C and G add to give zero at J. For the second half cycle the total strain is now the sum H + I + J giving K which is uniform as required. The ratchet strain accumulated over this period is shown between D and K. Figure 3.2(b) shows the corresponding analysis for ratchetting in the regime R2 where compressive yield occurs in the first half cycle. Here the analysis was carried out for 3 half cycles showing clearly the progressive accumulation of strain. The ratchet strain per cycle is in accord with theoretical ratchet rates.

After the first cycle the strain accumulated in each cycle will be that shown in F (Fig. 3.2(a)). This may be written as

$$\delta = 2.a\,\frac{2\sigma_t}{t}$$

and using Eqn. (3.16) this becomes

$$\delta = \frac{2\sigma_t}{E}\left[\,1 - 2\sqrt{(\sigma_Y - \sigma_p)/\sigma_t}\,\right] \qquad (3.17)$$

Bree introduced the quantity σ_e being

$$\sigma_e = \sigma_p + \tfrac{1}{4}\sigma_t - \sigma_Y$$

So that Eqn. (3.17) may be written

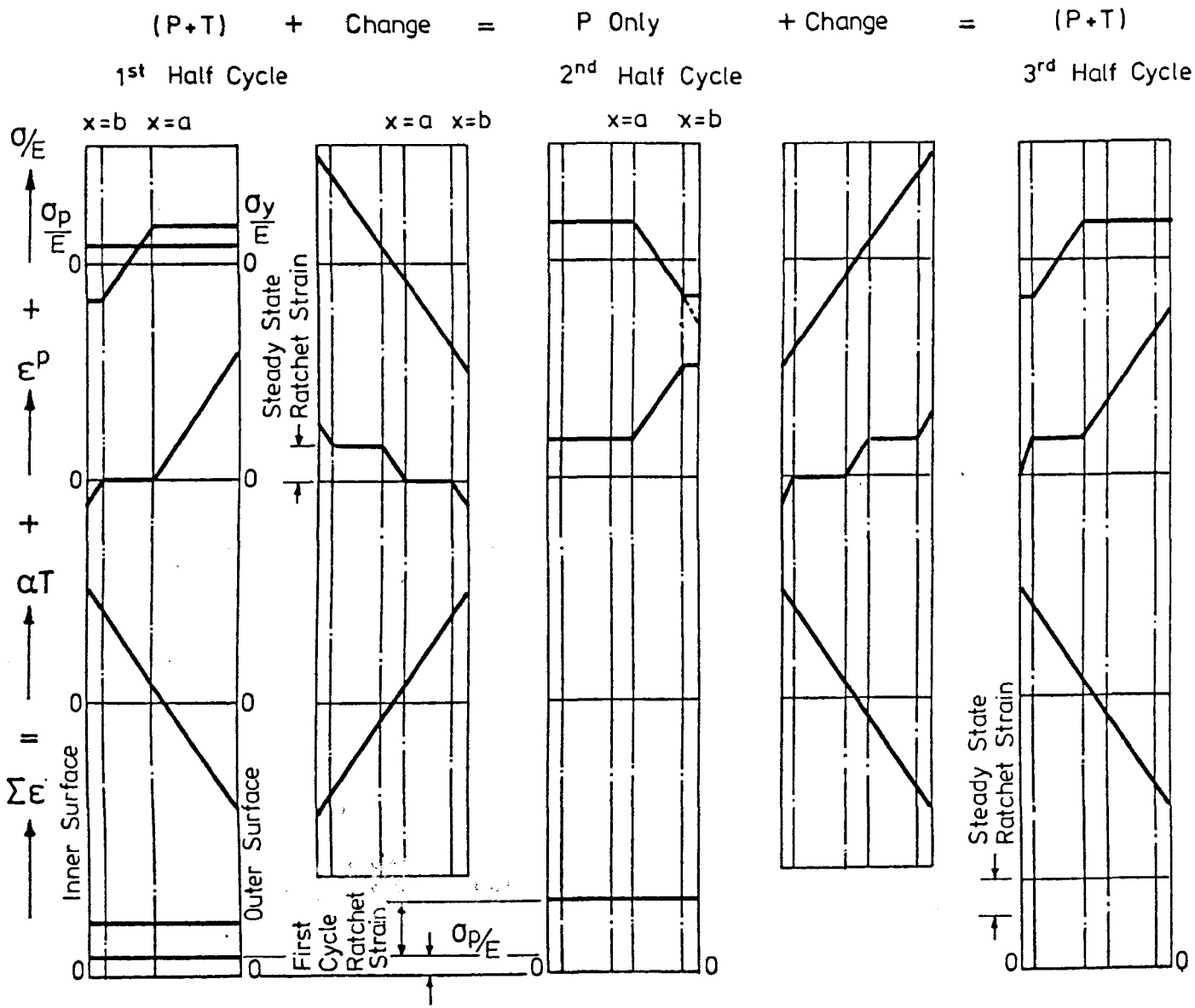

FIG. 3-2(b) Ratchetting R2 at Operating Point $\sigma_p/\sigma_y = 0{\cdot}5$, $\sigma_t/\sigma_y = 3{\cdot}0$.

$$\frac{E\delta}{2\sigma_t} = 1 - (1 - \frac{4\sigma_e}{\sigma_t})^{\frac{1}{2}} \qquad (3.18)$$

and if $\sigma_e \ll \frac{1}{4}\sigma_t$ then Eqn. (3.18) reduces to

$$\delta = \frac{4\sigma_e}{E} \qquad (3.19)$$

Fig. 3.3 shows a plot of ratchet strain against σ_e/σ_t as given by Equations (3.18) and (3.19).

For differing combinations of σ_p and σ_t the behaviour of the can material will be different. It is seen here the conditions which lead to ratchetting but other stress conditions may lead to shakedown, alternating plasticity or purely elastic performance.

For example Fig. 3.4 shows a combination of σ_p and σ_t in the same manner as Fig. 3.2(a). It is established that although yielding occurs repeatedly on both surfaces of the can no strain is accumulated. This condition is termed alternating plasticity.

Thus two distinct types of strain behaviour occurring for different combinations of σ_p and σ_t are identified. Clearly if neither σ_p nor σ_t violate the yield criterion then a condition of purely elastic behaviour will exist. A fourth type of strain behaviour occurs when after the first half cycle, during which the yield criterion is violated subsequent deformation is entirely elastic. This condition is termed shakedown. Shakedown can occur with yielding during the first half cycle on the surface under tensile stress (which is the outer surface) or in combination with compressive yielding on the inner surface. Figs. 3.5 and 3.6 show that in both cases no strain is accumulated with continued load cycling.

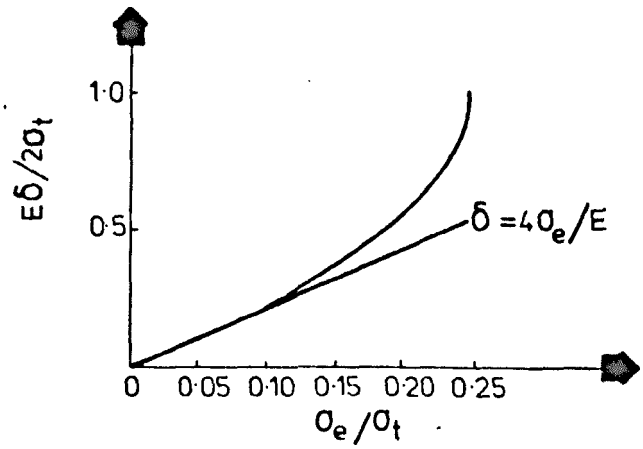

FIG. 3.3 Ratchet Strain per Cycle for the Stress Regime R1 of Fig. 3.5

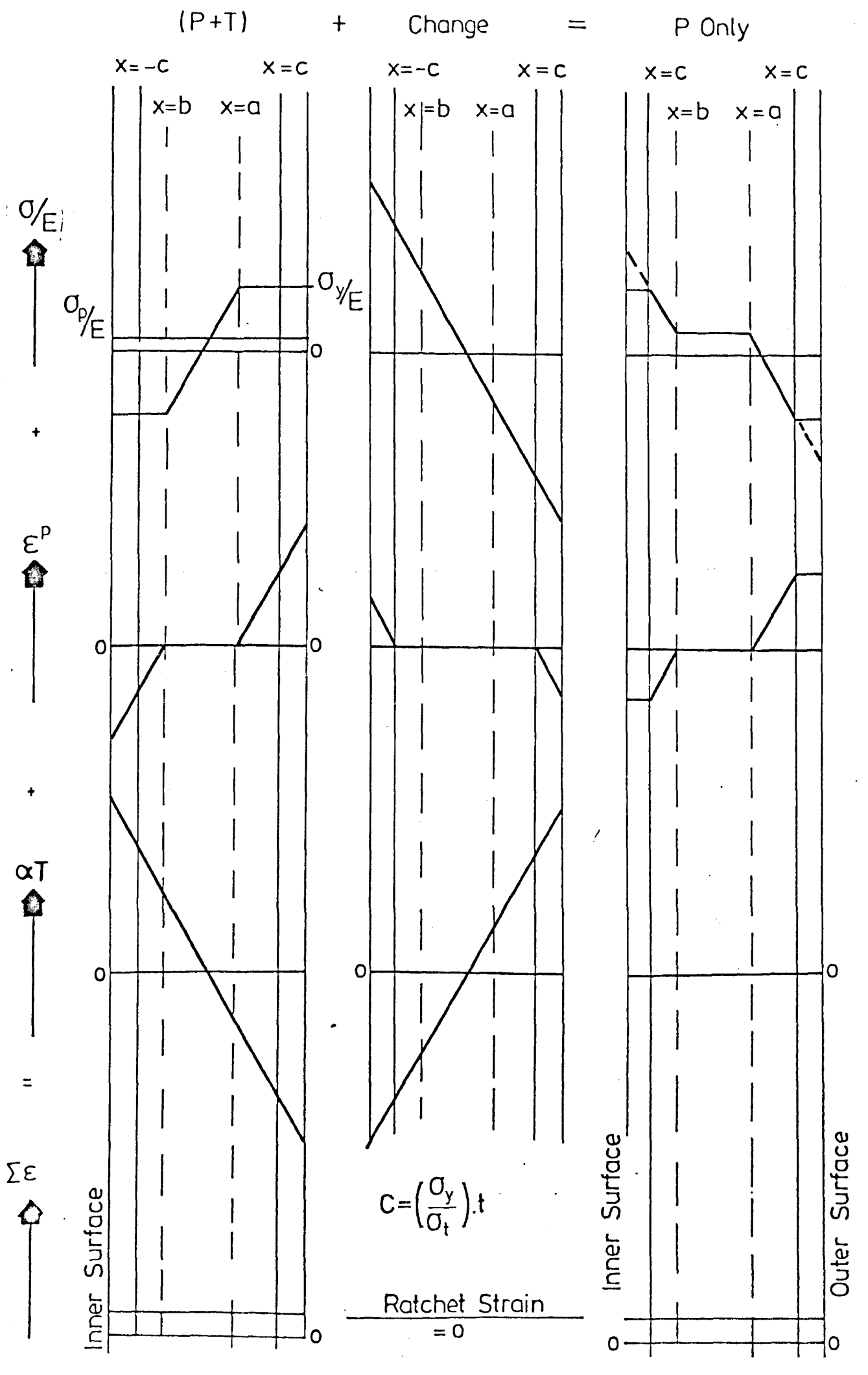

FIG. 3.4 Alternating Plasticity Regime P at Operating Point $\sigma_p/\sigma_y = 0.2$, $\sigma_t/\sigma_y = 2.7$

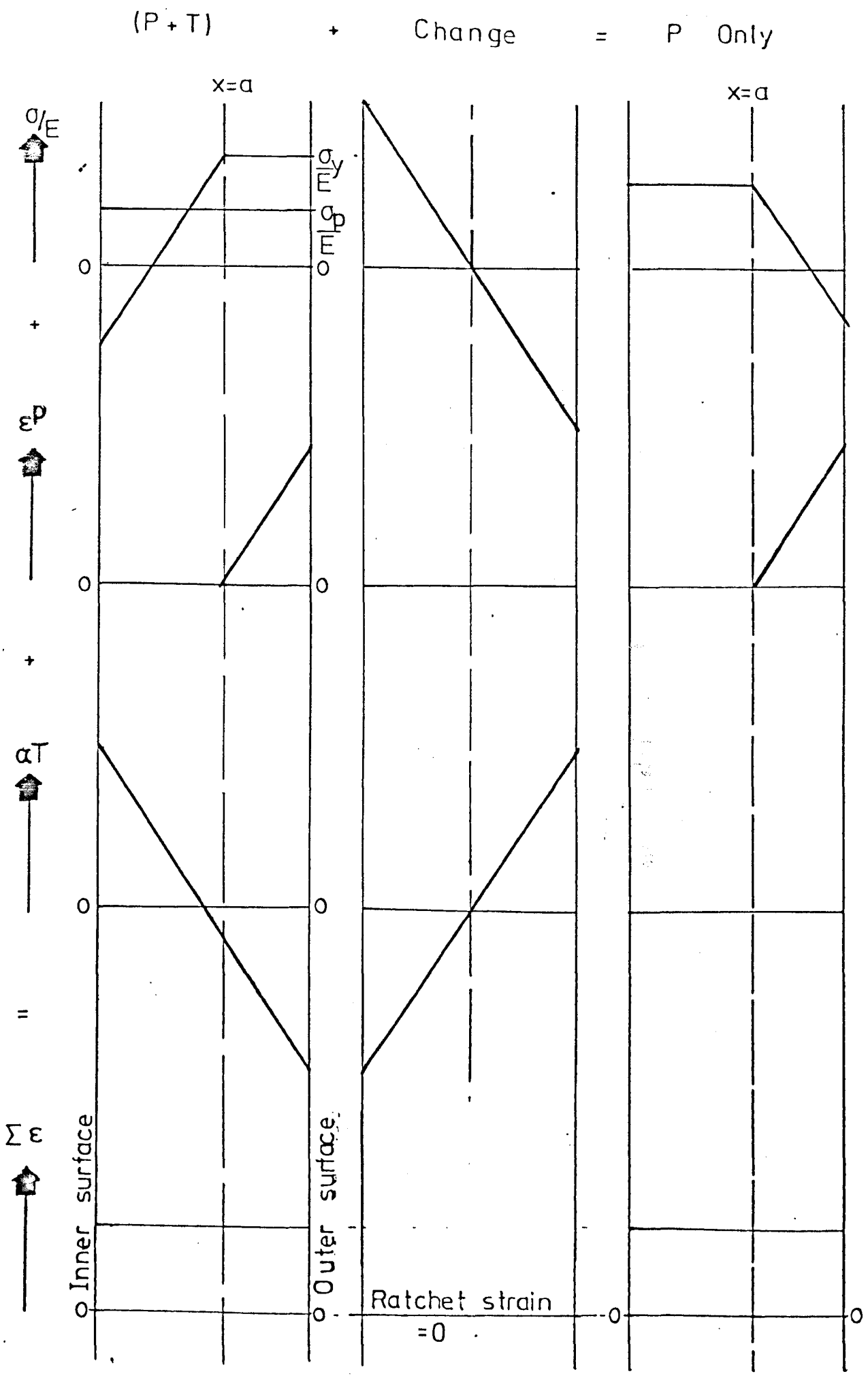

FIG. 3.5 Shakedown Regime S1 at Operating Point $\sigma_p/\sigma_y = 0.5$, $\sigma_t/\sigma_y = 1.5$

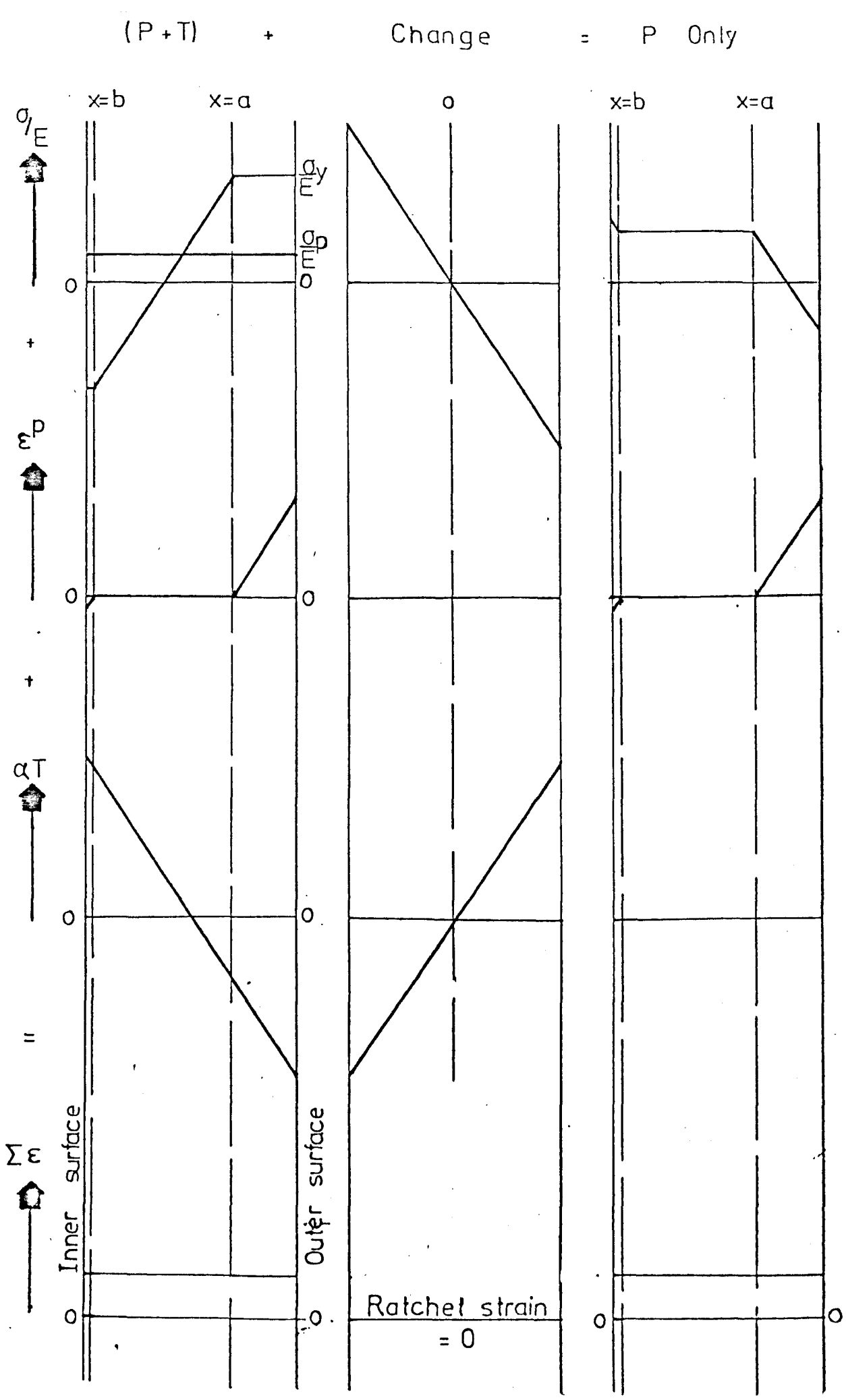

FIG. 3.6 Shakedown Regime S2 at Operating Point $\sigma_p/\sigma_y = 0.25$, $\sigma_t/\sigma_y = 1.5$

3.3 Analysis of the Bree Problem

3.3.1 The Solutions for the Bree Diagram Bounds

In this section the solutions for the Bree diagram's bounds which separates the various structural behaviour regimes are shown. The expressions governing the thermal stress and pressure stress parameters are given in the paper (2) but the analyses from which these are obtained were not given. It is therefore considered necessary to enter into the analyses for completeness.

In the analyses, the theorems by Frederick and Armstrong (20) are evoked. These theorems are concerned with the convergence of steady cyclic states of stress in a structure which is cyclically loaded. The theorems state that there are unique steady cyclic stress states existing in a structure when it has been cyclically loaded for a number of cycles. This is regardless of the initial stresses which are present in the structure - subsequent cycling will cause these stresses to converge to a unique steady cyclic stress state provided the repeated loadings are the same. The steady cyclic state is here defined as a state in which the stresses before and after the repeated application of a loading are the same; that is, the repeated application of a loading cycle produces no net change in the stress. These theorems have enormous implications in structural analysis because an analysis of a structure for a small number of cycles by incremental calculation are usually sufficient to calculate the steady cyclic stress state. This is provided that no large geometry changes are caused and material properties are not cycle dependent.

Incremental calculations shown in the previous section show that these states exist in the Bree structure and are reached after the first half cycle. The cyclic stress states in the form of stress through

thickness distributions are unchanged every alternate half cycle, that is, the elastic-plastic interfaces and constant elastic stress gradient stress interfaces remain in the same positions within the wall thickness. This is easily understood since the interface positions are uniquely determined from equilibrium considerations against external thermal and pressure load alone and independent of cycle number.

To obtain the bounds, it is necessary to obtain two equilibrium equations which are functions of the pressure stress (σ_p), thermal stress (σ_t), yield stress (σ_Y) and the interface positions (a, b, etc.) which are measured outwards from the mid-surface. Fig. 3.7 (a, b & c) show the necessary notation and aids for the analysis. In Fig. 3.7 (a), the sequence of loading is shown based on a $\frac{1}{2}$ cycle count. The first loading profile represents the cyclic thermal load (parameter X) of an arbitrary magnitude and the count begins with n which is to indicate that the analysis is performed in the middle of the operating life and that a steady cyclic stress state has been firmly established. Fig. 3.7 (b) and (c) are two stress distributions of the steady cyclic stress state during the n^{th} and $(n + 1)^{th}$ cycles. The n^{th} cycle coincides with the application of the pressure and thermal load and the $(n + 1)^{th}$ cycle with that of the pressure load only. The difference between the two figures lies in the yielding behaviour of the outer surface material. In Fig. 3.7 (b), no yield in compression has yet occurred whilst in Fig. 3.7 (c), compressive yielding has already taken place. This is to establish the regimes of type R1 and R2 behaviour. On the basis of Figs. 3.7 (b) and (c), two equilibrium equations are obtained as a result of summation of forces which when solved gives rise to the various bounds of structural behaviour. Therefore for convenience, equations so obtained using Figs. 3.7 (b) and (c) will be classified as Cases 1 and 2 respectively. Similar classification will also be adopted

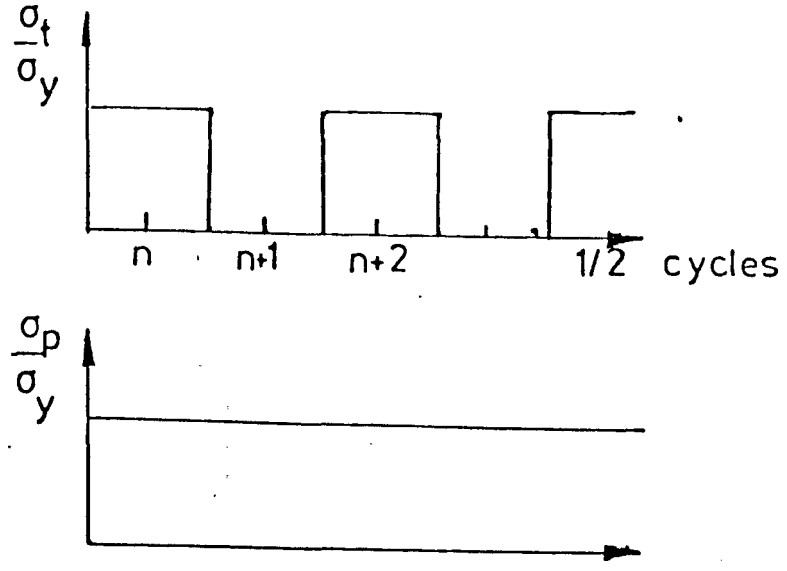

FIG. 3.7(a) Bree's Loading Sequence

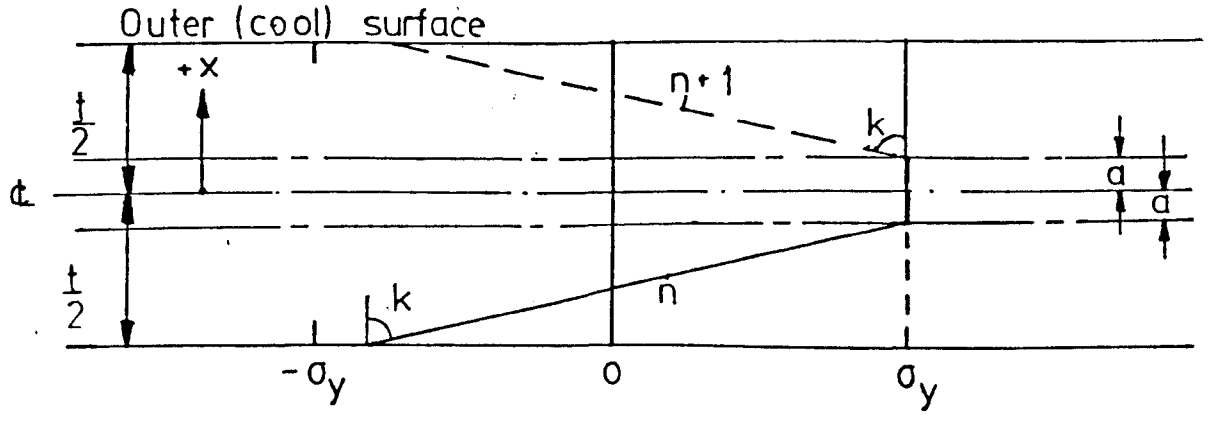

FIG. 3.7(b) Stress Distribution under R1 (Ratchetting) Condition

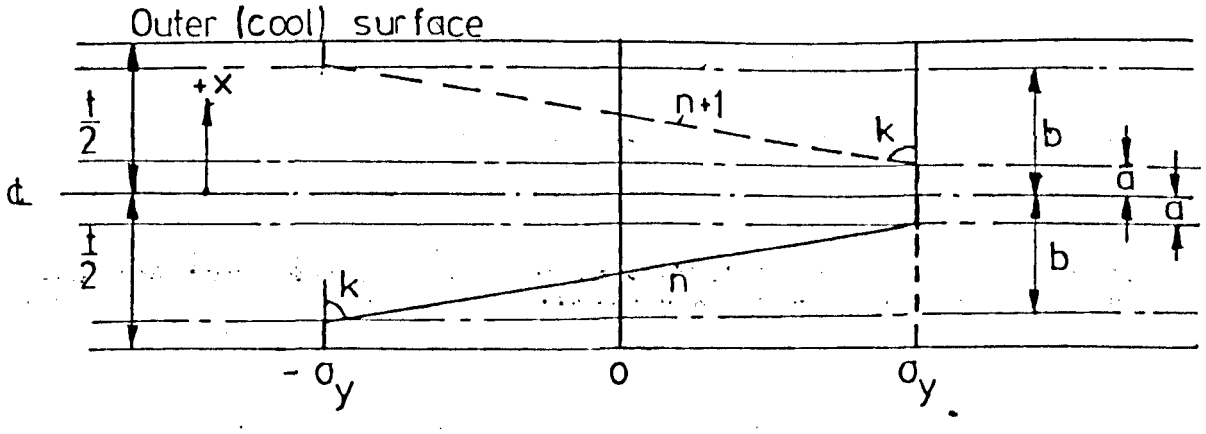

FIG. 3.7(c) Stress Distribution under R2 (ratchetting) Condition

for the analysis of the alternative loading sequences.

Finally, the analyses retain all the simplifying assumptions and conditions assumed by Bree. In particular, the elastic/perfectly-plastic material property and the linear quasi static loading were the most important assumptions.

The thermal stress gives rise to the stress through thickness gradient K which is given by the maximum thermal stress divided by the half thickness

$$K = \frac{\sigma_t}{t/2} = E\,\alpha\left(\frac{\Delta T}{2}\right)\left(\frac{1}{1-\gamma}\right)\left(\frac{2}{t}\right)$$

where ΔT is the temperature difference between inner and outer surfaces

γ is Poisson's ratio to account for the hoop stress component in the cylinder wall

Referring to Figs 3.7 (b & c), it is seen that the stress distributions at the n^{th} and $(n+1)^{th}$ cycles mirror each other about the mid-surface. This is a characteristic which will be seen later to be particular only to the loadings due to cyclic temperature and constant pressure. The elastic plastic interfaces a and b are therefore at equal distances from the mid-surface. In the n^{th} half cycle, the material has yielded in tension in a region from $x = -a$ to $x = +t/2$ while in the $(n+1)^{th}$ half cycle, tensile yielding has occurred from $x = +a$ to $x = -t/2$. The overlap region from $x = -a$ to $x = a$ has yielded in both successive half cycles while the regions on both sides have yielded at least once during each complete cycle. The total plastic strain incurred during this cycle is given by the overlap width multiplied by K/E

$$\delta = 2a\,\frac{K}{E}$$

This is the ratchetting strain per cycle.

For the stress regimes R1 and R2, the condition for the bounds separating ratchetting and non-ratchetting, is $\delta = 0$ or $a = 0$.

To obtain the expressions for the bounds, the equilibrium equations are firstly obtained. These are of the following forms.

$$\sigma_p.t = \int_{-t/2}^{t/2} \sigma(x).dx \qquad \text{for } n^{th} \text{ half cycle} \tag{3.20}$$

$$\sigma_p.t = \int_{-t/2}^{t/2} \sigma(x).dx \qquad \text{for } n+1^{th} \text{ half cycle} \tag{3.21}$$

The two forms are similar in this instance since the pressure stress is continuous.

Case 1

For the n^{th} half cycle, (Fig. 3.7(b)), the stress conditions are,

$$\sigma(x) = \sigma_Y - K(a - x) \quad \text{for} \quad -t/2 < x < -a$$
$$\sigma(x) = \sigma_Y \quad \text{for} \quad -a < x < t/2$$

Integrating Eqns. (3.20) for the above conditions gives,

$$\sigma_p.t = \int_{-t/2}^{-a} (\sigma_Y - K(a-x))\, dx + \int_{-a}^{+t/2} \sigma_Y.dx$$

$$\sigma_p = -\frac{K}{2t}\left(a + \frac{t}{2}\right)^2 + \sigma_Y \tag{3.22}$$

This is the equilibrium equation for Case 1 represented by Fig. 3.7(b). As the stress distributions in the n^{th} and $(n + 1)^{th}$ cycles are symmetrically opposed to each other, the resulting equilibrium equations for these two cycles will be similar. Hence only one equation is required.

Bound 1

For fully elastic behaviour, no yielding occurs during the 1st (or n^{th}) and 2nd (or $(n+1)^{th}$) half cycle. Therefore putting the boundary condition of $a = \frac{t}{2}$ (which in Fig. 3.7(b) can be seen as an extension of the yield interface to the outer surface) into Eqn. (3.22) gives,

$$\sigma_p = -\frac{Kt}{2} + \sigma_Y$$

since $\frac{Kt}{2} = \sigma_t$,

$$\therefore \quad \sigma_p + \sigma_t = \sigma_Y$$

Dividing throughout by σ_y and then substituting the non-dimensional parameters of $X = \frac{\sigma_p}{\sigma_Y}$ and $Y = \frac{\sigma_t}{\sigma_Y}$ gives,

$$X + Y = 1 \tag{3.23}$$

Bound 2

To obtain the bound of the S1 shakedown regime, the boundary condition of $a = 0$ is taken. The reason for assuming this boundary condition will be clarified in section 3.3.2. On substituting $a = 0$ into Eqn. (3.22)

$$\sigma_p = \frac{-Kt}{2} + \sigma_Y$$

$$\therefore \quad \sigma_p + \frac{\sigma_t}{4} = \sigma_Y \qquad \text{since } \frac{Kt}{2} = \sigma_t$$

Therefore

$$X + Y/4 = 1 \tag{3.24}$$

Case 2

Referring now to the stress distribution shown in Fig. 3.7(c) the

equilibrium equation is again obtained. Firstly, the stress distributions and their limits are as follows

$$\sigma(x) = -\sigma_Y \qquad \text{for } -\frac{t}{2} < x < -b$$

$$\sigma(x) = -\sigma_Y + K(b+x) \qquad \text{for } -b < x < -a$$

$$\sigma(x) = \sigma_Y \qquad \text{for } -b < x < \frac{t}{2}$$

Substituting the above conditions into Eqn. (3.20) gives

$$\sigma_p \cdot t = \int_{-t/2}^{-b} -\sigma_Y \cdot dx + \int_{-b}^{-a} (-\sigma_Y + K(b+x))\, dx + \int_{-a}^{t/2} \sigma_Y \cdot dx$$

On integrating, putting in the limits and simplifying gives

$$\sigma_p \cdot t = \sigma_Y (2a) + \frac{K}{2}(b - a)^2$$

Multiplying by 2K throughout gives

$$4\sigma_p\sigma_t = 4\sigma_Y Ka + K^2 (b - a)^2 \qquad (3.25)$$

This is the equilibrium equation for Case 2 which is represented by Fig. 3.7(b). It is seen that Eqn. (3.22) has a variable (b) less than Eqn. (3.25) by virtue of the consideration of compressive yielding in the material beneath the lower surface where b represents the distance from the mid-surface to the fibre at which yielding occurred. Similar comments concerning the symmetrical distributions of the n^{th} and $(n+1)^{th}$ half cycle applies.

Bound 3

Firstly, in this case, the bound which separates Case 1 and Case 2 type of distribution is found. By assuming the boundary conditions that

the inner surface stress is at the point of compressive yielding, i.e. $b = \frac{t}{2}$, and through the thermal stress gradient condition that

$$K\,(b - a) = 2\sigma_Y$$

the following is obtained.

On substituting the above into Eqn. (3.25)

$$4\sigma_p\sigma_t = 4\sigma_Y\,(\sigma_t - 2\sigma_Y) + 4\sigma_Y^2$$

$$\therefore \quad \sigma_t(\sigma_Y-\sigma_p) = \sigma_Y^2$$

$$Y(1-X) = 1 \qquad (3.26)$$

This bound separates the regimes of R1 and R2, S1 and S2.

Bound 4

The bound which separates alternating plasticity (P) and ratchetting (R2) behaviour is given if the boundary conditions of $a = 0$ and $K(b-a) = 2\sigma_Y$ are taken. The reasons for this will be clarified in section 3.3.2. Substituting into Eqn. (3.25) gives,

$$4\sigma_p\sigma_t = (2\sigma_Y)^2$$

$$\sigma_p\sigma_t = \sigma_Y^2$$

$$\therefore \quad XY = 1 \qquad (3.27)$$

Bound 5

For elastic/perfectly-plastic materials, the maximum shakedown load cannot exceed $2\sigma_Y$. This condition separates the alternating plasticity (P) and shakedown (S2) behaviour.

Therefore $$\sigma_t = 2\sigma_Y$$

$$\therefore \quad Y = 2 \tag{3.28}$$

The expressions (3.23, 3.24, 3.26, 3.27, and 3.28) completely define the bounds on the Bree diagram. The plot of the expressions are given in Fig. 3.11(a).

3.3.2 Ratchetting and Alternating Plasticity Strain Calculations

The ratchetting strain per cycle has been given by $\delta = 2aK/t$.

For R1 ratchetting strain, the width 'a' is found from Eqn. (3.22). Re-arranging to make 'a' the dependent variable and σ_p, σ_t, σ_Y the independent variables gives

$$a = -\frac{t}{2}\left(1 - 2\sqrt{(\sigma_Y - \sigma_p)/\sigma_t}\right)$$

therefore $$\delta = \frac{Kt}{E}\left(1 - 2\sqrt{(\sigma_Y - \sigma_p)/\sigma_t}\right)$$

$$= \frac{2\sigma_t}{E}\left(1 - 2\sqrt{(\sigma_Y - \sigma_p)/\sigma_t}\right)$$

$$= 2\left(Y - 2\sqrt{(1 - X)Y}\right)\sigma_Y/E \tag{3.29}$$

It is easy to obtain the ratchetting and non-ratchetting bound from Eqn. (3.29) by putting $\delta = 0$.

Therefore,

$$1 - 2\sqrt{(\sigma_Y - \sigma_p)/\sigma_t} = 0$$

$$\frac{\sigma_t}{4} + \sigma_p = \sigma_Y$$

$$\frac{Y}{4} + X = 1$$

This is similar to Eqn. (3.24) (Bound 2). Hence it is inferred that for the boundary conditions used in obtaining Bound 2, ratchetting will occur when the mid-surface undergoes tensile yielding.

For R2 ratchetting, a similar manipulation on equilibrium Equation (3.24) gives

$$4\sigma_p\sigma_t = 4\sigma_Y\sigma_t\left(\frac{2a}{t}\right) + 4\sigma_Y^2$$

$$2a = t((\sigma_p\sigma_t - \sigma_Y^2)/\sigma_Y\sigma_t)$$

$$= t(\sigma_p/\sigma_Y - \sigma_Y/\sigma_t)$$

Therefore

$$\delta = \frac{Kt}{E}(\sigma_p/\sigma_Y - \sigma_Y/\sigma_t)$$

$$= \frac{2\sigma_t}{E}(\sigma_p/\sigma_Y - \sigma_Y/\sigma_t)$$

$$= 2(XY - 1)\sigma_Y/E \qquad (3.30)$$

Again putting $\delta = 0$ in this second case gives,

$$\sigma_p/\sigma_Y - \sigma_Y/\sigma_t = 0$$

$$\sigma_p\sigma_t = \sigma_Y^2$$

$$\therefore \quad XY = 1$$

Again the above equation is similar to Eqn. (3.27) (Bound 4) which was obtained by assuming that tensile mid-surface yielding occurs at the onset of ratchetting. Hence, it may be generalized that for the Bree sequence of loading, the mid-surface yielding behaviour determines the occurrence of ratchetting.

Additionally, during each cycle, material at positions of $|x| > b$ undergoes an hysteresis loop of width

$$z = (|x| - b)\frac{K}{E}$$

$$= (|x| - b)\frac{2\sigma_t}{tE} \qquad (3.31)$$

For the alternating plasticity (P) regime, the mid-surface stress has not reached yield but the thermal stress σ_t at the inner and outer surface has exceeded $2\sigma_Y$. This means that material beneath the surfaces alternately yield in opposite senses at every half cycle. The loop width is given by

$$z = (|x| - c) \cdot \frac{2\sigma_t}{tE} \qquad (3.32)$$

where $$c = \frac{\sigma_Y}{\sigma_t} \cdot t$$

When the loop width is reduced to zero, the bound between alternating plasticity (P) and shakedown (S2) can be found.

Hence $$|x| - c = 0$$

where $$|x| = \frac{t}{2}$$

which gives $$c = \frac{t}{2}$$

$$\therefore \quad \sigma_t = 2\sigma_Y$$

$$\therefore \quad \underline{Y = 2}$$

Which is the same as Bound 5 Eqn. (3.28).

3.3.3 The Solutions for Bree Diagram Bounds Based on Classical Beam Theory

The stress combinations or bounds of the Bree uniaxial model under cyclic thermal and constant pressure can also be derived by means of elasto-plastic beam bending theory. In these solutions the beam is considered to be rectangular in cross-section having unit width and depth t and the loads imposed onto it are a cyclic maximum bending stress of σ_b which is induced by bending round a fixed curvature (r) together with a

constant axial stress of σ_a due to an axial load W. This 'equivalent' Bree beam will therefore be similar to the uniaxial model through the following terms

the slope $$K = \frac{\sigma_t}{t/2} = \frac{\sigma_b}{t/2}$$

$$= \frac{E\alpha\Delta T}{t(1-\gamma)} = \frac{E}{r}$$

and $$\sigma_p = \sigma_a$$

$$\frac{pR}{t} = \frac{W}{t} \qquad (3.35)$$

Concerning the strain distribution through the thickness, the thermal case has a constant total strain whereas in the bending case the total strain varies linearly through the thickness during the first half of each cycle. The difference in strain would be equal to $\frac{2\sigma_t x}{Et}$ between the two cases. On the second half of each cycle, the total strain between the two cases are the same.

3.4 Solutions for the Bounds of the Alternative Diagrams

In this section elasto-plastic solutions are obtained for Bree type or alternative diagrams which result from changes in the sequence of the cyclic loadings. The original Bree diagram is applicable to a loading type consisting of a constant pressure load and cyclic thermal load. The types of alternative loading to be considered are (a) Constant thermal load with cyclic pressure load, (b) Cyclic thermal and pressure loads applied in phase with each other and (c) Cyclic thermal and pressure loads applied out of phase with each other. For convenience, the abbreviations of C.T. (Continuous Temperature), I.P. (In-Phase) and O.P. (Out of Phase) may hereafter be used to refer to the alternative loading types of (a), (b) and (c) respectively.

All the alternative loadings have been simulated by computer programs and the stress regimes have been calculated and represented by Bree-type diagrams. These programs, together with others, are to be described in Chapter 5. The need for explicit expressions specifying the stress conditions or bounds for the stress regimes and expressions for calculating ratchetting strains necessitated a detailed analytical study. Examination of the stress through thickness distributions derived by numerical cycle by cycle calculations show that steady cyclic stress states are established after the first half cycle in all loading sequences. The half cycle numbers are named n^{th} and $(n+1)^{th}$ cycle since the steady cyclic stress states are already established.

To obtain the bounds separating the regimes of structural behaviour, the criteria of Bree are used where possible. In the paper of Bree, the criteria used are the yielding behaviour of the external wall surfaces during the first half cycle for the shakedown regimes (S1 and S2) and during the n^{th} cycle for ratchetting (R1 and R2) and alternating plasticity

(P) regimes. In the subsequent analysis, new regimes of P1 and P2 are required to differentiate type 1 and type 2 behaviour in the alternating plasticity regime (P). Table 3.1 shows the definition of the criteria used for all loading sequences.

The method of obtaining the bounds are similar to that shown in section 3.3.2. Firstly the stress distributions for the arbitrary loads are assumed and equilibrium equations obtained for two successive half cycles. The structural behaviour criteria of Bree are then applied. For ratchetting strain calculations, the elastic-plastic interface positions are calculated for two successive half cycles. If these positions are such that overlap occurs, that is the material within the overlap width (d) suffers yielding in tension twice while the material outside the width once in the successive half cycles, then ratchetting results. The ratchetting strain is given by,

$$\delta = \frac{d.K}{E} \quad *$$

using the usual notation of section 3.3.2.

The bounds for differentiating ratchetting and non-ratchetting regimes are obtained if $\delta = 0$. $\delta < 0$ gives the conditions of shakedown and alternating plasticity.

3.4.1 Continuous Thermal and Cyclic Pressure Loading (C.T.)

The loading sequence is shown in Fig. 3.8(a). Figs 3.8(b) and (c) show the stress distributions calculated incrementally at the shakedown regimes S1 and S2 respectively.

Case 1

For this first case, the general equilibrium equations for the n^{th} and $(n+1)^{th}$ half cycles are obtained based on Fig. 3.8(b) at the n^{th} half cycle,

* Ratchet strains calculated by this equation agree exactly with the numerical calculations of Chapter 5 and this equation is therefore deemed, by observation, to be correct.

Structural Behaviour	Loading Sequence	Yielding Behaviour at Wall Surfaces				Notes
		Inner (Hot) Surfaces		Outer (Cool) Surfaces		
		1st $\frac{1}{2}$	2nd $\frac{1}{2}$	1st $\frac{1}{2}$	2nd $\frac{1}{2}$	
Fully Elastic(E)	'Bree',IP OP, CT	Elastic	Elastic	Elastic	Elastic	Fully elastic behaviour without initial yielding.
Shakedown (S1)	'Bree' CT IP	Elastic Elastic Elastic	TY Elastic TY	TY TY TY	Elastic Elastic Elastic	Elastic shakedown after the first cycle for all loading sequences although yielding takes place at different half cycle numbers and surfaces.
Shakedown (S2)	'Bree' CT OP IP	CY Elastic CY CY	Elastic CY Elastic Elastic	TY TY TY TY	Elastic Elastic Elastic Elastic	Elastic shakedown after the first cycle in all cases. All inner surfaces must undergo compressive yielding during the first cycle.
		n^{th} $\frac{1}{2}$	$(n+1)^{th}$ $\frac{1}{2}$	n^{th} $\frac{1}{2}$	$(n+1)^{th}$ $\frac{1}{2}$	
Alternating Plasticity (P1)	OP IP	<u>CY</u> ER	<u>TY</u> TY	TY <u>TY</u>	ER <u>CY</u>	Alternating plasticity on one surface (underlined) only while the other surface undergoes shakedown.
Alternating Plasticity (P2)	'Bree' OP IP	CY CY CY	TY TY TY	TY TY TY	CY CY CY	Alternating plasticity on both surfaces. Except 'Bree', unequal (non-symmetrical) hysteresis widths are experienced on each surface.
Ratchetting (R1)	'Bree' OP IP	ER <u>CY</u> ER	TY <u>TY</u> TY	TY TY <u>TY</u>	ER ER <u>CY</u>	Ratchetting is attained with alternating plasticity on one surface (underlined) with the exception of 'Bree'.

Continued/

Structural Behaviour	Loading Sequence	Yielding Behaviour at Wall Surfaces				Notes
		Inner (Hot) Surfaces		Outer (Cool) Surfaces		
		$n^{th}\frac{1}{2}$	$(n+1)^{th}\frac{1}{2}$	$n^{th}\frac{1}{2}$	$(n+1)^{th}\frac{1}{2}$	
Ratchetting (R2)	'Bree' OP IP	CY CY CY	TY TY TY	TY TY TY	CY CY CY	Ratchetting is attained with alternating plasticity on both surfaces. For 'Bree', hysteresis widths are symmetrical whereas, for the others, these are dissimilar on both surfaces.

Table 3.1 General Classification of Structural Behaviour for Bree and Other Alternative Loading Sequences on the Basis of Initial Wall Surface Yielding Behaviour.
(CY for Compressive Yielding, TY for Tensile Yielding and ER for Elastic Response)

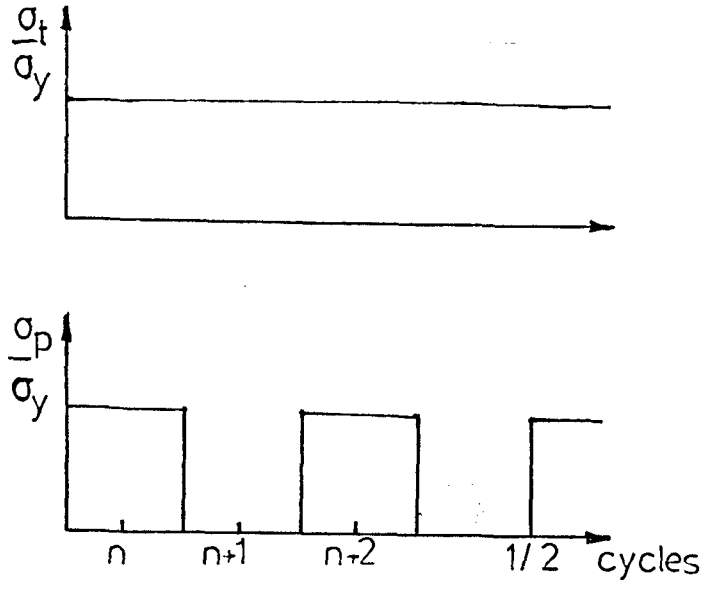

FIG. 3.8(a) Continuous thermal load with Cyclic Pressure Variation

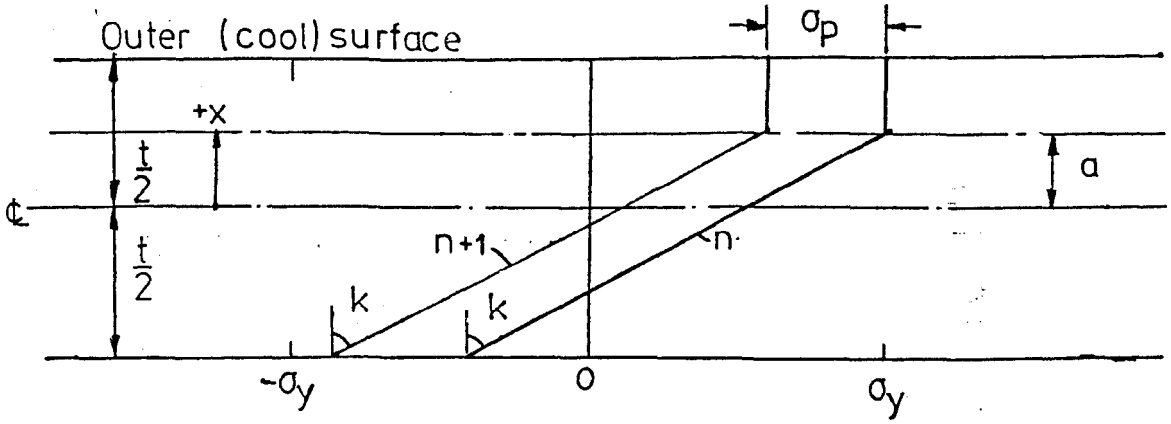

FIG. 3.8(b) Distribution of Stress Under S1 (Shakedown) Condition

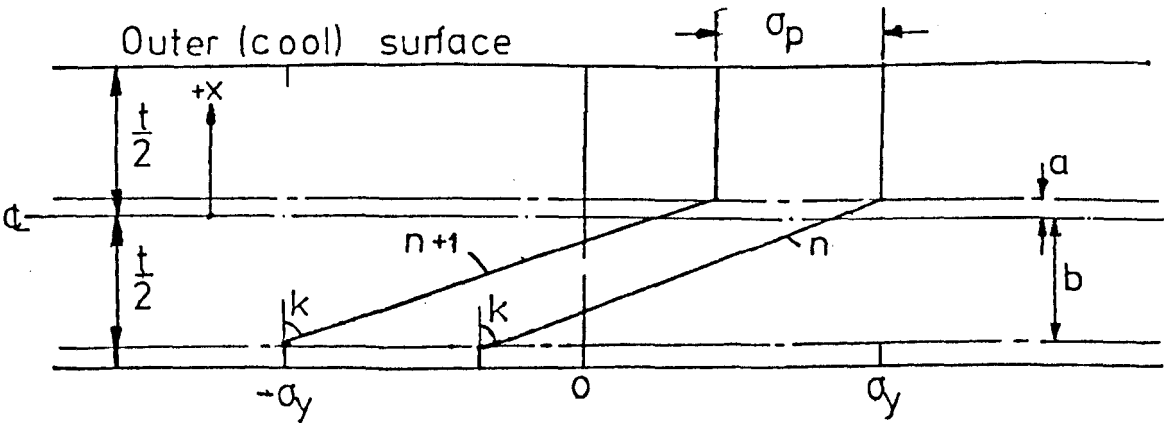

FIG. 3.8(c) Distribution of Stress under S2 (Shakedown) Condition

$$\sigma_p.t = \int_{-t/2}^{t/2} \sigma(x).dx$$

where the stresses and limits are,

$$\sigma(x) = \sigma_Y - K(a - x) \quad \text{for} \quad -\frac{t}{2} < x < +a$$

$$\sigma(x) = \sigma_Y \quad \text{for} \quad a < x < \frac{t}{2}$$

Therefore

$$\sigma_p.t = \int_{-t/2}^{a} ((\sigma_Y - K(a - x)).dx + \int_{a}^{t/2} \sigma_Y.dx$$

Integrating and Simplifying

$$\sigma_p.t = \sigma_Y.t - \frac{K}{2}\left(a + \frac{t}{2}\right)^2 \qquad (3.36)$$

<u>At the $(n+1)^{th}$ half cycle</u>,

$$0 = \int_{-t/2}^{t/2} \sigma(x).dx$$

where the stresses and limits are,

$$\sigma(x) = \sigma_Y - \sigma_p - K(a - x) \quad -\frac{t}{2} < x < a$$

$$\sigma(x) = \sigma_Y - \sigma_p \quad a < x < \frac{t}{2}$$

therefore

$$0 = \int_{-t/2}^{a} (\sigma_Y - \sigma_p - K(a - x).dx + \int_{a}^{t/2} (\sigma_Y - \sigma_p).dx$$

$$= (\sigma_Y - \sigma_p)(t) - \frac{K}{2}\left(a + \frac{t}{2}\right)^2 \qquad (3.37)$$

which is similar to Eqn. (3.36)

Bound 1

Firstly, Eqn. (3.36) can be simplified by multiplying throughout by $\frac{2K}{\sigma_Y^2}$ and substituting $X = \sigma_p/\sigma_Y$ and $Y = \sigma_t/\sigma_Y$.

$$\sigma_p . t . \frac{2K}{\sigma_Y^2} = \sigma_Y . t . \frac{2K}{\sigma_Y^2} - \frac{K^2}{\sigma_Y^2} \left(a + \frac{t}{2}\right)^2$$

$$Y.X = Y - \frac{K^2}{\sigma_Y^2} \left(a + \frac{t}{2}\right)^2$$

For fully elastic behaviour, $a \geq t/2$, and substituting $a = t/2$ into the above gives,

$$YX = Y - Y^2 \qquad \text{since } 2\sigma_t = Kt.$$

Hence
$$Y + X = 1 \tag{3.38}$$

Bound 2

For plastic collapse, $a = -t/2$. The entire cross-section is therefore at yield. Substituting $a = -t/2$ in Eqn. (3.36) gives,

$$X = 1 \tag{3.39}$$

This is the right side margin of the C.T. diagram.

Case 2

For the second case, the general equilibrium equations are obtained with reference to Fig. 3.8(c).

At the n^{th} half cycle

The stress distributions and the limits are,

$$\sigma(x) = \sigma_p - \sigma_Y \qquad \text{for } -\frac{t}{2} < x < -b$$

$$\sigma(x) = \sigma_p - \sigma_Y + K(b + x) \qquad \text{for } -b < x < a$$

$$\sigma(x) = \sigma_Y \qquad \text{for } a < x < \frac{t}{2}$$

therefore

$$\sigma_p . t = \int_{-t/2}^{-b} (\sigma_p - \sigma_Y).dx + \int_{-b}^{a} (\sigma_p - \sigma_Y + K(b + x)).dx + \int_{a}^{t/2} \sigma_Y . dx$$

integrating and simplifying gives

$$\sigma_p . t = \sigma_Y(-2a) + \frac{K}{2}(a + b)^2 + \sigma_p (a + \frac{t}{2}) \qquad (3.40)$$

<u>At the $(n+1)^{th}$ half cycle</u>

The stress distributions and the limits are,

$$\sigma(x) = -\sigma_Y \qquad \text{for } -\frac{t}{2} < x < -b$$

$$\sigma(x) = -\sigma_Y + K(b + x) \qquad \text{for } -b < x < a$$

$$\sigma(x) = \sigma_Y - \sigma_p \qquad \text{for } a < x < \frac{t}{2}$$

therefore

$$0 = \int_{-t/2}^{-b} (-\sigma_Y . dx + \int_{-b}^{a} (-\sigma_Y + K(b + x)).dx + \int_{a}^{t/2} (\sigma_Y - \sigma_p).dx$$

integrating and simplifying

$$0 = \sigma_Y(-2a) + \frac{K}{2}(a + b)^2 + \sigma_p (a - \frac{t}{2}) \qquad (3.41)$$

which is similar to Eqn. (3.40).

Equations (3.36), (3.37), (3.40), and (3.41) are equilibrium equations

where the parameters a and b are the distances of the stress interfaces from the mid-surface.

Bound 3

For the differentiation of regimes where compressive yielding occurs on the inside surface during the first half cycle, (see Fig. 3.8(c)) $b = \frac{t}{2}$. This implies that the inside surface is just at the point of yielding. Also from Fig. 3.8(c),

$$K(a + b) = 2\sigma_Y - \sigma_p$$

$$\therefore \quad Ka = 2\sigma_Y - \sigma_p - \sigma_t \quad \text{since} \quad 2\sigma_t = Kt$$

Substituting a and b into Eqn. 3.41, but firstly simplifying gives

$$0 = \frac{4\sigma_Y}{\sigma_Y^2}(-Ka) + \frac{K^2}{\sigma_Y^2}(a + b)^2 + \frac{2\sigma_p}{\sigma_Y^2}K(a - \frac{t}{2})$$

$$0 = -4(2 - X - Y) + (2 - X)^2 + 2X(2 - X - 2Y)$$

$$= 4X + 4Y - 4XY - 4 - X^2$$

$$Y = (2 - X)^2/4(1 - X) \qquad (3.42)$$

Next it is required to calculate ratchetting strains δ and bounds. It can be shown that the ratchetting regime does not exist for this type of loading. Only fully elastic and shakedown behaviour are possible. The reason is seen from Fig. 3.8(b) and 3.8(c). After initial yielding, subsequent cycles will cause the stress range between n^{th} and $(n+1)^{th}$ half cycle at every material point in the wall to be elastic and equal to

σ_p. Since σ_p is always less than σ_Y, the stress range is always elastic. Because of the elastic range, there is no tensile yielding during the $(n+1)^{th}$ half cycle. Therefore for all loads, d = 0, hence no ratchetting occurs.

In summary, the results are tabulated below.

Stress Distribution	Interface Conditions	Equation of Bound	Stress Regimes Differentiated
Case 1 (Fig.3.8b)	a = t/2	Y+X = 1	E/S1
	a = 0	X = 1	S1/Plastic Collapse
Case 2 (Fig.3.8c)	b = t/2 a+b = $(2\sigma_Y-\sigma_p)/K$	$Y = (2-X)^2/4(1-X)$	S1/S2

The plot of the bounding equations is shown in Fig. 3.11(b)

3.4.2 Out of Phase Cyclic Thermal and Pressure Loading (O.P.)

Fig. 3.9(a) shows the loading sequence in which both pressure and thermal loads are cyclical and out of phase. Figs 3.9(b) & (c) show the stress-through thickness distribution in the alternating plasticity regimes of P1 and P2 type respectively. In the P1 type, Fig. 3.9(b) shows that the outside surface has not yielded in compression while the inner surface undergoes alternate yielding in tension and compression in a full cycle. Fig. 3.9(c) shows P2 behaviour where both surfaces undergo alternate yielding or alternating plasticity. σ_x is the unknown elastic stress required to satisfy equilibrium during the imposition of the pressure load.

Case 1

Starting with the summation of forces in the first case which is represented by Fig. 3.9(b) to satisfy equilibrium for the thermal load only, the equilibrium equation is obtained.

At the n^{th} cycle, $0 = \int_{-t/2}^{t/2} \sigma(x).dx$ where the stresses and limits are

$$\sigma(x) = -\sigma_Y \quad \text{for} \quad -t/2 < x < -a$$

$$\sigma(x) = -\sigma_Y + K(a + x) \quad \text{for} \quad -a < x < +a$$

$$\sigma(x) = \sigma_Y \quad \text{for} \quad a < x < t/2$$

Therefore

$$0 = \int_{-t/2}^{-a} -\sigma_Y.dx + \int_{-a}^{+a} (-\sigma_Y + K(a+x)).dx + \int_{a}^{t/2} \sigma_Y.dx$$

integrating, putting in the limits and simplifying gives

$$0 = \sigma_Y(-2a) + K(2a^2) \qquad (3.43)$$

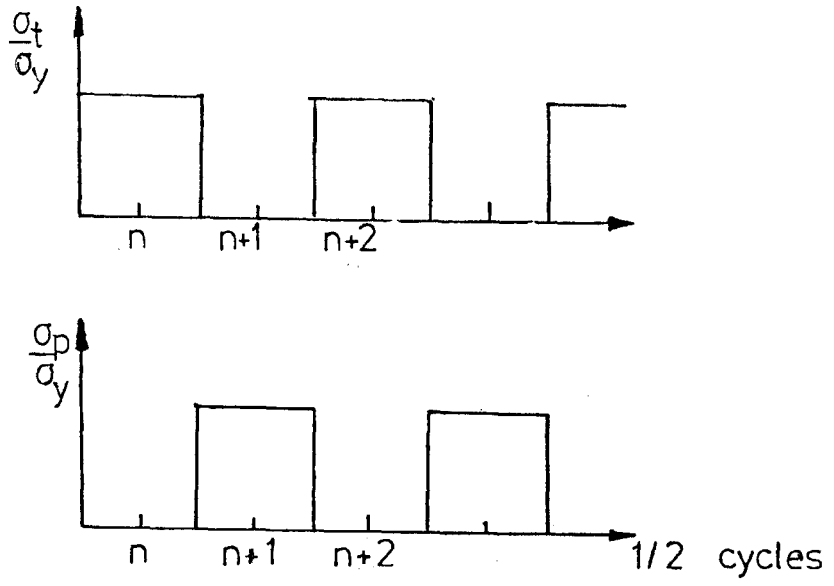

FIG. 3.9(a) Out-of-Phase Loading Sequence

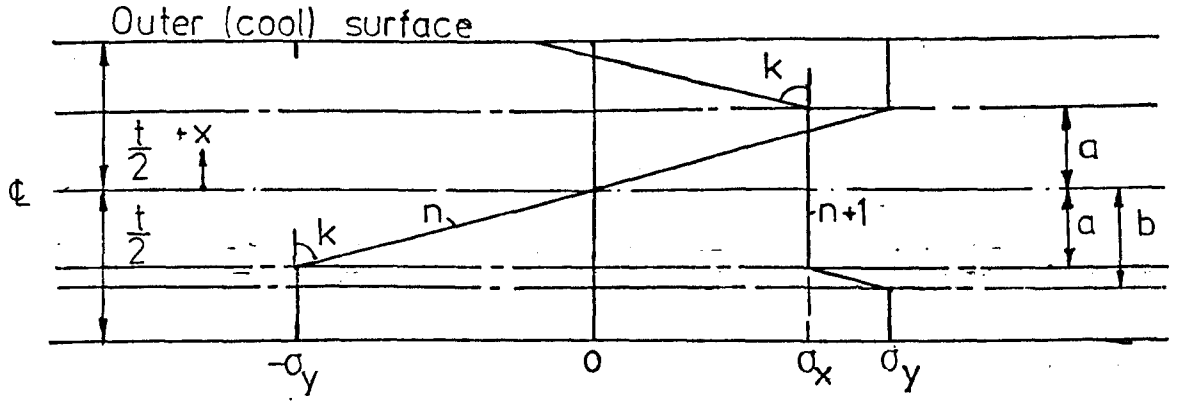

FIG. 3.9(b) Stress Distribution in the Alternating Plasticity Regimes (Type P1)

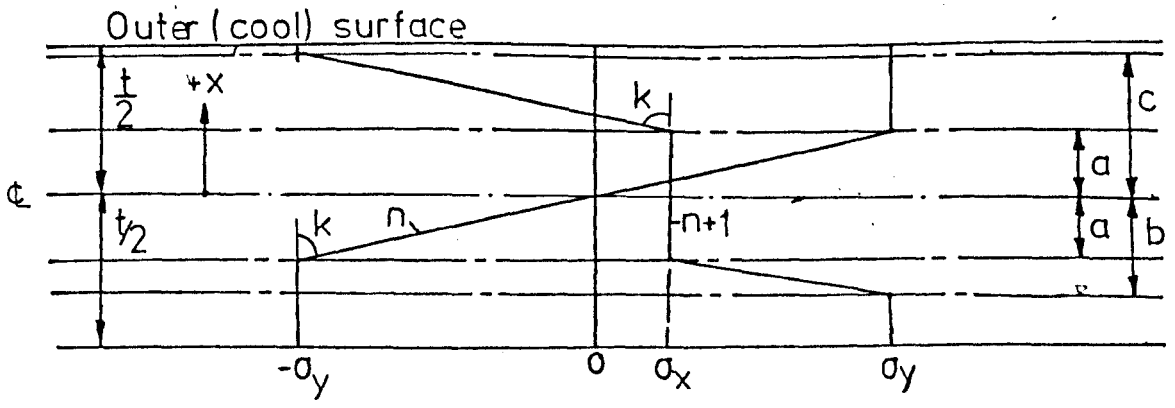

FIG. 3.9(c) Stress Distribution in the Type P2 Regime

At the $(n+1)^{th}$ cycle,

$$\sigma_p.t = \int_{-t/2}^{t/2} \sigma(x).dx \qquad \text{where } \sigma(x) \text{ and its limits are}$$

$$\sigma(x) = \sigma_Y \qquad \text{for} \quad -t/2 < x < -b$$

$$\sigma(x) = \sigma_Y - K(b + x) \qquad \text{for} \quad -b < x < -a$$

$$\sigma(x) = \sigma_x \qquad \text{for} \quad -a < x < a$$

$$\sigma(x) = \sigma_x - K(x - a) \qquad \text{for} \quad a < x < t/2$$

Therefore

$$\sigma_p.t = \int_{-t/2}^{-b} \sigma_Y.dx + \int_{-b}^{-a} (\sigma_Y - K(b + x)).dx + \int_{-a}^{a} \sigma_x.dx +$$

$$\int_{a}^{t/2} (\sigma_x - K(x - a)).dx$$

integrating, putting in the limits and simplifying gives,

$$\sigma_p.t = \sigma_Y \left(\frac{t}{2} - a\right) - \frac{K}{2}\left(a^2 + (b - a)^2 + \frac{t}{2}\left(\frac{t}{2} - 2a\right)\right) + \sigma_x\left(\frac{t}{2} + a\right) \qquad (3.44)$$

Thus, the equilibrium equations of Case 1 are obtained.

Bound 1

For shakedown, the necessary condition is $b = t/2$, that is the inner surface is at the point of yielding at the $(n+1)^{th}$ half cycle. The resulting stress distribution is then fully elastic at every material point. The regime is also of the S2 type because of the yielding that

occurred on both surfaces during the first thermal half cycle.

Also from Fig. 3.9(b) during the (n+1) cycle,

$$K(b - a) = \sigma_Y - \sigma_x \tag{3.45}$$

From Eqn. (3.43),

$$Ka = \sigma_Y$$

Solving for σ_x, using the above gives,

$$\sigma_x = 2\sigma_Y - \sigma_t \quad \text{since} \quad 2\sigma_t = K.t \tag{3.46}$$

Substituting the above into Eqn. (3.44), gives on re-arranging and simplifying,

$$4\sigma_p\sigma_t = 2\sigma_Y(\sigma_t - \sigma_Y) - (\sigma_Y^2 + (\sigma_t - \sigma_Y)^2 + \sigma_t(\sigma_t - 2\sigma_Y)) + 2(2\sigma_Y - \sigma_t)(\sigma_t + \sigma_Y)$$

Dividing throughout by σ_Y^2 and then substituting $X = \sigma_p/\sigma_Y$ and $Y = \sigma_t/\sigma_Y$ gives

$$4XY = 2(Y - 1) - (1 + (Y - 1)^2 + Y(Y - 2)) + 2(2 - Y)(Y + 1)$$

$$0 = Y^2(-4) + Y(8 - 4X)$$

$$\therefore \quad Y = 2 - X \tag{3.47}$$

Bound 2

For completely elastic behaviour with no initial yielding during the first half cycle, the bound can be obtained by simply letting $a = \frac{t}{2}$, that is no yielding occurs during the imposition of the first

thermal load.

From Eqn. (3.45),

$$K.\frac{t}{2} = \sigma_Y$$

$$\sigma_t = \sigma_Y$$

$$\therefore \quad Y = 1 \qquad (3.48)$$

The elastic regimes are therefore bounded by the maximum thermal stress being less than the yield stress.

Bound 3

To consider ratchetting behaviour, a point (σ_p, σ_t) is taken and assumed to lie well within the ratchetting regime. Equilibrium equations, that is (3.4) and (3.43), still hold although the interface positions 'a' in the n^{th} and $(n+1)^{th}$ cycle are no longer equal. If a_n and a_{n+1} now refer to the positions of 'a' at the n^{th} and $(n+1)^{th}$ half cycles respectively, the overlap width (d) where tensile yielding occurs on both successive half cycles will be given by

$$d = a_{(n+1)} - a_n \qquad (3.49)$$

with the prior provision that

$$\sigma_x = \sigma_Y.$$

If $d < 0$ that is $a_{(n+1)} < a_n$,

then either shakedown or alternating plasticity will occur,

and $\therefore \quad d = 0$

gives the bound for non-ratchetting/ratchetting.

From Eqn. (3.43), putting $a = a_n$ gives

$$Ka_n = \sigma_Y$$

From Eqn. (3.44), putting $a = a_{(n+1)}$, $\sigma_x = \sigma_Y$ and $Kb = Ka = Ka_{(n+1)}$ (the latter most derived from Eqn. (3.44)) gives

$$\sigma_p.t = \sigma_Y(\tfrac{t}{2} - a_{(n+1)}) - \tfrac{K}{2}\left[a^2_{(n+1)} + (a_{(n+1)} - a_{(n+1)})^2 + \tfrac{t}{2}(\tfrac{t}{2} - 2a_{(n+1)})\right] + \sigma_Y(\tfrac{t}{2} + a_{(n+1)})$$

$$= \sigma_Y.t - \tfrac{K}{2}(a_{(n+1)} - \tfrac{t}{2})^2$$

Further simplifying gives

$$a_{(n+1)} = \frac{2}{K}\sqrt{\sigma_t(\sigma_Y - \sigma_p)} + \frac{t}{2}$$

Since $a_{(n+1)} \leq t/2$, it is necessary always to take the negative root of the square root term of the R.H.S. of the above.

For the bound on non-ratchetting/ratchetting, $d = 0$ hence

$$a_{(n+1)} = a_n$$

$$\frac{2}{K}\sqrt{\sigma_t(\sigma_Y - \sigma_p)} + \frac{t}{2} = \frac{\sigma_Y}{K}$$

$$4\sigma_t(\sigma_Y - \sigma_p) = (\sigma_Y - \sigma_t)^2$$

Dividing throughout by σ_Y^2 and putting $X = \sigma_p/\sigma_Y$ and $Y = \sigma_t/\sigma_Y$ gives a quadratic equation in terms of Y.

$$4Y(1 - X) = (1 - Y)^2$$

$$Y^2 - Y(6 - 4X) + 1 = 0 \qquad (3.50)$$

Solving the quadratic for $0 \leqslant X \leqslant 1$ gives the following tabulation:

X	0	0.2	0.4	0.6	0.8	1.0	0.667
Y_1	0.17	0.2	0.24	0.30	0.42	1.0	0.33
Y_2	11.65	5.0	4.15	3.29	3.38	1.0	3.0

where Y_1 and Y_2 are the pair of real roots of the quadratic equation which are solved by,

$$Y_1, Y_2 = \frac{+(6 - 4X) \mp \sqrt{(6-4X)^2 - 4}}{2}$$

It is seen that Y_1 gives an impossible solution which lies within the elastic regime. Therefore Y_2 must be the correct solution.

To calculate the ratchetting strain per cycle (δ) in this regime (type R1), the plastic strain incurred in each cycle is given by

$$\begin{aligned}
\delta &= d.\frac{K}{E} \\
&= (a_{(n+1)} - a_n)K/E \\
&= \left(\frac{2}{K}\sqrt{\sigma_t\sigma_Y - \sigma_p}\right) + \frac{t}{2} - \frac{\sigma_Y}{K}\Big)\frac{K}{E} \\
&= \left(2\sqrt{\sigma_t(\sigma_Y - \sigma_p)} + \sigma_t - \sigma_Y\right)/E \\
&= \left(2\sqrt{Y(1 - X)} + Y - 1\right)\sigma_Y/E
\end{aligned} \qquad (3.51)$$

Remembering that the negative root is taken in the square root term.

Case 2

For the second case, the equilibrium equations are obtained with reference to Fig. 3.9(c).

For the n^{th} cycle, again

$$0 = \int_{-t/2}^{t/2} \sigma(x).dx \quad \text{where the stresses and limits are}$$

$$\sigma(x) = -\sigma_Y \qquad \text{for} \quad -\frac{t}{2} < x < -a$$

$$\sigma(x) = -\sigma_Y + K(a + x) \qquad \text{for} \quad -a < x < +a$$

$$\sigma(x) = \sigma_Y \qquad \text{for} \quad a < x < \frac{t}{2}$$

This gives a solution similar to Eqn. (3.43) where

$$Ka = \sigma_Y \tag{3.52}$$

For the $(n+1)^{th}$ cycle,

$$\sigma_p.t = \int_{-t/2}^{t/2} \sigma(x).dx$$

where the stresses $\sigma(x)$ and the limits are,

$$\sigma(x) = \sigma_Y \qquad \text{for} \quad -\frac{t}{2} < x < -b$$

$$\sigma(x) = \sigma_Y - K(b + x) \qquad \text{for} \quad -b < x < -a$$

$$\sigma(x) = \sigma_x \qquad \text{for} \quad -a < x < +a$$

$$\sigma(x) = \sigma_x - K(x - b) \qquad \text{for} \quad a < x < c$$

$$\sigma(x) = -\sigma_Y \qquad \text{for} \quad c < x < \frac{t}{2}$$

$$\sigma_p.t = \int_{-t/2}^{-b} \sigma_Y.dx + \int_{-b}^{-a} (\sigma_Y - K(b+x)).dx + \int_{-a}^{a} \sigma_X.dx +$$

$$\int_{a}^{c} (\sigma x - K(x - a)).dx + \int_{c}^{t/2} -\sigma_Y.dx$$

integrating and putting in the limits gives on simplifying

$$\sigma_p.t = \sigma_Y (c - a) - \frac{K}{2} (a^2 + (b - a)^2 + c(c - 2a)) + \sigma_x(c + a) \qquad (3.53)$$

Equilibrium equations are hence obtained for Case 2.

Bound 4

For deriving the bound where the outer surface is at the point of yielding in compression, $c = \frac{t}{2}$. The bound will separate the regimes of type 1 and 2 behaviour.

From Fig. 3.9(c) it is seen that

$$K(b - a) = \sigma_Y - \sigma_x \qquad (3.54)$$

$$K(c - a) = \sigma_Y + \sigma_x \qquad (3.55)$$

Solving Eqn. 3.54 and Eqn. 3.55 for σ_x and b gives

$$\sigma_x = \sigma_t - 2\sigma_y \qquad (3.56)$$

and

$$Kb = 4\sigma_Y - \sigma_t \qquad (3.57)$$

Since $Kc = \sigma_t$ and

$$Ka = \sigma_Y$$

Firstly multiplying Eqn. (3.53) by 2K throughout and then substituting the

above into it gives

$$2\sigma_p.Kt = 2\sigma_Y K(c - a) - K^2(a^2 + (b - a)^2 + c(c - 2a)) + 2\sigma_x(c+a)$$

$$4\sigma_p\sigma_t = 2\sigma_Y(\sigma_t - \sigma_Y) - (\sigma_Y^2 + (3\sigma_Y - \sigma_t)^2 + \sigma_t(\sigma_t - 2\sigma_Y)) +$$

$$2(\sigma_t - 2\sigma_Y)(\sigma_t + \sigma_Y)$$

Dividing throughout by σ_Y^2 and substituting $X = \frac{\sigma_p}{\sigma_Y}$ and $Y = \frac{\sigma_t}{\sigma_Y}$

gives

$$4XY = 2(Y - 1) - (1 + (3 - Y)^2 + Y(Y - 2)) + 2(Y - 2)(Y + 1)$$

$$0 = Y^2(0) + Y(-4X + 8) - 16$$

$$\therefore \quad Y = 4/(2 - X) \tag{3.58}$$

Bound 5

The solution method of obtaining Bound 3 and the ratchetting strain is followed here. In this case, there is compressive yielding on the outer surface hence the ratchetting regime is of type 2. Eqn. (3.49) applies, hence

$$d = a_{(n+1)} - a_n$$

and σ_x must be equal to σ_Y.

From Eqn. (3.52),

$$a_n = \sigma_Y/K$$

Also from Eqn. (3.54),

$$K(b - a) = 0$$

since $$\sigma_x = \sigma_Y$$

c is obtained from Eqn. (3.55) such that

$$Kc = 2\sigma_Y + Ka_{(n+1)} \quad \text{again since } \sigma_x = \sigma_Y.$$

Eqn. (3.53) on substituting the above becomes

$$2\sigma_p.Kt = 2\sigma_Y.2(2\sigma_Y + Ka_{(n+1)}) - (K^2a^2_{(n+1)} + (2\sigma_Y + Ka_{(n+1)})(2\sigma_Y - Ka_{(n+1)}))$$

$$4\sigma_p\sigma_t = 4\sigma_Y(2\sigma_Y + Ka_{(n+1)}) - 4\sigma_Y^2$$

$$\therefore \quad a_{(n+1)} = \left(\frac{\sigma_n\sigma_t}{\sigma_Y} - \sigma_Y\right)/K$$

For the bound on non-ratchetting/ratchetting, d = 0, hence

$$a_{(n+1)} = a_n$$

$$\left(\frac{\sigma_n\sigma_t}{\sigma_Y} - \sigma_Y\right)/K = \sigma_Y/K$$

$$\therefore \quad \sigma_p\sigma_t = 2\sigma_Y^2$$

or $$XY = 2 \tag{3.59}$$

The ratchetting per cycle in the R2 ratchetting regime is given by

$$\delta = d.\frac{K}{E}$$

$$= (a_{n+1} - a_n)K/E$$

$$= \left(\frac{\sigma_n\sigma_t}{\sigma_Y} - 2\sigma_Y\right)/E$$

$$= (XY - 2)\,\sigma_Y/E \tag{3.60}$$

The above completes the analysis on the O.P. diagram and the tabulation

below summarizes the results. The equations of the bounds, (3.47), (3.48), (3.50), (3.58) and (3.59) are plotted in Fig. 3.11(c).

Stress Distribution	Interface Conditions	Equation of Bound	Stress Regimes Differentiated
Case 1 (Fig. 3.9(b))	$b = t/2$ $K(b-a) = \sigma_Y - \sigma_X$ $Ka = \sigma_Y$	$Y = 2-X$	P1/S2
	$a = t/2$	$Y = 1$	S2/E
	$a_{(n+1)} = a_n$ $\sigma_X = \sigma_Y$	$4Y(1-X) = (1-Y)^2$	R1/P1
Case 2 (Fig. 3.9(c))	$c = t/2$ $K(b-a) = \sigma_Y - \sigma_X$ $K(c-a) = \sigma_Y + \sigma_X$ $Ka = \sigma_Y$	$Y = 4/(2-X)$	P1/P2 R1/R2
	$a_{(n+1)} = a_n$ $\sigma_X = \sigma_Y$	$XY = 2$	P2/R2

3.4.3 In-Phase Cyclic Thermal and Pressure Loading (I.P.)

This loading sequence is shown in Fig. 3.10(a). It is seen that during the n^{th} half cycle where both loads are imposed, the equilibrium equations are similar to the Bree sequence of loading at the same half cycle. Therefore the equations 3.22 and 3.24 are used. Figs 3.10(b) and 3.10(c) show the distributions of stress under the conditions of loading leading to P1 and P2 behaviour respectively. In these cases, the yielding behaviour that are of importance occur on the inside surface. The differentiation of type 1 and 2 behaviour depends on the compressive yielding during the n^{th} half cycle on the inside surface. σ_x is the unknown elastic stress required for equilibrium during the unloading half cycle.

Case 1

At the n^{th} half cycle,

Eqn. (3.22) is repeated here,

$$\sigma_p = -\frac{K}{2t}\left(a + \frac{t}{2}\right)^2 + \sigma_Y \qquad (3.61)$$

At the $(n+1)^{th}$ half cycle,

The summation of forces is given by

$$0 = \int_{-t/2}^{+t/2} \sigma(x).dx$$

where $\sigma(x)$ and the limits are,

$$\sigma(x) = \sigma_x \qquad \text{for} \quad -\frac{t}{2} < x < -a$$

$$\sigma(x) = \sigma_x - \hat{K}(x + a) \qquad \text{for} \quad -a < x < c$$

$$\sigma(x) = -\sigma_Y \qquad \text{for} \quad c < x < \frac{t}{2}$$

Therefore

$$0 = \int_{-t/2}^{-a} \sigma_x dx + \int_{-a}^{c} (\sigma_x - K(x + a)).dx + \int_{c}^{t/2} -\sigma_Y.dx$$

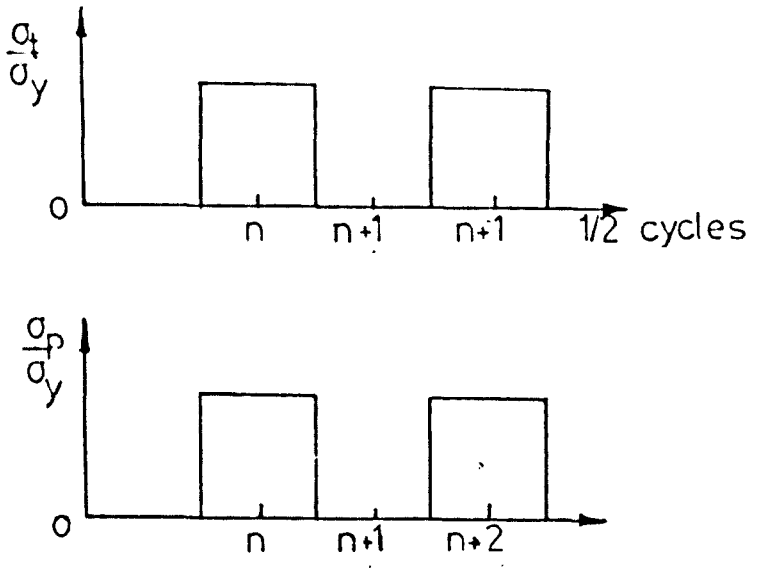

FIG. 3.10(a) In-Phase Loading Sequence

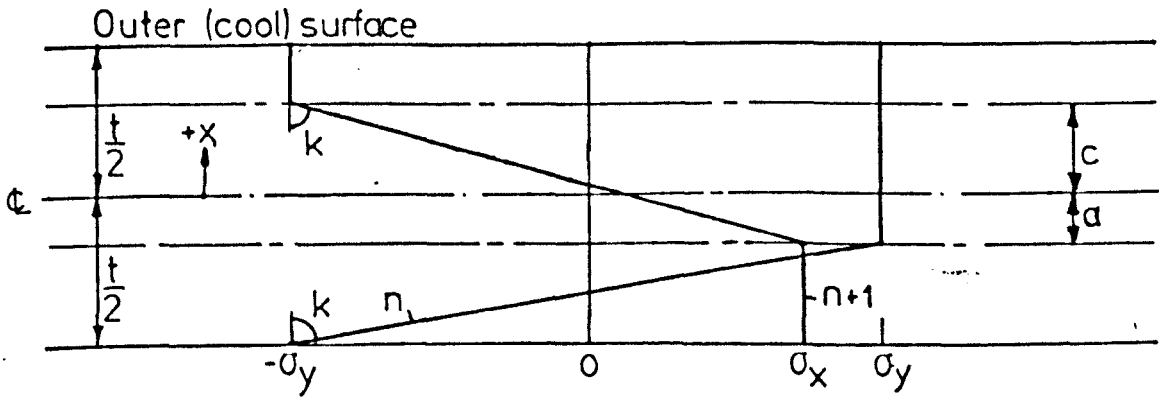

FIG. 3.10(b) Stress Distribution in the P1 Regime

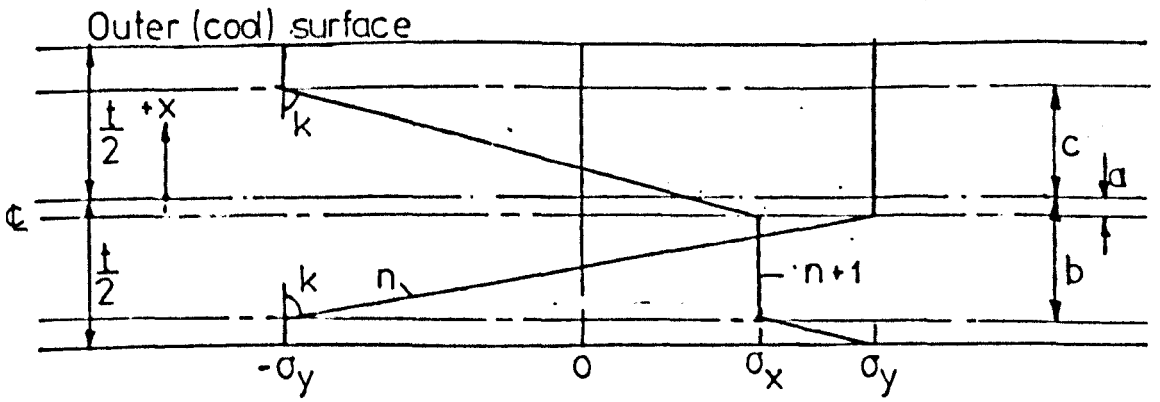

FIG. 3.10(c) Stress Distribution in the P2 Regime

integrating and putting in the limits gives

$$0 = \sigma_x(\frac{t}{2} + c) - \frac{K}{2}(a + c)^2 - \sigma_Y(\frac{t}{2} - c)$$

multiplying throughout by 2K gives

$$0 = 2\sigma_x K(\frac{t}{2} + c) - K^2(a + c)^2 - 2\sigma_Y K(\frac{t}{2} - c) \qquad (3.62)$$

This is the equilibrium equation for the $(n+1)^{th}$ cycle.

Bound 1

For fully elastic behaviour, no yielding occurs in the first half cycle. Using Eqn. (3.61) and substituting $a = \frac{t}{2}$ gives,

$$\sigma_p = -Kt/2 + \sigma_Y$$

$$\therefore \sigma_p + \sigma_t = \sigma_Y$$

$$\text{or } X + Y = 1 \qquad (3.63)$$

Bound 2

To calculate the bound for ratchetting, the overlap width d is equal to zero. Again as in Eqn. 3.49, the ratchetting/non-ratchetting bound is given by the condition that, $a_{(n+1)} - a_n = 0$.

The proviso that $\sigma_x = \sigma_Y$ also applies.

From Eqn. (3.61),

$$a_n = (2\sqrt{(\sigma_Y - \sigma_p)/\sigma_t} + 1)\,\sigma_t/K$$

From Eqn. (3.62)

$$0 = 2\sigma_Y.2(2\sigma_Y - Ka_{(n+1)}) - 4\sigma_Y^2$$

where

$$K(a_{(n+1)}+c) = 2\sigma_Y$$

$$\therefore \quad a_{n+1} = \sigma_Y/K$$

The bound is therefore

$$\sigma_Y - (2\sqrt{(\sigma_Y - \sigma_p)\sigma_t} + 1)\sigma_t = 0$$

$$4\sigma_t(\sigma_Y - \sigma_p) = (\sigma_Y - \sigma_t)^2$$

therefore

$$4Y(1 - X) = (1 - Y)^2 \qquad (3.64)$$

This is the same as Eqn. (3.50). The bound for ratchetting is therefore similar to that of the case of O.P. cyclic thermal and pressure load. The calculation of the root of the quadratic equation in Y follows the same argument as in the previous section. The expression for the ratchet strain per cycle δ is also similarly obtained.

Hence,

$$\delta = (2\sqrt{Y(1 - X)} + Y - 1)\sigma_Y/E$$

where the root of $\sqrt{Y(1 - X)}$ is taken to be negative in sign.

Bound 3

Shakedown occurs when the stress ranges of all material points is elastic following initial yielding behaviour. Hence for Case 1 (Fig. 3.10(b)) $c = \frac{t}{2}$ and

$$K(a + c) = \sigma_Y + \sigma_x$$

Also from Eqn. (3.61)

$$Ka = 2\sqrt{\sigma_t(\sigma_Y - \sigma_p)} + \sigma_t$$

Solving the above equations for σ_x gives

$$\sigma_x = -\sigma_Y + \frac{Kt}{2} + 2\sqrt{\sigma_t(\sigma_Y - \sigma_p)} + \sigma_t$$

$$= -\sigma_Y + 2\sqrt{\sigma_t(\sigma_Y - \sigma_p)} + 2\sigma_t \qquad \text{since } Kt = 2\sigma_t$$

Substituting the above into Eqn. (3.62),

$$0 = 2(-\sigma_Y + 2\sqrt{\sigma_t(\sigma_Y - \sigma_p)} + 2\sigma_t).2\sigma_t - (2\sqrt{\sigma_t(\sigma_Y - \sigma_p)} + 2\sigma_t)^2 + 2\sigma_Y(0)$$

$$= (2\sqrt{\sigma_t(\sigma_Y - \sigma_p)} + 2\sigma_t)(2\sigma_t - 2\sqrt{\sigma_t(\sigma_Y - \sigma_p)}) - 4\sigma_Y\sigma_t$$

$$= \sigma_t^2 - \sigma_t(\sigma_Y - \sigma_p) - \sigma_Y\sigma_t$$

$$= \sigma_t - 2\sigma_Y - \sigma_p$$

$$\sigma_t = 2\sigma_Y - \sigma_p$$

or

$$Y = 2 - X \tag{3.65}$$

This bound covers the S1 shakedown regime.

Case 2

The equilibrium equation for the n^{th} half cycle has already been obtained in section 3.32 and using the same notation for Fig. 3.10(c), is

$$4\sigma_p\sigma_t = 4\sigma_Y Ka + K^2(b - a)^2 \qquad \text{from 3.24} \tag{3.66}$$

At the $(n+1)^{th}$ half cycle, the summation of forces gives

$$0 = \int_{-t/2}^{t/2} \sigma(x).dx \qquad \text{where } \sigma(x) \text{ and the limits are}$$

$$\sigma(x) = \sigma_x - K(x + b) \qquad -b < x < -\frac{t}{2}$$

$$\sigma(x) = \sigma_x \qquad -a < x < -b$$

$$\sigma(x) = \sigma_x - K(x + a) \qquad c < x < -a$$

$$\sigma(x) = -\sigma_Y \qquad -\frac{t}{2} < x < c$$

Therefore

$$0 = \int_{-t/2}^{-b} (\sigma_x - K(x + b)).dx + \int_{-b}^{-a} \sigma_x.dx + \int_{-a}^{c} (\sigma_x - K(x + a)).dx$$

$$+ \int_{c}^{t/2} -\sigma_Y.dx$$

$$= \sigma_x(\tfrac{t}{2} + c) - \tfrac{K}{2}((a + c)^2 - (b - \tfrac{t}{2})^2) - \sigma_Y(\tfrac{t}{2} - c)$$

multiplying throughout by 2K gives

$$0 = 2\sigma_x K(\tfrac{t}{2} + c) - K^2((a + c)^2 - (b - \tfrac{t}{2})^2) - 2\sigma_Y K(\tfrac{t}{2} - c) \qquad (3.67)$$

This is the equilibrium equation for the $(n+1)^{th}$ half cycle in Case 2. Before calculating the various bounds, it is first necessary to obtain simple expressions of a and b from Eqn.(3.66). It is known that for all cases to be considered

$$K(b - a) = 2\sigma_Y \qquad (3.68)$$

is always true.

Solving Eqns. (3.66) and (3.68) for a and b gives

$$4\sigma_p\sigma_t = 4\sigma_Y Ka + 4\sigma_Y^2$$

$$\therefore \quad Ka = (\sigma_p\sigma_t - \sigma_Y^2)/\sigma_Y$$

and $$Kb = (\sigma_p\sigma_t + \sigma_Y^2)/\sigma_Y$$

using the non-dimensional parameters of X and Y gives the simplification

$$Ka = (XY - 1)\sigma_Y \qquad (3.69)$$

and

$$Kb = (XY + 1)\sigma_Y \qquad (3.70)$$

Bound 4

For shakedown of the S2 type, $c = \frac{t}{2}$ in order that all material points undergo elastic behaviour during cycling.

Since

$$K(a + c) = \sigma_Y + \sigma_x$$

Therefore

$$\sigma_x = Ka + K\frac{t}{2} - \sigma_Y$$

$$= (XY - 2)\sigma_Y + \sigma_t$$

putting the above and Eqns. (3.69) and (3.70) into (3.67) gives

$$0 = 2((XY - 2)\sigma_Y + \sigma_t)(2\sigma_t) - \left[((XY - 1)\sigma_Y + \sigma_t)^2 - ((XY + 1)\sigma_Y - \sigma_t)^2\right] - 2\sigma_Y \quad (0)$$

Dividing throughout by σ_Y^2 and substituting $X = \frac{\sigma_p}{\sigma_Y}$ and $Y = \frac{\sigma_t}{\sigma_Y}$ gives

$$= 2(XY - 2 + Y)(2Y) - ((XY + Y - 1)^2 - (XY - Y + 1)^2)$$

$$= -4Y + 4(2 - X)$$

$$\therefore \quad Y = (2 - X) \qquad (3.71)$$

This bound is the same as Bound 3.

Bound 5

The bound which differentiates type 1 and 2 behaviour is determined

by the criterion of whether there is any compressive yielding on the inside surface. Fig. 3.10(c) shows that compressive yielding would occur if $b \leq \frac{t}{2}$. In the limit the bound is for $b = \frac{t}{2}$.

Using Eqn. (3.70)

$$K\frac{t}{2} = (XY + 1)\sigma_Y$$

$$2\sigma_t = (XY + 1)\sigma_Y$$

$$Y(1 - X) = 1 \qquad (3.72)$$

Bound 6

The non-ratchetting/ratchetting bound is obtained in a similar manner as in the O.P. loading case. The conditions that $\sigma_x = \sigma_Y$ and $a_{(n+1)} = a_{(n)}$ are applied.

Firstly considering the n^{th} half cycle, Eqn. (3.69) gives

$$a_n = (XY - 1)\sigma_Y/K$$

Now considering the $n+1^{th}$ half cycle, firstly,

$$K(a_{(n+1)} + c) = \sigma_Y + \sigma_x$$

$$Kc = 2\sigma_Y - Ka_{(n+1)}$$

$$K(\tfrac{t}{2} - b) = \sigma_Y - \sigma_X$$

$$= 0$$

$$\therefore \quad Kb = \sigma_t$$

Substituting the above into Eqn. (3.67) and putting $\sigma_x = \sigma_Y$ gives

$$0 = 2\sigma_Y(2Kc) - (4\sigma_Y^2 - (0)^2)$$

$$= Kc - \sigma_Y$$

$$Ka_{(n+1)} = \sigma_Y$$

$$a_{(n+1)} = \sigma_Y/K$$

$$a_n = a_{(n+1)}$$

$$\therefore \quad (XY - 1)\sigma_Y = \sigma_Y$$

$$\therefore \quad XY = 2 \tag{3.73}$$

Again just as Bound 2 which is of type 1 ratchetting is the same as Eqn. (3.50) in the O.P. loading case, the bound above is also similar to its counterpart that is, Eqn. (3.59).

The ratchet strain per cycle is given by

$$\begin{aligned} \delta &= Kd/E \\ &= K(a_n - a_{(n+1)})/E \\ &= (XY - 2)\sigma_Y/E \end{aligned} \tag{3.74}$$

which is similar to Eqn. (3.60) in the O.P. loading case.

This completes the analyses of the final loading case. The tabulation below summarizes the results. The plot of the bounds is shown in Fig. 3.11(d).

Stress Distribution	Interface Conditions	Equation of Bound	Stress Regimes Differentiated
Case 1 (Fig. 3.10(b))	$a = t/2$	$X+Y = 1$	E/S1
	$K(a+c) = \sigma_Y+\sigma_X$ $c = t/2$	$Y = 2-X$	S1/P1
	$a_{(n+1)} = a_n$ $\sigma_X = \sigma_Y$	$4Y(1-X) = (1-Y)^2$	P1/R1
Case 2 (Fig. 3.10(c))	$c = t/2$ $K(a+c) = \sigma_Y+\sigma_X$	$Y = 2 - X$	S2/P2
	$b = t/2$	$Y(1-X) = 1$	S1/S2 P1/P2 R1/R2
	$a_{(n+1)} = a_{(n)}$ $\sigma_X = \sigma_Y$	$XY = 2$	P2/R2

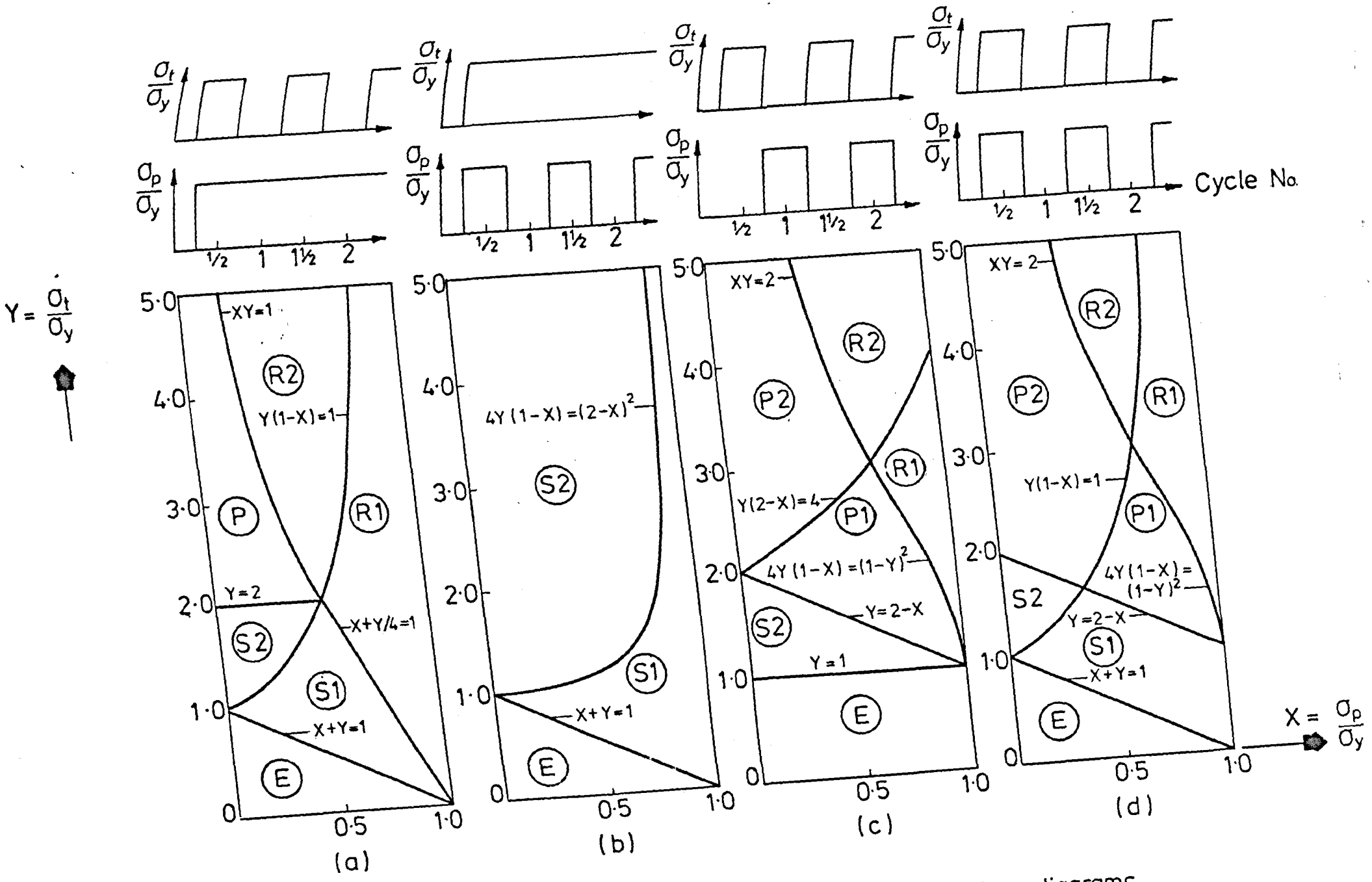

FIG. 3·11. The bounds of the Bree and alternative diagrams.

3.4.4 Discussion

Using the mathematical model of Bree, it has been possible to predict approximately the behaviour of the can wall in the hoop direction when subjected to different loading sequences. The Bree-type diagrams for these loading sequences together with the original Bree diagram are shown in Fig. 3.11. In the diagrams, the stress regimes are classified in seven categories (that is, E, S1, S2, P1, P2, R1 and R2) each being made on the basis of initial yielding behaviour and cyclic response. Table 3.1 which is compiled after the analyses shows the various criteria used and how these depended on the yielding behaviour of the inner and outer surfaces during the initial first half and second half cycle. Also there are differences in these criteria between the various loading sequences. To clarify this,as an example, in the alternating plasticity regime P1 of the O.P. and I.P. (Out-of-Phase and In-Phase) loading sequences, cyclic plasticity occurs on the inner surface in the O.P. loading sequence but on the outer surface in the I.P. loading sequence while the other corresponding surfaces undergo elastic reloading. These differences which occur in the other regimes of P2, R1 and R2 are not differentiated since this would warrant an unnecessarily cumbersome notation. It suffices, therefore, to categorize P1 as a regime where alternating plasticity occurs on any one surface and P2 where this occurs on both surfaces of the wall. For the sub-division of the R1/R2 regimes, type 1 behaviour is caused by either elastic reloading and/or compressive yielding behaviour on any one surface during the initial first cycle whilst type 2 has compressive yielding on both surfaces. The differentiation of S1/S2 shakedown depends on the compressive yielding of any one surface during the initial first cycle for S2 and no compressive yielding on

any surface for the S1 regime. These criteria are applied to the Bree-type diagrams in Fig. 3.11 and are found to be sufficient to account for all possible modes of behaviour investigated. Also, the original criteria used by Bree are preserved.

However, ignoring the actual surfaces, (that is by not defining inside or outside surfaces) which undergo the various behaviour has got its setbacks. This is seen in the P1 regime in the I.P. and O.P. loading sequence. Alternating plasticity has occurred on the inner surface in the O.P. loading sequence and on the outer surface in the I.P. loading sequence. Analytically, this has no significance but from a practical viewpoint, the cyclic plasticity (hysteresis strain) behaviour cannot be observed in the O.P. loading sequence case since the inner surface of the wall would not be accessible to inspection. Cyclic plasticity would eventually lead to fatigue failure of the inner surface while the outer surface remains undamaged due to its elastic reloading behaviour. This will thus give a false impression of the integrity of the wall. The I.P. loading sequence has the cyclic plasticity behaviour on the outer surface which may be observable and is inherently a safer loading sequence as far as this regime is concerned.

The above consideration would not have occurred to the Bree's loading sequence because the alternating plasticity regime P (equivalent to P2 according to the previously discussed criteria) was manifested in equal loop width of the hysteresis loop on both inner and outer surfaces. Thus an equal amount of deterioration would occur on both inner and outer surfaces as far as fatigue damage is concerned.

The regime P2 of the I.P. and O.P. loading sequences undergoes cyclic plasticity on both surfaces but unlike the P regime of the Bree loading sequence, the loop widths are not "symmetrical" on both surfaces. This is to mean that one surface undergoes a larger cyclic

plasticity loop width and hence greater fatigue damage than the other surface. In the I.P. loading sequence, the worst affected surface is on the outside whereas in the O.P. loading sequence, it is on the inner surface. Again the O.P. loading sequence would give a false indication of the overall behaviour while the I.P. loading sequence would be "conservative".

The ratchetting behaviour in the I.P., O.P. and Bree follow a similar trend. In the ratchetting regime of type R1 in the Bree loading sequence, elastic unloading and reloading follows after tensile yielding at every alternate half cycle, therefore there is no cyclic plasticity on any surface. In the O.P. and I.P. loading sequences, in addition to tensile ratchetting, cyclic plasticity occurs on the inner and on the outer surfaces respectively while on the corresponding surface in each loading sequence case, undergoes elastic reloading.

In the R2 ratchetting regime, both inner and outer surfaces undergo cyclic plasticity for all loading sequences (that is I.P., O.P. and Bree). Again similar differences exist. In the Bree loading sequence, there is "symmetrical" cyclic-plasticity behaviour (that is, equal loop width) on both surfaces while in the I.P. and O.P. loading sequences, the wall surfaces have unequal loop widths. Again in the I.P. loading sequence, the outer surface loop width is always greater than the inner surface while the reverse would occur in the O.P. loading sequence. Generally, in the stress regimes of P1, P2, R1 and R2, the above are always true.

The ratchet strain per cycle for the O.P. and I.P. loading sequences corresponding to the R1 and R2 types are given by equations (3.51) and (3.64) and (3.60) and (3.74) respectively. For the Bree loading sequence, the corresponding equations are (3.29) and (3.30). Comparisons

between the ratchet strain per cycle for the common operating points on the Bree and Bree-type diagrams show that the ratchet strain per cycle in the O.P. or I.P. loading sequences are less than in Bree's loading sequence. From Fig. 3.11, it is seen that in the comparisons of O.P. and I.P. diagrams to the Bree diagram the ratchetting area of the Bree diagram has decreased such that some ratchetting regimes on it have acquired alternating plasticity behaviour. A direct comparison of the ratchet strain per cycle is to calculate the ratio of the ratchet rate of the Bree to the I.P. or O.P. sequences. Hence, using the above equations, the ratios R_{R1} and R_{R2} can be obtained for ratchetting regime areas of R1 and R2 respectively and are common to the three loading sequences.

Hence, taking the ratio of Eqn. (3.51) to Eqn. (3.29) gives

$$\text{for common R1 area,} \quad R_{R1} = \frac{Y - 2\sqrt{(1 - X)Y} - 1}{2(Y - 2\sqrt{(1 - X)Y})} = \frac{1}{2}\left(1 - \frac{1}{(Y - 2\sqrt{(1 - X)Y})}\right) \tag{3.75}$$

and taking the ratio of Eqn. (3.60) to Eqn. (3.30) gives

$$\text{for common R2 area,} \quad R_{R2} = \frac{XY - 2}{2(XY - 1)} = \frac{1}{2}\left(1 - \frac{1}{(XY - 1)}\right) \tag{3.76}$$

where R_{R1} and R_{R2} take values of 0, 0.1 etc and X and Y are the load parameters.

The contours for X and Y where the ratios are constant are plotted on the Bree diagram in Fig. 3.12. Therefore the contour at ratio R_{R1} or R_{R2} of zero is therefore the ratchetting boundary in the I.P. and O.P. diagrams. It is to be noted that although the ratchetting ratio may be small for most of the ratchetting regimes of the Bree diagram, it is the absolute ratchet strain per cycle that is important. It is also

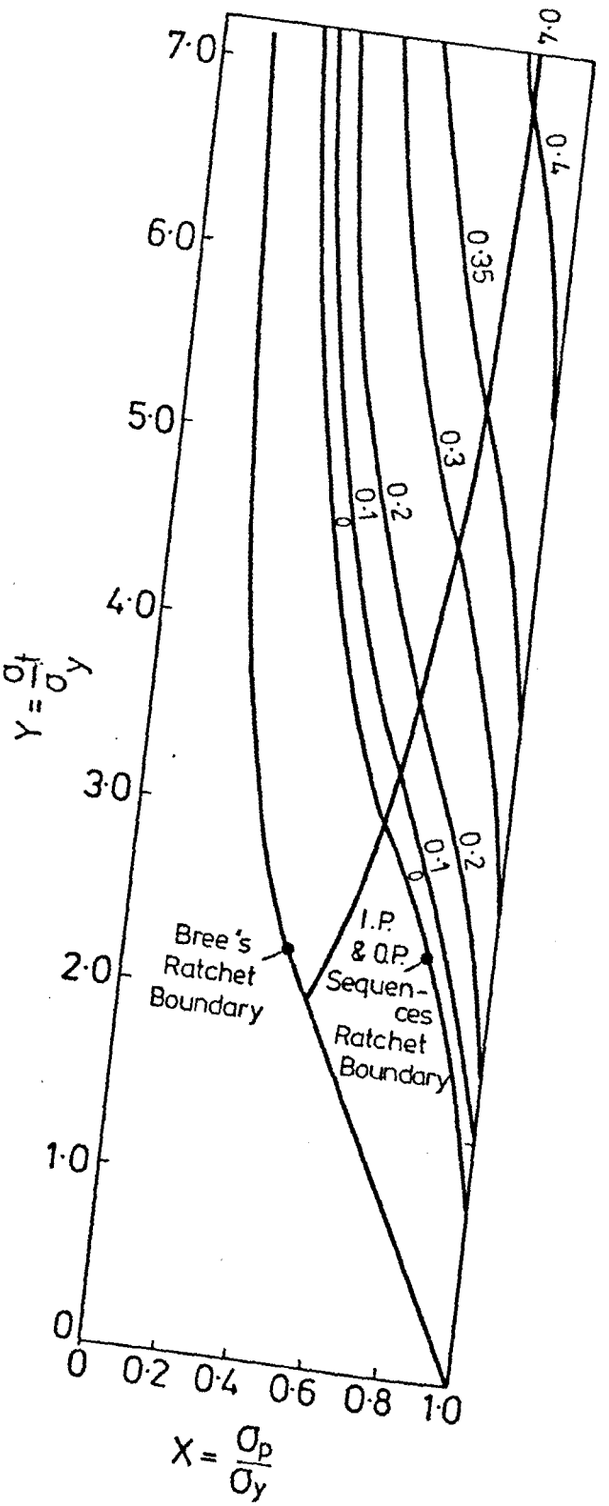

FIG. 3·12 Contours of constant ratios of ratchet strain/cycle between I.P. & O.P. loading sequences to that of Bree.

necessary to consider the effect of fatigue due to cyclic plasticity. In conclusion it is seen that the alternative loading sequences are all less severe than the loading sequence investigated by Bree.

CHAPTER 4

EXPERIMENTATION

4.1 Introduction

The experiments described in this thesis are primarily designed to obtain Bree Diagrams for mild steel at room temperature and Type 316 stainless steel at both room temperature and 400°C. The results are used individually to verify known theoretical behaviour of the Bree model and the computer models to be described in the following chapter. Mild steel was chosen for these experiments because of its near elastic/perfectly-plastic properties at room temperature. Type 316 stainless steel was chosen since it is a commonly used reactor material.

In order to verify the Bree Diagram experimentally for the case of a cylinder under steady internal pressure together with a cyclic through-the-wall thermal gradient, two severe problems of experimentation need to be overcome. Firstly there is the problem of strain measurement at elevated temperatures and secondly the problem of supplying and removing sufficient heat to maintain the necessary thermal stresses. The ORNL pipe ratchetting experiments (45) can be considered to have partially solved these problems by using pressurized liquid sodium circulating in pipes. The experiments could create transient thermal gradients which lasted about 32s before the temperature equilibriated to a uniform through thickness distribution due to the outside lagging of the pipes. For the experiment to simulate Bree's fuel can problem faithfully, the thermal gradients have to be maintained for much longer. This would involve the external cooling of the pipe while heat is supplied to the sodium to maintain the thermal gradient. Similar comments apply to the experiments of Yamamoto et al. (44) where

liquid sodium was circulated through externally lagged pipes which were not pressurized but which were instead axially loaded. It is clear that the conditions which can cause thermal ratchetting can be reproduced in laboratory conditions in a limited way. The conditions in which the fuel can and reactor core components operate cannot be reproduced realistically elsewhere except in situ.

The author devoted some effort to overcoming the strain measurement problem but could not find a method of strain measurement of sufficient accuracy for shakedown determination at temperatures above 200°C at moderate cost. An account of these efforts is given in the section 4.6 where the capability of elevated temperature resistance strain gauges are evaluated in four point bending experiments. Shakedown tests using T-section beams under four point bending demand an accuracy of 1 microstrain (1μ) which could not be achieved at 400°C. Similarly, the problem of sustaining the thermal gradient for a prolonged period of time seemed insoluble. It was thus concluded that experiments must be conducted using an artificial method of producing the stress system in a test specimen. Bree gives a comparison between the states of stress in a cylinder and that in a beam element which is subjected to a steady axial load together with cyclic deformation to a prescribed radius of curvature. Referring to Fig. 4.1, the analogy between the stress states of such a beam element and the Bree uniaxial model is easily understood. The axial stress in the beam is analogous with the hoop (pressure) stress of the cylinder whilst the bending stress is analogous to the thermal stress of the cylinder. It is seen from Fig. 4.1 that no thermal strain exists in this case so that the total strains vary through the thickness. However the steady state ratchet strain and the Bree Diagram obtained in this stress state is similar to the original Bree Diagram by

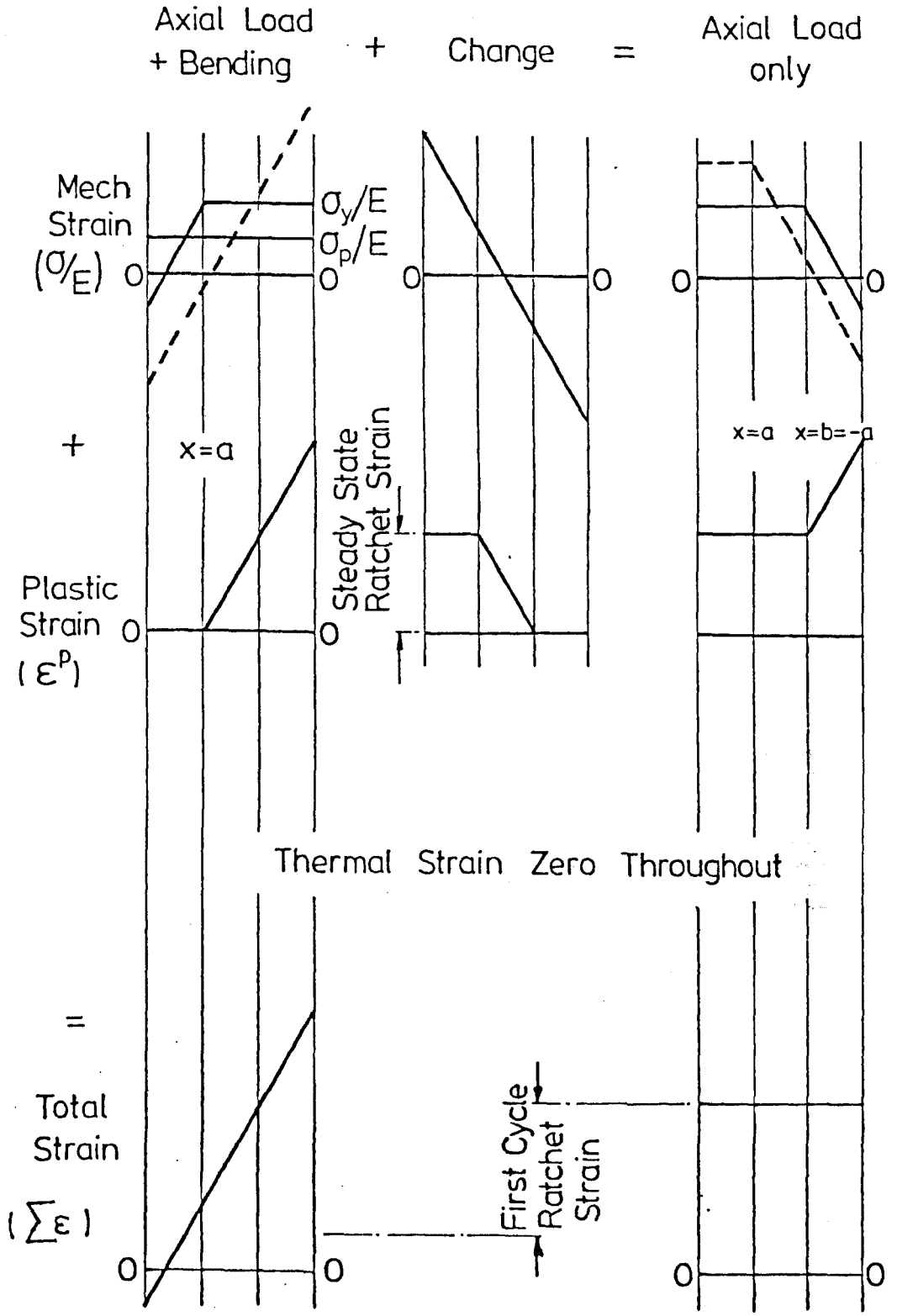

FIG. 4.1 , Ratchetting under Axial Load and Bending Stresses

the analysis shown in section 3.3.3. The uniform temperature in the beam is equivalent to the wall averaged temperature in the cylinder while the thermal gradient is controlled by the curvature. The effect of a change in the uniform temperature of the beam is to cause a uniform change in the temperature dependent properties of the material through the beam thickness. In the cylinder, the absolute temperature varies through the wall thickness by reason of the thermal gradient causing non uniform temperature dependent material property variation through the wall thickness. This difference in conditions is not considered to be a serious shortcoming because the temperature difference between the inside and outside of the cylinder wall is often small in comparison to the wall average absolute temperature. Bree had assessed the effect by comparing the Bree Diagrams obtained with a temperature dependent yield stress (low at the higher temperature half cycle and vice versa) and a yield stress which is the average of the high and low temperature values. He found the Bree Diagrams were negligibly different. Therefore the shortcoming is reduced if the wall averaged temperature is taken as the beam test temperature.

Goodall and Cook (41) and Anderson (42, 43) experimented with the beam method on Type EN58J and Type 304 stainless steel respectively. The former used beams bent by bending moments applied through linkages while Anderson used mandrels with curved surfaces for bending the beams. In the present work, experiments were conducted using long strips of steel as test specimens and cyclically deforming these to a prescribed radius of curvature whilst applying a steady axial load. The experimental approach is shown schematically in Fig. 4.2 which is self explanatory. The actual rig which was designed for the test is shown in Fig. 4.3. In this rig, the strip was formed over the wheel and the ends of the strip

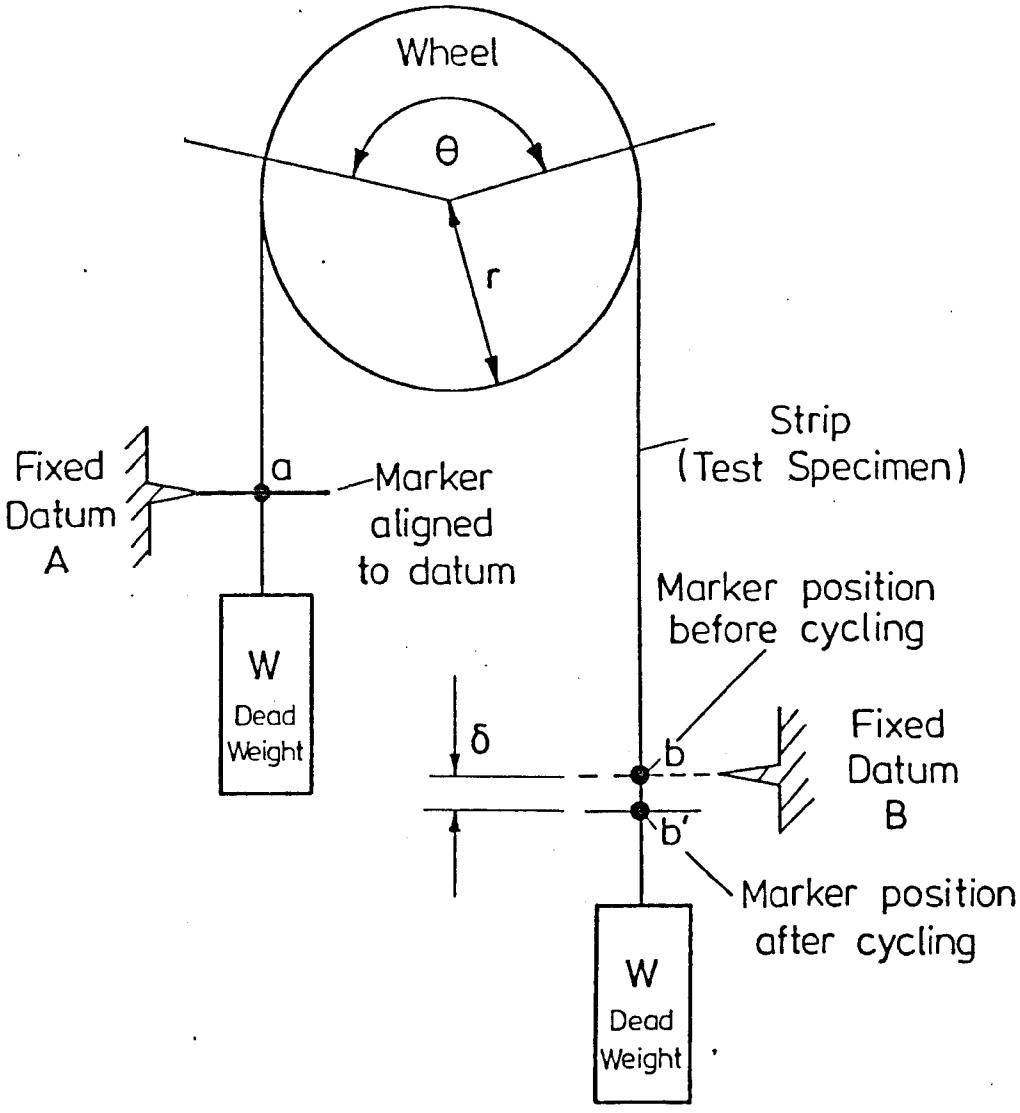

δ = Deflection or ratchet obtained after rotating the wheel through an angular range θ a few times.

FIG. 4.2 The Experimental Concept

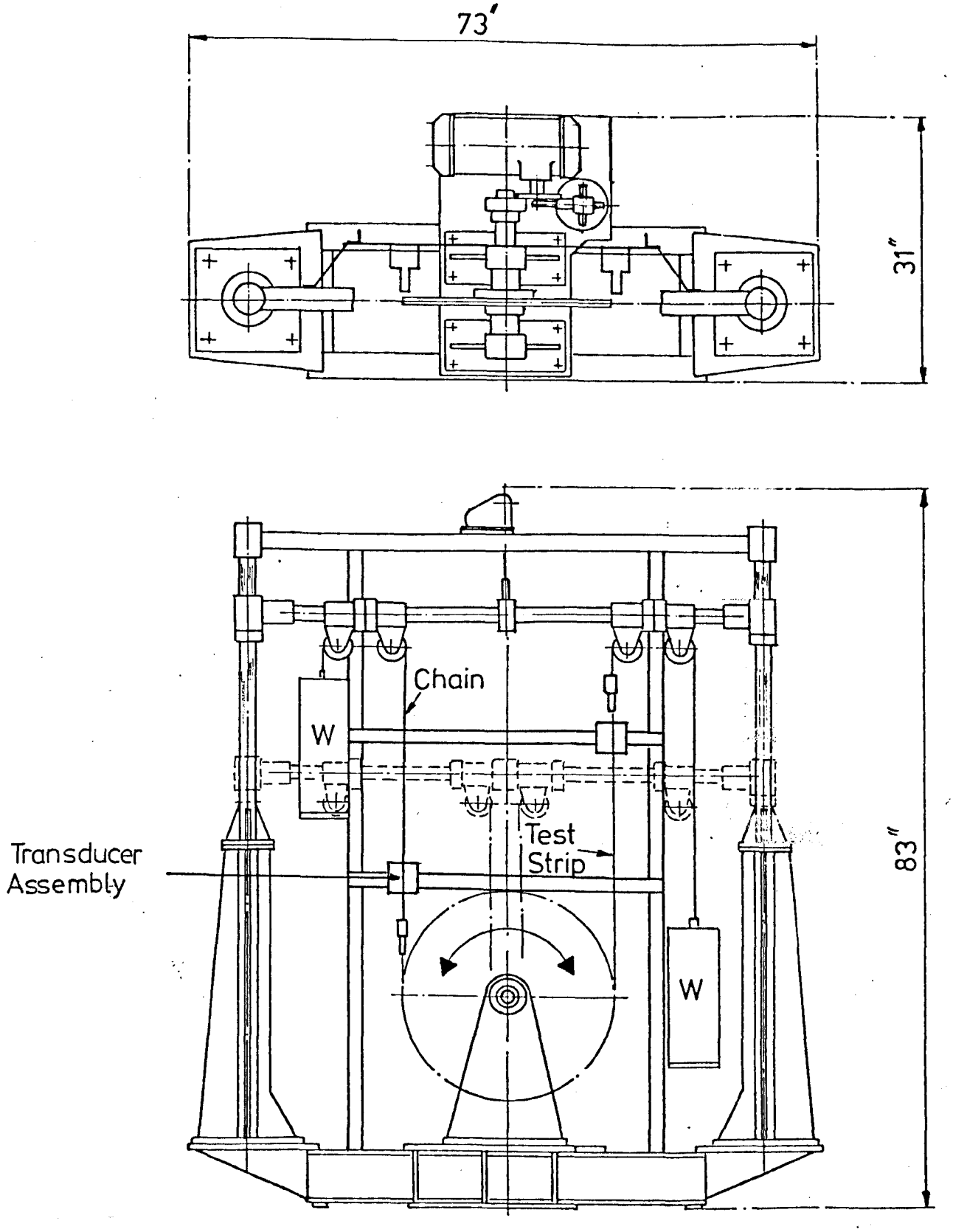

FIG. 4.3 The Experimental Wheel Rig Not Showing Heating System

were attached to chains. These chains were passed over the pulleys and carried dead weights at their ends. The wheel was driven by an electric motor through a rack and pinion and crank train. The wheel was rotated about 108^{o} before the motion was reversed by the crank. By this means, a length of the strip equal to the length of the arc subtended by 108^{o} was brought into contact with the wheel taking its curvature and then returned to its initial position. This is the test section of the strip which is cyclically deformed between the radius of curvature of the wheel and zero curvature whilst carrying a constant axial stress due to dead weight loads. The rate of cycling was initially fixed at 41s/ cycle though the effect of cycling rate was also investigated.

Any chosen location on the Bree Diagram could be investigated by choosing the wheel size and end loads (for a fixed strip thickness) to give the desired σ_t/σ_y and σ_p/σ_y ratios. The deformation of the strip was measured by strain gauges bonded onto the strip and by strain gauged cantilever displacement transducers at the ends of the tested length of the strip. The latter was found to give more repeatable results than the former and the results presented thereafter were obtained by this means. The transducer had a resolution which was dependent on the tested length or gauge length of the strip (which is in turn indirectly dependent on the wheel radius) and each of the 6 adjustable positions which varies the output sensitivity of the transducer. The resolution for most wheel radii used were better than 1 microstrain (1μ). The technique is only able to detect the state of ratchetting or non-ratchetting. Hence the regimes of alternating plasticity and shakedown cannot be differentiated. This is not a severe setback because ratchetting is regarded as a more serious problem than alternating plasticity and is therefore of greater interest.

Ratchetting tests were performed for three material/temperature combinations. Firstly tests were conducted on mild steel at room temperature. This material gives a nearly elastic/perfectly-plastic stress-strain response and was considered suitable for verifying the elastic/perfectly-plastic Bree Diagram. After successfully completing these tests and proving that reasonably good results could be obtained, tests were conducted on Type 316 stainless steel in the same manner. The latter tests were conducted at larger number of cycles (over 1000) in comparison to the mild steel tests (approximately 100) in order to assess the effect of strain hardening on ratchetting strains. The elevated temperature conditions within which most structural components operate require that realistic tests should be conducted at elevated temperatures. For this reason, a test on Type 316 stainless steel was conducted at a temperature of 400^{o}C. The temperature was chosen to suit the temperature at which many Type 316 stainless steel components operate in a power plant environment and also the limitations of size and cost of the experimental rig. Modifications shown in Fig. 4.4 were made to the original rig to include an enclosure to contain hot air for heating the strip and wheel. The air which was circulated by means of ducting through a bank of quartz bar heaters was pumped by a centrifugal fan. Other additional systems included the integral temperature control and data acquisition (for both strain and temperature) which were organized by a PET Commodore 2001 Computer via a control and monitoring system interface. The system was designed to automatically read and record both temperature and strain as well as control heating power to keep the temperature within the required limits.

The format of this chapter consists of six main sections. Section 2 deals with the effect of the anticlastic curvature on the strip. An

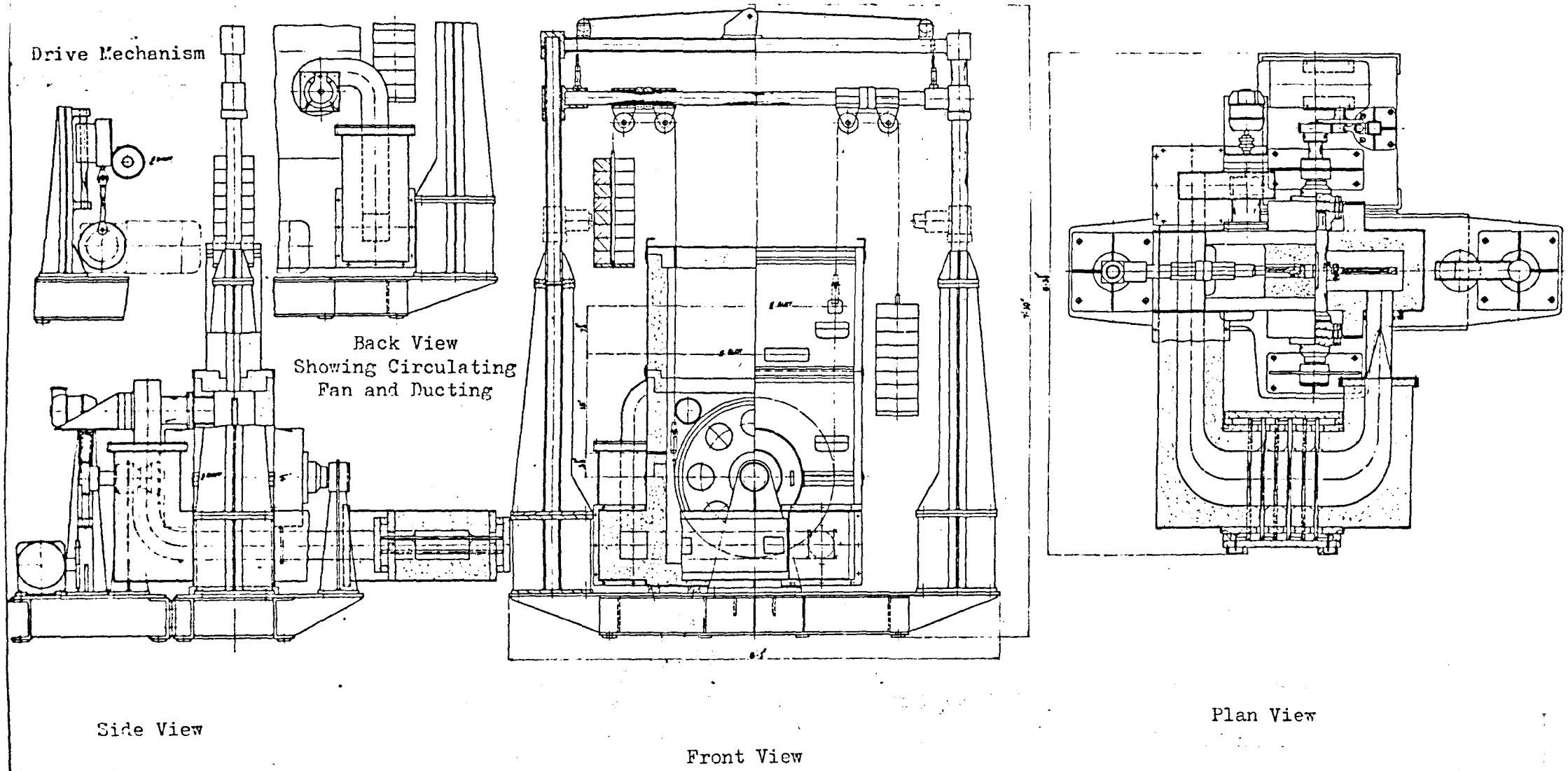

FIG. 4.4 Various Sectioned Views of the Hot Wheel Rig Incorporating Ducting, Heating Elements and Hot Enclosures

experiment was conducted to show that the technique is valid. Section 3, 4, 5 deals with the three material/test temperature combinations. Each section presents the experimental details, results and finally a short discussion. The detailed discussion is given in chapter 6. Information which has been given in the previous section is not repeated. In the final section (6) results of 'T' section beam tests were presented.

Reference of engineering drawings of the test rigs and other minor components are given in Appendix A.

4.2 A Preliminary Investigation to Justify the Basis of the Technique

A preliminary investigation was made to confirm the validity of the technique on an important theoretical aspect. This concerns the question of stress biaxiality due to anticlastic effects in the strip when it is deformed around a radius. This is analysed theoretically and experimentally to show that the stress conditions in the strip are valid. It is well known that when the width of a strip is comparable to the thickness, no stresses are induced in the transverse direction. Such a strip would be classified as a beam and classical analysis will show that the longitudinal radius of curvature r is accompanied by lateral distortion of the cross-section to a circular arc of radius γr where γ is the Poisson's ratio. This lateral distortion is caused by the transverse contraction of the fibres in the strip. Strains in the transverse direction will then be negative ($-\gamma\varepsilon_1$) where ε_1 is the tensile strain in the longitudinal direction. This consideration which is shown by Timoshenko and Goodier (87) can often be used as a means for measuring γ.

If, on the other hand, the lateral distortion is prevented such that the cross-section remains rectangular (that is, in a condition of plain strain) the longitudinal fibres through the thickness will suffer not only the longitudinal tensile stress σ_1 but also a transverse tensile stress $\gamma\sigma_1$ which must be such as to prevent the lateral contraction of the fibre. The fibre experiences biaxial stresses and the transverse strain becomes zero.

When the beam has a much wider dimension compared to the thickness, it is then classified as a plate and plate bending theory is applied. Bending will cause the longitudinal stress σ_1 accompanied by transverse stress $\gamma\sigma_1$ at all points near the centre region thus causing a state of

plain strain in this region. The transverse stress will decay in magnitude from the centre at $\gamma\sigma_1$ to zero at the beam edges since these are free. Also the transverse strain will be zero at all points except near the edges. For larger curvatures, this effect will be seen to cause an anticlastic curling of the edges with the central region remaining flat. In the condition where the entire strip remains undistorted, biaxial stresses of σ_1 and $\gamma\sigma_1$ exist in the whole strip. The transverse strain is then zero at all points.

In the experiments presented in this thesis, the strip is subjected to an axial tensile stress whilst cyclically rotated over a wheel of a fixed radius of curvature. The dimensions of the strips used are 0.2 by 0.020 and 0.2 by 0.015 inches giving width to thickness ratios of 10 and 13 respectively. There are no available analytic or empirical criteria which can be used to determine whether the strip is a beam or a plate on the width to thickness ratio basis. Since the values of width to thickness ratio are large, there is a great possibility that a biaxial stress condition will exist on the strip and plate analysis will apply. In that case, the fictitious maximum bending stress σ_b is modified to $\sigma_b/(1-\gamma)$ to account for the tensile transverse stresses. This is proposed by Bree who applied a reduction of the maximum thermal stress value by dividing the wall to wall temperature difference ΔT by $(1-\gamma)$ to account for the stress in the axial direction of the can wall. If the strip is shown to be a beam this will then not be necessary since there are no transverse stresses. The above has an important effect on the σ_b/σ_y axis of the Bree Diagram. By a reduction in σ_b, of a factor of $(1-\gamma)$, an operating point on the Bree Diagram will exhibit the same behaviour for a smaller bending stress in a plate than in a beam.

It is possible to determine which of the above applies by measuring the outer surface strains on the strip in both longitudinal and transverse

directions. Knowing that a beam under longitudinal stress only, will have to satisfy the provision that the ratio of the transverse to longitudinal strains equals the Poisson's ratio, an experiment was conducted. Biaxial strain gauges were attached to the centre-line of mild steel strip surfaces which were then subjected to a constant radius of bending. Strains were recorded during the initial bending and at a constant load of 10 lbf (22N) to ensure that the strip acquires the radius. Seven radii of curvature were used and these ranged from the smallest of 1.375" to the largest of 12". A further test subjected the strip to only increments of axial loads to determine the Poisson's ratio and the yield strain ε_y.

The results are plotted in Fig. 4.5 which is a plot of the Poisson's ratios that is the ratio of the transverse (ε_2) to longitudinal strains (ε_1) against the longitudinal strain. Also plotted is the variation of Poisson's ratio against longitudinal strain obtained using elastic/perfectly-plastic theory for bending in a beam. The Poisson's ratio is assumed to be 0.3 and 0.5 for elastic and plastic load respectively.

On the beam surface, the transverse strain ε_2 is given as

$$\varepsilon_2 = 0.5\varepsilon_1^{\,P} + 0.3\varepsilon_1^{\,e} \qquad \text{for } \varepsilon_1 \text{ greater than the yield strain } \varepsilon_y$$

and

$$\varepsilon_2 = 0.3\varepsilon_1^{\,e} \qquad \text{for } \varepsilon_1 \text{ less than the yield strain } \varepsilon_y \tag{4.1}$$

The plastic strain component ε^P is given by

$$\varepsilon_1^{\,P} = \varepsilon_1 - \varepsilon_y$$

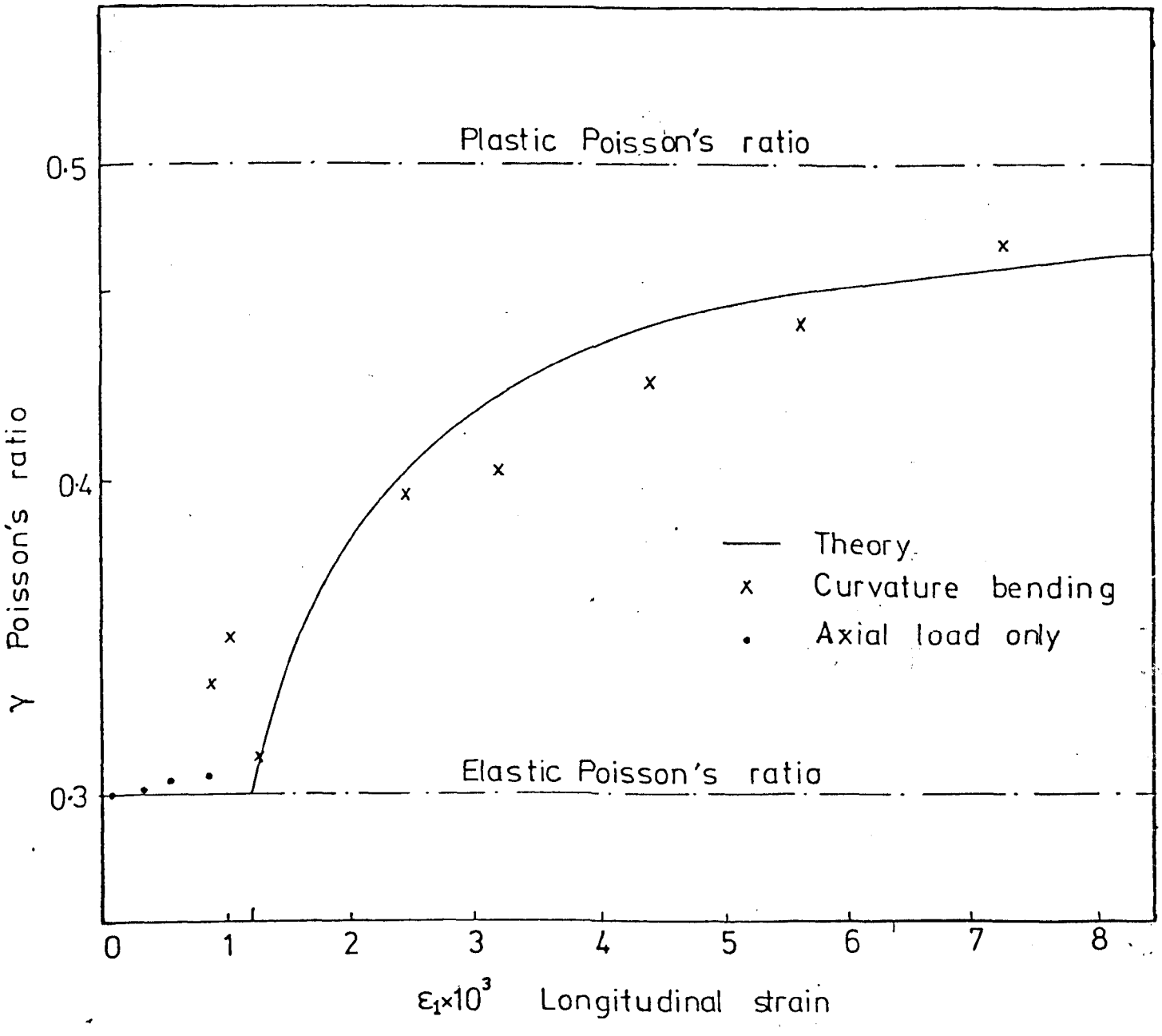

FIG. 4.5 Comparison of Experimental and Theoretical Poisson's Ratios at the Outer Surface of Beam

while the elastic strain component ε^e is given by

$$\varepsilon_1^e = \varepsilon_y \qquad \text{provided } \varepsilon_1 > \varepsilon_y$$

and

$$\varepsilon_1^e = \varepsilon_1 \qquad \text{for } \varepsilon_1 \leqslant \varepsilon_y$$

Hence for plastic loading,

$$\gamma = \frac{\varepsilon_2}{\varepsilon_1} = \frac{0.5\varepsilon_1 - 0.2\varepsilon_y}{\varepsilon_1} = 0.5 - 0.2\frac{\varepsilon_y}{\varepsilon_1} \qquad (4.2)$$

The above shows that γ tends to 0.5 for large ε_1 and equals 0.3 when $\varepsilon_1 \leqslant \varepsilon_y$.

Fig. 4.5 shows the experimental data plotted against the theoretical curve for both elastic and plastic regions. The data presented indicate that the strains recorded are fully 'expressed' by the anticlastic curvature in the beam. The conclusion is that the transverse stress is insignificant and that beam theory is applicable. The assumption of a uniaxial state of stress in the strip is confirmed on the grounds of this investigation.

4.3 Ratchetting Tests on Mild Steel at Room Temperature

4.3.1 The Test Rig (1)

It needs firstly to be mentioned that the test rig described previously and shown in Fig. 4.3 was built after a period of preliminary investigation on a different and much more simple rig. The rig which is built very much according to the basic idea illustrated in Fig. 4.2 consisted simply of a portal framework which supported a freely rotating wheel at a height above the floor which was sufficient to allow for the required movement of the weights. This rig, together with a set of different wheels and the necessary instrumentation were used to carry out much of the initial experimentation for assessing the feasibility of the technique so far described and the methods of measuring the deformation or extension of the strip. The procedures, results and discussion of these experiments are included in this section. It was on this rig that having established its capability to carry out the required ratchetting tests that a proper test programme was formulated.

The rig consisted of a wheel 2 in. (5cm) wide which rotated on needle race bearings on a 1.5 in. (3.8cm) diameter shaft. The shaft was located in holes bored out of a large steel block which was bolted over the top members of the portal frame. The strip which carried the weights moved freely in the centre of the framework. Two cross members on the framework supported the displacement transducer assembly which operated in conjunction with the corresponding contact arms attached to the strip to measure the extension. The basic elements of the rig were highly modular, that is, most of the parts including the length of strip used can be adjusted and varied in position and size. This modularity was an important factor for a fast preliminary study. Rotating the wheel between two fixed stops attached to the frame brought a part of the

strip onto the wheel and subjected it to a bending curvature while the rest of the strip was under tension only. Therefore the actual length of the strip that was cycled was that part subjected to bending. This length, or more appropriately the gauge length, of the strip can be easily calculated knowing that it equalled $r.\theta$ where r and θ are the radius of the wheel and the angular range in radians respectively. It is seen that for either large r or θ, the gauge length is large. In practice, the gauge length is limited by the height of the wheel since this restricted the travelling range of the weights. Hence for a maximum fixed gauge length, the angular range and radius are inversely proportional to one another and the maximum measurable extension of the strip are dependent on them.

When testing, the wheel was rotated slowly at approximately a cycle a minute. At this speed, the vibration and swinging of the strip and weights respectively were minimal and for the purposes of the tests, they constituted no problems to the displacement measurement.

4.3.2 Ratchet Strain Measurement

The cyclic extension of the strip was measured by two methods. The initial method was based on strain measurement by strain gauges bonded to the upper surface of the strip. This was found not suitable and was replaced by a second method which relied on measuring the total extension of the strip length during cycling. The extensions were measured by the deflection caused to the displacement transducer by the contact arms. Three displacement transducers were simply strain gauged cantilever beams which were deflected by the contact arms at the free ends. This method gave more repeatable and consistent results and was used in all the extension measurements in all the further tests.

It was realised that a strain gauge measures the strain behaviour on

a part (that is, the gauge length of the strain gauge) of the strip whilst the displacement transducer measures the total extension over the cyclically stressed or gauge length of the strip. The strain gauge therefore measured local behaviour whilst the displacement transducer measured the average behaviour. Initial tests showed that results using strain gauges were not as repeatable as displacement transducers and this was attributed to local variations in material properties of the strip. The causes for these variations may be speculated to be due to the non uniform heat treatment temperature or inconsistent strain gauging practice. Besides being unrepeatable, the results obtained from strain gauged strips showed very poor agreement with theory.

The transducer method for measuring the cyclic extension of the strip is illustrated in Fig. 4.6. The working of the transducers depended on two such devices, each situated at the ends of the strip where it has neared the end of its travel. Referring to Fig. 4.3 these positions are shown as boxes at the top right and bottom left of the frame. At these positions, the strip carrying contact arms reached the furthest point of travel and if there were any extensions of the strip, these extreme points of travel would extend further at every cycle. The contact arms move into progressively lower positions at the end of cycles and these cyclic displacements were measured by the strain gauged cantilever beams on which they contact and depress.

The cantilever beams were clamped rigidly onto movable platforms which were guided on the main bodies. These bodies were rigidly bolted to the framework. The movable platform enabled the adjustment of sensitivity of the cantilever beam response to deflection via strain gauges bonded on both sides of the beam. The beam length and the position of the strain gauges on it were constant in relation to the clamping plate.

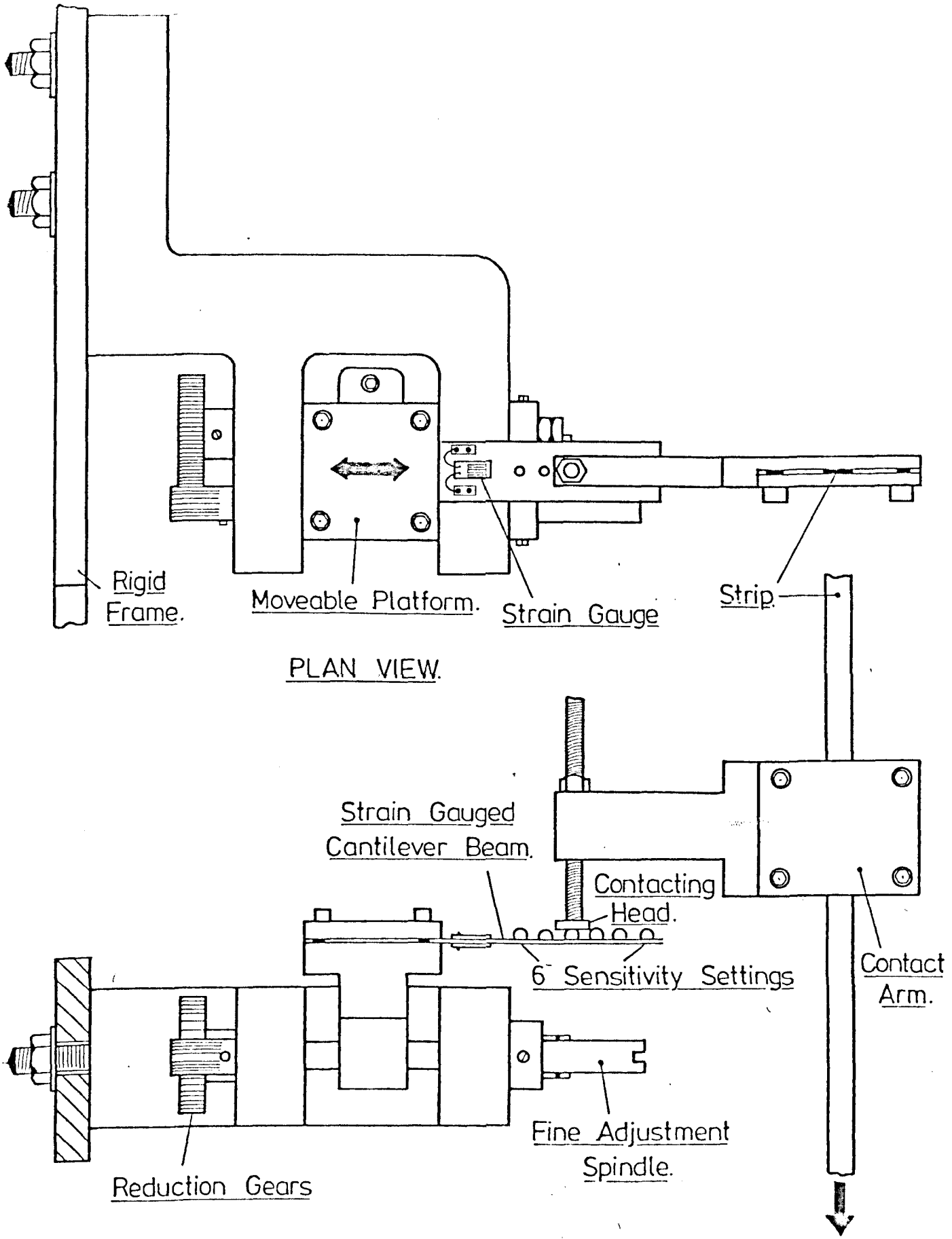

FIG. 4.6 Two Views of Displacement Measuring Assembly with the Strip Carrying the Contact Arm Making Contact Just Before the End of the Downward Stroke (Full Scale)

The beam had six graded sensitivity settings which were obtainable by the depression of the beam at various distances from the strain gauge. These settings were achieved by having 6 small holes drilled into the beam at the distances required. 2mm ball bearings were seated into these holes such that about two thirds of the diameter were above the upper surface of the beam. Epoxy Resin glue was applied on the bottom surface in small amounts to secure the bearings. These bearings were to ensure that the beam could only be deflected at precise positions. By this means the distance between the applied deflection position and the strain gauge centre remained constant. Because of the slight vibration of the contact arm the contacting head which was machined flat and in a plane perpendicular to its axis could contact the same bearing at slightly different points of its 5mm diameter circular area without causing error. The vibration of the contacting head would have caused errors in strain reading if it contacted the beam directly.

The two beams were made from the same material (a type of spring steel) and were of similar dimensions. Great care was taken by drilling and cutting the beams together to ensure similarity of dimensions. Simple beam bending calculations were made initially to determine the appropriate detailed dimensions and these took into account the expected gauge length of strip to be tested and the precision of displacement measurement that was desired. Strain gauges were carefully bonded and wired to both surfaces of the beams at locations that were carefully determined. These locations were to be similar in both beams in order that both beams gave exactly similar strain responses when deflected by equal amounts. The beams were then rigidly clamped at one end to the platform by a clamping plate utilizing four screws which were tightened to the same torque. Prior to tightening, the beams were matched in their

responses by deflecting them by equal amounts using a micrometer screw gauge and re-adjusting the beam positions until equal strain to deflection responses were obtained. After tightening, the beams were calibrated individually and the result showed that they were matched. However the wiring configuration to be used in the rig was different and this is described in appendix B.

Briefly, the wiring configuration was designed to measure only the extension of the strip and to be insensitive to slippage of the strip on the wheel or to a limited amount of over and under rotation of the wheel. It relied on a full bridge wiring of the two pairs of gauges on the beams. Referring to Fig. 4.3, the transducer beam in the top right (henceforth called beam 1) will be deflected upwards while the beam (beam 2) on the bottom left will be deflected downwards by the cyclic extension of the strip. As the extension increases, beam 1 will gradually be deflected less and beam 2 more. The full bridge circuit was configured such that as the extension increases, the total indicated strain also increases.

Calibrating the displacement transducer required two micrometer screw gauges, each rigidly attached over each beam in situ. Gradual depression of the beams simultaneously in steps of five thousandths of an inch gave rise to an indicated strain which was recorded. Beam 1 received an upward deflection while beam 2 was deflected downwards.* This was carried out for the 6 sensitivity settings in both beams. Fig. 4.7 shows the calibration curves so obtained for all the 6 sensitivity settings which were designated H1 to H6 in increasing order of sensitivity. The settings allow for most of the ratchetting tests to be achieved with an accuracy better than 1μ. The figure also shows the responses are linear for the range of deflection tested. If greater deflection were

---

*During calibration, beam 2 although initially deflected downwards, was allowed to return upwards. Thus the movement of both beams during calibration was in the same direction.

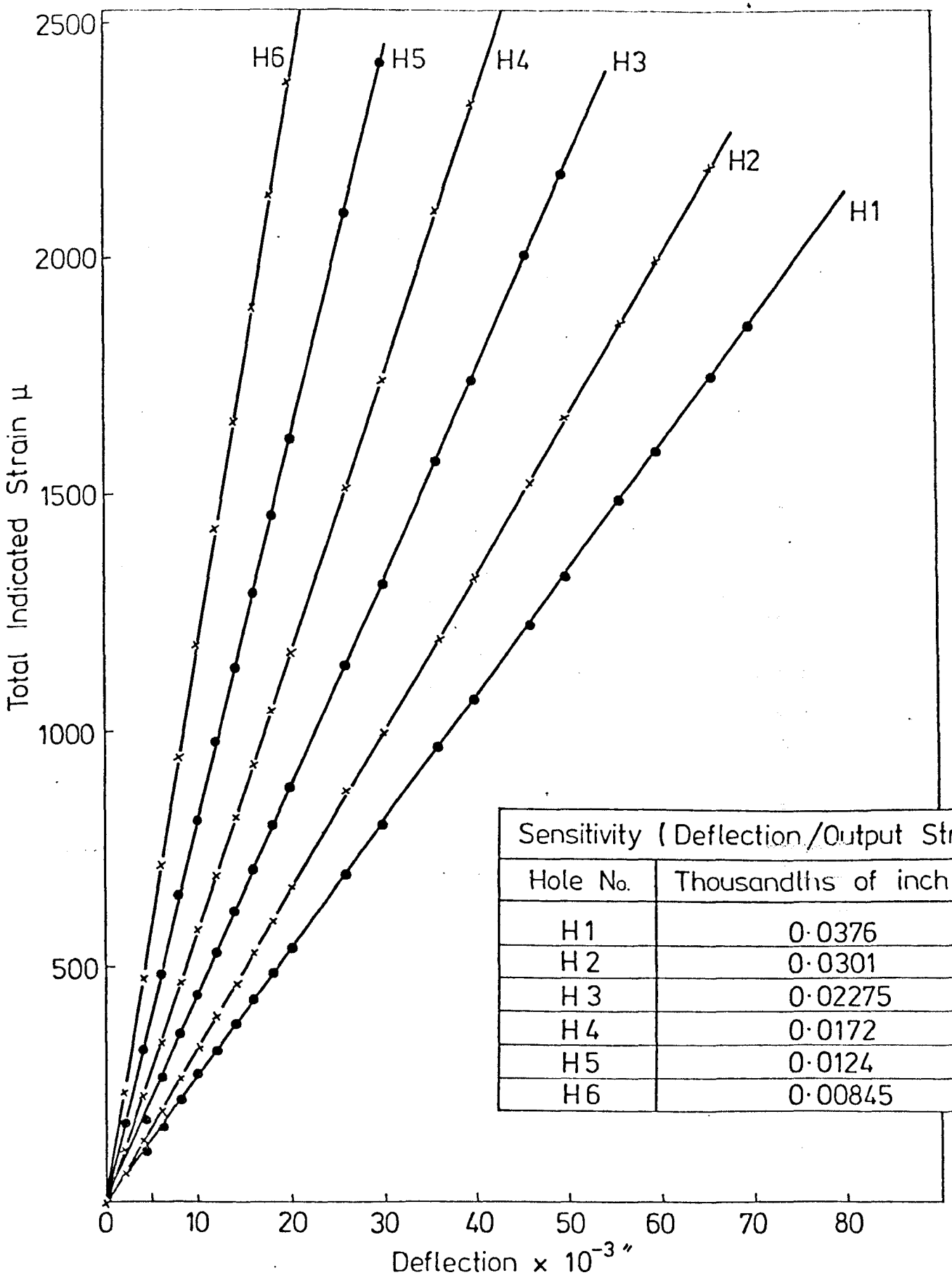

Sensitivity (Deflection / Output Strain)	
Hole No.	Thousandths of inch/μ
H1	0·0376
H2	0·0301
H3	0·02275
H4	0·0172
H5	0·0124
H6	0·00845

FIG. 4.7 Calibration Curves of Strain Gauged Cantilever Beams by Equal and Simultaneous Deflection of Both Beams

imposed, the relationship would be non-linear because of geometry changes, that is, the distance between the point of applied deflection and the strain gauge becomes significantly altered and the possibility of yielding of the beams exist. Care was taken in the use of the transducer in subsequent experiments so as not to deflect beyond an indicated strain of 2500μ. Additionally, the bridge configuration was tested for its response to a simulated slippage of the strip by the expedient of increasingly depressing the beams in the same directions. The result was that the indicated strain remained unaltered thus showing that the bridge configuration operated in accordance to the analysis given in appendix B.

It needs also to be mentioned that the actual strain in the strip is related to the indicated strain by the following relation, that is,

$$\text{actual strain} = \frac{\text{indicated strain x beam calibration}}{\text{gauge length of strip}}$$

where (a) the indicated strain is directly measured from the strain indicator (microstrain),

(b) the calibration is the slope of deflection against indicated strain for the sensitivity setting used (inch per microstrain),

(c) the gauge length is the actual length of the strip which undergoes cyclic bending which is equal to $r\theta$ where θ is the angular range of rotation in radians and r the wheel radius (inches).

4.3.3 Instrumentation

The instruments required for the test rig were a Bruel and Kjaer (hereafter known as B & K) strain indicator Type 1526, a chart recorder

and an oscilloscope. Both the chart recorder and oscilloscope received their input from the two output ports in the B & K and hence readings made were in units of strain. The oscilloscope enabled the strain vs time behaviour of the displacement transducers and strain gauges on the strips to be examined whilst the chart recorder recorded on paper. For ratchetting tests, strain readings were recorded manually using the maximum strain hold facility on the B & K. This facility stores and displays the maximum strain recorded during a transient input and this was found suitable for the ratchetting tests. The B & K strain indicator was used to either indicate strain direct from strain gauges on the strip or from the displacement transducers.

4.3.4 Specimen Preparation

The test strips were obtained from a commercial supplier in the form of coils having an inside radius of 3.0 in. and outside radius of 6.0 in. The cross-sectional dimensions of the strips were 0.20 in. (5mm) wide by 0.020" (.5mm) thick. According to the supplier, the strips were manufactured by rolling and shearing sheet steel to the desired dimensions. This process of manufacture was expected to create large residual stresses on the strips and these were removed by a stress relieving heat treatment. The heat treatment consisted of a one hour soak at 650^{o}C followed by slow in-furnace cooling. Before heat treatment, sufficient 4ft. (1.22m) lengths of strip were cut from the coils and because of the residual bending stress of the coiling, they had a tendency to curl lengthwise. To straighten the strips, they were pulled through a fixture which consisted of three cylindrical posts set a distance apart. The posts applied bending in the reversed direction to the natural curl of the strip and by setting the correct separation distances between the posts, most of the curvature was removed. The next

procedure of heat treatment involved laying the strips flat on a flat plate on the furnace floor. After heat treatment, straight strips were obtained - the annealing process having softened the strips to the extent that they took to the flatness of the furnace plate. At this stage, specimen preparation was complete and a straight residual stress-free strip was achieved.

A sample of the treated strip was chemically analysed by wet analysis technique and the results showed that C = 0.077%, Mg = 0.40% and there were no alloying elements greater than 0.03% present.

A tensile test using strain gauges showed that the material had a yield stress of 202 MN/m^2 and at this stress the strain was greater than 40,000μ, thus exhibiting nearly perfect-plasticity of the material. The elastic modulus was calculated to be 172 GN/m^2. Calculations involving the Bree analysis will be based on the above data.

4.3.5 Test Procedure and Planning

Initially, a number of trial experiments were made to check the loading procedure and solve any problems that arose from the rig. A number of problems were caused by swinging of the weights and the necessity of ensuring that the test section of the strip remains undisturbed during loading. The former problem was reduced by slowing the cycling rate to about 1 min/cycle. The second problem was resolved by devising a loading procedure which was carefully and consistently adhered to during the entire tests. These trials showed that for consistent and repeatable results, the loading procedure had to be rigidly followed with the overriding concern that the strips are to be treated with the greatest care and that they are not unintentionally bent thereby causing residual stresses.

The loading prodedure was simply as follows. Firstly the ends of the strips were clamped between clamping blocks having previously ensured that the strip was centrally located along the axes of the blocks. The clamping action of the blocks was provided by tightening the two rows of 6 socket head screws which bring together the two parts of the block. Markers on the blocks ensured that the alignment of the strip end to the centreline of the block was accurate so that the tensile stress was completely transferred without any bending of the strip near the block. After clamping, the strip was transferred to the rig and one end was located to the block holder and secured with a pin. The block holder contained a hole through which the weight hanger hook was attached. The required weights were put onto the hanger. Whilst ensuring the strip was straight throughout this procedure, the strip was draped over the wheel for the first time and the other clamping block was attached to the other block holder. The alignment of the strip was checked to ensure that it was central to the wheel rim. The weight hanger was then attached to the block holder and the required weight was put on. At this stage, the position of the strip was at one of the extreme positions of its travel. The pair of displacement measuring assemblies were brought into position and secured to the support frame. This was carried out once for each wheel size. The contact arms were next clamped onto the strip at positions where they were within contact and adjustment distance of the beam transducers on the displacement measuring assembly. The contact head screws were then adjusted until they were in contact with the bearings mounted on the beam transducer. The sensitivity settings were selected to give the accuracy of measurement of about 1 microstrain by taking into account the test length (or gauge length) of the strip which was dependent on the wheel size and angular range. When

the sensitivity was selected, the movable platform was adjusted to bring the setting into position. Before measuring the strain, the wheel stops were locked onto the rim of the wheel thus limiting the angular range. This was predetermined together with the sensitivity selection. Final adjustments were made on the contact head screw height so that they now contacted and depressed the beam transducer giving a strain reading which was indicated on the B & K indicator. The locking nut on the contact head screw was tightened to lock it into position and a final check was made on all lock nuts to ensure that all adjustable parts were secure. The final step taken was to set the zero on the indicated strain so that the accumulated strain was read directly.

The wheel was rotated between the stops and strain recordings were taken with the use of the maximum hold facility on the B & K. Because of the time required for a large number of cycles, only about 80 - 100 cycles were performed on each strip. This was considered to provide sufficient data for assessment.

In the test plan, five wheel sizes were used, giving a range of σ_t/σ_y values of 1.943 to 5.05. Six to seven values of weights were applied in 5 lbf (22.2N) steps on each weight carrier. New strips were used for each test, a test being considered as one carried out on one wheel size and weight. A total of 31 tests were conducted. The calculation of the ratios of stresses were based on a yield stress of 202 MN/m^2. Table 4.1 shows the test positions or co-ordinates on the Bree Diagram. The positions of the test points are chosen to lie on and outside the ratchetting boundary in order to facilitate the determination of the experimental ratchetting boundary by interpolation and so validate the theoretical analysis of Bree.

D inches (cm)	σ_t/σ_y	σ_p/σ_y						
4.04 (10.26)	5.050	.071	.142	.213	.283	.354	.425	-
5.50 (13.97)	3.710	.213	.283	.354	.425	.496	.567	-
6.13 (15.57)	3.328	.213	.283	.354	.425	.496	.567	.638
6.95 (17.65)	2.996	.283	.354	.425	.496	.567	.638	-
11.50 (29.21)	1.943	.425	.496	.567	.638	.708	.779	-

Table 4.1 Wheel Sizes Used and the Co-ordinates of Test Positions on the Bree Diagram for Mild Steel

4.3.6 Results and Discussion

Apart from a number of tests conducted to verify the loading procedure, functioning of the rig and on repeatability testing, 31 additional tests were conducted to provide a good range of experimental data on which to perform a parameter study. The test points are tabulated in Table 4.1 and the experimental results are shown in Figs. 4. (8, 9, 10, 11, 12, 13).

Figs. 4.8 and 4.9 show two examples of the results which are obtained at two σ_t/σ_y ratios. The curves on each figure represent the accumulated strain which were plotted against the cycle number for various values of σ_p/σ_y. Initially the cyclic ratchetting response was that of an elastic/perfectly-plastic material and as cycling proceeded, the rate of ratchetting decreased. From the results known of Type 316 stainless steel tests (section 4.4), it was expected that the rate of ratchetting will continuously reduce and will asymptotically approach zero.

Fig. 4.10 shows the comparison of the initial rates of strain accumulation which were taken over the first few cycles (about 5) of the data with the theoretical rate both plotted against σ_p/σ_y. The theoretical rates are given by the Eqns. (3.29) and (3.30) in chapter 3 for the ratchetting in the R1 and R2 regimes respectively. It can be seen that agreement in the rates only existed at small strain accumulation rates. This means that the ratchetting boundary is confirmed by experiment. At the greater incursions into the ratchetting regimes, the strain accumulation rates were much lower than the predictions. The experimental rates increase gradually at small incursions into the ratchetting regimes but this rate of increase becomes progressively more at greater incursions. The curves appear to become parallel to the theoretical Bree

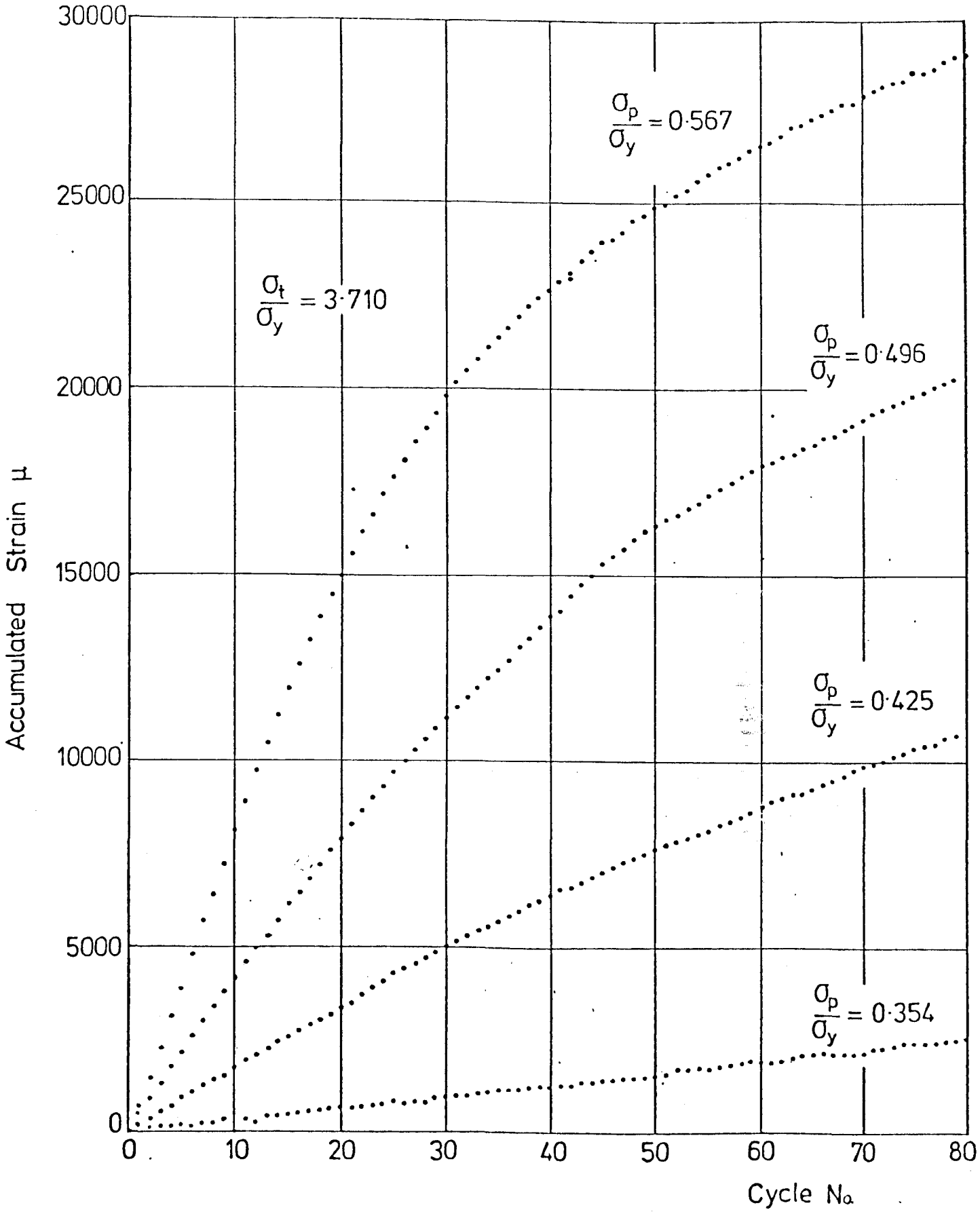

FIG. 4.8 Experimental Ratchet Strain Accumulation (Mild Steel)

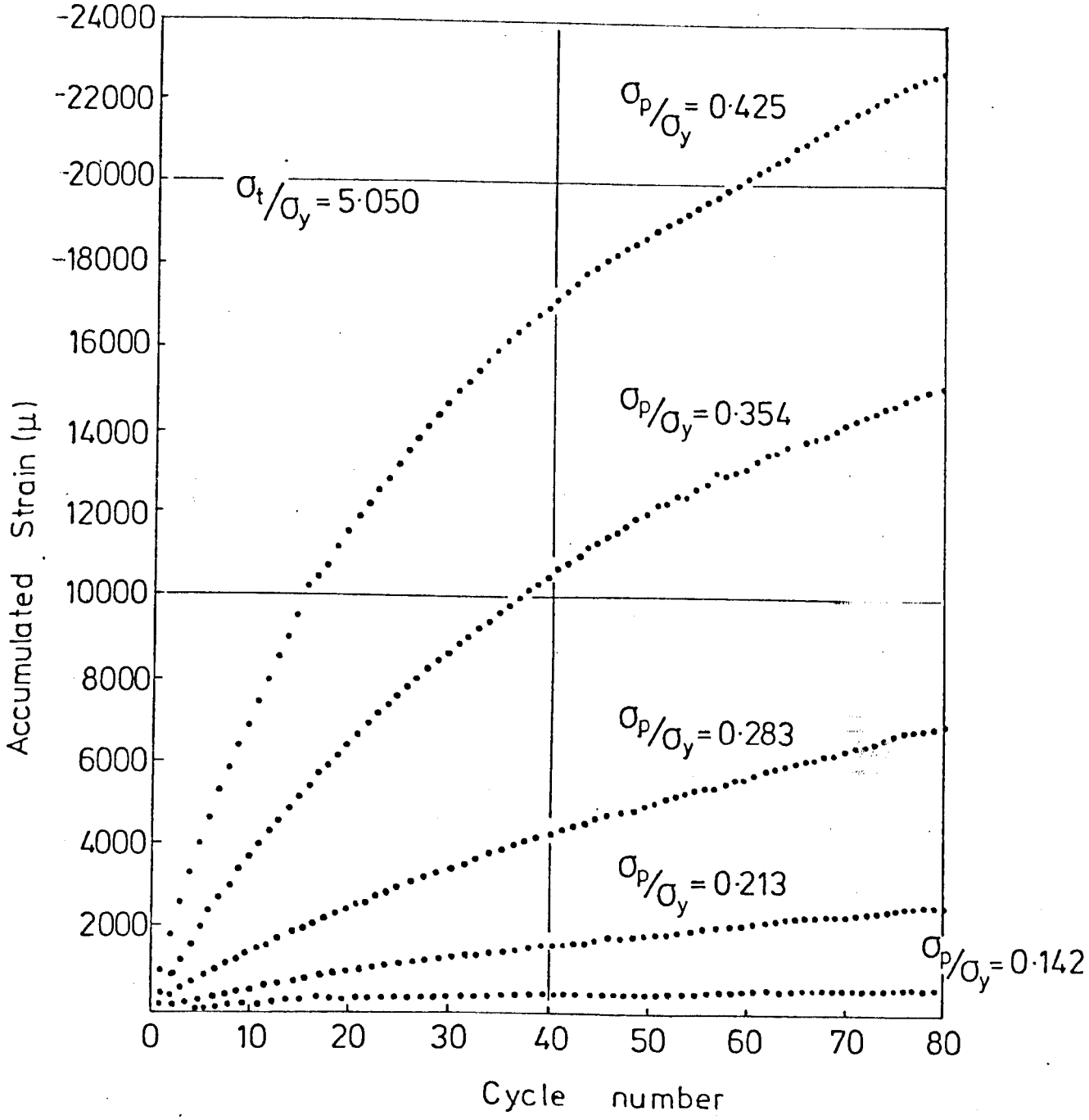

FIG. 4.9 Experimental Ratchet Strain Accumulation (Mild Steel)

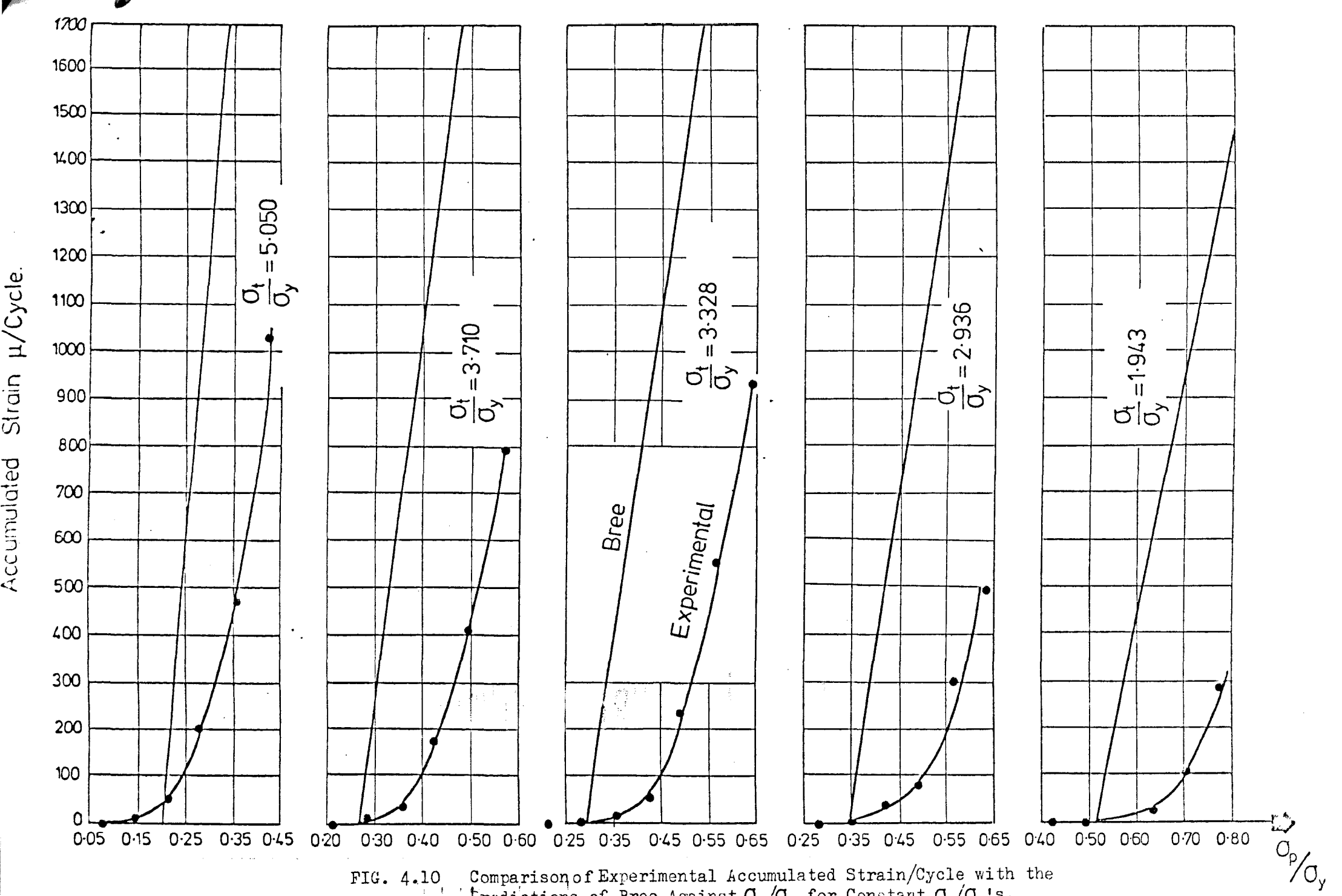

FIG. 4.10 Comparison of Experimental Accumulated Strain/Cycle with the Predictions of Bree Against σ_p/σ_y for Constant σ_t/σ_y's. (Mild Steel)

curve. Hence, at large incursions into the ratchetting regimes, it may be said that the slopes of the predicted and experimental rates when plotted against σ_p/σ_y approach one another. This observation in practical terms means that the predicted ratchetting rates will be achieved experimentally by displacing the σ_p/σ_y value (at which the prediction is calculated) a constant displacement to the right of the plot. It is important to stress again that only the initial rates of strain accumulation were considered. Hence, it may be concluded that not only does the initial rate vary non-linearly with the depth of the incursion into the ratchetting regime but the rate also progressively decreases with the number of cycles experienced.

Fig. 4.11 shows the same data of Fig. 4.10 plotted in the form of the Bree Diagram. The strain accumulation data are plotted as contours of constant strain accumulation rates. Intermediate values were interpolated directly from Fig. 4.10. Since this information has been obtained from the initial few cycles, the contours will show a pessimistic picture for any beam subjected to greater than that number of cycles. Therefore if the strain accumulation rates are at a larger cycle number the contours will be shifted further away from the Bree boundary and also be separated more.

When the total accumulated strain after 80 cycles were plotted against σ_p/σ_y for each σ_t/σ_y value, it will be seen that similar to Fig. 4.10 the upper part of the curves have steeper slopes than the lower parts. This again implies that at larger σ_p/σ_y values, the total strain accumulation becomes more sensitive to changes in σ_p/σ_y. This tendency decreases with the values of σ_t/σ_y. At small incursion into the ratchetting regimes, the strain accumulation is not so sensitive.

Finally Fig. 4.12 shows contours of constant strain accumulation

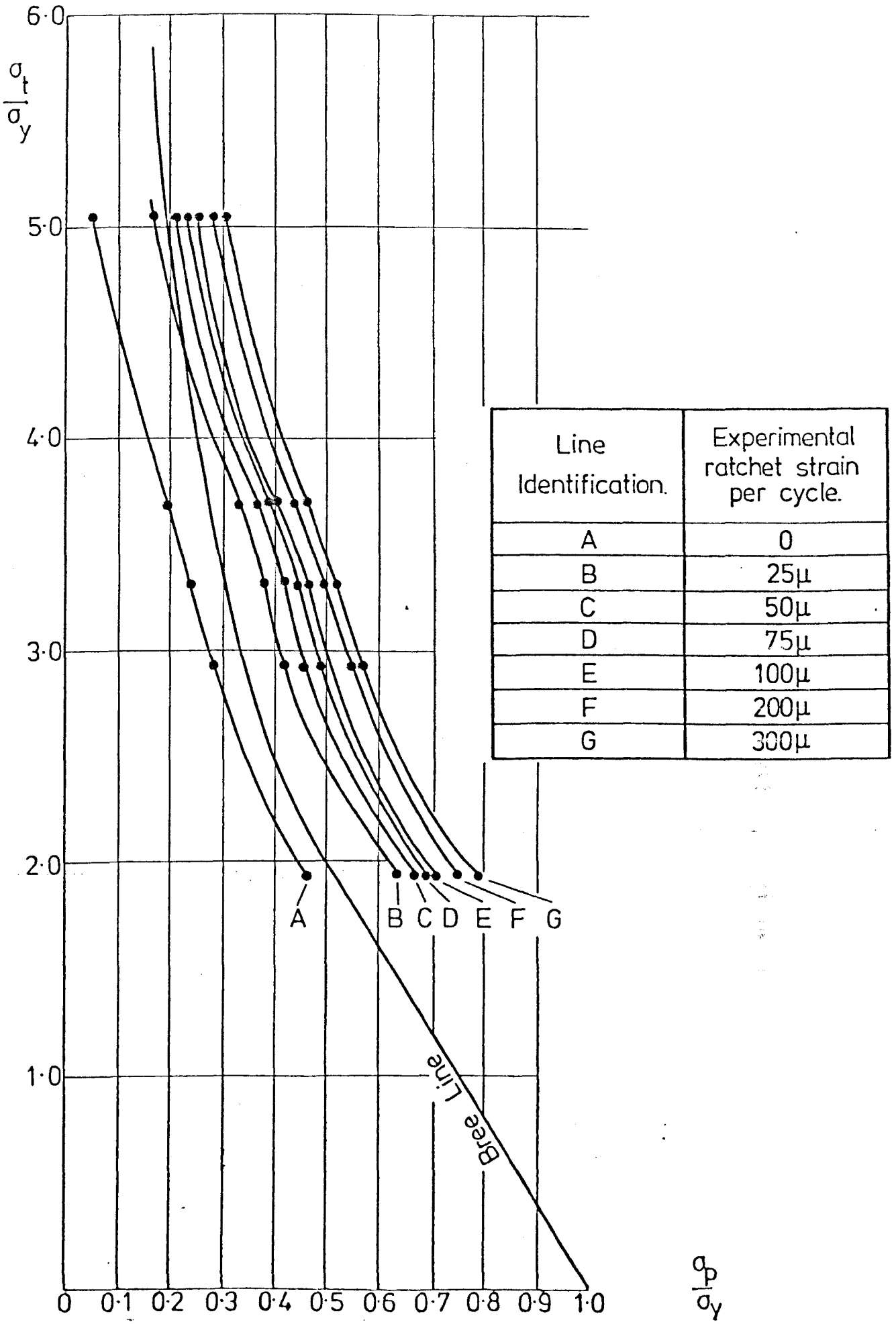

Line Identification.	Experimental ratchet strain per cycle.
A	0
B	25μ
C	50μ
D	75μ
E	100μ
F	200μ
G	300μ

FIG. 4.11 Contours of Constant Strain Accumulation Rates on the Bree Diagram (Mild Steel)

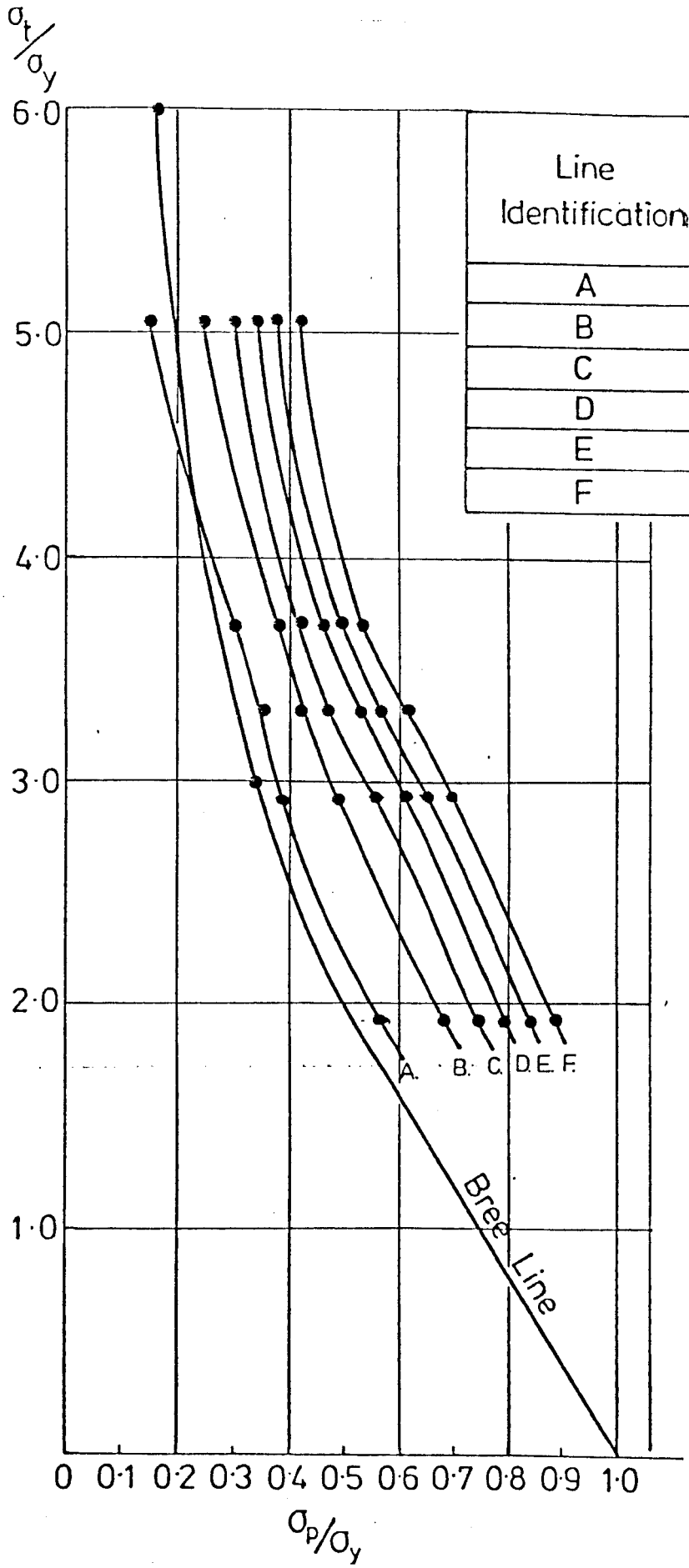

Line Identification	Experimental Total Strain Accumulation/μ After 80 Cycles
A	1000
B	5000
C	10,000
D	15,000
E	20,000
F	25,000

FIG. 4.12 Contours of Constant Total Strain Accumulation on the Bree Diagram (Mild Steel)

plotted on the Bree Diagram. Firstly it can be seen that the contours are all nearly parallel to the Bree line for the onset of ratchetting with the line for 1000μ accumulation being the closest. The equal separation between the contours at and above 5000μ show a nearly linear relationship with the σ_p/σ_y values. This figure also shows steeper slopes at larger σ_t/σ_y values. This may mean that in a design within a limited total accumulated strain, a small variation in σ_p/σ_y will produce a larger variation in allowable σ_t/σ_y values than when σ_t/σ_y values are small (that is, at the lower part of the diagram). This is a fortuitous characteristic in a practical situation because at large cyclic thermal stresses, the pressure stresses are not unduly compromised.

In conclusion, the experimental results have shown that the technique used in representing cyclic thermal loading by means of cyclically imposed curvature bending and the continuous pressure loading by constant axial loading is a viable one. The essential agreement that is required lies in showing that the experimental ratchetting boundary is in accord with the theoretical prediction. The primary objectives of this series of tests have been achieved and the next experimental program is to obtain experimental data for Type 316 stainless steel.

4.4 Ratchetting Tests on Type 316 Stainless Steel at Room Temperature

4.4.1 The Test Rig (2)

A second test rig was designed and constructed from the experience acquired from operating the previous rig. Although the conceptual design of the rig remained unchanged, improvements were made to remove some of the shortcomings of the previous rig. The main improvements were the inclusion of a power drive and automation of some of the data logging operations. The design was conceived to allow for the future use of the rig in elevated temperature testing while maintaining as many as possible of the existing components. The details of the modifications that were incorporated into the rig for elevated temperature tests will be described in the next section (4.5) in which ratchetting tests of Type 316 stainless steel at 400°C are described.

The rig, which is shown in Fig. 4.3, consisted of two symmetrical halves. Each half consisted of two pulleys, a chain and a weight carrier which hung from the structure. The chain which ran over the two pulleys transferred the tension due to the weights onto the strip. On the strip end of the chain, a clamping block and holding tackle formed the link between strip and chain. The clamping block gripped the strip while the holding tackle connected the clamping block to the chain. All the pulleys were mounted in pulley blocks which were freely adjustable on a tubular cross member spanning two vertical pillars. Adjustment of the pulley blocks allowed the chain and strip to move vertically. The pulley blocks were locked in position with split collars.

The wheel shaft at the centre of the rig was supported by two bearing pedestals. The shaft rotated within two needle bearings which were mounted in the pedestals. A thyristor controlled D.C. motor having a continuous speed variation from 0.2 to 0.006 revs per second drove the

wheel through a gear train. The driving train mechanism which is shown in Fig. 4.4 begins from the driving disc which was keyed to the motor shaft. A connecting rod was mounted at a distance from the centre of the driving disc at the lower end and linked to a rack via a universal joint at the upper end. This converted the rotary motion of the motor to the reciprocating motion of the rack. The rack meshed with a pinion gear wheel which was on the main wheel shaft thereby causing the test wheel to oscillate from one angular limit to another. The travel or stroke of the rack directly controlled the angular range of the wheel. The angular range of the wheel could be controlled to a limited extent by moving the connecting position of the connecting rod in the driving disc along its radial slot. In practice, a fixed position was taken and there was no necessity for adjustment.

Most of the wheels were 1 inch (2.54 cm) thick mild steel plates having flanges at the rims to prevent the strip from running off the wheel. Other wheels, particularly those of small radii, were made as a single unit. In this unit, there were four wheel sizes. The rim surfaces of all wheels were machined to normal machining tolerances of 0.001 inch. In tests, the strip rested on the rim surface and did not contact the sides of the flanges.

The wheel, strip, chains and pulleys were designed to lie on the same vertical plane to reduce the transverse or edgewise bending of the strip. This was achieved by mounting all the pulleys on the same cross member which was supported on two pillars. These were located on a base plate which was machined flat after fabrication. The wheel was attached to a boss which was keyed to the shaft and located and locked in position. No wobble or swashing of the wheel were detected during rotation.

Friction was reduced on the shaft and pulleys by mounting in needle

bearings. This was done primarily to remove juddering of the wheel at low speeds particularly at the end of rotation. Secondly, it must be noted, friction on the pulleys would cause more tension in the strip over to that due to the weights alone. Friction on the moving parts such as the rack, pinion and sliders were reduced in the usual way by applying grease.

Because the angular range was fixed at 108°, changing a wheel size during experimentation involved a number of adjustments. A larger wheel required a longer stroke or test length of strip and would require greater travelling distance for the weight carrier. To compensate for this, cross-members on which the pulley blocks were mounted were adjustable for height. The displacement measuring transducers were mounted on beams which were also adjustable vertically and horizontally.

The gear train design permitted the driving motor to rotate in one direction only while the test wheel oscillated from one stop to another. This has a number of advantages. Possible complications such as overheating of the motor were eliminated at low 'stop and reverse' speeds. Also the installation of microswitching circuitry that would be necessary for stopping and reversing the motor were not necessary. Furthermore, the exact step positions of the wheel may not have been repeatable since this would have depended on the angular momentum of the wheel when the microswitch was activated. The stopping will also be likely to be more abrupt. Although the bridge network for the displacement measuring transducers were designed to ignore small slippages of the strip and measure only its extension, its effectiveness would be considerably impaired by abrupt halts and large amount of variation in stopping positions. Finally, the gear train design produced a sinusoidal angular velocity variation with time which meant that the velocity decreases gradually to zero at the end of rotation. It also

ensured that the stop positions were repeatable for most of the motor speeds selected in the tests. However, the mechanism had an acceleration characteristic which is sinusoidal and maximum when the velocity was zero. In practice strain measurement on the strip away from the test section showed that the strain fluctuations during rotation were negligible. This also showed that the restraints due to pulley friction were negligible and had little effect on the strains on the strip. This was a necessary condition for these tests.

At particular angular velocities, the weight carrier had a tendency to swing in an harmonic manner. To remove the swing, two pairs of wires were attached and tensioned along the sides of the carrier path. Pairs of smooth guide rings were stringed along the wires and attached the carriers thereby damping the oscillations. This simple expedient removed the swinging without adding to the friction of the pulleys.

The displacement measuring transducer assemblies which were described in section 4.3.2 measured only the extension of the strip. They were mounted on two horizontal cross bars which were in their turn mounted on two vertical posts. The assemblies moved in slots in the cross bars and the vertical posts each had a row of holes through which the cross bars could be bolted.

4.4.2 Ratchet Strain Measurement

The method of measuring the strain accumulation was similar to that of the previous section and was fully described in section 4.3.2.

4.4.3 Instrumentation

The output from the displacement transducers were sensed by a Bruel and Kjaer (or B & K) strain indicator Type 1526 which provided a digital display of the strain and two analogue output channels for display of

data and a digital output port for data acquisition. The analogue output channels were at times used for observation of strain-time dependent behaviour during preliminary tests. A Rikadenki chart recorder provided a permanent record of the output of the displacement transducer assembly during ratchetting test. The records which were line traces joining the minimum and maximum oscillation of strain during each cycle were used as the data base. The measured length of the traces represented the total strain accumulation after scaling by the appropriate chart and displacement transducer calibration factors. A cycle count was kept by an electronic counter which was triggered at every cycle via a micro-switch installed at the lower extremity of the rack travel.

4.4.4 Specimen Preparation

The Type 316 stainless steel material used in the tests was obtained in coil form from a commercial supplier. Specimens were cut from the coils in lengths suitable for the wheel sizes used. Ten specimens were cut for each wheel size although only seven tests were planned. Eight wheel sizes were used to give an even spread of data. In addition to the 80 specimens thus prepared, some extra lengths were prepared for initial trials and expected wastage.

After the specimens were cut, they were straightened mechanically by bending in the opposite direction of the original curvature. The strips were subjected to heat treatment at the solution treatment temperature of 1050°C (1950°F) for an hour and allowed to cool in the furnace. A vacuum furnace was used and during cooling, an atmosphere of nitrogen was introduced. This is a typical solution heat treatment widely used for this alloy and now recommended in BS 5500 (9). The vacuum heat treatment prevented oxidation and left the specimens in good condition. The specimens were laid horizontally on a flat plate and the

longer specimens were hung vertically in the furnace. This produced reasonably straight specimens after heat treatment.

A chemical analysis of the specimens was carried out after heat treatment and the following percentage composition was analysed. Carbon - 0.062, Nickel - 10.8, Molybdenum - 2.13, Chromium - 16.8, Titanium - 0.018 and Niobium - 0.01. Reference handbook data confirmed this as that of Type 316L stainless steel.

The specimens were all of dimensions 0.016 by 0.199 in. (0.4 by 5.1 mm). Samples were subjected to tensile tests to determine the stress-strain behaviour. The first of two tests was conducted under slow loading conditions in which loads were applied only after cold creep has run its course. The second test was carried out without waiting for creep strains to become established. Both tests were carried out by dead weight loading on strain gauged specimens and were hence load controlled tests. Strain controlled tests were also considered but were not conducted for a number of reasons. The strain rate is known to be very influencial on the resulting stress-strain response of stainless steels. A simple analysis showed that the strain-time behaviour of the different material points on the strip during progressive bending to a curvature from straight is complicated. The strain rate is at a maximum on the outermost surface and decreases linearly towards the neutral axis of the strip and this is dependent on the cyclic speed and the curvature of bending. This has the implication that for each wheel size (or σ_t/σ_y value), there is a specified stress-strain characteristic due to the different strain rate experienced. It was decided that for its complications, the increased effort would not yield useful results.

Cyclic tests involving reversed or compression loadings were not

conducted. These tests are admittedly very important for cyclic hardening or softening information which can be used for analysing ratchetting results from the tests. The main problem and obstacle to these tests was that the strip will buckle under compressive loading.

A decision was therefore taken to use simple load controlled stress-strain properties. The stress-strain characteristics of the 'fast' and 'slow' tensile tests are shown in Fig. 4.13. Based on yield strength defined as a first departure from linearity: a 'slow' yield strength of 75.0 MN/m^2 was measured. The corresponding 'fast' yield strength was 75.4 MN/m^2. The 'slow' tensile test took two days to complete while the 'fast' test took a few hours. Most ratchetting tests of up to 1000 cycles cycling at a rate of 4ls per cycle take up to 12 hours to complete and it was decided that the fast tensile test data would be most representative of the strain rates involved. Fig. 4.13 also shows the 0.1 and 0.2% proof stresses and the yield stress based on a linear kinematic hardening fit to the 'fast' tensile stress-strain curve. These values will be referred to in the discussion of the results of ratchetting tests.

4.4.5 Test Procedure and Planning

A number of preliminary tests were firstly conducted to ascertain the best loading procedure. The first few stages of setting up the strip were similar to that for the mild steel strips described in section 4.3.5 but the later stages were more involved. Initially the wheel size and weight were decided and the wheel was installed on the wheel shaft. The wheel was rotated until it was at one of the extreme positions ready for the placement of the strip. The strip which was already clamped to clamping blocks was linked to the chains by the tackle and the required weights were loaded onto the load carriers.

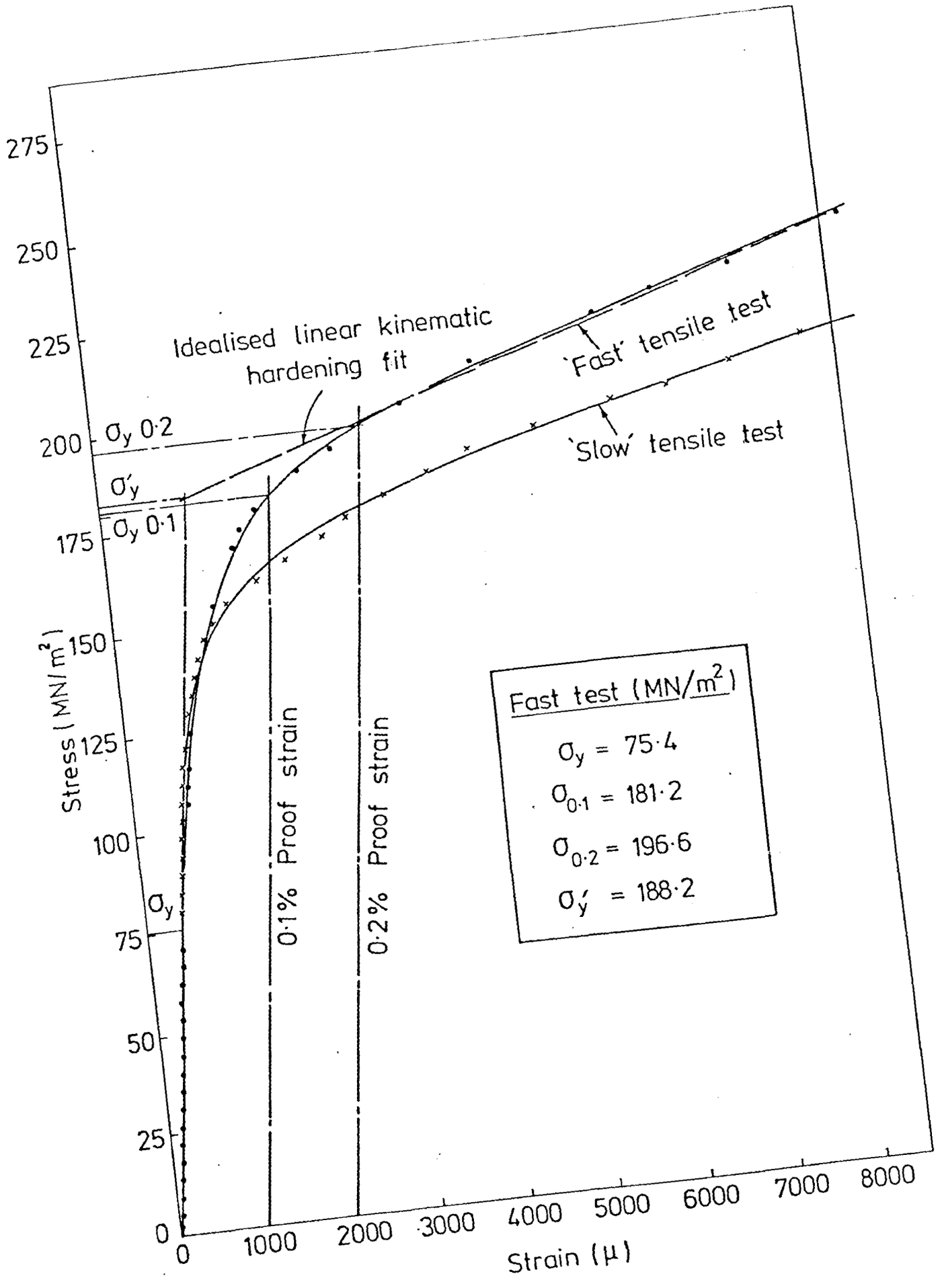

FIG. 4.13 Two Tensile Tests on Type 316 Stainless Steel Strips and Some Yield Stresses

The contacting arms were clamped onto the strip such that they were in position to contact the displacement transducers. After clamping, the transducer beams were aligned until the correct sensitivity setting was achieved. The cycle counter and the strain indicator were set to zero, and the calibration of both the displacement transducer and the chart recorder were noted. The driving motor was switched on to commence the test. After 1000 or more cycles, the test was stopped and the chart paper was endorsed with all the relevant details of the test. This was repeated with a new strip and a new load. When the required load range had been covered the next wheel was installed.

The next stage after the actual test was to process the results which was in a form of a trace on chart paper. The trace had to be digitised in order to obtain quantified data for analysis. Digitisation was carried out on the Ferranti Freescan Digitiser at the University computer laboratory which converts graphical information into digital form for subsequent processing by the mainframe computer. In using the digitiser, the trace was regarded as a graph and digitisation was carried out normally. The mode of operation and the necessary instruction for operating and using the software packages for replotting and data analysis in the Liverpool 1906S computer system is given in the guide 'A Guide to the Digitiser' (88). Briefly, the devices which make up the Ferranti Digitiser are: a large drafting board and control console, a movable cursor, a keyboard unit for input of text and control instructions on the tape and a paper tape punch. In use, the graph or diagram to be digitised was taped onto the drafting table and the movable cursor was used to pinpoint the features on the diagram through a cross hair window. By depressing a button on the cursor, the built-in co-ordinate system resolved the position of the cross hair on the cursor into the x and y co-ordinates with respect to

a datum point previously set by the user. The x, y co-ordinate was then immediately punched onto paper tape. Using the many options available on the digitiser, the incremental and absolute systems of co-ordinates can be selected. Also the speed of digitisation can be 'discrete' (for controlled point by point digitisation) or a 'fast stream' of 10 points per second (for curve tracking digitisation). The keyboard is used for keying in instructions on the tape such that it contains job input and routine instructions for reading in and processing by the computer using existing software options and user programs. The resolution of the system is 0.001 inch.

Digitisation on the test output was based on the absolute mode for convenience. The datum was set at the first cycle on the chart trace. The 'discrete' option was chosen to digitise at every 10 cycles. This reduced the chart trace information for 100 data points, each point thus representing 10 cycles. The y co-ordinate represented the strain accumulation and the x co-ordinate the tenth cycle position on the trace. The factors for converting the y co-ordinate into the true strain accumulation on the strip is given by

true strain accumulation = y (in) x chart recorder calibration C_R (μ/in) x transducer beam calibration C_T (in/μ) $\div$ length of test section of the strip L (in)

Since, $y \times C_R$ = strain (μ) indicated by B & K strain indicator

and $(y \times C_R) \times C_T$ = extension (in) of the strip measured by displacement transducer

therefore, $(y \times C_R \times C_T)/L$ = extension (in) divided by test length

= true strain on the strip

The chart recorder was usually calibrated at 100μ/in and the test length of the strip was fixed by the formula of $L = \pi r.(108/180)$ for a wheel of radius r.

By inputting the calibration factors (C_R and C_T) and the test length (L) into the tapes, the actual or true strain was computed. This was carried out by a program written by the author. The program reads in the tape co-ordinates and computes lists and plots the data against the cycle number. Plotting was made on good quality paper via a Calcomp 936 Drum Plotter. The software for plotting consisted of a subroutine library called GHOST (for Graphical Output System) which is fully documented by (89) which contain the most commonly used graph plotting facilities such as labelling, axes notation and logarithmic-axis scaling. An example of such a plot is shown in Fig. 4.14 for $\sigma_t/\sigma_y = 2.67$ and $\sigma_p/\sigma_y = 1.55$. All the test results were digitised and read into the author's user-file-store. This facilitated the plotting of the results in different ways so that the relationships between different test parameters could be examined. For example, when plotting the computed incremental strain per cycle against the log of the cycle number, shown in Fig. 4.15, it is seen that incremental strain approaches a finite value asymptotically. Therefore the digitised data when stored in a computer filestore enable one to analyse data more rapidly.

Ignoring a few preliminary tests, a total of 57 test locations on the Bree Diagram were investigated. These were subdivided into eight different wheel sizes and an average of seven different tensile loadings at each wheel size. The wheel radii and the calculated combination of σ_t/σ_y and σ_p/σ_y of the tests are tabulated in Table 4.2. σ_y is based on first yield on the 'fast' stress-strain curve taken as 75.4 MN/m^2. The σ_t/σ_y values ranged from 1.67 to 9.09 while the σ_p/σ_y values ranged from 0.33 to 1.84. The tensile load includes the weight of the clamping

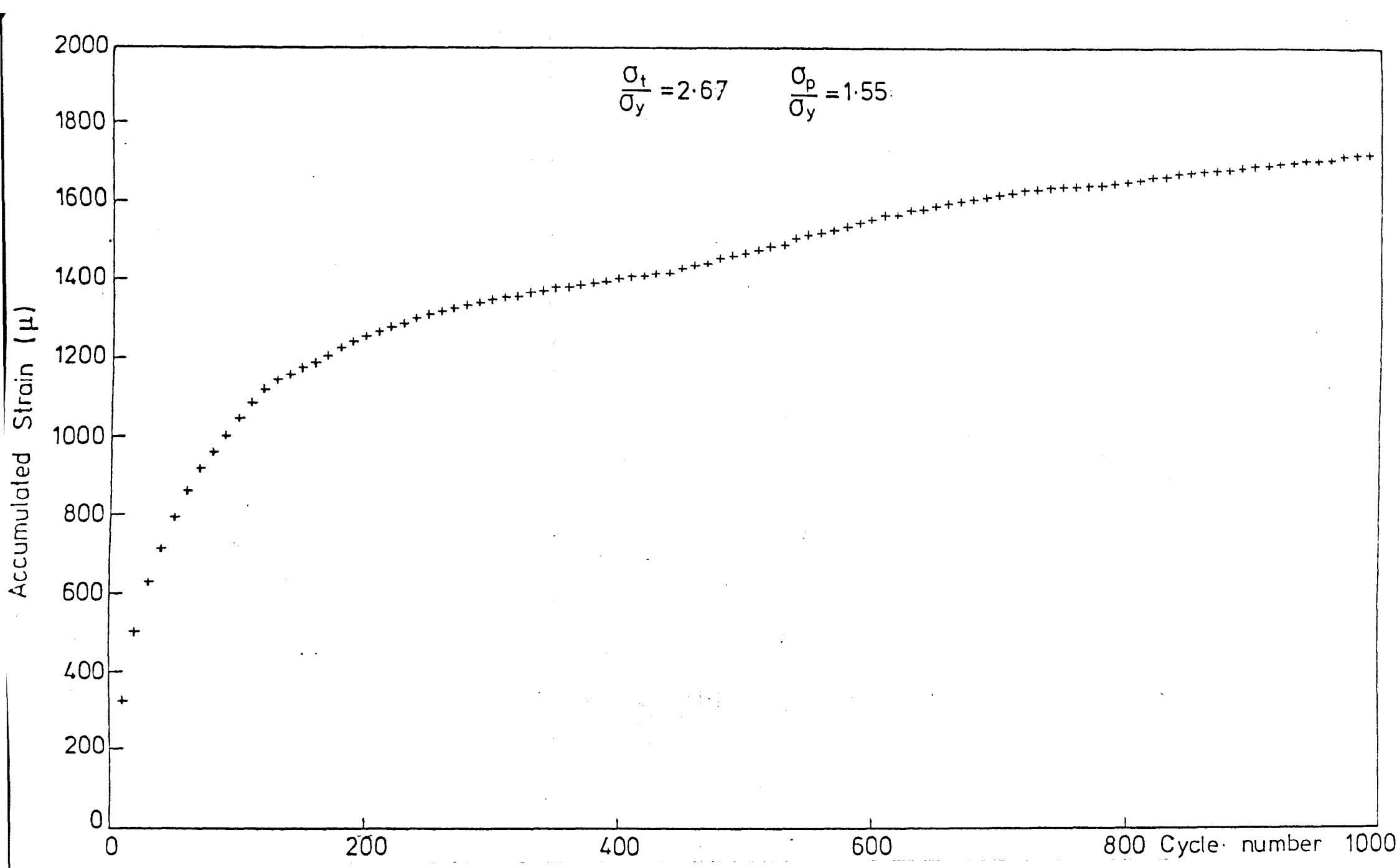

FIG. 4.14 Experimental Accumulated Strain up to 1000 Cycles (Type 316 Stainless Steel)

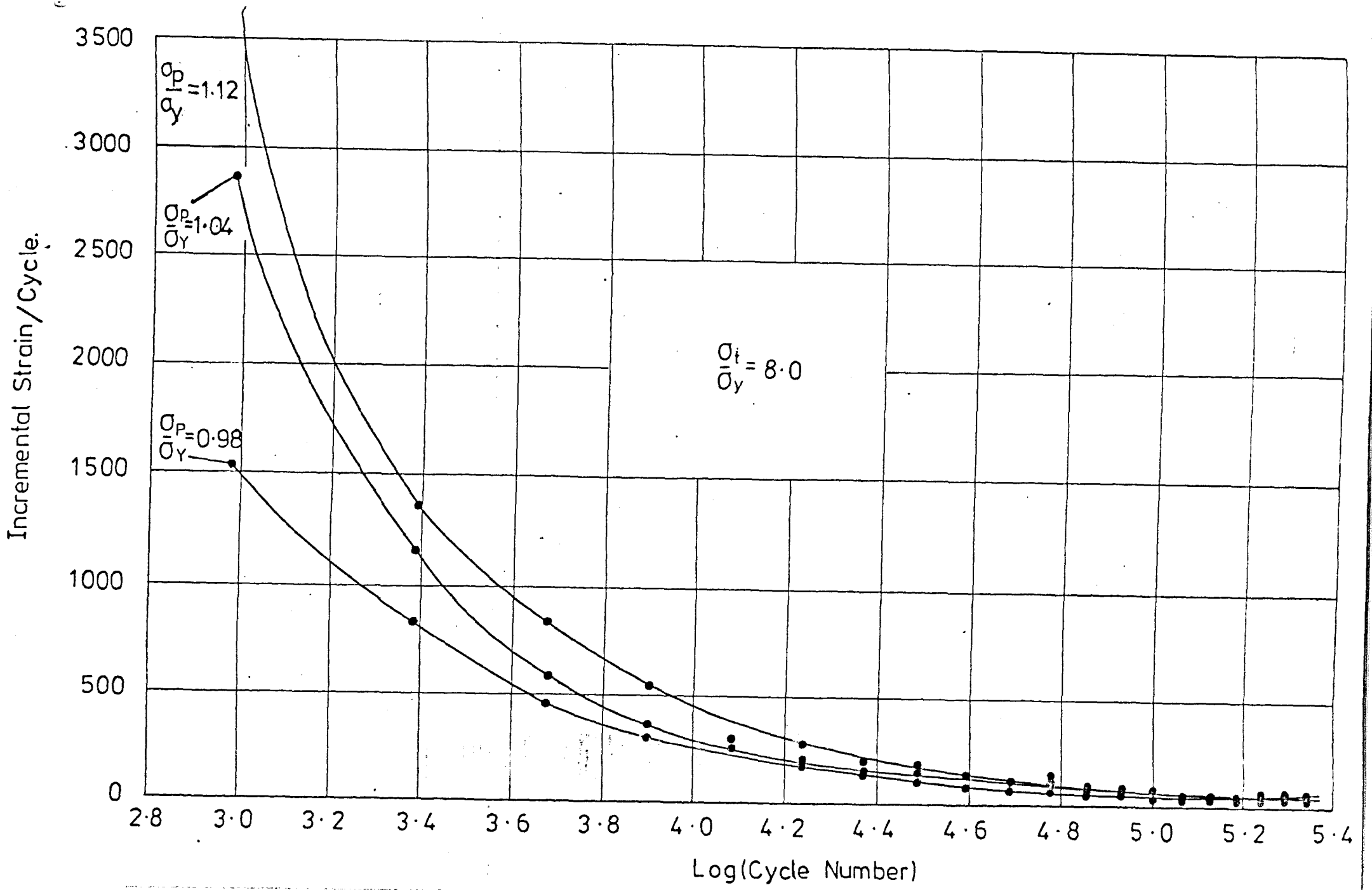

FIG. 4.15 Experimental Incremental Strain Against Log of Cycle Number (Type 316 Stainless Steel)

r/in	σ_t/σ_y	σ_p/σ_y							
2.2	9.09	0.33	0.40	0.47	0.55	0.69	0.83	0.98	1.12
2.5	8.00	0.55	0.62	0.69	0.83	0.98	1.04	1.12	
2.875	6.96	0.55	0.69	0.83	0.98	1.12	1.26		
3.313	6.04	0.55	0.62	0.69	0.83	0.91	0.98	1.12	
4.0	5.00	0.69	0.76	0.83	0.91	0.98	1.12	1.26	1.41
5.0	4.02	0.83	0.91	0.98	1.12	1.26	1.34	1.41	
7.5	2.67	0.69	0.83	0.98	1.12	1.26	1.41	1.55	1.70
12.0	1.67	0.98	1.12	1.26	1.41	1.55	1.70	1.84	

thickness of strip = 0.016"
1st yield strain = 400μ
1st yield stress = 75.4 MN/m^2

Table 4.2 Stress Combinations of Ratchetting Tests on Type 316 Stainless Steel

block, half the weight of the chain and the weight carrier which was approximately 4 lbf (17.8 N). The equal distribution of σ_t/σ_y values involved wheels of diameters ranging from 4.4 in (0.11 m) to 24 in (0.6 m) and because of the inverse proportion of σ_t/σ_y to diameter, there is a predominance of smaller wheels than larger ones.

All tests were cycled at a rate of 41 s/cycle up to over 1000 cycles. This rate was chosen because at this speed, there was less vibration and disturbance on the rig. Tests exploring the effects of the variation on the cycle time was also performed afterwards.

4.4.6 Results and Discussion

Before performing this series of ratchetting tests, preliminary tests were conducted to ascertain the repeatability and to establish operational experience of the rig. These objectives were satisfactorily achieved. The complete set of results consisted of 57 ratchet tests each yielding 102 lines of digitised output listing. In order to reduce the number of pages, the results are shown in compacted and tabulated form and in the form of graphs for comparison of the data. Firstly, some of the raw data is shown in Tables 4.3 and 4.4. In Table 4.3, the total strain accumulated after 200, 400, 600, 800 and 1000 cycles are shown for their respective σ_t/σ_y and σ_p/σ_y test conditions for every test in the series. Table 4.4 shows the rate at which strain would accumulate per cycle at various cycle numbers beginning with the 1st to the 200th cycles in steps of 50 cycles and from the 200th to the 1000th cycle in steps of 200 cycles. These are again listed against the respective test conditions which consist of four equally distributed σ_t/σ_y steps which is half the complete complement of results so as to reduce the number of graphs to be plotted. The smaller steps of 50 cycles

Stress Combinations		Total Strain Accumulated (μ) at the end of Cycle				
σ_t/σ_y	σ_p/σ_y	200	400	600	800	1000
9.09	0.40	216	254	299	243	384
	0.47	80	97	113	127	139
	0.55	195	234	250	263	275
	0.69	690	882	909	1127	1236
	0.83	3755	4406	4481	4521	4704
	0.98	9177	9462	9578	9600	9613
	1.12	12545	13954	14314	14410	14745
	1.26	17364	18950	19680	20130	20430
8.00	0.55	121	146	144	143	148
	0.62	121	188	189	194	175
	0.69	323	394	448	464	514
	0.83	1020	1348	1566	1691	1790
	0.98	4560	5183	5482	5671	5848
	1.04	6756	7317	7671	7866	7970
	1.12	8476	9268	9579	9817	9921
6.96	0.55	241	298	307	304	293
	0.69	393	480	517	542	562
	0.83	906	1107	1240	1297	1343
	0.98	2600	3238	3614	3865	4000
	1.12	8636	9417	10045	10403	10565
	1.26	12556	13749	14081	14395	14574
6.04	0.55	235	244	237	250	244
	0.62	111	122	133	144	133
	0.69	561	622	650	708	759
	0.83	465	572	651	744	814
	0.91	1155	1427	1613	1749	1811
	1.12	6330	7069	7372	7493	7558

Table 4.3 Strain Accumulated at Various Cycle-Numbers for all Type 316 Stainless Steel Tests at Room Temperature

Table 4.3 Continued ...

σ_t/σ_y	σ_p/σ_y	200	400	600	800	1000
5.00	0.69	131	133	135	130	130
	0.76	185	189	193	197	199
	0.83	484	516	512	508	512
	0.91	500	586	610	639	668
	0.98	742	857	934	995	1033
	1.12	2429	3060	3516	3791	3912
	1.26	7253	8071	8500	8736	8936
	1.41	11750	12640	13190	13520	13790
4.02	0.91	62	77	77	75	65
	0.98	178	232	272	297	305
	1.12	319	423	493	549	598
	1.26	2349	3102	3548	3916	4163
	1.34	4614	5367	5843	6145	6325
	1.41	7300	8313	9157	9542	9765
2.67	0.69	103	115	121	125	126
	0.83	78	87	92	96	96
	0.98	129	142	152	158	166
	1.12	246	265	278	290	297
	1.26	288	422	495	533	575
	1.41	2613	3231	3501	3679	3833
	1.55	4446	5578	6083	6386	6693
1.67	0.98	65	84	65	67	63
	1.12	95	114	135	151	162
	1.26	150	190	212	241	248
	1.41	134	186	226	253	274
	1.55	551	670	776	867	957
	1.70	4726	5713	6553	7067	7350
	1.84	6384	7408	8000	8462	8756

Stress Combinations		Strain Accumulation (μ) per Cycle at								
σ_t/σ_y	σ_p/σ_y	1	50	100	150	200	400	600	800	1000
9.09	0.55	10.5	0.4	0.0	0.3	0.0	0.0	0.0	0.0	0.0
	0.69	21.5	2.3	2.0	1.2	0.4	0.0	0.9	0.3	0.2
	0.83	104.4	15.8	7.9	7.6	4.5	0.0	0.0	0.0	0.0
	0.98	176.5	11.1	3.9	3.9	3.1	1.1	0.3	0.0	0.0
	1.12	483.8	51.8	17.6	13.8	10.9	2.4	1.6	0.1	0.7
	1.26	741.7	51.9	21.0	16.6	11.5	4.8	5.2	1.8	2.2
6.96	0.69	10.5	1.5	1.8	1.0	0.7	0.4	0.4	0.0	0.0
	0.83	17.4	3.4	3.0	1.5	1.3	0.8	0.3	0.6	0.0
	0.98	39.5	13.8	10.3	4.7	4.3	2.3	0.9	0.4	0.8
	1.12	317.9	31.4	11.9	7.6	6.7	2.7	2.0	1.7	1.4
	1.26	526.7	38.6	19.9	6.5	9.0	3.7	1.3	1.0	1.0
4.02	0.98	4.5	0.8	0.0	0.4	0.0	0.2	0.6	0.0	0.0
	1.12	5.6	1.5	0.8	0.6	0.6	0.4	0.4	0.3	0.0
	1.26	28.3	11.5	9.0	7.4	5.9	2.4	2.0	1.3	1.2
	1.34	104.5	22.7	8.3	6.9	5.1	3.1	1.8	1.3	1.1
	1.41	187.4	30.0	14.8	9.2	6.5	3.4	2.8	2.1	0.7
1.67	1.26	2.9	1.0	0.4	0.1	0.0	0.1	0.2	0.1	0.1
	1.41	2.4	0.8	0.2	0.1	0.3	0.3	0.2	0.1	0.0
	1.55	9.4	2.7	1.1	1.0	0.8	0.7	0.8	0.5	0.4
	1.70	60.9	21.2	19.2	14.9	8.3	3.8	3.4	2.0	1.0
	1.84	123.6	34.4	10.4	8.5	6.1	3.8	3.1	1.4	1.1

Table 4.4 Rates of Strain Accumulation at Various Cycles Numbers for Four σ_t/σ_y Values and Several σ_p/σ_y Steps

were necessary to show the initial rapidly changing cyclic strain accumulation rate. The tables indicate that all the results have a similar pattern of strain accumulation and increment per cycle. Strain accumulates rapidly during the initial cycles and thereafter gradually decelerates towards zero strain increment which is classified as shakedown or alternating plasticity. Others decelerated towards a steady state positive strain increment which can be termed as indefinite or continuous ratchetting. Further discussion on these results will be based on figures shown later.

Firstly, Fig. 4.16 shows a set of typical results consisting of three σ_p/σ_y values at a constant σ_t/σ_y value which have been digitised and plotted on the Calcomp plotter and then traced. The plots show the trends shown by most ratchetting test results. These show evidence of 'continuous' ratchetting at large cycle numbers commencing at about the 500th cycle in this particular set. Also the initial strain accumulation rates were large but they depreciated very rapidly after the 100th cycle and thereafter approached the continuous or steady state ratchetting rates. The cycle number at which the steady state condition was reached was seen to vary with σ_p/σ_y magnitude. Generally, the lower σ_p/σ_y conditions induced steady state conditions at lower cycle numbers. Finally at large cycle numbers (>800) the steady state ratchetting rates are nearly equal for all three curves. Thus, based on this set of results, it appears that these rates are independent of the σ_p/σ_y loads and may be dependent on σ_t/σ_y loads.

Using the same set of results ($\sigma_t/\sigma_y = 4.02$ and $\sigma_p/\sigma_y = 0.98$, 1.12, 1.25, 1.34 and 1.41), the strain accumulation per cycle is analysed against cycle numbers. This analysis shows that 'shakedown' (here taken to include alternating plasticity) has occurred for two of the tests because the strain accumulation rate is reduced to zero after a

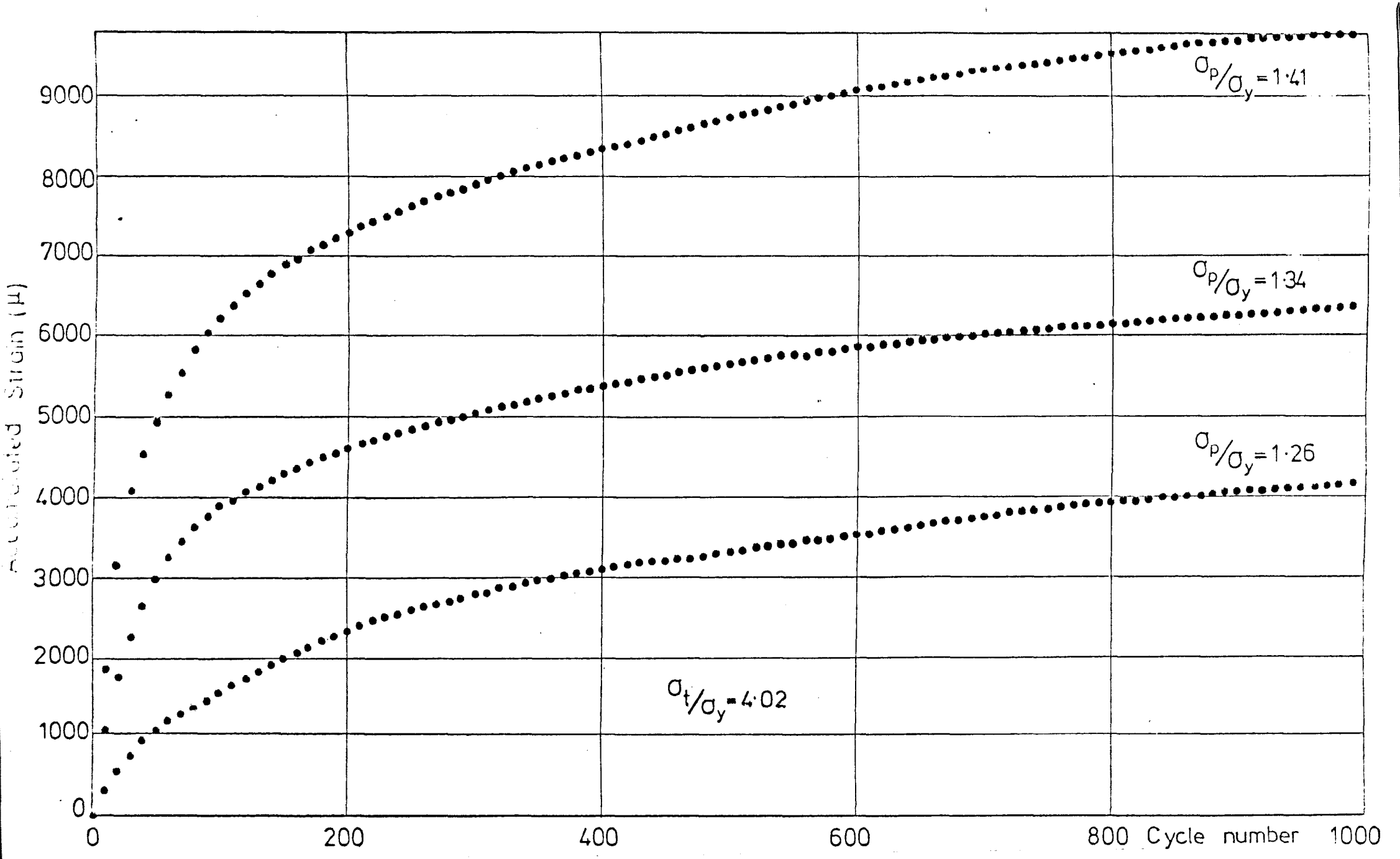

FIG. 4.16 Experimental Accumulated Strain up to 1000 Cycles (Type 316 Stainless Steel)

number of cycles. The curves for the other tests show a rapid decrease in the strain accumulation rates such that after about 200 cycles, the rates become common.

The initial strain accumulation rate is highly dependent on σ_p/σ_y and consequently determines the major portion of the total amount of strain accumulation. Then the ratchetting rate appears to be less influenced by σ_p/σ_y and the strain then accumulated is a minor part of the total accumulated strain. From data given in Table 4.4, showing the rates of strain accumulation for this later part ratchetting is strongly dependent on σ_t/σ_y.

Regarding the total strain accumulation, Fig. 4.17 shows curves of constant σ_t/σ_y plotted with the accumulated strain after 200 cycles as the y axis and σ_p/σ_y as the x axis. In this plot, a point (x, y) on the curve σ_t/σ_y will accumulate 'y' amount of strain after 200 cycles at a load of 'x', σ_p/σ_y. Each curve corresponds to one of the eight σ_t/σ_y levels tested. It is seen that for each curve, there is a linear portion at the larger values of σ_p/σ_y and a gradually varying portion at smaller values of σ_p/σ_y. For the range of σ_t/σ_y from 9.09 to 4.02, the linear portions tend to be parallel to one another and for σ_t/σ_y = 2.67 and 1.67, the linear portions appear to deviate from the others by having smaller slopes. However there is insufficient data for the σ_t/σ_y = 2.67 and 1.67 curves to be confident of the slopes. If this deviation is genuine, it may be speculated that the differences between Type R1 and R2 ratchetting may be the cause. Generally, the curves are similar to that of the mild steel ratchetting tests.

It is useful to know the number of cycles needed to accumulate say 2/3 of the total strain accumulated in say 1000 cycles. The ratio of the accumulated strain at intervals of 200, 400, 600, 800 and 1000

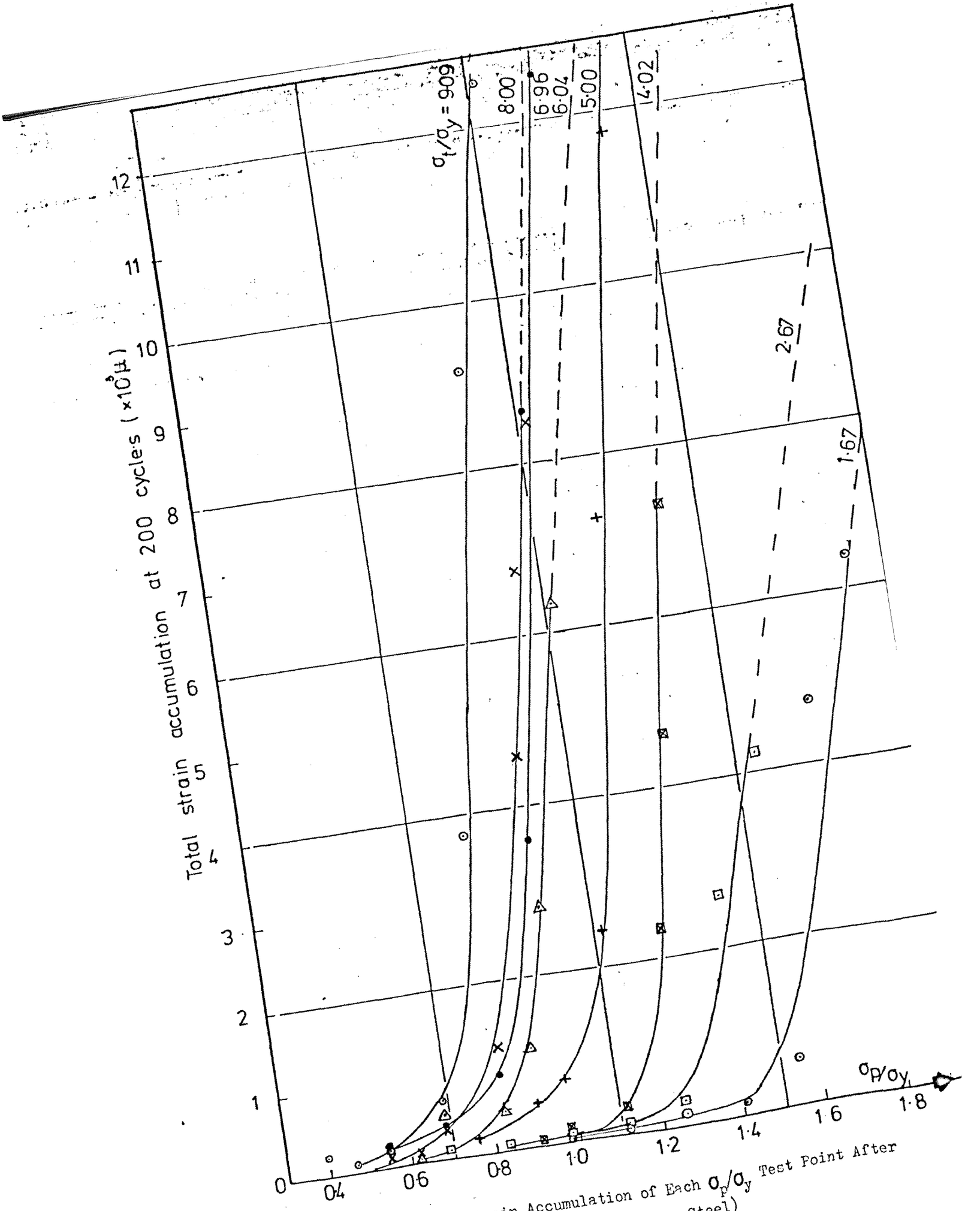

FIG. 4.17 Total Strain Accumulation of Each σ_p/σ_y Test Point After 200 Cycles (Type 316 Stainless Steel)

cycles to the final total accumulated strain at 1000 cycles is compared with various σ_p/σ_y and σ_t/σ_y combinations. In these comparisons, the major contribution of 67% (2/3) of the total strain at 1000 cycles is accumulated between 100 to 400 cycles.

The Bree Diagram for a strain-hardening material is not bounded at $\sigma_p/\sigma_y = 1$ as in the diagram for an elastic/perfectly-plastic material provided that σ_y is defined as some stress below the ultimate tensile stress. Fig. 4.18 shows the results of all the tests on a Bree Diagram. For tests conducted at various σ_t/σ_y and σ_p/σ_y values the boundary for ratchetting is defined as those locations where shakedown is or is not achieved within 100 cycles. Shown on this figure are the locations where shakedown was achieved within 100 cycles and those where it was not achieved even after 1000 cycles. Two sets of axes are drawn, firstly that using σ_y as the first departure from linearity and secondly that defining σ_y as

$$\sigma_y = 1.35.P_{0.2}^{*}$$

where $P_{0.2}$ signifies the 0.2% proof stress. This is the ASME III (3) recommendation

The values used are obtained from the 'fast' stress strain curve in Fig. 4.13. Also shown on Fig. 4.18 is the Bree ratchetting boundary assuming an elastic/perfectly-plastic idealisation based upon 200 MN/m^2. This figure has been chosen using the equal area criterion with the experimental 'fast' stress-strain curve.

Also, two contours are drawn in Fig. 4.18 representing the experimental contours at which 5000μ (0.5%) and 10000μ (1%) strain will be accumulated after 200 cycles. Therefore any operating point on the contours is expected to accumulate at most that amount of strain within 200 cycles. The contours do not follow the shape of the Bree boundaries

* $1.35.P_{0.2}$ corresponds to the stress restriction applied to Primary Local and Bending Stresses (that is $P_L + P_B \leqslant 1.5$ Sm). The value of $0.9\ P_{0.2}$ corresponding to 1.0 Sm has been suggested as more appropriate. This then considers the stresses are Primary membrane stresses only that is $P_M \leqslant 1.0$ Sm.

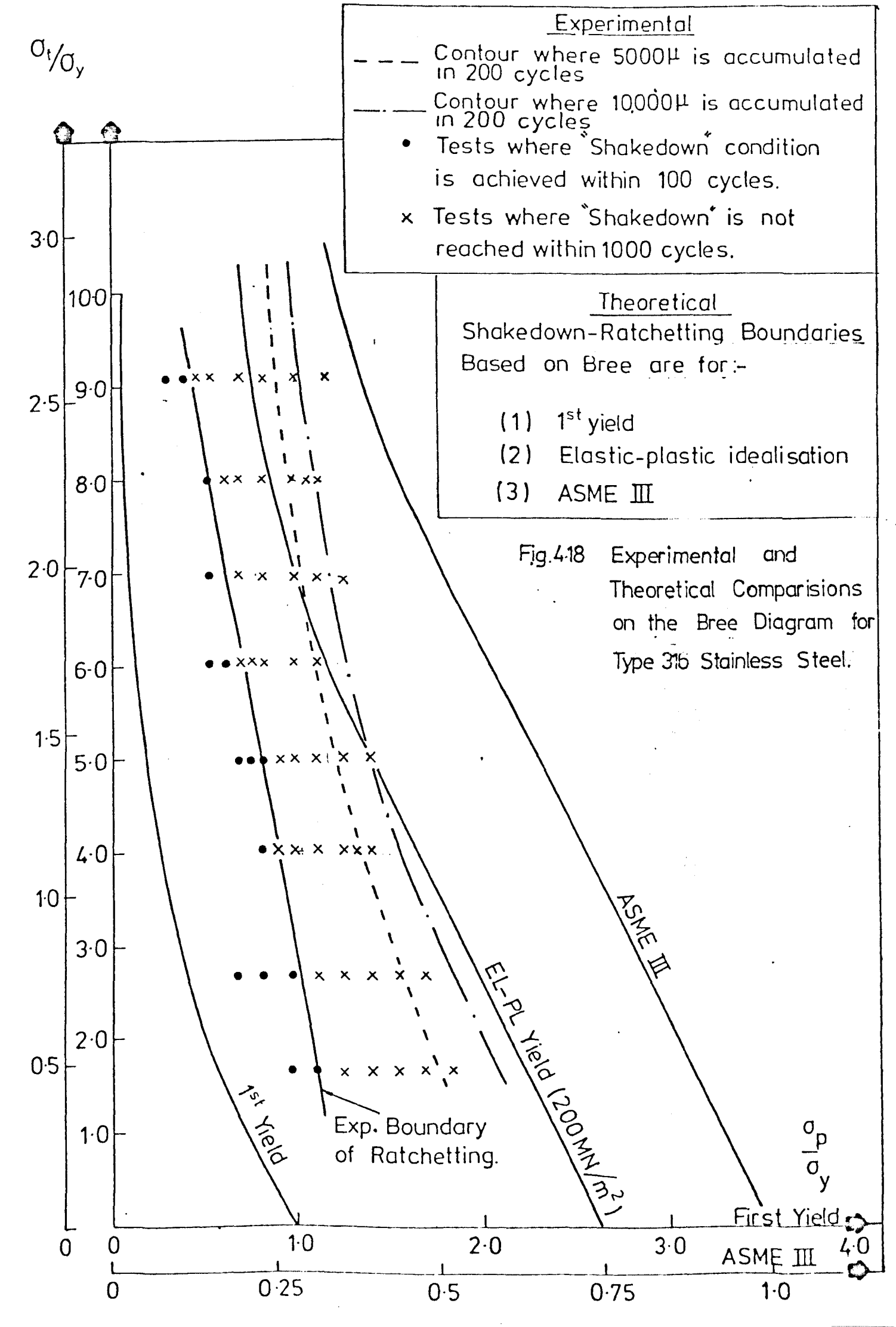

Fig.4.18 Experimental and Theoretical Comparisions on the Bree Diagram for Type 316 Stainless Steel.

based on any of the definitions of the yield stress. If the total accumulated strain is a design requirement the gradient of these contours above $\sigma_t/\sigma_y \simeq 5.0$ should be carefully considered. A small design change in σ_p/σ_y will clearly result in a significant change in the allowable thermal stress. It is also noted that the 1% strain accumulation contour lies inside the ASME III contour which is based on restrictions on the primary and secondary stresses. From Chapter 2, Section 2.3.1, the ASME III, N47 Code also allows for 1% strain accumulation calculated over the expected lifetime of the structure under consideration. The experimental data here shows that design based on strain limits may be the more conservative of the two restrictions.

Fig. 4.19 shows the effect of varying the cycle rate by the plotting of the strain accumulation against the number of cycles for four cycle rates of 8, 13, 22 and 41s/cycle. The results show that the primary effect is to change the rate of strain accumulation in the first 200 cycles. Then the rates of the accumulation of strain became closely similar. This latter observation shows that the operating mechanisms which cause the strain accumulation have reached a steady state. The mechanisms which cause the final strain accumulation at each cycle are complicated. For Type 316 stainless steel, it is to be expected that a number of phenomena such as the cyclic process of hardening, cold creep and rate of straining (cycle rate) effects operate and may even interact with one another. In the ratchetting tests, the resulting strain accumulation is the end result of the effects of the competing mechanisms mentioned above. These mechanisms act at various strengths each dependent on time, strain rate and the number of cycles and also the state of other mechanisms. A knowledge based on the behaviour of how these individual mechanisms operate has been investigated in uniaxial

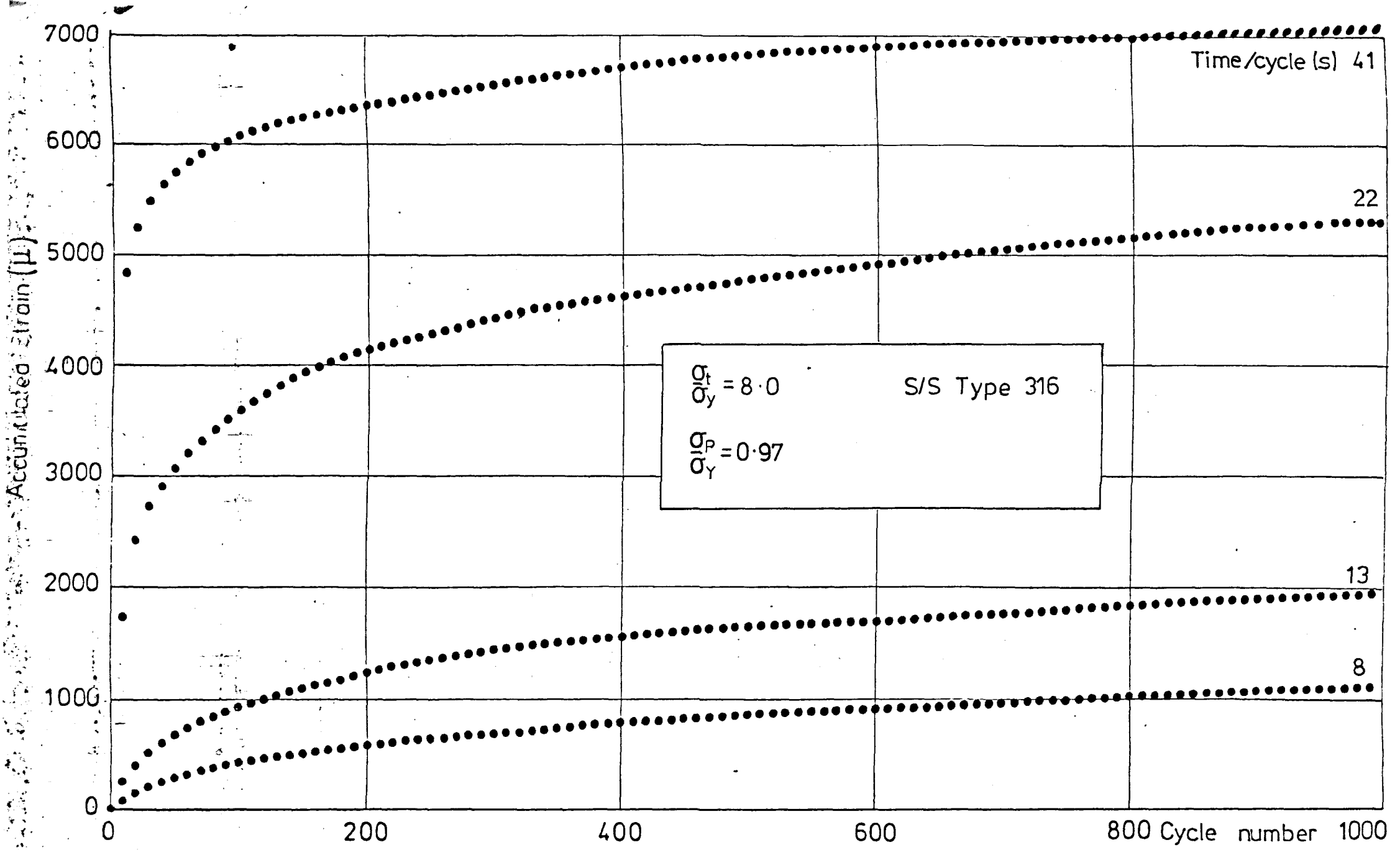

FIG. 4.19 The Effect of Cyclic Rate on Ratchet Strain Accumulation at the Same Loading Condition. (Type 316 Stainless Steel)

tests. Section 2.7.2, Chapter 2, reports on these developments. In subsection (1) and (6) hardening due to strain controlled cycling and strain rate in stress-strain tests have been shown to exist. In the ratchetting tests on the strip, hardening is dependent upon the number of cycles and the cycle rate. The cycle rate which affects the rate of straining on the various fibres of the strip thickness causes different levels of hardening within the strip. This form of hardening together with the cyclic hardening which is due to repeated cycling on each fibre alone quickly reduces the strain accumulation seen in the ratchetting tests.

It is also noted that in subsection (9) creep rates in a uniaxial test became reduced when the material was previously subjected to strain controlled pre-cycling as compared to an uncycled specimen. Also, it has been shown that in uniaxial load controlled cyclic tests, creep is observed during the maximum load duration but this decreases after some time. During the next cycle, creep is revitalized and the same phenomena is repeated each cycle. This tendency for revitalization of the propensity for creep gradually reduces with cycling.

The likely causes for the initial variation of strain accumulation in the four cycle rates can be attributed largely to cold creep which is the initially dominant mechanism. The faster tests therefore showed less strain accumulated/cycle. In the later cycles, the 'constant' strain accumulation rate may be caused by a steady state being reached between the competing mechanisms which are that of (a) a steadily reducing creep, (b) ratchetting due to plasticity and (c) increasing hardening. The above speculative explanation is not adequately supported by the scant material data that are quoted and the set of results shown in Fig. 4.19 also needs more comprehensive augmentation.

It has been noted that the variation of cycle rates needed in obtaining this set of results have reduced the repeatability of the tests. For this reason the results have been treated qualitatively.

Finally, a comparison is made between the experiments and the predictions of strain accumulation based on linear kinematic hardening material model. The predictions were made by a computer model written by the author. The results of the computations have been checked against the analytical results of Mulcahy (21) and shown to agree. The predictions are made on the assumption of a yield stress (σ_y') of 183.2 MN/m^2 and a linear hardening modulus (βE) where $\beta = 0.038$. Fig. 4.13 shows how β and σ_y' are defined against the 'fast' stress-strain curve. Table 4.5 shows the experimental strain accumulation at $\sigma_t/\sigma_y = 9.09$ and several values of σ_p/σ_y compared with the computation. The computation shows that the strain accumulation always ultimately reaches a state where no further strain is accumulated. This is a 'shakedown' state. The tabulations show that the predicted 'shakedown' strain accumulated reached after a small number of cycles were very much below the strain accumulated experimentally at the end of 1000 cycles. The strain accumulated experimentally at the cycle numbers at which shakedown was predicted were more in accord. For two cases (i.e. 39 and 44 lbf tensile loads) the comparisons were poor. Finally the strain accumulated during the first cycle were all less than predicted by an average of 50%.

Wheel Radius = 2.2 in. Tensile Load (lbf)	Prediction. Strain Accumulation (μ) at		Experiment. Strain Accumulation (μ) at		
	1st Cycle	Shakedown After ( ) Cycles	1st Cycle	Cycle at which Shakedown was Predicted	1000 Cycles
29	262	1085 (19)	104	1580	4704
34	589	2440 (22)	177	2034	9613
39	914	2796 (24)	484	3910	14743
44	1241	5151 (25)	742	10843	20430

Table 4.5 Comparison of Prediction Based on Linear Kinematic Hardening Model (taking a yield stress (σ_y') of 183.2 MN/m^2 and a hardening modulus (β) of 0.038) and the Experimental Results Obtained from One Wheel Radius and Several Tensile Loads

4.5 Ratchetting Test on Type 316 Stainless Steel at 400°C

4.5.1 Modifications to the Test Rig (2)

Major modifications were undertaken to adapt the room temperature test rig so that ratchetting tests could be performed at elevated temperatures. A heating system was designed and built around the rig and the data gathering system was upgraded and incorporated into a 'PET' microcomputer system. The 'PET' microcomputer was used primarily to monitor and control the temperature of the rig. Plate I shows the external view of the rig and microcomputer system.

A thermally insulated chest was built around the wheel and the strip. The size of the chest was large enough to include the largest 12" wheel and completely enclose the strip at all positions of movement. Openings in the chest allowed the wheel shaft, chains and displacement measuring arrangement to protrude. These openings were sealed where possible to reduce heat loss. The heat was supplied by means of recirculating hot air which was heated by the heater box containing six quartz bar heaters. The heater box was connected to the chest by ducting and air was forced to circulate by a centrifugal fan located near the exit duct on the chest. This closed loop air heated system is shown in Figs. 4.20 and 4.21. All components of the heating system were insulated on the inside with 3 in. thick 'hot board' insulation. A metal skin on the outside provided rigidity and support. The chest was made in several pieces which were removable for access in order to load the specimen and make other adjustments.

A microcomputer system based upon the Commodore 'PET' was developed to function as the temperature controller and data logger. The need for an advanced temperature control system was realized initially because of the complexity of the heating system and the accuracy of control

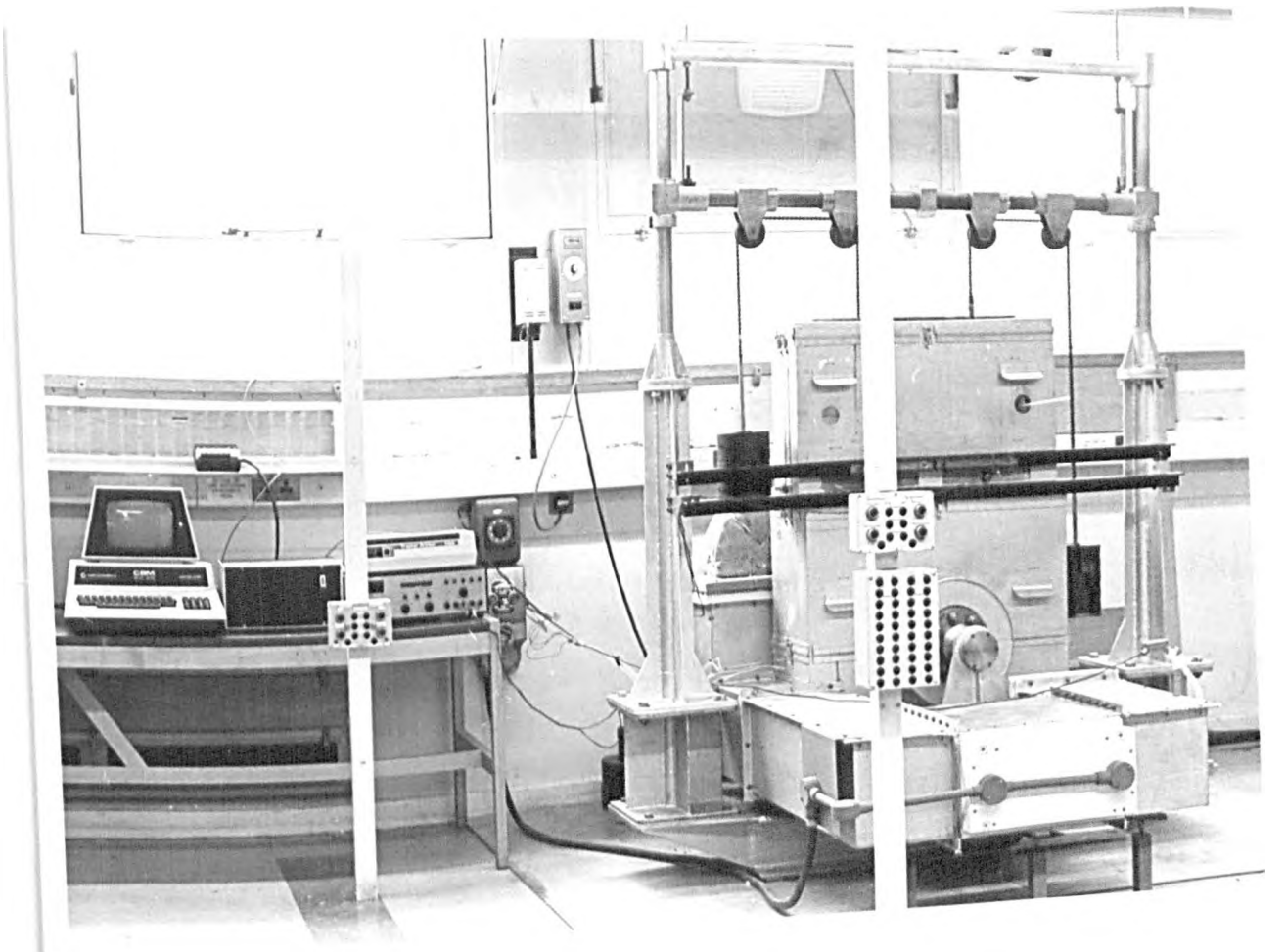

Plate 1. Fully Assembled Test Rig and Instrumentation for an Elevated Temperature Ratchet Test

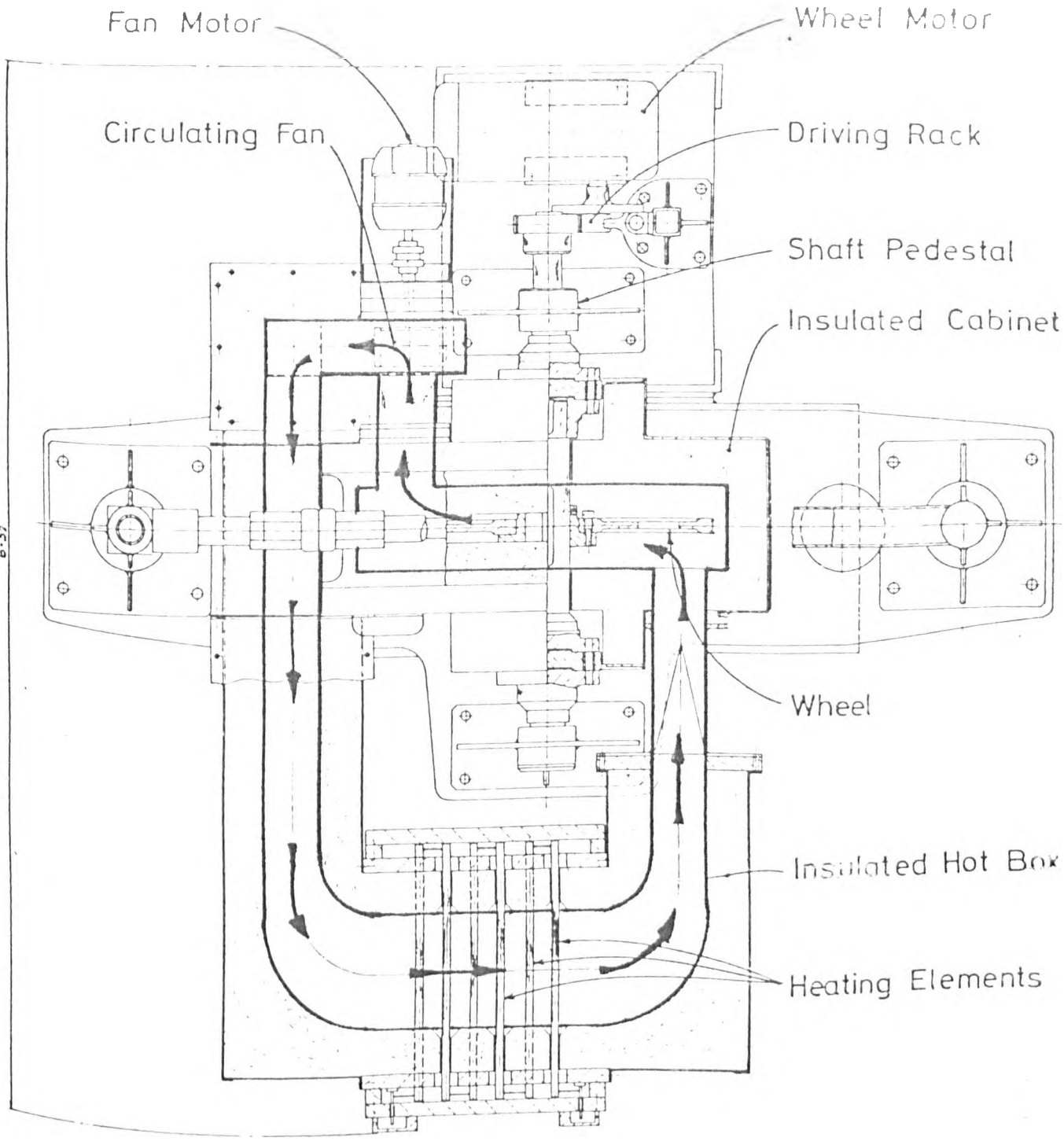

FIG. 4.20 Plan View of Elevated Temperature Ri , Showing Flow Path of Hot Air.

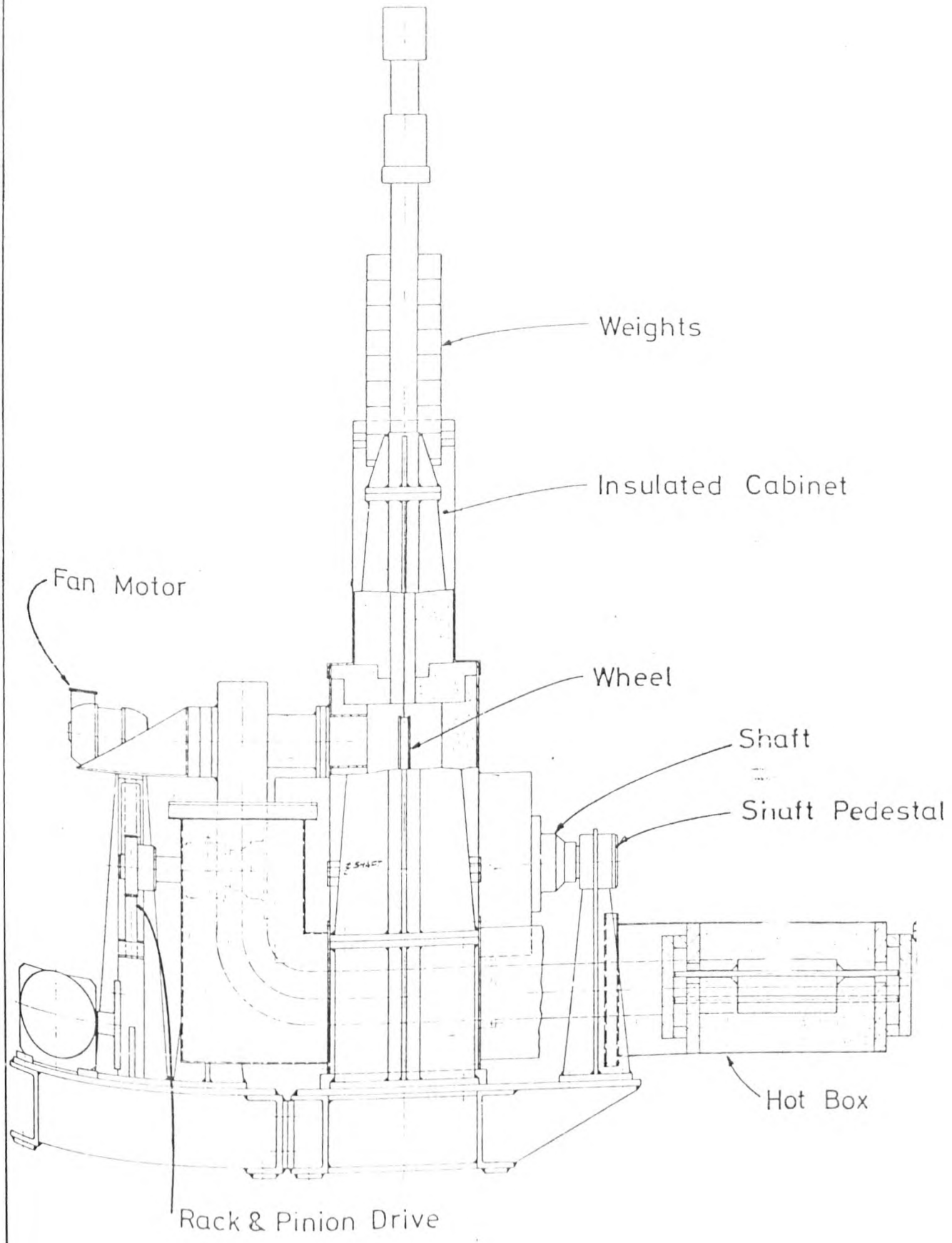

FIG. 4.21 Side View of Elevated Temperature Air

required. Intelligent temperature control has to be based on several temperature inputs at various positions in the chest and software incorporating an advanced control theory is usually required. For these reasons a microcomputer system was chosen. It was also capable of reading in, recording, and analysing strain data from the displacement transducer via the B & K strain indicator using appropriate software.

All the above functions of the system were dependent on an interface unit whose function was to convert and control the transfer of signals between the platinum resistance thermometer, strain gauges (known as input) and heater (output) and the 'PET' microcomputer. Heater power was regulated from the 'PET' via the interface unit by a thyristor controller. The design and other details of the interface unit is described in Ref. (90).

The complete rig was able to function automatically for prolonged periods when testing at large cycle numbers. A safeguard against damage due to runaway heating during fan failure was installed and utilized an independent heater power trip which was controlled by a Honeywell unit sensing a thermocouple located in the heater box.

4.5.2 Ratchet Strain Measurement

The method as used in Section 4.3.2 was employed together with an additional lever arm which protruded into an opening made in the insulated chest. The complete arrangement is shown in Fig. 4.22. It is seen that the strain gauged cantilever beam and the contact arm is retained. The lever arm was pivoted at its centre and had at the equidistant ends, contacting heads. These heads periodically made contact at both ends with the contact arm and the cantilever beam. This happened when the strip was at the end of its travel at each cycle. The strain accumulation was measured with the B & K strain recorder in

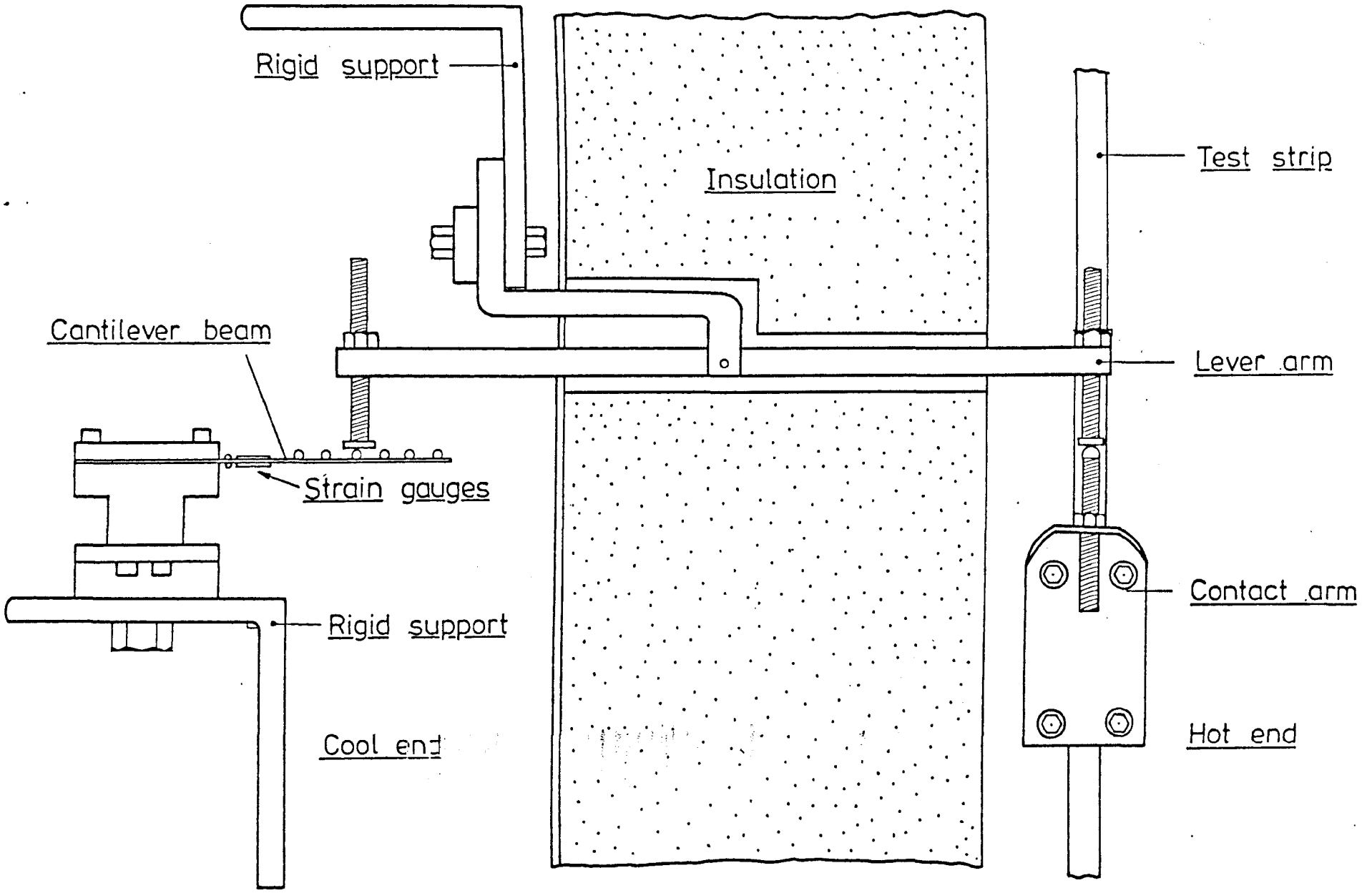

FIG. 4.22 Lever Arm Displacement Measuring Assembly for Elevated Temperature Rig. (Full Scale)

in the usual way.

The lever arm arrangement enabled the cantilever beam to remain relatively cool since it need not contact the contact arm directly. However, contact between the hot lever arm and the cantilever beam had to be kept to a minimum in order to reduce any heat transfer on contact. The 'warming' of the cantilever beam may cause the strain gauge output to drift, or indeed the gauges to fail. This warming up did occur due to radiant heat transfer and caused an initial gauge drift of 5μ which remained unchanged thereafter. This simple method of measuring the displacement gave acceptable accuracy provided the distances of the contact heads at the pivots were known accurately and that the two arms were identical. For greater accuracy, in situ calibration was carried out. The conversion of the strain measured on the beam cantilevers to true ratchet strain was given in Section 4.4.5.

4.5.3 Instrumentation

By interfacing the strain gauge measurement to the 'PET' micro-computer, it will be possible to store and analyse the results quickly provided that the required software is developed. At the time of experimentation, this was not available and results of the test were recorded on the chart recorder. It is envisaged that these options of manipulation, printing and storing of output will present no problems to future users of the equipment.

4.5.4 Specimen Preparation

The specimen used in the tests were of the same batch as those that were treated in Section 4.4.4.

4.5.5 Test Procedure and Planning

Following the commissioning of the heating and microcomputer systems, the rig was first raised to temperature with only a dummy specimen in order to test the temperature control. Using software written in BASIC, the control theory was implemented and was able to maintain a temperature to within $\pm$ 2°C for several hours. This duration was sufficient to maintain suitable conditions for a single test. A heating up period of three hours was necessary to ensure that the strip and the wheel reached uniform test temperature. This was confirmed by mounting platinum resistance thermometers in a block of steel similar in thickness to that of the wheel. Mercury in glass thermometers provided confirmation of the air temperature.

During temperature raising trials, strips were installed with the complete displacement measuring arrangement to ensure that they functioned correctly.

In this material/temperature combination, only a single ratchet test was conducted. The reason for this was firstly a comprehensive series of tests similar to that at room temperature could not be accommodated within the timescale of this thesis. Secondly, it was necessary to ascertain that the technique could be extended into the elevated temperature regime and for this, a single test was sufficient. Having assured oneself of the applicability for the extension into elevated temperature, it would be only a matter of time to conduct tests for various temperatures.

A test point of σ_p/σ_y = 1.41 and σ_t/σ_y = 2.67 (both values being based on σ_y at room temperature) was selected in order to facilitate comparison of results. The cyclic rate of 41s/cycle was also similar.

4.5.6 Test Results and Discussion

The result of the single test is compared with that at room temperature for up to 250 cycles in Fig. 4.23. This shows two prominent details. Firstly, the total strain accumulation was reduced (by about 40% at the 200th cycle) in the 400°C test. Secondly 'shakedown' was achieved by the same test in about 100 cycles while the room temperature did not 'shakedown' up to 1000 cycles. These surprising results appear to be in opposition to most expectations. However, this behaviour does have support in the form of material tests at this temperature. In strain controlled cyclic tests at 427°C Jaske and Frey (83) (see Section 2.7.2, Chapter 2) showed that cyclic hardening increased with temperature for most strain ranges. At 21°C, some cyclic softening was observed. Therefore there is a possibility that cyclic hardening has reduced part of the total strain accumulated.

The second consideration concerns creep strains. According to the isochronous stress-strain curves shown in Fig. T-1800-B1 of the ASME N47 Code Case (6) creep strains were negligible even up to dwells of 3×10^5 hours. Whilst at 21°C, cold creep strains may have increased the strain accumulation during the initial cycles. The combination of these two factors may explain in a limited way the experimental results. However due to the complexity of the mechanisms that operate in these tests and the scarcity of experimental data, caution is urged in its interpretation. More tests are required for a thorough analysis.

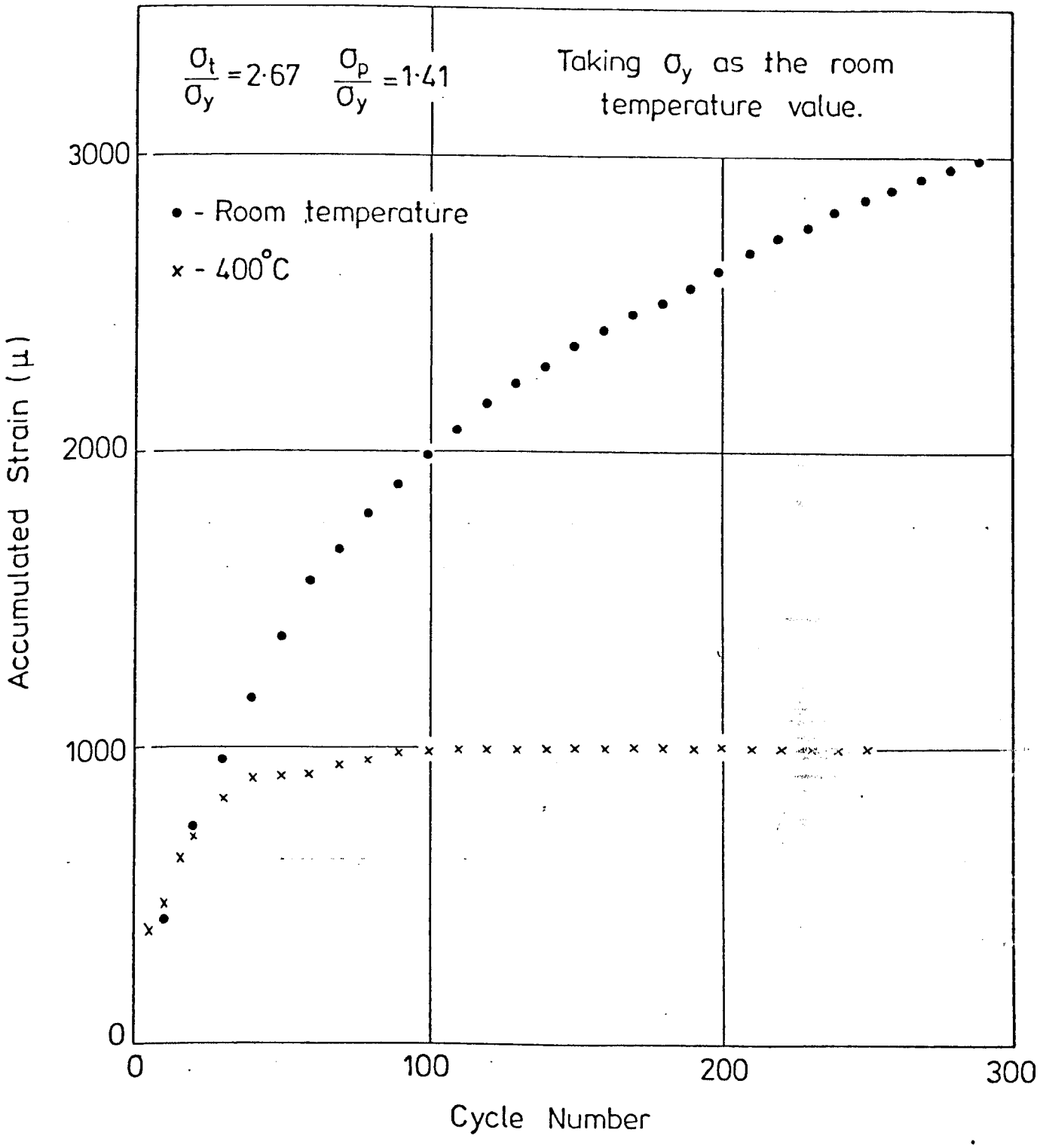

FIG. 4.23 Comparison of Experimental Strain Accumulation of Type 316 Stainless Steel at Two Test Temperatures

4.6 Shakedown and Ratchetting Tests on 'T' Section Beams

4.6.1 Introduction

Cyclic bending tests were conducted on 'T' section beams made from Type 316 stainless steel (in a solution treated condition) to determine the shakedown load of the beam and the ratchetting strain accumulation. The tests originally were planned at room and at elevated temperature (400°C). The objective of these two tests was to establish if such high temperature tests were feasible and if so to compare the results obtained in order to identify the effects of temperature. Considerable efforts were put into maintaining the temperature of the beam constant (at ± 1°C) and in making accurate strain measurement at elevated temperature (better than 5μ). It was found that although the former could be achieved, the latter posed considerable problems. Firstly, the strain gauges used (a type FNWFB full bridge weldable gauge supplied by BLH Ltd.) were not stable enough for operating for long periods at the temperature required. Gauge output drift was particularly serious and compensating techniques could not be reliably used. Secondly, testing in air caused oxidation attack on the strain gauges which in the long term caused weakening of the spot welded bonds. It was therefore decided that long term shakedown tests using this type of strain gauges were unsatisfactory and the tests produced little useful data. The report by Strong and Daniels (91) also attributed the failure of the gauges to the above causes and suggested that they can only be used in short term tests or transient strain measurements. The outcome of the elevated temperature test demonstrated that the direct measurement of strains using electric resistance strain gauges has its limits. The capacitance strain gauges appeared to have less of the problems suffered by the resistive counterpart but the cost of using these strain gauges is

considerable and new signal conditioning equipment would have been required. This has led the author to experiments based on the Bree beam.

The theoretical background of the 'T'-section beam shakedown problem has been discussed by Moreton (92) who performed these tests on a Type 321 stainless steel. It is not the aim of this thesis to discuss in great detail the background involved in 'T'-section beam tests although a simplified version is given. This section is added to the main work in order to complete the other experimental work that the author has carried out in his initial research.

4.6.2 'T'-section Beam Investigations

'T'-section beam tests were initially conceived for finding the maximum shakedown factor of beams subjected to a repeated bending moment load. The shakedown factor is represented by M/M_y where M is the applied moment and M_y is the moment at which yielding is first detected on the highest stressed fibre in the beam. This occurs at the surface of the rib of the 'T' beam. For an idealized elastic/perfectly-plastic material, the highest possible value of M/M_y at which shakedown can occur is $M/M_y = 2.0$. This is because removal of a higher load would cause reversed yielding at the rib surface and the unloading would no longer be elastic. When the maximum shakedown load is exceeded, two types of cyclic deformation can occur. One mode of inadaptation is alternating cyclic plasticity which is manifested by equal and opposite yielding stress states at each end of a cycle. Alternating cyclic plasticity does not cause progressive deformation of the structure although fatigue failure will ultimately result. The other type of cyclic behaviour is that of ratchetting or incremental collapse. The

structure suffers unequal yielding at the end of each half cycle causing a finite amount of permanent strain. This behaviour has been discussed in connection to the regimes of behaviour on the Bree Diagram. In the tests, the maximum shakedown load is first determined followed by repeated loading above the shakedown load to cause ratchetting.

4.6.3 The 4 Point Bending Rig

The rig for applying the bending moment is shown in Fig. 4.24. It consisted of a loading trolley and a support frame. The bending moment was applied to the 'T' beam through two pairs of rollers. The inner pair were held in bearings within the loading trolley which applied a downward force through a loading frame incorporating a weight carrier. The outer pair of rollers were also held in bearings within the support frame. The outer pair supported the 'T' beam via a pair of extension bars and the combined weight of the loading trolley, weights and the weight carrier. The bending moment diagram can be easily drawn to show that the bending moment is constant within the distance between the inside rollers. Thus the applied bending moment is known. The function of the roller bearings was to eliminate the possibility of any end load being applied to the beam.

4.6.4 Test Specimen

The test specimen was machined from a different source of Type 316 stainless steel as those used in the previous test. The dimensions of the beam are given in Fig. 4.25 and the length was $7\frac{1}{2}$ in. (16.9 mm). The specimen had been firstly rough machined to within 1/16" of actual dimension and heat treated at 1050^{o}C for one hour and furnace cooled. It was then cleaned and carefully machined to final dimensions. From

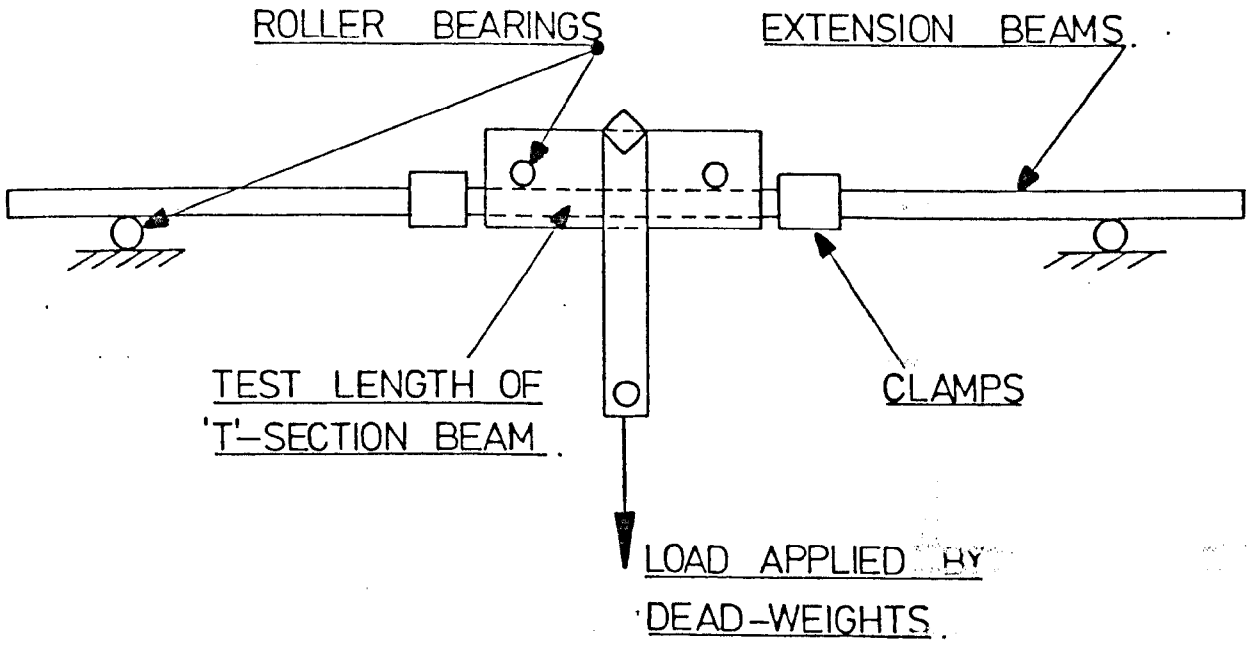

FIG. 4.24 Schematic Diagram of the Four Point Loading Rig Used for T-Section Beam Shakedown Tests

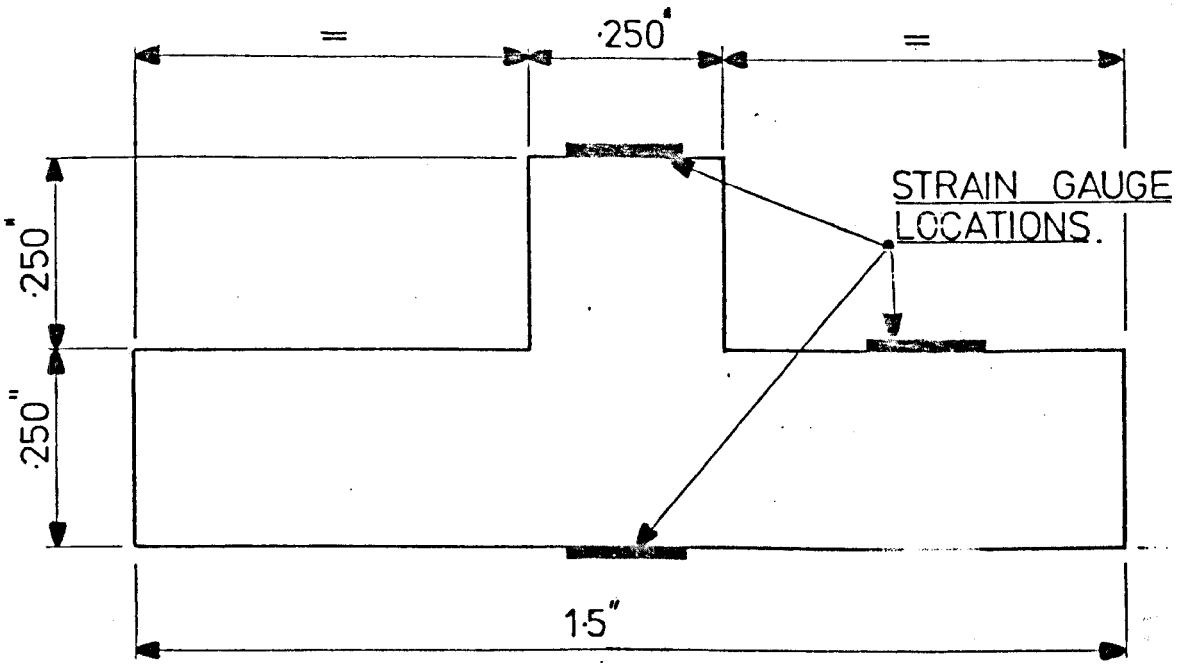

FIG. 4.25 Nominal Cross-Section Dimensions of 'T' Section Beams

the same source of material, a tensile test specimen was machined for determining the stress-strain characteristics. Both specimens were strain gauged with conventional electrical resistance strain gauges. The tensile test specimen was gauged with two diametrally opposed uniaxial strain gauges and the 'T' beam was gauged with three uniaxial strain gauges located respectively at the outer surface of the rib, the bottom surface and at the step. Although only the strain gauge at the rib was necessary for determining shakedown, the other strain gauges were for determining strain distributions.

The tensile test revealed a yield stress at first departure of linearity of 102 MN/m^2 (6.6 $Tonf/in^2$). Using this value, the elastically calculated first yield bending moment of the beam was 28 Nm (20.6 lbf.ft) and this could be created with an applied load of 93N (42 lbf).

4.6.5 Loading Procedure

The load was firstly applied in steps of 9N (2 lbf) until the beam yielded by a small amount. This was indicated by departure from linearity on a moment/strain plot. Subsequent unloading and reloading of the same load were repeated until there was no longer any increase in the strain. When there was no increase after three successive cycles, a state of shakedown was considered to have been reached. The load was in most of the cases increased by a step of 22N (5 lbf) and the procedure repeated. The M/My value was, at each step, calculated and noted. The strain was noted at each repeated reloading. This procedure was continued until the maximum shakedown load was achieved and further ratchetting tests were continued. About 20 load steps ranging from M/My = 1.267 to 3.268, were applied.

4.6.6 Results and Discussion

Fig. 4.26 shows the plots of strain accumulated against the number of reloadings for each M/My step. It is seen that for loads below M/My of 1.648 the beam rapidly shakes down within about 5 cycles. At M/My between 1.933 and 2.076, lies the maximum shakedown load. This value was however close to M = 2.0 for elastic/perfectly-plastic material idealization. It would be expected to be larger for hardening material. For all M/My steps greater than 2.076, ratchetting was seen in all the plots. The rates of strain accumulation follow a trend which decreases with applied cycles. For most of the plots, the total strain accumulation increases with the applied M/My loads although in the small number of cycles tested, it was not possible to determine whether there was any prospect of shakedown at large cycles.

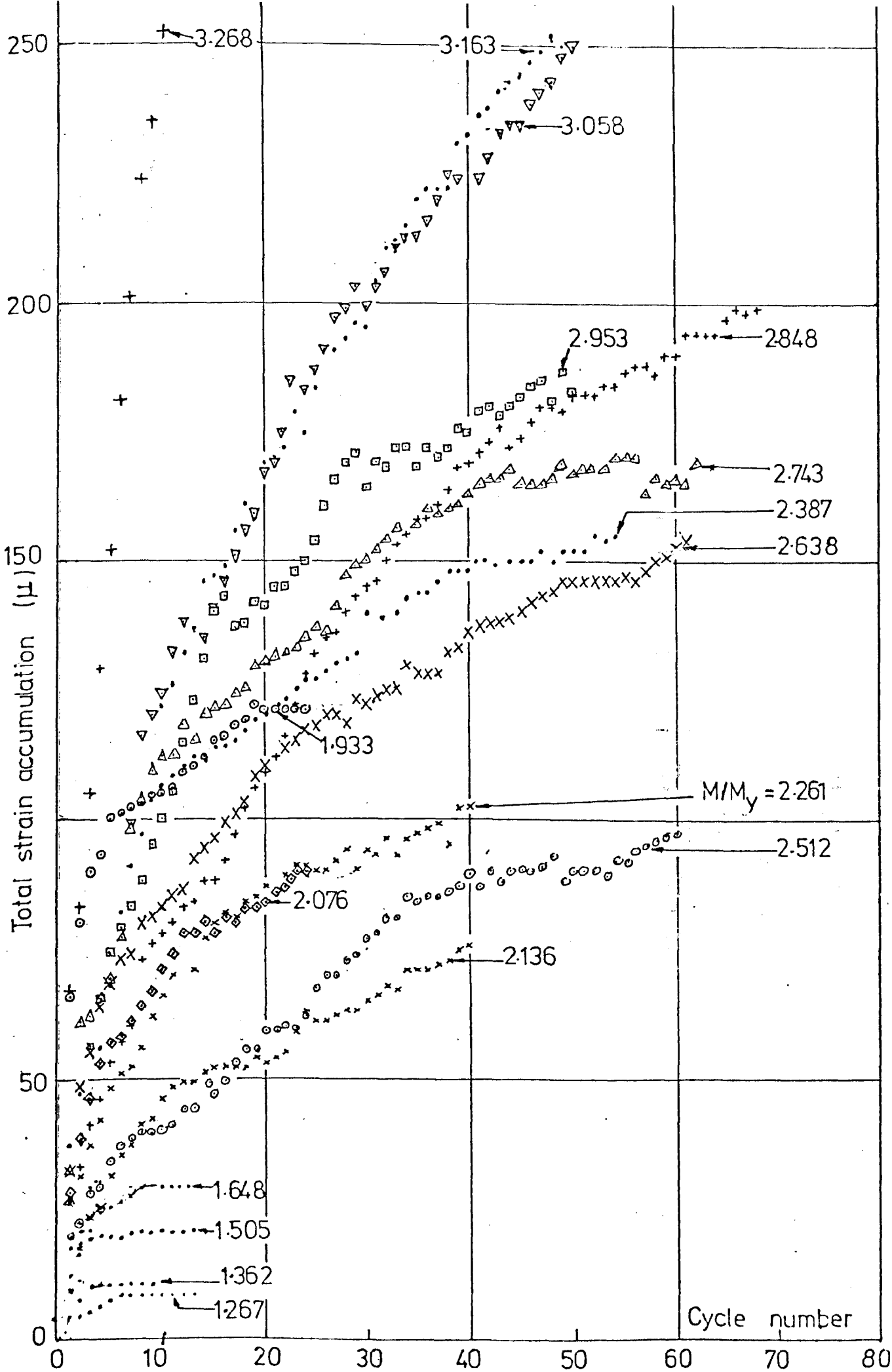
3·268
3·163
3·058
2·953
2·848
2·743
2·387
2·638
1·933
M/My = 2·261
2·512
2·076
2·136
1·648
1·505
1·362
1·267
Total strain accumulation (μ)
Cycle number
0
50
150
200
250
0
10
20
30
40
50
60
70
80

CHAPTER 5

COMPUTATIONAL ANALYSIS

5.1 Introduction

Computer calculations were performed on the uniaxial Bree beam model to study its behaviour under various loading sequences and utilizing several material models. The former considers the effects of the variation in the loading sequences of the curvature bending and axial loads on the beam model. The loading sequence of Bree's original analysis was not representative of the loadings that are imposed on many components of power generating plants. It is therefore desirable to assess the effects on the response of the beam model should a change in sequence occur.

In the computation of the beam model subjected to variation in the loading sequence, an elastic/perfectly-plastic material was assumed. By varying the cyclic relationship of the two loads in a quasi-static manner which means that the two loadings assumed stepped values and did not overlap upon one another, three new phase relationships were obtained. These were the In Phase (abbreviated I.P.), Out of Phase (O.P.) and Continuous Thermal and cyclic pressure loadings (C.T.) sequences of loading. It needs to be noted that in the computations of this chapter, the beam bending model has been considered but because of the necessity to maintain a consistent abbreviation, the thermal analogy was retained. This however does not alter the solutions as has been pointed out in Section 3.3.3. where the numerical calculations were analytically proven. The computer programs developed for modelling the variations of loading sequence are briefly described in Section 5.2. As the results of the analyses were examined and interpreted in the discussion of Chapter 3, it was decided not to repeat the results.

The second objective of the computation was to predict the strain accumulation of the uniaxial Bree beam based only on the loading sequence of Bree which is that of continuous axial loading superimposed by a cyclic curvature bending load. These calculations were used to assess the capability of classical or conventional material models as well as less conventional models in predicting the strain accumulation of experimental tests carried out in this work.

The capability of accurate prediction depended both on the method of computation and the material model. Since the uniaxial beam model was a simple structural model the accuracy of prediction depended greatly on the chosen material model. Such a model is required to be able to simulate elastic and inelastic uniaxial stress strain behaviour realistically. With the availability of experimental results on tests using strips of mild and stainless steel materials, the former being nearly elastic/perfectly-plastic and the latter was strain hardening, such material models can be tested.

It is known that inelastic design methods usually require expensive computational techniques and for complicated structures were often impossible. Apart from the expense, the final design is often significantly influenced by the material model incorporated in the analysis. An unsuitable model often leads to wrong and sometimes unsafe conclusions. Furthermore, it is often uneconomical to experimentally substantiate calculated results. Hence the computational studies were thought to be a necessary adjunct to the experimentation performed in this work.

In the calculation, it has firstly been pointed out that time dependent properties such as creep will not be considered. This lack of time dependency in the programs was not thought to be a severe disadvantage since the ratchet tests were performed at room temperature and at relatively fast cycle times when compared to the low creep strain rates

due to cold creep at room temperature.

The exclusion of time as a parameter in the programs firstly will greatly reduce the complexity of programming. Works by Goodman (29), Philips (30) and Owais & Otter (34) have already considered creep due to dwell times on loadings imposed on the uniaxial Bree beam. The inclusion of a time parameter in the program was considered by the author to be no longer necessary in such an analysis since it was likely that the results will be repeated.

The author has instead concentrated on material effects which are cycle dependent. These include cyclic hardening/softening and cyclic relaxation. These are material properties which are generally exhibited by stainless steels and are modelled by the 'less conventional' material models in this work.

It is well known that predictions on ratchetting strain accumulation based on the classical or conventional material models of linear and non-linear kinematic hardening (by which the latter is based on a strain hardening curve) will always shakedown after a small number of cycles. The model of elastic/perfect-plasticity on the other hand predicts a state of constant ratchetting rate. All the above predictions however were unable to agree with the experiments.

Less conventional material models were sought such as those capable of cyclic hardening/softening. Such a model based on the numerical method of Jhansale (25) was used. This model represents the gradual cyclic hardening or softening by means of the Yield Range Increment (YRI) concept. The concept enabled the determination of transient cyclic stress-strain curves before complete saturation of hardening or softening was reached as a function of the strain amplitude and cycle number. The model could not predict the experimental results well.

Another model which was derived from the empirical model of yield locus behaviour was examined. The model was attributed to Moreton et al. (93) who investigated yield locus movements of a number of steels including Type 316. When implemented, the material model (hereafter known as the model of Moreton et al. (93)) was able to reproduce the continuous ratchetting observed in tests at large cycle numbers as well as closely approximating the magnitude of strain accumulated. The program for implementing this model is by far the most complex and provided a means for understanding the mechanisms causing the continuous ratchetting.

The listings of all the programs used in this study will take up an excessive number of pages. It was considered necessary however to include at least some of the important programs. These are chosen to be the programs for the following: non-linear kinematic hardening material model, In Phase loading sequence and the model of Moreton et al. (93). These are listed in Appendix C as C1, C2 and C3 respectively.

5.2 Program Description

5.2.1 General Program Description for the Uniaxial Bree Beam Model

The calculations were based on the division of the beam thickness into 50 elements and subjecting each to a specified strain range. The beam was assumed to have a unit width. In the Bree sequence of loading, the beam was subjected to a through thickness strain distribution which was linearly varying when the curvature bending of the first half cycle was imposed. In the second half cycle, a uniform strain distribution was imposed by the continuous axial load. Hence every element was subjected to unique strain history and responded with a stress which was in accordance with the material model. A numerical solution was obtained for each half cycle by summing the forces of all the elements and ensuring that this was equal to the applied axial load; that is, satisfying the equilibrium condition. At the same half cycle, compatibility and the material model were also satisfied. The procedure for attaining equilibrium was by adjusting the magnitude of the strain distribution as a whole (that is, strain in every element was adjusted uniformly) thus maintaining constant through thickness slopes of the strain distribution which satisfied the compatibility condition. For each adjustment of the strain distribution, the stress responses of all the elements were recalculated based on the material model. Convergence of the applied axial load and the total force of all the elements was achieved rapidly using an efficient search method. When each adjustment of strain reached one microstrain, which was the specified tolerance, iteration ceased. The final stress and strain distribution were the solution for that half cycle. At every two half cycles (or one full cycle) the strain of the outermost element was stored. The strains stored after two and a half full cycles enabled the behaviour of the beam to be

determined using the appropriate differentiating criteria.

The relevant conditions to be satisfied can be stated as

(i) Material Model (described in later sections).

(ii) Equilibrium,

$$\frac{t}{50} \sum_{i=1}^{i=50} \sigma(i) = \frac{W}{w}$$

where $\frac{t}{50}$ is the element thickness in a beam of depth t

(iii) Compatibility,

for the 1st half cycle,

$$\varepsilon_T = \varepsilon_p + \frac{x}{r} + \varepsilon_a$$

for the 2nd half cycle,

$$\varepsilon_T = \varepsilon_p + \varepsilon_a$$

where: x is the distance from beam midsurface

r the radius of curvature

ε_p the plastic strain

ε_T the total strain and

ε_a the axial elastic and inelastic strain due to the axial load only

5.2.2 The Procedures in the General Program

All the programs written in this work have the same basic structure. The flow chart in Fig. 5.1 shows the procedures used in the calculations. The structure can be divided into four segments based on these procedures.

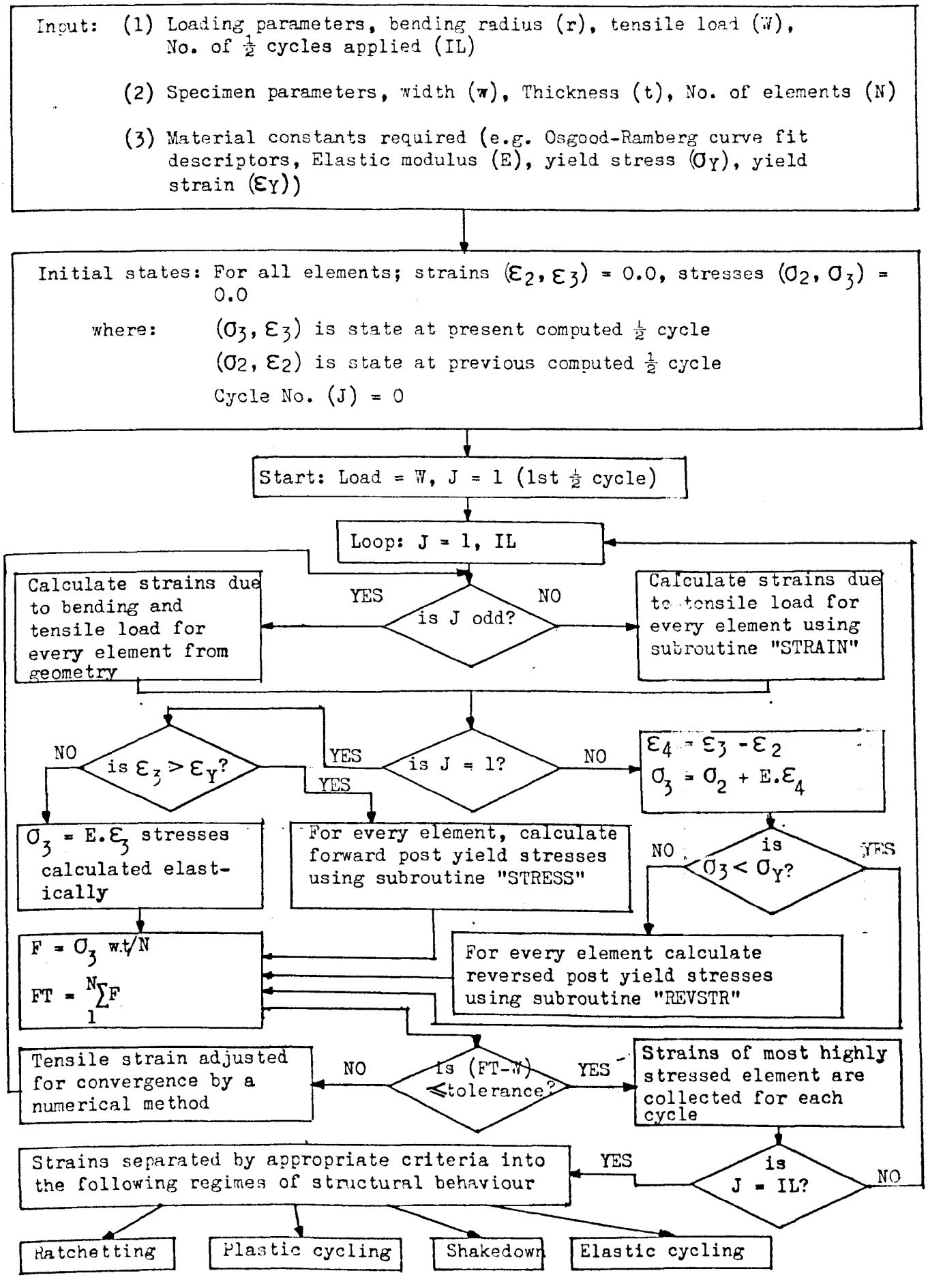

Fig. 5.1 Flow Chart for a Program to Predict Ratchet Strains on a Uniaxial Bree Beam Model on an Arbitrary Material under Combined Bending and Tensile Loadings

The first synchronizes the loading sequences by applying the correct strain distributions at every alternate half cycle. The second segment implements the material model by calling the subroutines STRAIN, STRESS and REVSTR (for REVersed STRess). The third segment ensures that equilibrium be attained. The final segment applies the criteria for differentiating the regimes of behaviour.

Following the general description above, the detailed procedures are now given step by step as follows:

(1) Determine the σ_t/σ_y and σ_p/σ_y ratios on the Bree Diagram to be investigated.

(2) Input the material constants to be used and the specimen dimensions.

(3) Calculate the bending radius and axial load as a result of (1) and (2).

(4) Initiate the conditions for an unstrained and unstressed specimen at zero cycles for all elements.

(5) Calculate the strain in all elements due to axial load and bending on the 1st $\frac{1}{2}$ cycle from geometry.

(6) Test if material in each element has yielded in the 1st $\frac{1}{2}$ cycle and if so post yield stresses are calculated by subroutine "STRESS". Otherwise stresses are calculated elastically.

(7) Sum the forces in each element.

(8) Test for equilibrium of applied axial load and repeat from (5) to (8) each time adjusting strain to search for equilibrium.

(9) Store all stress and strain values of every element for use in the next half cycle.

(10) Initiate 2nd half cycle where axial load only is applied.

(11) Calculate initial strain distribution due to tensile load using subroutine "STRAIN".

(12) Calculate stresses from initial strains (11) and the stresses and strains from the previous half cycle (9) using subroutine "REVSTR".

(13) Sum all forces in each element.

(14) Test for equilibrium of applied axial load repeat (11) to (14) each time adjusting strain to search for equilibrium.

(15) Store all stress and strain values of every element for use in the next half cycle.

(16) Initiate 3rd half cycle.

(17) Impose initial strain distribution equal to that of (9).

(18) Calculate stresses in every element which have yielded in the previous half cycle by using subroutine "REVSTR" and stresses and strains from previous half cycle from (15).

(19) Repeat (13) to (15).

(20) Store the strain value at the outermost element at each half cycle.

(21) Continue for the 4th and 5th half cycle.

(22) Exit from the loop and analyse strains stored from (20) by employing a set of criteria. There are now five strain values stored from the 1st to 5th half cycles. These are designated as ε_1 to ε_5. Additionally, the inner surface strain (ε_0) on the innermost surface on the 1st half cycle is also stored.

(23) Calculate, (i) Loop Width (LW) = $\varepsilon_5 - \varepsilon_4 - 2\varepsilon_y$

(ii) Ratchet Strain

$$(RS) = \varepsilon_5 - \varepsilon_3$$

(iii) Plastic Strain (PS) incurred on the outermost surface at the 1st half cycle $= \varepsilon_1 - \varepsilon_y$

(iv) Plastic Strain (PS') incurred on the innermost surface at the 1st half cycle $= \varepsilon_o - \varepsilon_y$

(24) Sort according to the flow chart in Fig. 5.2. R2, P2, and S2 regimes of behaviour correspond to ratchetting, alternating plasticity and shakedown respectively where there is yielding on both inner and outer surface during the first half cycle .

(25) End of computation.

The program for which the flow chart and the above procedure is exactly applicable is given in Appendix C.1. The material model for this program is that of non-linear kinematic hardening. With some modifications, a different material model can be implemented in the program.

5.2.3 Program Implementation for the Variations of the Sequence of Loading

The alternative loading sequences mentioned previously were implemented only with the elastic/perfectly-plastic material idealization. The necessary modifications to segment 1 were the synchronization into each half cycle of the applied axial load and the initial strain distribution. The rest of the program operated unchanged. The program for in-phase loading sequence is shown in Appendix C.2.

5.2.4 Material Modelling for Elastic/Perfectly-Plastic Material

The material was assumed to be representative of mild steel strips used in the test. It has a yield stress of 202 MN/m^2 and a Young's modulus of 172 GN/m^2.

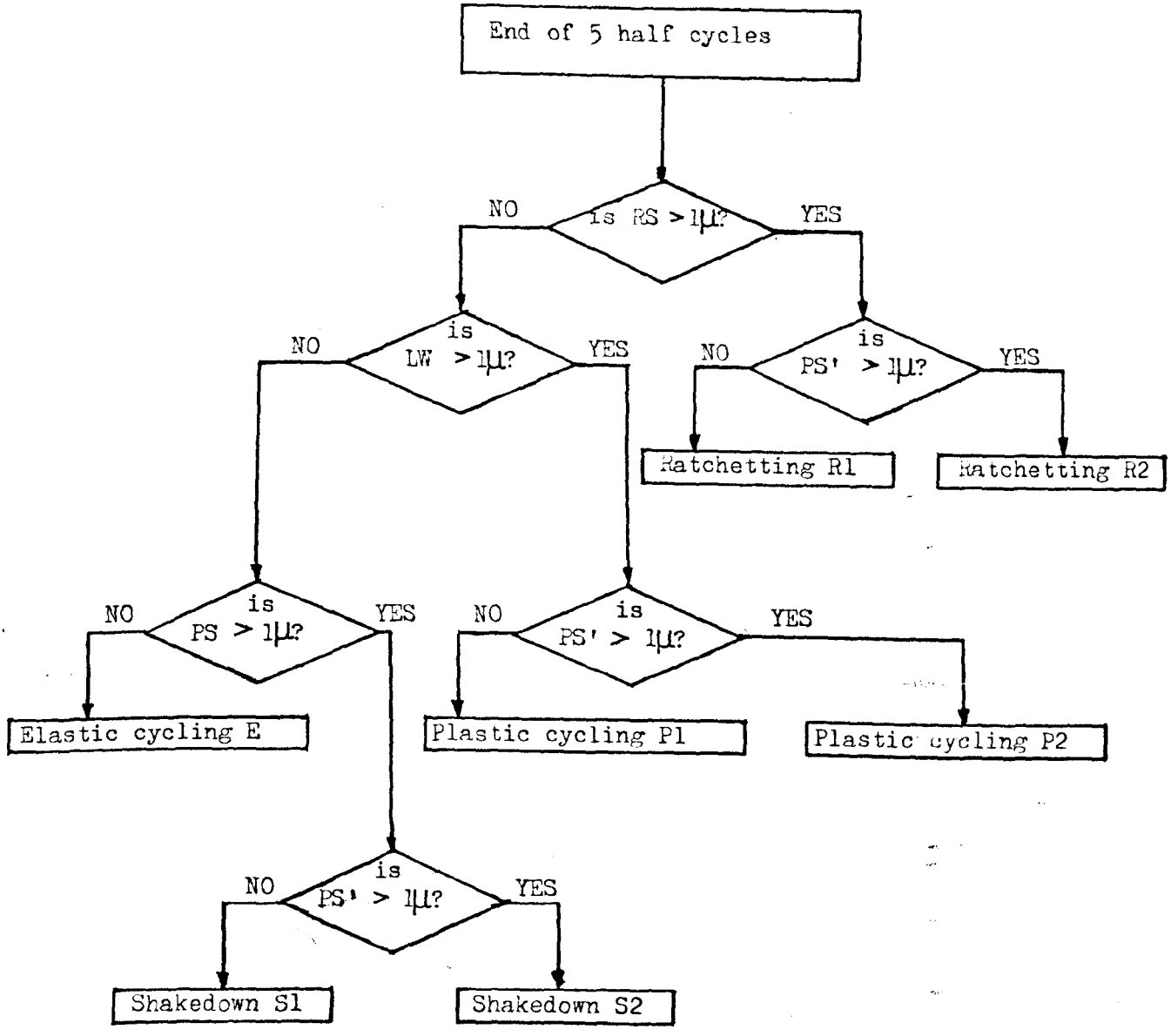

Fig. 5.2 Flow Chart for Differentiating the Regimes of Structural Behaviour

5.3 Formulations of Material Models in the Uniaxial Bree Beam Model

5.3.1 Computational Considerations

Inelastic deformation analyses require that material models of inelastic behaviour be capable of simulating the stress-strain behaviour realistically. In monotonic loading, the simulation can be simple and realistic. However under cyclic loading, the situation becomes more complex. This then involves cycle dependent phenomena such as cyclic hardening, softening, relaxation and creep. The formulation of these models has been conducted mathematically and by programming techniques. Mathematical models for which a large number of literature references exist use phenomenological descriptions or are based on microstructural studies. These models are often difficult to apply and are not suited for digital computation. The models that are suitable are those which can be implemented as simple sets of rules governing uniaxial stress-strain behaviour. Such rules are used in the formulation of material models to be described in the following sections. Rules used for the conventional models of elastic/perfect-plasticity and linear-kinematic material models are simple to apply. Other rules, for example the Mroz model (74) or Mechanical Sub-layer model are more difficult and require greater storage facilities.

From the computing viewpoint, the difference between uniaxial tests and structural tests was noted. In a uniaxial cyclic test, the cross section of the specimen is assumed to be subjected to a uniform stress and strain. A structural cyclic test, such as on the Bree beam, subjects each element in the beam to a unique stress and strain history and the behaviour of the beam is the sum of the responses of the individual elements. Calculations performed by the programs are complicated and involve the repeated computation of the stresses in every element according

to the rules of the models described until equilibrium and compatibility are attained. Some of the models used in this work are described in necessarily quantitative terms because they are not easily amendable to mathematical description. They are however empirically based.

5.3.2 Linear Kinematic Hardening Model

Fig. 2.4 of Chapter 2 shows schematically this material model for inelastic forward and reversed loading. The quantitative parameters are fitted to the stress-strain curve of Type 316 stainless steel. This has a yield stress of 183 MN/m^2 and a linear hardening modulus (βE) where $\beta = 0.058$ and $E = 188\ GN/m^2$. These terms were defined in Fig. 4.13 of Chapter 4.

5.3.3 Non-Linear Kinematic Hardening Model

An Osgood-Ramberg power law (23) was used to represent the experimental stress-strain curve with a least squares fit. The expression used is

$$\varepsilon = \sigma/E \qquad \text{for } \sigma \leqslant \sigma_y$$

$$\varepsilon = \sigma/E + \left(\frac{1-m}{m}\right)\left(\frac{E}{S}\right)^{n-1}\left(\frac{\sigma}{E}\right)^{n} \qquad \text{for } \sigma > \sigma_y$$

The values of the constants m, S and n are given in Fig. 5.3. The curve was fitted to experimental data of up to 2% strain and extended to 35% strain. The model is represented in hysteretic behaviour by a Mroz model (74) in Fig. 5.4. which shows the stress response to strain cycling of $\pm$ 0.35%. It is seen that this model does not show cyclic dependence as it is based on the Mroz model. The unloading and reloading curve is of the same geometric shape as the initial monotonic curve but

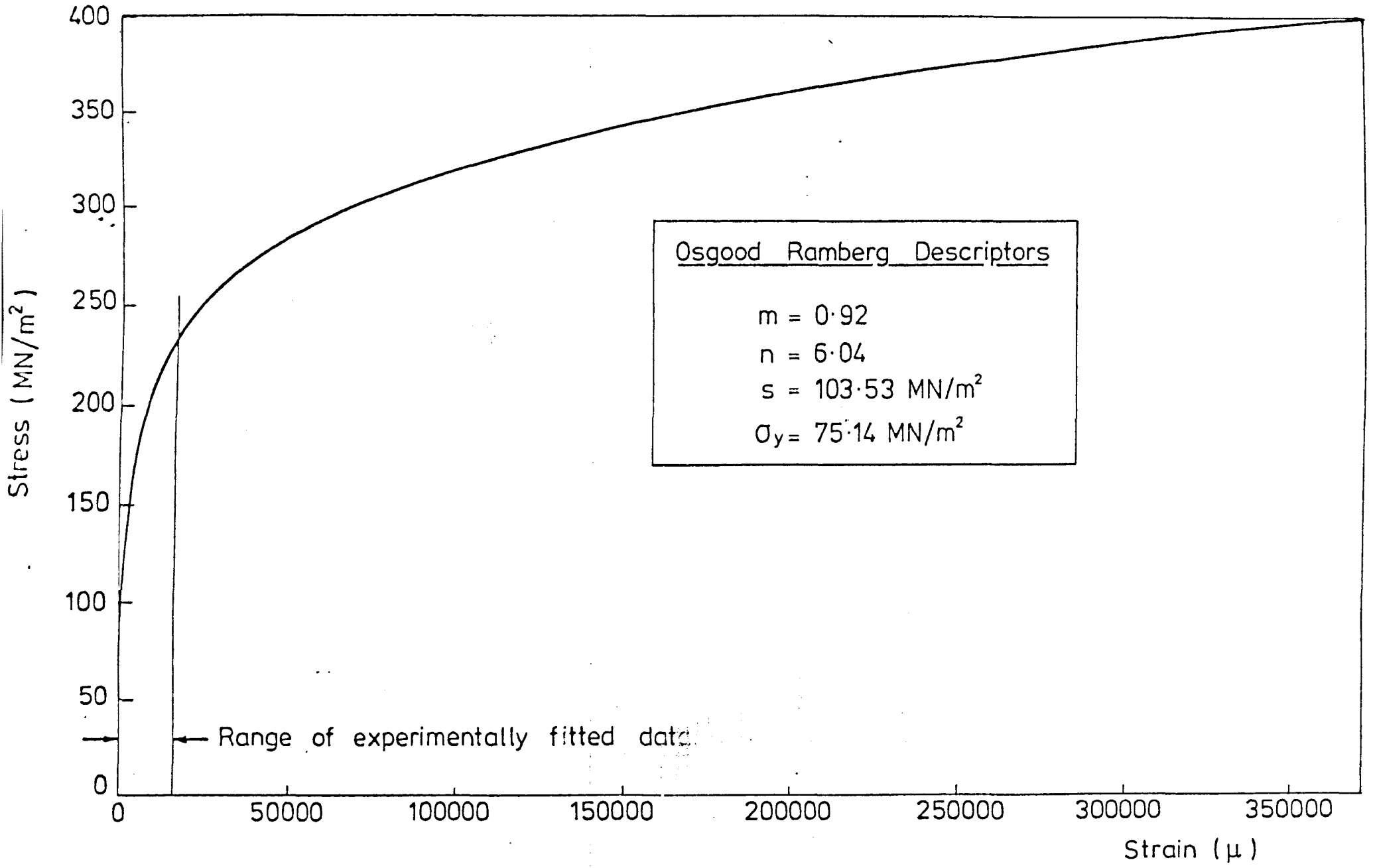

Fig. 5.3. Type 316 Stainless Steel Stress-Strain Curve Being Represented by an Osgood & Ramberg Power Law

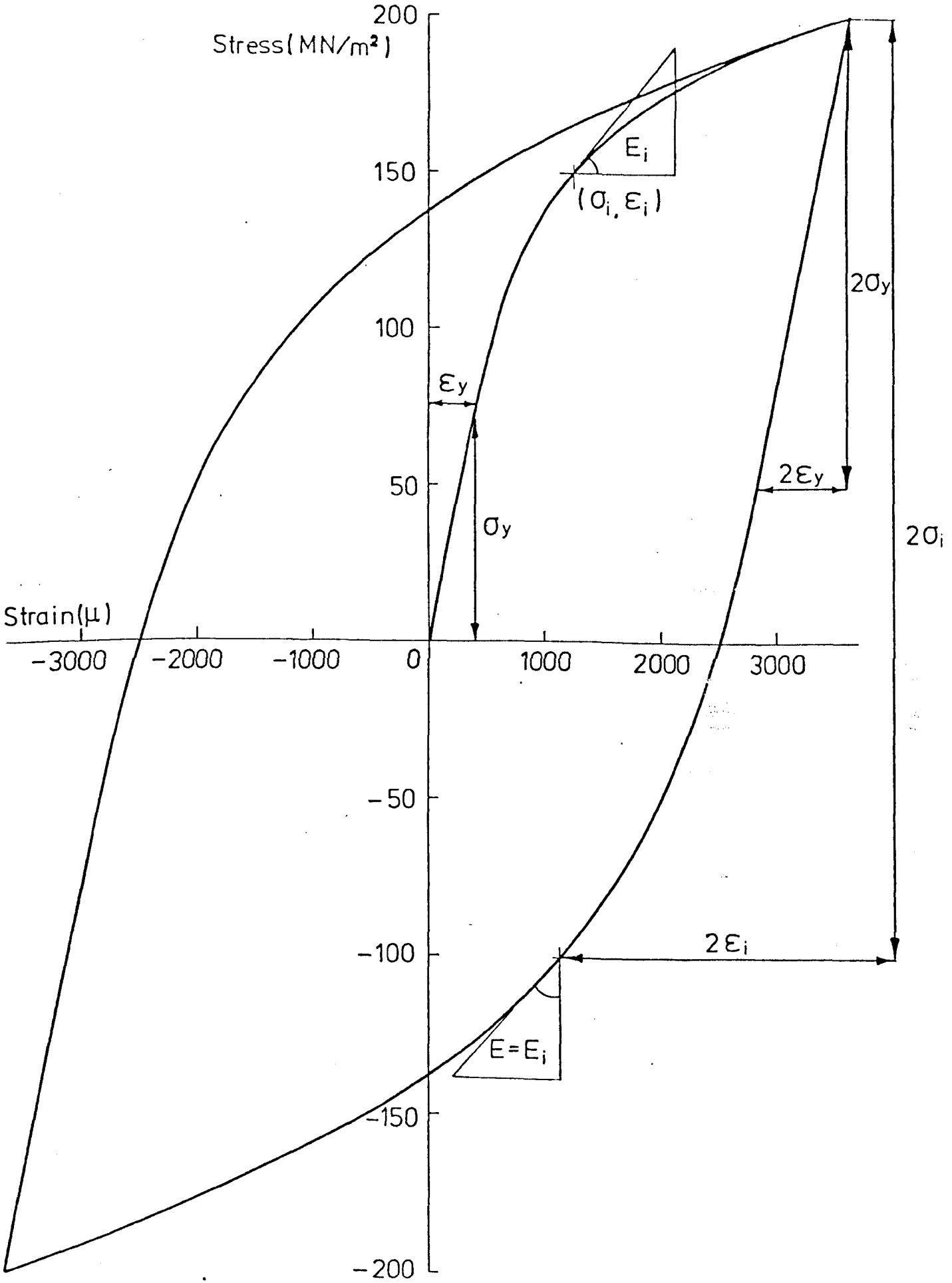

Fig. 5.4. Non-Linear Kinematic Hardening Material Model Based on Type 316 Stainless Steel Properties

multiplied by a factor of two. Reverse yielding therefore occurs after unloading to a load $2\sigma_y$ below the forward prestress point.

5.3.4 Model of Jhansale (25)

The third model was based on a concept proposed by Jhansale (25) for modelling cycle dependent transient behaviour in metals. The phenomena of cyclic hardening, cyclic softening, cyclic creep and mean stress relaxation have been observed in constant strain or cyclic stress amplitude conditions. In general these are transient in nature and a stable state is approached rapidly. These effects are considered as being cycle dependent because they are thought to be a consequence of microstructural changes associated with reversed inelastic straining. Studies by Jhansale of the hysteretic behaviour of some steels and aluminium alloys showed that the transient changes in stress-strain curves during constant amplitude cycling were primarily due to changes in the initial "linear" parts while the non-linear portions remained virtually unchanged in shape. This change in the elastic part is defined as the Yield Range Increment (YRI) as it denotes a change in the yield strength. A cycle dependent increase or decrease in YRI between two consecutive reversals describes cyclic relaxation or cyclic creep depending on the controlled limits (strain or stress). This is illustrated for cases of cyclic hardening, cyclic relaxation and cyclic creep in Fig. 5.5. a, b and c. The YRI's ab, cd and ef account for the transient phenomena whereas the non-linear portions bc, de and fg remain identical in shape. As saturation is approached the difference in YRI's between consecutive reversals decreases. Thus during the transient period the hysteresis loops are not fully closed but at saturation they are identical as the YRI's in the tensile and compressive

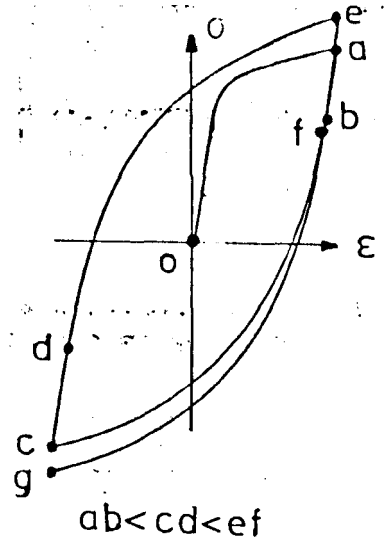

ab<cd<ef

(a) Cyclic hardening under strain control

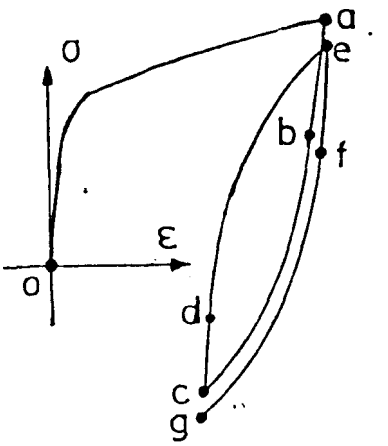

ab>cd<ef

(b) Cyclic relaxation under strain control

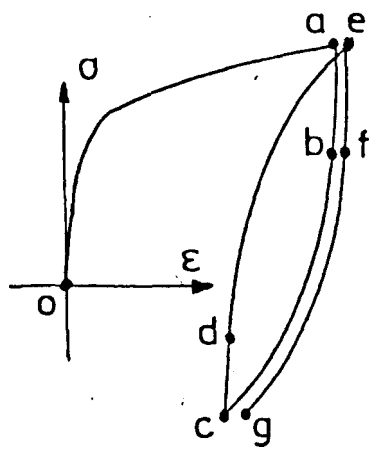

ab>cd<ef

(c) Cyclic creep under stress contrd

Fig. 5.5. Reversal to Reversal Variation in YRI during Transient Behaviour. AB, CD, and EF are YRIs Corresponding to Reversals AC, CE, and EG. Portions BC, DE, and FG are Identical in Shape and are Described by Doubled Skeleton Stress-Strain Curves. Jhansale (25)

hysteresis curves reach a common saturation level. In structural steels studied (SAE/1045), the saturation level of YRI appears to be dependent on the strain amplitude. The rate per reversal at which the YRI approaches saturation appears to be proportional to the difference between the saturation and current values of YRI and inversely proportional to the number of reversals. The above have been assumed and adopted for the author's model.

The technique required the experimental monotonic and stabilized cyclic stress-strain curves. Although the former requirement was obtained, the latter was not possible using the strips as specimens. The slenderness of the strips meant that any compression forces would immediately cause buckling. Hence it was necessary to use data obtained elsewhere. This state of affairs was not desirable but in order to assess qualitatively the behaviour of the model it was necessary. This data was obtained from the results of Jaske et al. (80) and Jaske and Frey (83).

These two references report an extensive study of fatigue and cyclic stress behaviour of Type 316 stainless steel at temperatures from 21 to 649°C. Taking only the 21°C results into consideration, it was found that at strain ranges of $< .5\%$, there is a slight amount of cyclic softening followed by stable response. A strain range of 1.0% showed cyclic hardening. At higher temperatures the material consistently cyclically hardened. From the 21°C data, a cyclic softening model was assumed and implemented in the program for non-linear kinematic hardening.

The saturated cyclically softened stress-strain curve was represented by an Osgood and Ramberg Power law of exponent $n = 9$ while the monotonic stress-strain curve remained at $n = 6$. The exponent n is

one of the three parameters required for describing the stress-strain curve. In the beam, every element is subjected to a specified strain range. The stress response of each element is now dependent on the YRI which is proportional to the difference between the saturated stress at that strain range and the current value of YRI. As the cycle number increases, the saturated stress is approached.

5.3.5 Model of Moreton et al. (93)

This final model utilized an approach suggested by the yield surface investigations of Moreton et al. (93) on a range of pressure vessel steels which included Type 316 stainless steel. This reference presented the results of a series of experimental investigations on the yield surface movement under a range of prestress directions and magnitude. An empirical relationship was derived from these results to represent the yield locus movement using only three parameters, the yield stress, the prestress magnitude and the prestress direction.

Previous theoretically based models predict that the yield surface is constrained to pass through the point of prestress.

The empirical model of Moreton et al. which is illustrated in Fig. 5.6 is not thus constrained and suggests that the current yield surface will lie between the origin of stress and the prestress point. This model was also used by Moreton and Moffat (94) to predict the shakedown pressures of three pressure vessel components. These were two torispherical drumheads and a nozzle/sphere intersection manufactured from Type 321 stainless steel. Predictions of the shakedown pressure were in agreement with experimentation by better than 10% for the drumheads and 19% for the nozzle.

Briefly, this model gives the distance e of the centre of the

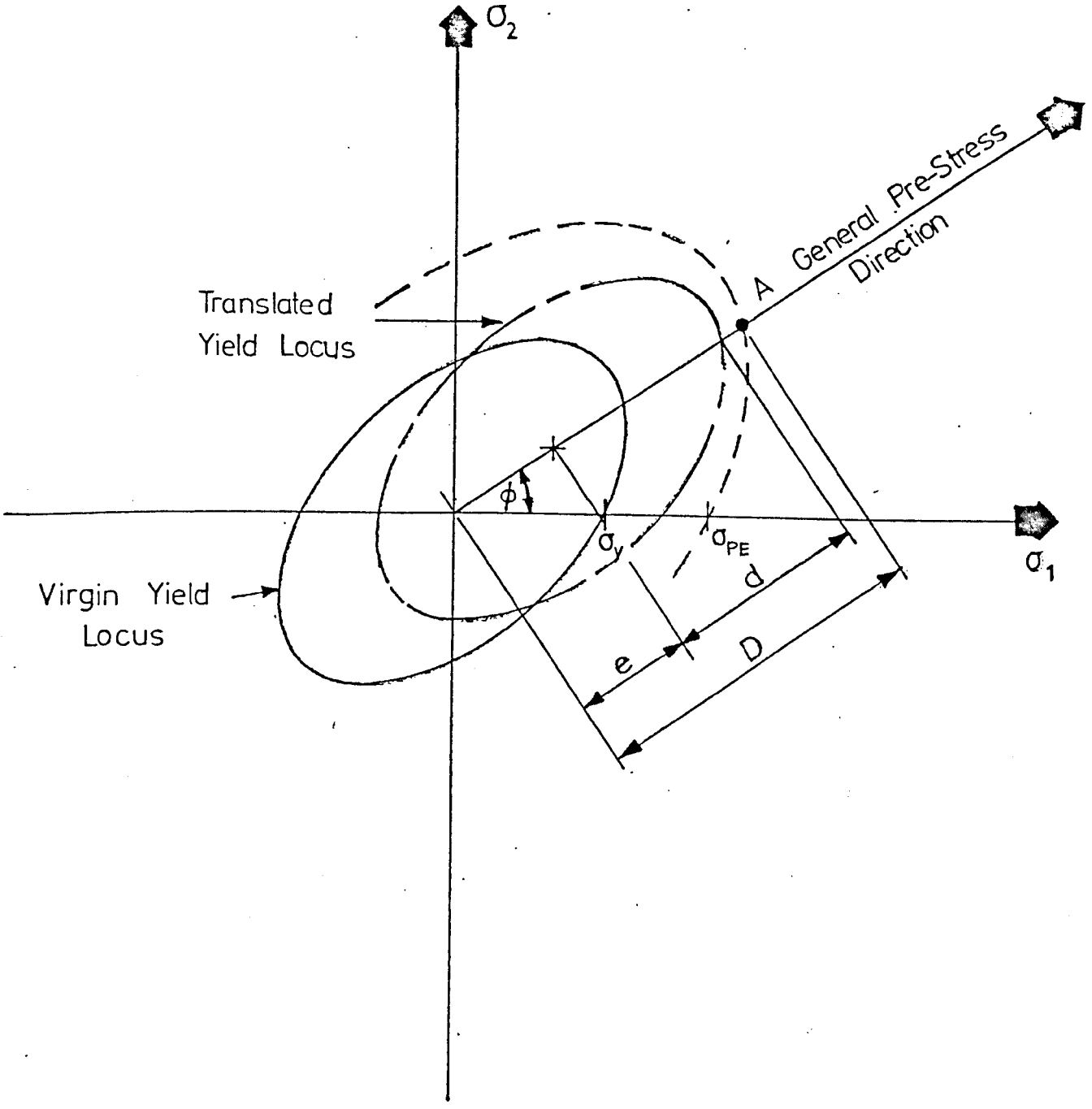

Fig. 5.6. The Yield Surface Model of Moreton et al. (93)

yield locus from the origin of stress as a function of the effective prestress σ_{pE} and the prestress direction ϕ. The model states that

$$\frac{e}{\sigma_y} = g(\phi) . \frac{\sigma_{pE}}{\sigma_y} - g(\phi)$$

where $g(\phi) = \frac{1}{1.115} . f(\phi)$ and $f(\phi)$ is defined as

$$f(\phi) = \left[\frac{1}{1 - \frac{1}{2} \sin 2\phi} \right]^{\frac{1}{2}}$$

For a uniaxial system of stresses $\phi = \pi/2$ and hence $f(\phi) = 1$. The model then reduces to

$$e = \frac{1}{1.115} (\sigma_{pE} - \sigma_y)$$

The yield locus is then assumed to move through the distance e without rotation or change of size. This model may be compared with the kinematic model for which the coefficient 1/1.115 above would be unity. The work of Moreton et al. showed that the direction of translation was that of the prestress vector. This uniaxial representation gives predictions of the prestress and reloading stress difference, the value of which decreases with the number of reloadings after a single prestress and increase with the magnitude of the prestress. This characteristic was also represented in the cyclic relaxation model of Jhansale (25) and is illustrated in Fig. 5.5(b). Because there was more relevant empirical data available from this study the model of Moreton et al. was employed. This model has been implemented in the non-linear kinematic hardening program and listed in Appendix C.3. Some experiments on the uniaxial cyclic plasticity of Type 316 stainless steel were conducted by Goodman (94). The results show that the above model when converted into a uniaxial representation agrees qualitatively.

Analytical work by Goodman and Goodall (96) on the constitutive relationships for this steel has been noted by the author although these could not be applied in the basic programs.

5.4 Results and Discussion

Some of the results of the computation are shown in Figs. 5.7, 5.8 and 5.9. Fig. 5.7 shows the computed accumulated strain against cycle numbers for a non-linear kinematic hardening idealization of Type 316 stainless steel. In Fig. 5.8, total strain accumulations are plotted on a Bree-like diagram as contours. A comparison between some of the predictions and experimental results for the total strain accumulation up to 90 cycles are shown in Fig. 5.9.

Firstly, the computer programs for elastic/perfect-plasticity and linear kinematic hardening were verified against the analytical solutions of Bree (2) and Mulcahy (21). The results which were in accord confirmed that the correct solution method was used. The results of the above publications have been reported in Chapter 2. Mulcahy's results showed that ratchetting will progressively decrease and eventually stop within a small number of cycles. This was due solely to monotonic strain-hardening. The constant ratchet rate of an elastic/perfectly-plastic material is therefore due to the absence of strain-hardening. Strain-hardening is therefore the primary characteristic for preventing ratchetting growth, that is, if no other mechanisms are acting.

Fig. 5.8 shows that due to strain hardening, it is possible to operate at stresses which would have led to collapse had the material been elastic/perfectly-plastic. The total (maximum) accumulated strains at shakedown which were used in this figure were low for most of the loads. For example, any load point lying between the Bree line and line F will accumulate a maximum strain which will always be less than 0.2% for any number of cycles. The shakedown area in the diagram is however not significantly increased when the strain limit is at 1%.

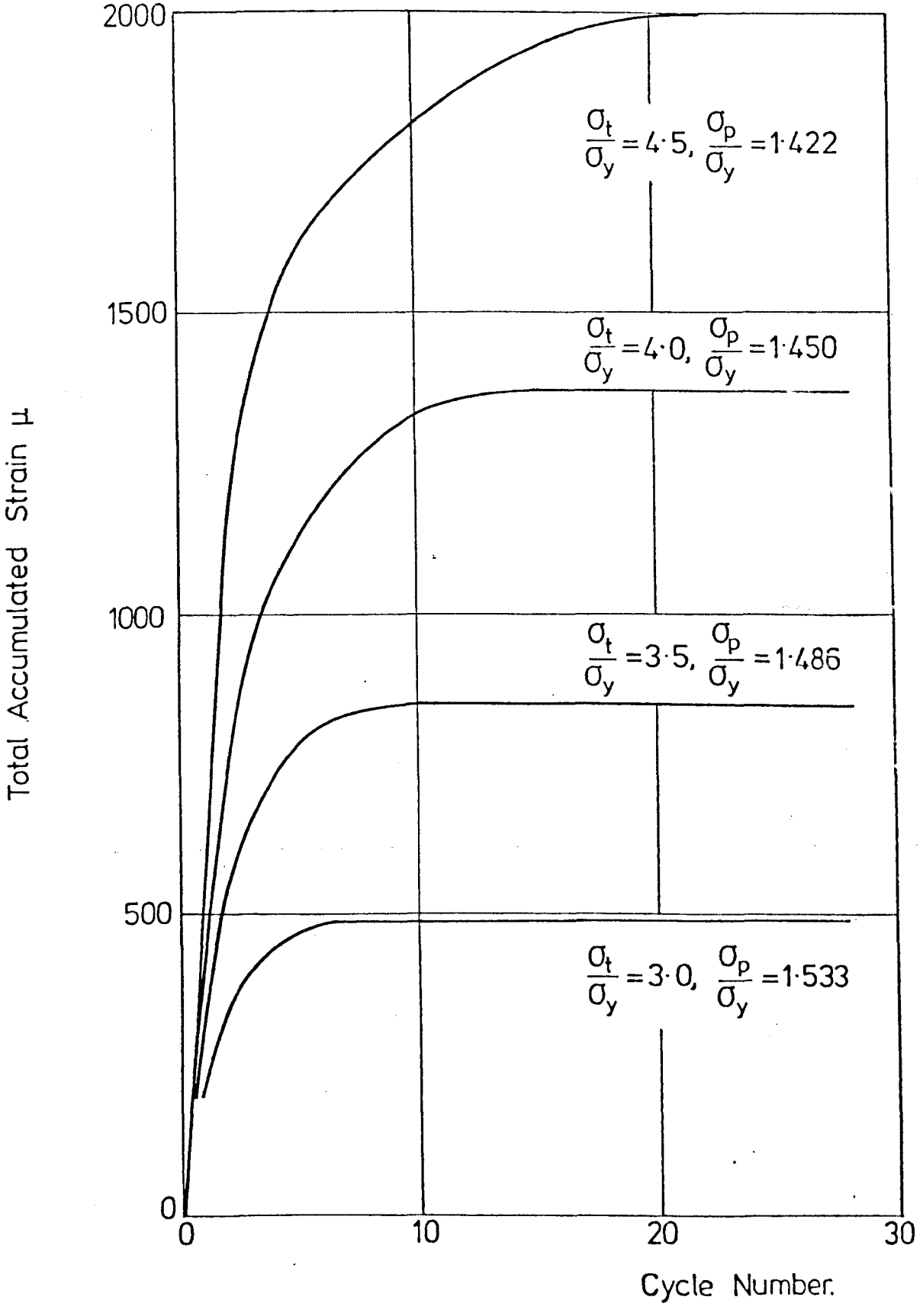

Fig. 5.7 Computed Accumulation of Strain Against Cycle Number from the Non-Linear Kinematic Hardening Material Model

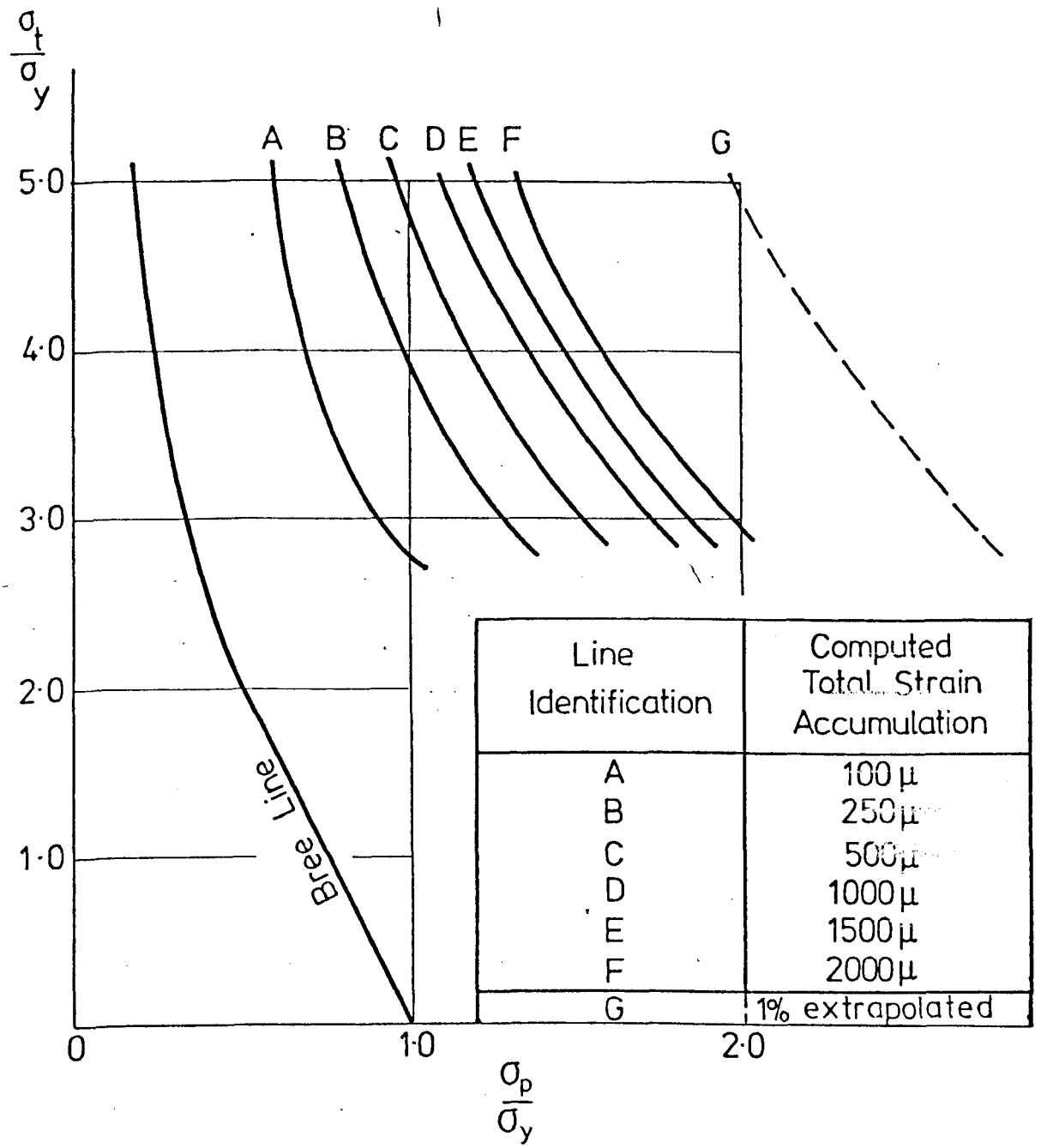

Fig. 5.8. Computed Contours of Total Accumulated Strain at Shakedown Based on the Non-Linear Kinematic Hardening Material Model

This contour has been extrapolated from the other results . Therefore accumulated strains are liable to increase very rapidly at points further away from the line F. The 1% strain limit is used by the ASME III Code Case N47 (6) to limit deformation and will be discussed further in Chapter 6.

It is seen therefore that strain hardening gives rise to a highly advantageous situation to the designer provided a certain amount of deformation can be tolerated. However in real materials and operating conditions, effects due to temperature, material degradation and a host of other environmentally dependent material properties tend to reduce this advantage.

The author's work on non-linear kinematic hardening also shows that ratchetting will cease after a cycle number which is less than that for linear-kinematic hardening at the same loads. Furthermore the final strain accumulated by that cycle number was also less. The difference in the final strain accumulation between the two models was insignificant and depended upon the graphical fitting of the experimental stress-strain curve to the respective material models. Variation of the fit upon the experimental curve alters the descriptive parameters used in the models and affects the computed results. It may be concluded that although the non-linear kinematic hardening model may produce more precise results, this gain over the linear kinematic model is not sufficiently significant for the increased complexity entailed in the programming of the former model to be worth its while. From the computing viewpoint, the linear kinematic hardening model would give answers of sufficient precision provided the curve fitting was made over a large strain range.

Although precision is an obvious requirement in these calculations

the accuracy of these predictions are poor when compared with ratchetting tests. In the experiments on mild steel and Type 316 stainless steel (described in Chapter 4) comparisons have been made against predictions made by Bree (elastic/perfectly-plastic) and the author's linear kinematic hardening results respectively. For mild steel comparisons, the tendency of the calculations has been to overestimate the total strain accumulation while the reverse occurs for stainless steel (see Section 4.3.6 and 4.4.6 for results and discussion for mild steel and stainless steel respectively). Briefly, it was found that Bree predicted the bound for the onset of ratchetting closely but in the ratchetting regimes, the initial ratchetting rates were greatly overestimated. The linear kinematic hardening model has altered the Bree Diagram by converting much of the ratchetting areas in shakedown areas (that is, shakedown which occurs only after an initial ratchetting phase). The experimental results for stainless steel showed that although the strain accumulation could be predicted reasonably for the first few cycles, the predictions will then 'fall' away towards a shakedown state and the experimental strain continues to 'climb' or ratchet, appearing to shakedown only after a large number of cycles. For some tests which were more severely loaded, shakedown did not occur even after 1000 cycles. Such tests showed the phenomena of 'continuous' ratchetting. For these tests the strain accumulation would be greatly in excess of predictions by the linear kinematic model after a large number of cycles. Fig. 5.9 illustrates this point by comparing the strain accumulation in a test at $\sigma_p/\sigma_y = 0.83$ and $\sigma_t/\sigma_y = 8.0$ against the non-linear kinematic hardening model (shown in the figure as the two lowest curves). The non-linear kinematic hardening model was compared with the knowledge that deviations from the predictions of linear kinematic hardening model would not be great.

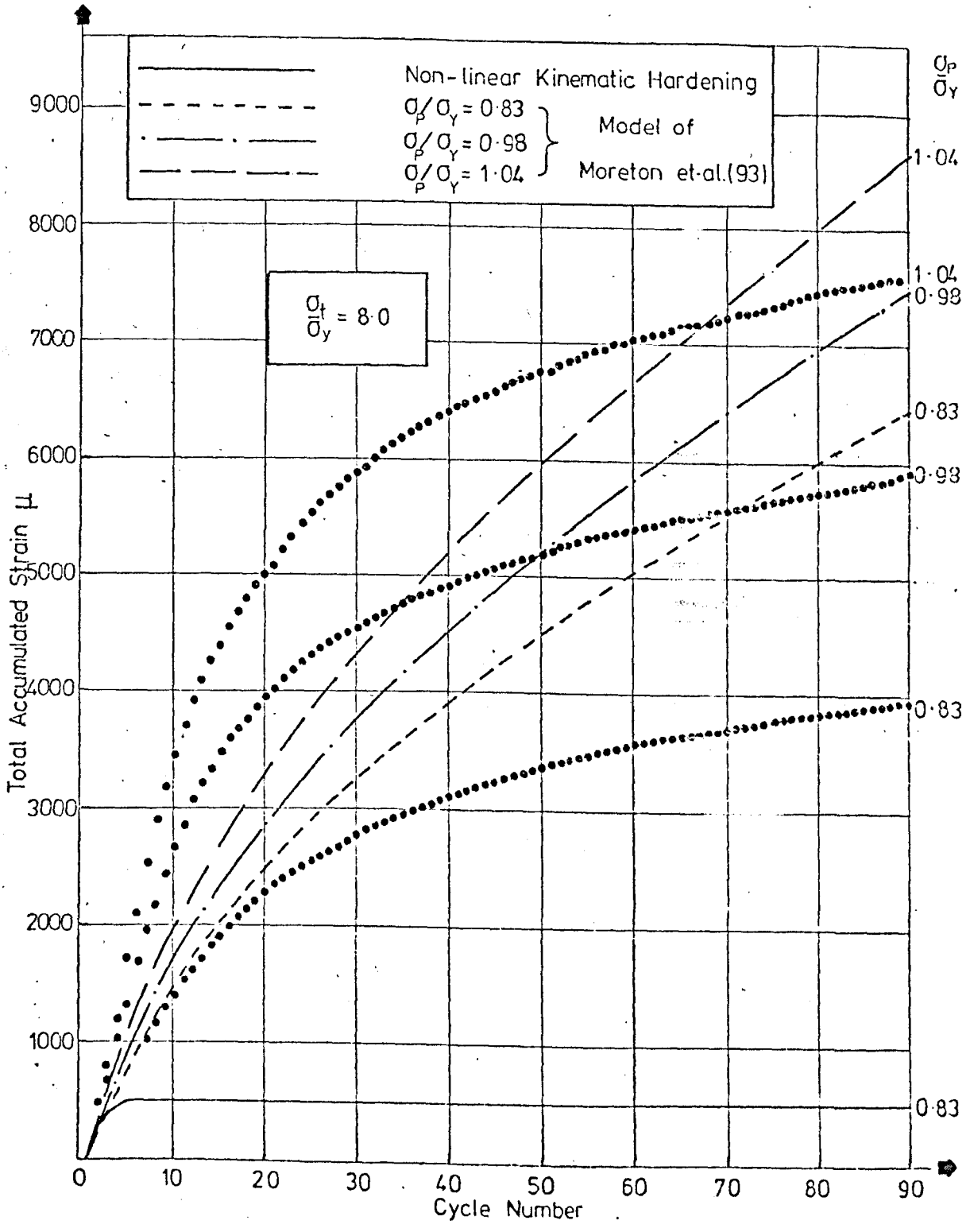

Fig. 5.9. Comparisons between some Predictions and Experimental Results for the Strain Accumulation against Cycle Numbers

Jhansale's Model (25) for transient cyclic softening predicted slightly more strain accumulation than the non-linear kinematic model at identical loads and cycle numbers. The strain accumulation, however, in common with that predicted by the other models, achieved a shakedown state after a few cycles due to the fact that the material soon attained a stabilized state in which the softening was halted. Continued cycling on the cyclically stabilized material accumulates no additional strains. Therefore the cyclic hardening and softening properties as proposed in the model will not be useful if these properties are only transient in nature. A form of continous cyclic softening in this model may be able to predict the large magnitudes of strain required but the model would be highly unrealistic. Continuous cyclic softening would imply that the material will ultimately be unable to support any load.

The model of Moreton et al. (93) when employed on this problem was able to provide the required large strain magnitudes and continuous ratchetting. The model was derived from monotonic tests on a range of steels of widely differing stress/strain characteristics including that of Type 316 stainless steel. When applied in the context of cyclic loading between two strain limits, the model gives a relaxation effect similar to that seen in Fig. 5.5(b). Fig. 5.9 also shows the comparison between this model and the experimental results for up to 90 cycles. It is seen that although the magnitudes of the accumulated strain were correct to within an order of magnitude initially, there was poor agreement at larger cycle numbers. Concerning ratchetting rates, limited experimental work to 5000 cycles show that ratchet strains at the same σ_t/σ_y and σ_p/σ_y combinations dropped to less than 1μ/cycle. Computations up to the same number of cycles show ratchet strains of the order of

6μ/cycle. Clearly, the model of Moreton et al. (93) used in these computations could be modified in the prestress factor (of which a value of 1.115 was used in the computation) to 'correct' for this variation. In view of the generality of the materials used in defining this factor, such a modification would not be considered unreasonable. Even if this was done, poor agreement during the early cycles of loading would persist due to cold creep effects. This has been explained in Section 4.4.6. in connection with tests at different cycle rates.

It is seen that so far the model of Moreton et al. has given the most promising results and it may be possible to speculate that the effects of cold creep and cyclic stress relaxation have been the major causes of the large initial strains and that the effect of cyclic stress relaxation which is continuous and persists longer causes the continuous ratchetting at large cycle numbers. It may also be that during initial straining the material relaxed more than that after a number of cycles have been imposed. After large numbers of cycles, the material relaxes to an asymptotic state which produces at each cycle a constant ratchet strain.

CHAPTER 6

DISCUSSION, CONCLUSIONS AND RECOMMENDATIONS FOR FUTURE WORK

6.1 Discussion

In the past chapters, the analytical, experimental and computational work have each been briefly discussed. In this chapter, the discussion will be further developed and brought together in a cohesive manner. The important results will be examined in greater detail and their implications on engineering problems brought into perspective. Where it is possible to correlate with similar work performed by other workers such correlations will be made. It should firstly be appreciated that the results and conclusions drawn are applicable mainly to the problem of an internally pressurised cylinder subjected to a cyclic thermal gradient through its wall thickness. Mention must also be made of the underlying assumptions which are inherent in Bree's uniaxial model. This is the modelling of biaxial thermal stress into a uniaxial stress case by means of a Poisson's factor of $\Delta T/(1-\gamma)$ where ΔT is the temperature difference between the wall surfaces and the stresses in the axial direction of the cylinder are neglected. These two main assumptions enabled the problem to be analysed with ease to yield conservative solutions.

Based on Bree's uniaxial model, the author has extended the analyses into cyclic loading sequences which were not considered by Bree. These cyclic loading sequences are the following: continuous thermal and cyclic pressure loading, in-phase cyclic thermal and pressure loading and out-of-phase cyclic thermal and pressure loading. The analyses were also repeated for the Bree sequence of loading (continuous pressure and cyclic thermal loading). Using a temperature independent elastic/perfectly-plastic material model, the solutions for all four sequences were obtained.

These solutions were in the form of expressions of the boundaries separating the regimes of structural behaviour. Fig. 3.11 has shown the plots of the Bree type diagrams for the loading sequences. Also, expressions for the ratchetting rates as functions of the normalized applied loads were obtained.

Examining Fig. 3.11, it is seen that the ratchetting regimes of types 1 and 2 cover the largest area in the Bree loading sequence. Both the Bree-type diagrams for the I.P. (In-Phase) and the O.P. (Out-of-Phase) loading sequences have smaller areas of the ratchetting regimes. The C.T. (continuous thermal and cyclic pressure) loading sequence shows no alternating plasticity or ratchetting behaviour in the Bree-type diagram. Therefore as far as the regimes of ratchetting behaviour are concerned, the Bree loading sequence has the greatest tendency to cause ratchetting than any other sequences that were investigated. From the design viewpoint of limiting ratchetting it was therefore the most conservative.

When the ratchetting rates were compared between the Bree and the I.P. or O.P. loading sequences, it was found that at the same loads, the Bree sequence had a larger value. As the loads are increased by the location of points towards the upper left of the Bree diagram, the rates converge in magnitude. This point is illustrated in Fig. 3.12. Although the Bree sequence appears to be worst in terms of ratchetting, it has a small area of the regime where alternating plasticity occurs. The other two sequences (I.P. and O.P.) have a larger area of the same regime. Also, some areas in the Bree diagram which exhibit shakedown behaviour have been converted into alternating plasticity behaviour. Therefore in the terms of alternating plasticity or fatigue failure, the I.P. and O.P. loading sequences are more severe. Therefore, there is in

effect a 'trading off' between alternating plasticity and ratchetting behaviour. Depending on which is the worst case in a practical situation (that is fatigue or gross deformation failure), it is not possible for one to decide which is actually the 'worst' sequence of loading application.

Because of the behaviour of the elements within and on the surfaces of the beam considered in the analyses, there are peculiarities and differences between identical regimes of structural behaviour in the four loading sequences. Taking the alternating plasticity regime of type 2 (P2) as an example, it is known that the Bree sequence will have symmetrical alternating plasticity cycling on both surfaces of the beam. This is to mean that the loopwidth of the hysteresis loops of the stress-strain behaviour of the outer surface is equal to that on the inner surface. The I.P. loading sequence is dissimilar in that the inner surface (here taken to be the hot surface) suffers from a smaller loopwidth than on the outer (cool) surface. The opposite situation occurs for the O.P. loading sequence, that is, the inner surface loopwidth is larger than that on the outside surface. This effect also occurs in the regime of R2 where there is a hysteresis loop superimposed on the ratchetting stress-strain behaviour. In the Bree loading sequence, the loopwidths are equal on both inner and outer surfaces while in the I.P. and O.P. loading sequences, the loopwidths are similarly differentiated as that in the P2 regime. Considering the P1 and R1 regimes, the loopwidths of all three cases are reduced. This, in the Bree sequence, implied that there is pure ratchetting without a superimposed hysteresis loop. In the I.P. loading sequence the inner surface which suffered from the smaller hysteresis loop now undergoes pure ratchetting while the outer surface maintains a reduced hysteresis loop. The completely reverse

situation occurs for the O.P. loading sequence. Analytically, the above differences in the surface behaviour are caused by the shifts in the elastic/plastic interfaces of the stress distribution within the beam when the loading sequences are imposed. Referring to Fig. 3.7 (b & c) for the Bree sequence, the stress distribution during the two successive half cycles at loadings corresponding to the R1 and R2 ratchetting regimes are shown. It is seen that the distributions during the successive half cycles are reflections of each other along the midsurface. In the I.P. and O.P. loading sequences, the surfaces of symmetry are not on the midsurface for the ratchetting regimes (R1 and R2). This is shown in Figs. 3.8 (b & c) and 3.9 (b & c) by making σ_x equal σ_Y. The distance a of the surface from the midsurface can be determined, for example, from Eqn. (3.43) and Eqn. (3.44) for the R1 regime. Each equation gives the distances a_n and $a_{(n+1)}$ for the elastic/plastic interfaces during ratchetting . The average value a is given by

$$
\begin{aligned}
a &= (a_n + a_{(n+1)})/2 \\
&= (\sigma_Y/K + 2\sqrt{(\sigma_t(\sigma_Y - \sigma_p)}/K + \tfrac{t}{2})/2 \\
&= \frac{t}{4} + \frac{\sigma_Y}{2K}\sqrt{(4Y - 4X + 1)}
\end{aligned}
$$

Hence a is dependent on the applied pressure (X) and thermal load (Y). A different expression can be obtained for the R2 regime. For the I.P. and O.P. loadings, this surface lies between the inner surface and the midsurface for the former and between the outer surface and the midsurface for the latter. The variation of the position of these surfaces are seen to be a direct result of the loading sequence and reflect upon the subsequent differences in behaviour at the beam surfaces which were described earlier.

It is thought that for practical applications of the models, these differences may have interesting consequences. On the assumption that loadings are of the type and sequence which is out-of-phase, the inner surface will be subjected to a more severe fatigue loading than the outer surface because of the differences in the hysteresis loopwidths of the wall surfaces. Fatigue failure will occur first on the inner surface whilst the outer surface is less damaged. This will thus give a false impression of the integrity of the wall should inspection rely on observation alone. The I.P. loading sequence has the more severe cyclic plasticity behaviour on the outer surface and is inherently a safer or more conservative loading sequence as far as the ratchetting and alternating plasticity regimes are concerned. This consideration does not apply to the Bree loading sequence because the alternating plasticity (P) and ratchetting regime (R2) were associated with equal loop-widths on both inner and outer surfaces.

A more important consequence of the determination of those surfaces of symmetry is in the determination of the onset of ratchetting. These surfaces will be the first to yield in two successive half cycles while the rest of the material yielded only once. The load condition at which this occurs is the load at the boundary of ratchetting. In the Bree sequence this surface lies on the midsurface and ratchetting occurs when the midsurface yields. Because of the symmetry of the stress distribution in the two half cycles, it necessarily implies that the midsurface will yield again in the next half cycle. To determine the ratchet rate, the width of the material which yields on both successive half cycles is multiplied by K/E. It is therefore seen that in the Bree sequence of loading, the yielding of the midsurface alone directly determines the onset of ratchetting. Therefore the

boundary for ratchetting depends only on the input of the yield stress of the material and is independent of any other properties such as monotonic or cyclic hardening, and other time dependent behaviour. These properties may however determine the amount of accumulated strain as a function of cycle number thereafter.

Similarly the ratchetting/non-ratchetting boundaries of the alternative loading sequences rely on the yielding of the respective surfaces of symmetry and not on the post yield properties of the material. Ratchet strains are obtained in the same way as above.

The final alternative loading sequence is that of continuous thermal loading with cyclic pressure loading. As seen in Fig. 3.11(b), only three regimes of behaviour were found possible. These were, elastic cycling and shakedown of the S1 and S2 types. The surfaces of symmetry cannot be found analytically and this substantiates the absence of the ratchetting or alternating plasticity regimes.

Although the Bree sequence of loading has arisen as a result of the development of the LMFBR, the alternative sequences of loading that have been developed can be applied to other problems of cyclic loading. It is thought that the I.P. loading sequence exists in many shell structures. In such structures, the application of cyclic internal pressure will cause simultaneous bending and membrane stresses. Also many pressure vessels and piping systems such as heat exchanger tubes operate under the in-phase cyclic thermal and pressure loading conditions. It should however be appreciated that the discussion of the above sequences are strictly valid for quasi-static loading whereby time dependent effects are ignored. Many real systems have a time lag or lead so that the sequence of loading is rarely completely in or out of phase. Such cases have been considered by Goodman (29), Philips (30) and Owais and Otter (34) where the load cycles were more like the conditions

present in the reactor.

Following the theoretical analyses, the computer studies are now discussed. It has been shown that the boundaries for the onset of ratchetting of the Bree and other loading sequences depend uniquely on the yielding of the symmetry surfaces. The amount of total strain accumulated then depended on the material model. For example, for elastic/perfectly-plastic material, the ratchet rate is constant for the particular load and the strain accumulated is hence proportional to the number of cycles. The aims of the computer studies were firstly to validate experimental data and secondly to investigate the predictions of the accumulated strain under the rules of various conventional and less conventional material models. The results of the latter will help to indicate which of the material properties are best able to simulate the experimental data whilst being the least complicated.

The first material model to be examined was that of elastic/perfect-plasticity. Programs were written for all four loading sequences, all based on the same material model. The results showed that the ratchet rates and the bounds separating the various regimes of structural behaviour obtained by Bree and the author's analytical results on alternative loading sequences could be repeated. This result verified the programs. When the material model was altered to that of linear kinematic hardening, the results of Mulcahy (21) could be repeated.

The next material model was one of non-linear kinematic hardening. Initially, the model was a piecewise linear fit to a stress-strain curve of Type 316 stainless steel. This was later replaced by a power law expression attributed to Osgood and Ramberg (23). Based on this model, cyclic hardening/softening was added. The cyclic hardening or softening stabilised stress-strain curve was represented by another power law

expression. The rules for cyclic hardening/softening were based on the procedure devised by Jhansale (25). The final model to be examined was based on a stress relaxation model using numerical parameters described by Moreton et al. (93). All the above models were examined only in the Bree sequence of loading because of the existence of experimental data from the wheel tests for comparison.

Firstly a comparison of the various material models at a single load point which is in terms of absolute stresses is discussed. When comparing the predictions by the models incorporating linear kinematic hardening, the yield stress is taken to be the corner in the bilinear fit to the experimental Type 316 stainless steel stress-strain curve. For non-linear kinematic hardening, the yield stress was that of first yield. For cyclic-softening, the stabilised cyclic stress-strain curve used the power law with an increase in the exponent $n = 9$ while the monotonic stress-strain curve had the exponent $n = 6$, where n is one of the constants of the power law.

On comparing the results of the accumulated strain against number of cycles, very similar curves were obtained. All curves achieved a shakedown state after a few cycles. The strains accumulated at shakedown were not significantly different. It is seen that in increasing order of magnitude, these are linear kinematic hardening, non-linear kinematic hardening followed finally by the cyclic softening model. On the cyclic softening model, the increased strain was due to the temporary or transient softening suffered by the material model. This softening was soon exhausted and the model reached a stabilised state. The model then ceases to be cyclic softening, instead it follows the non-linear hardening model. The relevance of the model shows that cyclic hardening or softening cannot achieve the strains accumulated

experimentally as long as a stabilised state is ultimately reached. However the softening cannot continue indefinitely because after a time the material will no longer be able to support any load. On this last point; the model cannot therefore be justified.

Comparison of the predicted strain accumulation shows, more importantly, that the addition of cyclic hardening/softening element into the model has few benefits over the increased complexity of calculation. The non-linear strain hardening model can be used to represent the stabilised cyclic-stress-strain curve and would ensure a conservative estimate of the strain accumulation. Also, the linear kinematic hardening model is able to predict strains which are in close agreement with the non-linear and cyclic models while being the most simple model. Provided the bilinear fit to the experimental monotonic stress-strain curve is made over a large strain range, it is certainly the most useful model on which to make preliminary estimations.

The above are only comparisons between the capabilities of three different models and not with experiments. The experimental strain accumulation at the same loads were used and comparisons show that these were greatly underestimated by the predictions (Fig. 5.9). It is not surprising that these differences between the experiment and prediction exist. This is because the models are strictly only valid for time independent effects and do not account for creep, rate effects and stress relaxation. The significance of time dependent effects is shown in Fig. 4.19. The figure shows the resulting strain accumulation of tests at the same loads but where the cyclic rates were varied for each test at 8, 13, 22, 41 s. It is observed that most strain was accumulated at the slowest cyclic rate of 41s and decreases with the cyclic rate. The greatest effect on the strain accumulation occurs in the initial

cycles (less than 600). In the following cycles, the strain rates were in close approximation to each other in all four tests. The strain rates in these later cycles tend to asymptotically approach zero but in the cycles investigated were regarded as the 'continuous ratchetting'. It is seen that the continuous ratchetting is a behaviour which is independent of the cyclic rate but dependent on the cycle number and on the applied load. The total strain accumulated was strongly influenced by the cyclic rate due to the large strains accumulated initially. The mechanisms causing the cyclic rate effect (on the initial strain accumulation) and the continuous ratchetting were explained as follows.

The cyclic rate effect was caused primarily by creep at room temperature. A slower cyclic rate allowed more creep strain to accumulate. Another effect which caused more strain to accumulate initially is that due to initial plastic strains of the virgin material. This latter effect is not dependent on the cyclic rate and contributed a large part of the initial strain accumulation in all the ratchetting tests. The continuous strain rates were thought to be caused by a stress relaxation mechanism. In this mechanism, the peak stress in the hysterectic stress-strain behaviour of each layer in the beam is relaxed to a stress below that which would have been attained monotonically. In the general redistribution of all the stresses in the layers, a net strain increment is incurred in order to achieve equilibrium with the external applied axial load. These mechanisms act in unison such that the total effect is a sum of the individual strengths of each mechanism. Cold creep is the dominant mechanism during the initial cycles while the stress relaxation is continuous in effect. The former is supported by work (see Section 2.7 (9)) which showed that the propensity of cold creep to recur is reduced by prior strain controlled cycling, the strain

accumulation characteristic described above may be explained. The explanation drawn out above is appreciative of the current lack of knowledge concerning this complex behaviour.

Having explained the possible mechanism for the strain accumulation of the Bree beam, the material model of Moreton et al. (93) was formulated and implemented into the non-linear kinematic hardening program. This model was utilized to implement the stress relaxation onto the stress-strain behaviour of the material. In this model under variation of strains in each element of the beam, the maximum stress due to monotonic strain hardening is not reached due to the applied stress relaxation. When the variation of strain has a maximum which exceeds that of the previous cycle, then an increment which is equivalent to the monotonic increase is added. Results from this program show that the magnitude of strain accumulation was more in accord with the strain accumulated experimentally (Fig. 5.9). Also when computed for a large number of cycles (2500), the continuous strain rate could be obtained. This showed an asymptotic tendency to approach a zero rate of accumulation and thus is also cycle dependent. This result has shown that cyclic stress relaxation can be one of the causes of the continuous strain rate as observed in the experiments. An explanation now exists to cover the poor performance of linear and non-linear kinematic hardening and cyclic hardening/softening models.

A main part of this work consisted of experimentation based on the Bree uniaxial model. The equivalent to the Bree uniaxial model as used by the author was a beam subjected to an axially applied tensile load and a bending load which was effected by deformation to a prescribed radius of curvature. The experimental technique utilized a strip of the test material which was tensioned by weights attached to the ends and curved around a wheel. It has been rigorously shown that the technique is

equivalent to applying a thermal gradient across the thickness of a beam while it is subjected to an axial load and restrained from bending. Theoretical and experimental efforts were made to ensure that the conditions were valid for the strip. Theoretical equivalence was easily shown by classical beam theory. The experimental work conducted was to show that the anticlastic effect on the strip did not induce large biaxial or transverse stresses such that a situation of uniaxiality is maintained. Tests were performed by attaching weights to the end of the strip and bending the strip around several radii of curvature. Results showed that for the dimensions of the strip used, the transverse stresses were negligible compared to the longitudinal stresses.

Three experimental programmes were conducted based on this concept. Experimental rigs were built to test specimens of mild steel, Type 316 stainless steel at only room temperature for the former and room and 400°C temperature for the latter. Strain accumulation at each cycle was obtained by measuring the extension of the strip and converting into strain. For elevated temperature extension measurement, a lever arm arrangement was used to separate the transducers from the hot area. Tests at 400°C involve the rebuilding of the rig to accommodate a heating enclosure and a microcomputer temperature control and data logging systems. The testing times were short (4ls) in order to reduce creep strains.

The important result for mild steel tests at room temperature was that the accumulated strain/cycle for the initial cycles was in agreement with the theoretical predictions near the ratchetting boundary (Fig. 4.10). The initial cycles were used as data because the later cycles may not be valid due to possible strain hardening of the material. However away from the ratchetting/non-ratchetting boundary, the initial accumulated strain/cycle was less than that predicted. Therefore the

predictions only agree where there are little or no accumulated strain (that is, near the boundary for the onset of ratchetting).

Over a number of cycles, the accumulated strain rate (or incremental strain) is seen to decrease (Fig. 4.9). The small number of cycles tested do not permit a determination of whether the strain will reach a shakedown state (as predicted by the strain/cyclic strain hardening material models) or continue to accumulate indefinitely.

When the entire set of data was considered in the form of contours of total strain accumulation after 80 cycles on the Bree Diagram, (Fig. 4.12) the contours lie in lines parallel to the Bree ratchetting/non-ratchetting boundary. The contour corresponding to a total accumulated strain of 1% was found on recalculation to require a newly defined yield stress of 1.7 times the elastic-plastic yield stress. This design stress will enable a designer to accumulate a maximum of 1% strain deformation within 80 cycles. The contour for zero strain accumulation coincided well with the Bree line for the onset of ratchetting. On the basis of the experiments on mild steel, it can be concluded that the technique has demonstrated its function by verifying the solutions of Bree insofar as the Bree ratchetting line is concerned. It has also demonstrated, that due to strain hardening inherent in the material, the predictions of Bree on ratchet strain rate have been over-pessimistic at all loads away from the Bree ratchetting line. It has to be appreciated, however, that the room temperature tests do not account for temperature dependent properties.

The second experimental programme was to experiment on commercially available Type 316 stainless steel strips. Element composition revealed that it was a variant of Type L of this steel. Heat treatment procedures for this commonly used reactor material was not clearly prescribed. However

it was felt that the most representative procedure for this material was to subject the strip to a solution heat treatment at 1050°C. This treatment was conducted in a vacuum furnace with the strips cut to length and laid flat in the furnace. The variability of this material was well known and so care was taken to ensure a sufficient supply of strip for all planned tests. The uniaxial stress-strain curve of the material was obtained for use in all calculations. It was not however possible to subject the strip to any cyclic stress-strain test which included compressive loading because of the problem of buckling. Cyclic properties required for formulation of the material model for cyclic hardening/softening had to rely on published data for this material at the relevant temperatures (Jaske et al. (80) and Jaske and Frey (83)). Due to this, the results of computer calculations on this model were necessarily informative only.

Ratchetting tests were performed in the same way as with mild steel and because of the improvements made on the rig, it was possible to extend the tests to many more cycles. It was decided to test up to 1000 cycles. This is double the number of operational cycles experienced in a lifetime of a LMFBR.

If a total strain accumulation of 1% strain is assumed to be accumulated in 200 cycles, it is possible to interpolate and find the loads at which this condition is met. The locus of the load locations was plotted on the Bree Diagram (Fig. 4.18) and resulted in a design curve. Similarly a line for 0.5% was plotted. The 1% total strain accumulation curve was calculated to correspond to a Bree line based on a yield stress of 200 MN/m^2. This stress corresponded to the yield stress based on elastic/perfectly-plastic idealisation. The approximation is not however exact, as the two curves cross each other at $\sigma_t/\sigma_Y = 5.0$. This may

lead to an underestimation of the allowable design area above σ_t/σ_Y= 5.0 and an overestimation below the same value.

Also drawn on Fig. 4.17 is the experimental boundary of ratchetting. This line separates tests which 'shakedown' within 100 cycles from those that do not. Although a small amount of strain was accumulated in the initial cycles to shakedown, it was thought that this will cause only a small error when compared to a line which is based on zero accumulated strain. A sample of the data was analysed to find that the separation between the two lines was equivalent to a shift on the σ_p/σ_Y axis of approximately 0.01 σ_Y (where σ_Y is the yield stress based on first yield). The relationship for the experimental boundary is nearly linear and can be represented by a straight line equation which in terms of absolute stresses (MN/m^2) is given below:

$$\sigma_t = 961.0 - 10.8\ \sigma_p$$

which applies in the range:

$$34.0 < \sigma_p < 83.0\ MN/m^2$$

A Bree boundary which would approximately fit this line would have a design stress of 132 MN/m^2.

Both ASME III (3) and Code Case N47 (6) have provisions for preventing the occurrence of thermal stress ratchetting. In ASME III Miller's solutions (1) which were identical to Bree (2) were used where the elastic/perfectly-plastic yield stress was defined at 1.5 S_m. S_m is the design stress recommended by the same code to be 0.9 $\sigma_{0.2}$ ($\sigma_{0.2}$ is 196.6 MN/m^2 for the Type 316 stainless steel material). Code Case N47 imposes a strain limit of 1% averaged through the thickness on the maximum accumulated inelastic strain for components operating at elevated temperatures. Although it is realised that N47 is applicable at temperatures greater than 427°C, the 1% strain limit is considered a suitable

limit on which to compare room temperature results. The non-linear kinematic model had been used to compute the 1% strain accumulation (Fig. 5.8). The model was based on the experimental stress-strain curve of the test material. This limit was found to correspond to a Bree boundary of a design stress of 245 MN/m^2. The strain of 1% was calculated to be the total strain accumulated at shakedown. In other words all loads corresponding to this limit will ultimately accumulate 1% at shakedown irrespective of the number of cycles required to achieve it. Having shown how the various limits were obtained it is now possible to discuss and compare against the experimental results. Both limits were outside their experimental counterparts as Table 6.1 will indicate.

Fig. 4.17 shows that the experiment ratchetting boundary and the experimental 1% limit both fall within the ASME III curve but lie outside the theoretical Bree line based on the first yield stress. Therefore the Bree line at first yield will certainly prevent ratchetting but will be too conservative whereas design based on the ASME III stress limit will be unsafe. It is estimated by extrapolation that the experimental strains accumulated at a load on the ASME III stress limit is approximately 3% after 200 cycles. The experimental boundary has a design stress of 132 MN/m^2 which is about half the 1.5 S_m value recommended by ASME III. This last statement implies that ASME III has overestimated the ratchetting onset boundary by about 100% as far as this work is concerned.

Having seen that strains of up to 3% can be experimentally achieved on the ASME III stress limit, it may be necessary to reduce the design stress. The definition of a suitable design stress has been an issue of contention over a number of years. The use of a lower design stress which is closer to the stress where there is initial yielding has given more consistent and reliable results in the determination of shakedown

	Design Stress (*) For Onset of Ratchetting	Design Stress (*) for 1% Strain Accumulation
Experimental (Type 316 Stainless Steel)	132 MN/m^2 (0.5)	200 MN/m^2 (0.75) after 200 cycles
Code Recommendations	265 MN/m^2 (1.0) after ASME III	245 MN/m^2 ‡ (0.9) after Code Case N47

Table 6.1 A Comparison of 'Design' Stresses for Ratchetting Boundaries Based upon Experimental Results and the Codes (ASME III and Code Case N47)

(*) Values in brackets are normalized w.r.t. 1.5 S_m (equal to 1.35 $\sigma_{0.2}$ or 265 MN/m^2)

‡ This value is extrapolated from computation of the total accumulated strain (Fig. 5.8) at shakedown using the non-linear kinematic hardening model. The model uses a curve fit to Type 316 stainless steel stress-strain curve.

factors of stainless steel pressure vessel components by Moreton and Moffat (94). The results of this work also show that a lower design stress does provide a better correlation with the experimental 'shakedown' boundaries on the Bree Diagram.

The experimental 1% boundary is also more conservative than the ASME III boundary. This line corresponded to a design stress of 200 MN/m^2 which also coincided approximately to the elastic/perfectly-plastic yield stress idealisation to the experimental stress-strain curve (Fig. 4.13). It is important to point out that the 1% strain is interpolated at the 200th cycle of the test results. At this cycle number shakedown was not yet attained and this value is liable to increase with a larger cycle number. This point has to be taken into consideration when comparing between the stress limits of the 1% experimental strain accumulation and that based on N47. The comparison shown in Table 6.1 shows that the experimental 1% limit is still more conservative than the N47 limit and the degree of conservativeness is expected to increase (that is, the experimental design stress will decrease) when greater numbers of cycles in excess of 200 are assessed.

It is desirable therefore to be able to estimate the proportion of strain accumulated with cycles. It is seen that at large cycle numbers experimental strain accumulation tends to be nearly static since the continuous ratchetting is of such small magnitude. Analysis of all the data of the Type 316 stainless steel test showed that two thirds of the total strain accumulated at the end of 1000 cycles tended to be accumulated within the first 100 to 400 cycles. More strain was accumulated in the early cycles. Therefore the 200 cycles used for estimating the 1% limit may be conservatively applicable for a wide range of operational cycles in the lifetime of a structure.

The continuous ratchetting phase seen in the experiments at large cycle numbers (exceeding 400) may not be experienced in the LMFBR design lifetimes. Therefore the strain accumulated during this phase which is low compared with the initial cycles may be of lesser importance than at first thought.

The final test combination was a single test at 400°C and at loads of $\sigma_t/\sigma_Y = 2.67$ and $\sigma_p/\sigma_Y = 1.41$ and at a cyclic rate of 4ls, where σ_Y is the room temperature yield stress. The result surprisingly showed less strain accumulation than a similar test at room temperature. Shakedown occurred after approximately 100 cycles with 0.1% strain accumulation while for the room temperature test at identical load, the strain was 0.2% at 100 cycles and ratchetting continued up to 1000 cycles (Fig. 4.23). Two possible explanations for the reduced strain accumulation are the increased cyclic hardening at 400°C and the reduced creep at elevated temperature.

Speculating on the basis of the single test result, two inferences are made in relation to the Code stress limits. Firstly, the reduced yield stress at a temperature of 400°C would cause an inward shift of the Bree ratchetting boundary (using the relevant ASME III design stress at temperature) on the Bree Diagram which is replotted on stress axes. Previously, the Bree Diagram was plotted on axes of stresses normalized to the first yield stress. Secondly, because of the lesser amount of strain accumulation and the reduced number of cycles to shakedown at 400°C, the experimental Bree ratchetting boundary would be shifted outwards. This thereby causes a net improvement in the agreement between experiment and the Codes. At the higher temperature of 400°C, a better agreement between experiment and the Codes is expected.

The test at elevated temperature affected the material properties

to the same extent through the strip thickness. Application of the curvature bending only implied a thermal stress gradient through the strip without actually imposing a real temperature on the surfaces. Therefore the temperature dependent properties such as yield stress remain constant throughout the strip thickness. In a real thermal stress situation, a temperature gradient across the thickness causes the temperature dependent properties to vary through the strip thickness. This difference was considered by Bree (2) who showed that temperature dependent yield stresses caused negligible variations of the ratchetting boundary (see Section 2.4) compared to mean temperature properties.

Comparison with the small number of published experimental works (Section 2.5) shows an interesting trend. This has been in spite of the differences in testing techniques, and testing temperatures. The Bree boundary for ratchetting was affected by the problems of the definition of the design stress while the ratchet rates in the initial cycles were affected by material variability.

On the agreement with the Bree boundary, the test results of Goodall and Cook (41) at 600°C on EN58J stainless steel were in accord with a boundary defined by elastic/perfectly-plastic idealisation to the stress-strain curve. This value was approximately 1.1 $\sigma_{0.2}$. Anderson (42) found that tests on Type 304 stainless steel at 649°C indicated that the ratchetting boundary corresponded to a design stress of 1.0 S_m (0.91 $\sigma_{0.2}$). Yamamoto et al. (44) performed tests on Type 304 stainless steel at 550° to 250°C and demonstrated that the ratchetting boundary will be in agreement if the design stress was 20% greater than $\sigma_{0.2}$ or 1.2 $\sigma_{0.2}$. The author's own experiments on mild steel showed agreement with the elastic/perfectly-plastic yield stress

while for Type 316 stainless steel at room temperature, the ratchetting boundary would agree on a design stress of 0.7 times $\sigma_{0.2}$. The expected boundary for ratchetting at 400°C for the same steel will be greater than the latter value of $0.7\,\sigma_{0.2}$. These comparisons appear to indicate a trend that as the test temperature rises, there is a gradual reduction in the separation between experimental boundaries and the ASME III boundary based on stress limits. However this separation will still exist at the maximum temperature tested since the ASME III limit is at $1.35\,\sigma_{0.2}$.

When the initial ratchet rates were compared, Yamamoto et al. found that the initial rates were greatly overestimated by Bree at loads away from the ratchetting boundary. This finding is in keeping with the author's experience with mild and stainless steel. This however could be due to the difference in test technique. Yamamoto et al. used a single test piece for all their tests therefore the possibility that residual stresses have reduced the strains exists. Goodall and Cook (41) and Anderson (42) both found agreement with the predicted initial ratchet rates. The tests of Goodall and Cook involved cycle times of 4 cycle/min. while for Anderson, dwell times were imposed such that there were about 10 to 16 cycles in 24 hours. It is therefore possible that creep strains were included in Anderson's results. The comparison was therefore not conclusive.

Finally the work described above may be applicable not only to LMFBR's (characterized by high cyclic temperatures and moderate pressures) but also to less specific areas such as those present in conventional power plants and PWR's (low cyclic temperature and high pressure) where thermal cycling superimposed on constant mechanical loads exists.

6.2 Conclusions

1. For an idealized elastic/perfectly-plastic material Bree-type diagrams have been obtained for I.P., O.P. and C.T. loading sequences. It has been found that the original Bree Diagram is the most conservative in designing against ratchetting whereas the I.P. and O.P. Bree-type diagrams are more conservative against fatigue. The C.T. Bree-type diagram is least conservative of all since it predicts shakedown at all loads.

2. The theoretical boundaries for the ratchetting/non-ratchetting regimes on the Bree, I.P. and O.P. loading sequences are uniquely dependent on the monotonic yield stress and are independent of the post yield characteristics of the material. When the stress at a critical layer in the wall/beam exceeds the yield stress during the first cycle, ratchetting is initiated.

3. While the boundary for ratchetting/non-ratchetting is dependent on the yield stress, the amount of strain accumulation caused as a consequence of an incursion into the ratchetting regime is dependent on the material model. For the elastic/perfectly-plastic material model, the cyclic rate of strain accumulation is constant whereas for a kinematically hardening material, the cyclic rate decreases to zero after a sufficient number of cycles.

4. Cyclic hardening or softening material models which achieve a stabilized or saturated cyclic stress state indicate that shakedown will occur after a sufficient number of cycles.

5. Predictions of strain accumulation using the linear and non-linear kinematic hardening models gave essentially the same results. Since the non-linear model required considerably greater computational effort it is concluded that this effort is not worthwhile

and the linear model is to be preferred.

6. Although the material models agree well amongst each other, these greatly underestimate the experimental strain accumulation of Type 316 stainless steel on two aspects. These are the magnitude of the strain accumulated and the low but continuous ratchetting rates at large cycle numbers.

7. For Type 316 stainless steel the experimental boundary for shakedown within the first 100 cycles does not coincide with the Bree boundary for ratchetting using a yield stress of 75.4 MN/m^2 (first yield). The experimental boundary required a 'yield' stress of 1.7 times the first yield (132 MN/m^2).

8. For mild steel, the experimental boundary for zero strain accumulation agrees well with the Bree boundary for ratchetting.

9. For both mild steel and Type 316 stainless steel, the strain accumulation rate during the initial cycles for tests at loads away from the respective experimental ratchetting boundaries do not agree with elastic/perfectly-plastic predictions.

10. For both test materials, the experimental boundaries are however in reasonable agreement to the shape of the Bree boundary.

11. As far as this work is concerned, the ASME III design stress for room temperature has been found inadequate in preventing ratchetting. A design stress value approximately 50% of that recommended is thought more suitable.

12. Similarly, the ASME III Code Case N47 limitation of 1% strain accumulation has been found to be a more conservative restriction than the design stress limitation. This conclusion is based upon computations using the non-linear hardening model and upon experimental

evidence. This is made in recognition that N47 is only relevant at above 427°C.

13. In the Type 316 stainless steel test, slower cyclic rates of the experiments were found to increase the rate of strain accumulation during the first few hundred cycles. Thereafter the rate of strain accumulation became independent of the cyclc rate and became only cycle number dependent. Some of the initial strain accumulation was due to cold creep which gradually becomes exhausted after a few hundred cycles. The 'continuous' ratchetting thereafter was caused by the cyclic relaxation of the material.

14. The cyclic relaxation model was able to predict to a satisfactory degree of accuracy the experimental strain accumulation in both the magnitudes and the 'continuous' rate of ratchetting. Hence, the cyclic relaxation model is a realistic model for predicting ratchet strains for Type 316 stainless steel.

15. The rig developed to conduct ratchet tests at 400°C has been shown by a single test to be a satisfactory technique. This single result indicates that at load conditions which produce ratchetting at room temperature, 'shakedown' was achieved at 400°C.

6.3 Recommendations for Future Work

1. Although this work has gone some way towards developing a greater understanding, the ratchetting mechanism of strain hardening materials is still not fully understood. The direction that future work should take is not clear, but it must initially be towards formulating a sound knowledge of the cyclic properties of material such as Type 316 stainless steel. This, together with some input of time dependent properties should enable the computer programs, developed during this work to make better estimates of the ratchetting rates. Such an approach is to be preferred over analytical solutions since the material models etc. are bound to be too complex to be handled by such means.

2. The work can now be extended to elevated temperatures and it is envisaged that a three dimensional Bree Diagram which incorporates an additional temperature axis could be obtained experimentally. Thus a 'surface' which defines the onset of ratchetting could be obtained for this one simple loading case. This work would in fact help that outlined in (1) above since from the one test reported here, whatever causes the 'continuous' ratchetting at room temperature is removed at 400^{o}C.

3. Ultimately, what is needed is some tests utilizing pressure vessels under various loading cycles at elevated temperatures. Such work requires the solution to the problem of strain measurement at elevated temperatures. In this work the problem has been circumvented using the wheel rig but the basic problem remains.

4. In this work, only the regime of ratchetting in the Bree Diagram was investigated in detail. The regime of alternating plasticity

which results in fatigue should be a subject to be investigated particularly in the O.P. and I.P. loading sequences.

REFERENCES

1. MILLER, D. R. - 'Thermal Stress Ratchet Mechanism in Pressure Vessels'. Trans. ASME, Series D, Vol. 81, No. 2, June 1959, pp. 190-196.

2. BREE, J. - 'Elastic-Plastic Behaviour of Thin Tubes Subjected to Internal Pressure and Intermittent High-Heat Fluxes with Application to Fast-Nuclear Reactor Fuel Elements'. J. of Strain Analysis, 1967, Vol. 2, 3, pp. 226-238.

3. A.S.M.E. Boiler and Pressure Vessel Code, Section III, Nuclear Power Plant Components. 1977, ASME, New York.

4. O'DONNELL, W. J. and POROWSKI, J. - 'Upper Bounds for Accumulated Strains due to Creep Ratchetting'. J. of Pressure Vessel Technology, Trans. ASME, Vol. 96, 1974, pp. 150-154.

5. A.S.M.E. Boiler and Pressure Vessel Code, Code Case 1592, 1974, ASME, New York.

6. A.S.M.E. Boiler and Pressure Vessel Code, Code Case N-47-12, 1977, ASME, New York.

7. ROBERTS, J. J. A. - 'Structural Materials in Nuclear Power Systems', Plenum Press, New York, 1981.

8. FAWCETT, S. - 'Nuclear Power Plant', Thermal Stress, Ed. Benham et al., Pitman Ltd., London, 1964, pp. 340-358.

9. BS5500 'Specification for Unfired Fusion Welded Pressure Vessels', British Standards Institution, 1976.

10. PRAGER, W. - An Introduction to Plasticity, Addison Wesley Publ. Ltd., 1959.

11. GILL, S. S. - 'A Simple Illustration of Incremental Collapse'. Bull. Mechanical Engineering Education, Vol. 6, No. 1, January 1967.

12. RUIZ, C. - 'The Inclusion of Incremental Collapse Problem in Undergraduate Courses'. Bull. Mechanical Engineering Education, Vol. 6, No. 1, January 1967.

13. HILL, R. - The Mathematical Theory of Plasticity, Oxford University Press, London, England, 1950, pp. 287-294.

14. EDMUNDS, H. G. and BEER, F. J. - 'Notes on Incremental Collapse in Pressure Vessels'. J. of Mechanical Engineering Science, Vol. 3, 1961.

15. BURGREEN, D. - 'The Thermal Ratchet Mechanism'. J. of Basic Engineering, Trans. ASME, Series D, Vol. 90, No. 3, 1968, pp. 319-324.

16. A.S.M.E. Boiler and Pressure Vessel Code, Section III, Nuclear Power Plant Components, Division 1, Subsection NB-3222.5, 1974.

17. BURGREEN, D. - 'Structural Growth Induced by Thermal Cycling'. J. of Basic Engineering, Trans. ASME, Series D, Vol. 90, No. 3, 196, pp. 469-485.

18. COFFIN, L. F. - 'A Study of the Effect of Cyclic Thermal Stresses on a Ductile Metal'. Trans. ASME, 1954, Vol. 76, p. 931.

19. BREE, J. - 'Incremental Growth due to Creep and Plastic Yielding of Thin Tubes Subjected to Internal Pressure and Cyclic Thermal Stresses'. J. of Strain Analysis, Vol. 3, No. 2, 1968, pp. 122-127.

20. FREDERICK, C. O. and ARMSTRONG, P. J. - 'Convergent Internal Stresses and Steady Cyclic States of Stress', J. Strain Analysis, Vol. 1, No. 2, 1966, p. 154.

21. MULCAHY, T. M. - 'Thermal Ratchetting of a Beam Element Having an Idealised Bauschinger Effect'. J. of Engineering Materials and Technology, Trans. ASME, Vol. 98, 1976, pp. 264-271.

22. MORETON, D. N. and NG, H. W. - 'The Extension and Verification of the Bree Diagram'. Paper L10/2, Vol. L, Trans. Sixth Int. Conf. Struct. Mech. in Reactor Techn., Paris, 1981.

23. RAMBERG, W. and OSGOOD, W. R. - 'Description of Stress-Strain Curves by Three Parameters'. NACA Report No. 902, Washington, July 1943.

24. NG, H. W., and MORETON, D. N. - 'The Bree Diagram - Origins and Literature: Some Recent Advances Concerning Experimental Verification and Strain-Hardening Materials'. Recent Advances in Creep and Fracture in Engineering Materials and Structures. Eds. Owen, D. R. J. and Wilshire, B., Pineridge Press, June 1982.

25. JHANSALE, H. R. - 'A New Parameter for the Hysteretic Stress-Strain Behaviour of Metals'. J. of Engineering Material and Technology, Trans. ASME, Vol. 97, January 1975, pp. 33-38.

26. LECKIE, F. A. - 'A Review of Bounding Techniques in Shakedown and Ratchetting at Elevated Temperatures'. W.R.C. Bulletin No. 195, June 1974, pp. 1-32.

27. PICKEL, T. W., YAHR, G. T., SARTORY, W. and GREENSTREET, W. L. - 'Study of Thermal Ratchetting Behaviour and Elastic Design Requirements'. High-Temperature Structural Design Methods for LMFBR Components, Quarterly Progress Report for period ending September 30, 1972, ORNL-TM-4058, p. 190, January 1973.

28. O'DONNELL, W. J., POROWSKI, J. S., CORUM, J. M., YAHR, G. T. and SARTORY, W. K. - 'Biaxial Model for Bounding Creep Ratchetting in Shells'. Paper L11/15, Trans. Sixth Int. Conf. Struct. Mech. Reactor Techn., Vol. L, Paris, 1981.

29. GOODMAN, A. M. - 'The Influence of Rapid Thermal Transients on Elastic-Plastic Ratchetting'. C.E.G.B. Berkeley Nuclear Laboratories, Report No. RD/B/N4492, February 1979.

30. PHILLIPS, J. - 'The Accumulation of Damage in Plates Subjected to Mechanical and Thermal Loading'. C.E.G.B. Berkeley Nuclear Laboratories U.K., Report No. RD/B/N4314.

31. ROBINSON, E. L. - 'Effect of Temperature Variations on the Long Time Rupture Strength of Steels'. Trans. ASME, Vol. 74, 1952, pp. 777-784.

32. MINER, M. A. - 'Cumulative Damage in Fatigue'. J. of Applied Mechanics, Trans. ASME, Vol. 12, 1945, pp. A159-164.

33. ABO-EL-ATA. - 'Simplified Methods in Pressure Vessel Analysis'. Pressure Vessel and Piping Division Publication (PVP-PB-029), Ed. Barsoum, R. S., 1978, ASME, New York.

34. OWAIS, M. K. and OTTER, N. R. - 'Non-Linear Analysis of Beams Subjected to Mechanical and Thermal Cyclic Loading'. Paper C322/80, Proc. of the Inst. of Mech. Engrs, 1980.

35. AINSWORTH, R. A. and GOODALL, I. W. - 'Proposals for Primary Design Above Creep Threshold Temperature. C.E.G.B., Berkeley Nuclear Laboratories Report No. RB/B/N4394, October, 1978.

36. AINSWORTH, R. A. and GOODALL, I. W. - 'Simplified Methods of Inelastic Analysis for Components Operating Within the Creep Range', Paper L11/8, Vol. L., Trans. of Fifth Int. Conf. Struct. Mech. in Reactor Techn., Berlin, 1979.

37. WEIL, N. A. and RAPASKY, F. S. - 'Experience with Vessels of Delayed Coking Units'. Preprint of paper submitted to a session on pressure vessels, American Petroleum Institute, Division of Refining, Los Angeles, California, May 13, 1958.

38. COFFIN, L. F. - 'The Resistance of Materials to Cyclic Thermal Strains'. Paper No. 57, A-286.

39. MORETON, D. N. and MOFFAT, D. G. - 'Shakedown of Three Stainless Steel Pressure Vessel Components'. 3rd Int. Conf. on P.V. Tech., Tokyo, 1971, pp. 233-245.

40. PARKES, E. W. - 'Wings Under Repeated Thermal Stress'. Aircraft Engineering, Vol. 26, 1954, pp. 402-406.

41. GOODALL, I. W. and COOK, T. - 'Behaviour of Beams Subjected to Combined Direct Load and Varying Curvature'. Int. J. Mechanical Sciences, Vol. 14, 1972, pp. 137-143.

42. ANDERSON, W. F. - 'Ratchetting Deformation as Affected by Relative Variation of the Loading Sequence'. Part I - Design and Analysis, 2nd Int. Conf. Pressure Vessel Techn., San Antonio, Texas, USA, ASME, 1973, pp. 277-289.

43. ANDERSON, W. F. - 'Creep Ratchetting Deformation and Rupture Damage Induced by a Thermal Transient Stress Cycle'. Design for Elevated Temperature Environment, ASME, New York, 1971, pp. 1-11.

44. YAMAMOTO, S., KANO, J. and YOSHITOSHI, A. - 'Thermal Ratchetting Experiment of Type 304 Stainless Steel Pipes under Alternating Cold and Hot Thermal Shocks with Varying Axial Loads'. Elevated Temperature Design Symposium, ASME, New York, 1976, pp. 25-32.

45. CORUM, J. M., YOUNG, H.C. and GRINDELL, A. G. - 'Thermal Ratchetting of Pipes Subjected to Intermittent Thermal Downshock at Elevated Temperatures', 'Verification and Qualification of Inelastic Analysis Computer Programs', Eds. Corum, J. M. and Wright, W. B., Pressure Vessel and Piping Publication, 1975, ASME, New York.

46. CORUM, J. M. - 'Appendix Material Property Data for Elastic-Plastic Creep Analysis of Benchmark Problems'. Ibid.

47. CLINARD, J. A., CORUM, J. M. and SARTORY, W. K. 'Comparison of Typical Inelastic Analysis Predictions with Benchmark Problem Experimental Results'. Ibid.

48. PARKES, E. W. - Structural Effects of Repeated Thermal Loading, Thermal Stress, (Ed. Benham et al.), Pitman Ltd., London, 1964.

49. BRUNSVOLD, A. R., AHMED, H. U. and STONE, C. C. - 'Thermal Ratchetting with Kinematic Hardening in a Two-Bar Assembly with Unequal Areas and Properties'. J. Engineering Materials and Technology, Trans. ASME, Vol. 98, 1976, pp. 256-263.

50. MULCAHY, T. M. - 'An Assessment of Kinematic Hardening Thermal Ratchetting'. J. of Engineering Materials and Technology, Trans. ASME, Series H, Vol. 96, 1974, pp. 214-221.

51. MEGAHED, M. M. - 'Influence of Hardening Rule on the Elasto-Plastic Behaviour of a Simple Structure under Cyclic Loading'. Int. J. Mechanical Sciences, Vol. 23, 1981, pp. 169-182.

52. AINSWORTH, R. A. - 'Approximate Solutions for Creeping Structures Subjected to Periodic Loading'. Int. J. of Mech. Sci., Vol. 18, 1976, pp. 149-159.

53. GATEWOOD, B. E., GROTHOUSE, A. P. and VON HAUSEN, W. W., 'Experimental Data on Strain Accumulation Under Equivalent Cycling'. J. of Aeronautical Sci. Vol. 28, 1967, pp. 502-503.

54. SWAROOP, A. V. A. and McEVILY, Jr. A. J. - 'Analytical and Experimental Study of Thermal Ratchetting', Fatigue at Elevated Temperatures, ASTM. STP525 American Society of Testing and Materials, 1973, pp. 563-572.

55. UGA, T. - 'An Experimental Study on Thermal-Stress Ratchetting of Austenitic Stainless Steel by Three Bars Specimen'. Nuclear Engineering and Design, Vol. 26, 1974, pp. 326-335.

56. MEGAHED, M. M. - 'Behaviour of Simple Structures Under Cyclic Loading Conditions'. Parts 1 and 2, Department of Engineering, University of Leicester, Report No. 77-12/13, December 1977.

57. AINSWORTH, R. A. - 'An Experimental Study of a Three Bar Structure Subjected to Variable Temperature', Int. J. Mechanical Sciences, Vol. 19, 1977, pp. 247-256.

58. INOUE, K., NAKAGAWA, K. and FUJIYAMA, M. - 'Accumulation of Axial Strain of a Cylindrical Bar Under Combined Cyclic Torsion and Axial Load'. Technology Reports, Osaka University, Japan, 26 March, 1976, pp. 223-231.

59. NOZUE, Y., UDOGUCHI, T., ASADA, Y. and MITSUHASHI, S. - 'An Experimental Study on Cyclic Strain Induced Creep, Relationship between Different Modes of Stress and Strain Superposition'. Fracture 1977, Vol. 2, ICF4, Waterloo, Canada, June 1977, pp. 767-775.

60. LEBEY, J., ROCHE, R. L. and COUSSERAN, P. - 'Experimental Tests on Ratchet of Structural Elements Diagrams for Primary Tension and Secondary Twist', Paper C99/80, Proc. of the Inst. Mech. Engrs, 1980, pp. 281-285.

61. COUSSERAN, P., LEBEY, J., MOULIN, D., ROCHE, R. and CLEMENT, G., - 'Ratchetting - Experimental Tests and Practical Method of Analysis', Paper C208/80, Proc. of the Inst. Mech. Engrs, 1980, pp. 143-151.

62. ROCHE, R. L. and MOULIN, D. - 'Safety Margin Against Ratchetting in and below the Creep Range'. Paper E5/1, Trans. of the 5th Int. Conf. Struct. Mech. in Reactor Techn., 1979, Berlin.

63. KRAUS, H. - 'International Benchmark Project on Simplified Methods for Elevated Temperature Design and Analysis. Problem I - The Oak Ridge Pipe Ratchetting Experiment, Problem II - The Saclay Fluctuating Sodium Level Experiment'. Welding Research Council Bulletin No. 258, May 1980.

64. GOODMAN, A. M., - 'Incremental Plastic Deformation of a Cylinder Subjected to Cyclic Thermal Loading', Non-Linear Problems in Stress Analysis, Ed. Stanley, P., Applied Science Publishers Ltd., London, 1978, pp. 317-344.

65. PONTER, A. R. S. - 'Shakedown and Ratchetting below the Creep Range', Part 1: Design Codes, Material Ratchetting and the Behaviour of Some Simple Structural Configurations'. University of Leicester, Report 81-7, May 1981.

66. RIVOLET, J. C. and MOULIN, D. - 'Ratchetting Experiments on a Cylindrical Vessel with Variable Sodium Level', Paper L10/6, Trans. Sixth Int. Conf. Struct. Mech. in Reactor Techn., Paris, 1981.

67. COUSIN, M., JULLIEN, J. F., LAUER, H., VOUILLOUX, F. and CASIER, J. - 'Rochet Thermique: Experimentation'. Paper L7/6, Trans. Sixth Int. Conf. Struct. Mech. in Reactor Techn., Paris, 1981. (Translated to English).

68. ARNAUDEAU, F., ZARKA, J. and GERIJ, J. - 'Thin Circular Cylinder under Axisymmetrical Thermal and Mechanical Loading', Paper L615, Trans. Fifth Int. Conf. on Struct. Mech. on Reactor Techn., Berlin, 1979.

69. WOOD, D. S. - 'Mechanical Properties Data Needs in Type 316 Steel for Fast Reactor Application'. Paper 36, Metals Society International Conference on Mechanical Behaviour and Nuclear Application of Stainless Steel at Elevated Temperature, Varese, 1981.

70. LECKIE, F. A. - 'Approximate Procedures in High Temperature Design', Paper C273/77, Proc. of the Inst. of Mech. Engrs, 1977, pp. 37-44.

71. PONTER, A. R. S. and LECKIE, F. A. - 'Bounding Solutions for a Plate Subjected to Variable Surface Temperature'. J. of Applied Mechanics, Vol. 41, 1974, p. 941.

72. AINSWORTH, R. A. - 'Approximate Solutions for Creeping Structures Subjected to Periodic Loading'. Int. J. of Mechanical Sciences, Vol. 18, 1976, p. 149.

73. MROZ, Z. - 'An Attempt to Describe the Behaviour of Metals Under Cyclic Loads Using a More General Workhardening Model'. Acta Mechanica, Vol. 7, No. 2-3, 1969, pp. 199-212.

74. MROZ, Z. - 'On the Description of Anisotropic Hardening'. J. Mechs. and Physics of Solids, 15, 1967, p. 163.

75. PRAGER, W. - 'The Theory of Plasticity, A Survey of Recent Achievements', Proc. of the Inst. of Mech. Eng. Vol. 89, 1955, pp. 41-57.

76. ZIEGLER, H. - 'A Modification of Prager's Hardening Rule', Quart. Appl. Mech., Vol. 17, 1959, pp. 55-65.

77. WOOD, D. S. - 'Material Data for Severe Variable Loading', Paper C276/77, Proc. of the Inst. of Mech. Eng., 1977, pp. 65-70.

78. KREMPL, E. - 'An Experimental Study of Room-Temperature Rate Sensitivity, Creep and Relaxation of AISI Type 304 Stainless Steel', J. of Mech. and Phys. of Solids, Vol. 27, pp. 363-375.

79. WOOD, D. S. and WILLIAMSON, K. - 'Deformation Behaviour of Type 316 Steel at 400°C, UKAEA Report.

80. JASKE, C. E., MINDLIN, H. and PERRIN, J. S. - 'Development of Elevated Temperature Fatigue Design Information for Type 316 Stainless Steel'. Paper C163/73, Proc. of the Inst. Mech. Engrs, Conference Publication 13, 1973.

81. ELLIS, J. R., ROBINSON, D. N. and PUGH, C. E. - 'Behaviour of Annealed Type 316 Stainless Steel under Monotonic and Cyclic Biaxial Loading at Room Temperature, Nuclear Eng. and Design, Vol. 47, 1978, p. 115.

82. BLACKBURN, L. D. - 'Isochronous Stress-Strain Curves for Austenitic Stainless Steels', Proc. of the ASME Winter Annual Conference, 1972. New York, pp. 15-48.

83. JASKE, C. E. and FREY, N. D. - 'Long Life Fatigue of Type 316 Stainless Steel of Temperatures up to 593°C', Joint Conference of Pressure Vessels and Piping, Materials, Nuclear Engineering and Solar Divisions, ASME, June 21-25, 1981, Colorado.

84. GOODALL, I. W., HALES, R. and WALTERS, D. J. - '3rd I.U.T.A.M. Symposium on Creep in Structures', University of Leicester, 1980.

85. GOODALL, I. W., CHUBB, E. J. and WALTERS, D. J. - 'I.A.E.A. Specialist Meeting, Time and Load Dependent Degradation of Pressure Boundary Materials,' Innsbruck, 1978.

86. GOODALL, I. W. - 'Structures Subjected to Loading Above the Shakedown Limit at High Temperature', Paper C271/77, Proc. of the Inst. of Mech. Engrs. 1977, pp. 15-26.

87. TIMOSHENKO, S. P. and GOODIER, J. N. - Theory of Elasticity, McGraw Hill, New York (1951), p. 254.

88. COX, G. B. - 'A Guide to the Digitiser', Report NWD14, Edition 1, University of Liverpool Computer Laboratory, Nov. 1977.

89. NOLAND, G. S. (Editor) - 'The GHOST Graphical Output System', Report NWD26, Edition 1, University of Liverpool Computer Laboratory, April 1979.

90. STEPHEN, G. and WRIGHT, M. - 'Microprocessor Control of a Bree Test Rig'. Final Year Project Report, 1982, School of Engineering Science and Industrial Management, University of Liverpool.

91. STRONG, J.T. and DANIELS, W. J. S. - 'Determination of the Potential of a Full Bridge E.R. Strain Gauge for Creep Strain Measurement at 565°C', C.E.G.B. Berkeley Nuclear Laboratories U.K., Report RD/B/N3204, Nov. 1974.

92. MORETON, D. N. - 'Shakedown of Pressure Vessel Components made of Strain Hardening Materials'. Ph.D. Thesis, University of Liverpool, 1976.

93. MORETON, D. N., MOFFAT, D. G. and PARKINSON, D. P. - 'The Yield Surface Behaviour of Pressure Vessel Steels'. J. of Strain Analysis, Vol. 16, No. 2, 1981, pp. 127-135.

94. MORETON, D. N. and MOFFAT, D. G. - 'The Use of an Empirical Yield Surface Model in Predicting Shakedown Loads'. IUTAM Symposium/ France 1980. Eds. Hult and Lemaitre. Pub. Springer-Verlag, Berlin, p. 181.

95. GOODMAN, A. M. - 'Uniaxial Cyclic Plasticity in Type 316 Stainless Steel'. Risley Nuclear Development Laboratories, U.K. Private Communication.

96. GOODMAN, A. M. and GOODALL, I. W. - 'Constitutive Relations for Stainless Steels'. C.E.G.B. Berkeley Nuclear Laboratories, Report RD/B/5040N81, 1981. Also presented at the Conference on 'Mechanical Behaviour and Nuclear Applications of Stainless Steel at Elevated Temperature', Varese, Italy, May, 1981. Proceedings in print.

APPENDIX A

LIST OF ENGINEERING DRAWINGS

The following are engineering drawings of minor and major mechanical components of test rigs that were used in this work. These drawings are filed with the Drawing Office of the Mechanical Engineering Department and are referenced with drawing numbers.

Drawing No.	Title
	Four Point Bending Rig
ME.M.B.087	Blank Material
ME.M.B.087/1	T-Section Beam Specimen
ME.M.B.087/3	Tensile Specimen
ME.M.E.087/4	Assembly
ME.M.E.087/5	Main Welded Frame
ME.M.D.087/6	Top Welded Frame
ME.M.C.087/7	Bearing Housing
ME.M.C.087/8	Rollers
ME.M.B.087/9	Locating Bolt
ME.M.E.087/10	Components
ME.M.F.087/13	Grip Plate
	Room Temperature Wheel Rig
ME.M.E.091	Assembly
ME.M.E.091/1	Details
ME.M.E.091/2	Details
ME.M.E.091/3	Bedplate
ME.M.E.091/4	Rack Support Details
ME.M.E.091/5	General Details

Room Temperature Wheel Rig

ME.M.D.091/6	Details of Wheel
ME.M.D.091/7	Housing and Shaft
ME.M.D.091/8	Hub Wheel
ME.M.D.091/9	Wheels

Elevated Temperature Wheel Rig

ME.M.E.091/11	New Bedplate
ME.M.E.091/12	Hot Enclosure
ME.M.E.091/13	Hot Enclosure Housing
ME.M.E.091/14	New Shaft Detail
ME.M.E.091/15	Assembly
ME.M.E.091/16	General Details
ME.M.E.091/17	Insulation Cover
ME.M.E.091/18	Insulation Steel Jacket
ME.M.E.091/19	Heater Box and Duct
ME.M.E.091/20	Fan Duct
ME.M.E.091/21	Fan Box Duct
ME.M.E.091/22	Fan Motor Bracket
ME.M.E.091/23	Heater Element Assembly
ME.M.E.091/24	New Assembly
ME.M.C.091/26	Sindanyo Insulation Disc

APPENDIX B

BRIDGE CIRCUIT FOR STRAIN GAUGED CANTILEVER TRANSDUCER

It may be shown that for a bridge circuit shown in Fig. B.1(a), the output signal E is given by

$$E = \left[\frac{R_1R_3 - R_2R_4}{(R_1+R_2)(R_3+R_4)} \right] V \qquad B1$$

and the change in the output dE as a result changes in the four resistances is given by

$$dE = V. \frac{R_1R_2}{(R_1+R_2)^2} \left[\frac{dR_1}{R_1} - \frac{dR_2}{R_2} + \frac{dR_3}{R_3} - \frac{dR_4}{R_4} \right]$$

In a full Bridge Circuit using 120 ohm resistance strain gauges, i.e. $R_1 = R_2 = R_3 = R_4 = R$, the general expression is

$$dE = \frac{V}{4R} \left[dR_1 - dR_2 + dR_3 - dR_4 \right] \qquad B2$$

where V/4R is the constant of proportionality or bridge sensitivity. It now depends on how the strain gauges are arranged based on the knowledge of their expected behaviour that one can obtain the desired output. In most cases the maximising output signals in relation to small changes in resistance are often the primary aim of using a full bridge configuration as against other configurations such as half and quarter bridge. In the strain gauge cantilever transducer, the aims are

(a) to be able to measure the extension of the strip in a linear manner and

(b) to ensure that the configurations so devised do not measure unwanted effects such as slippage of strip on wheels and thermal strains.

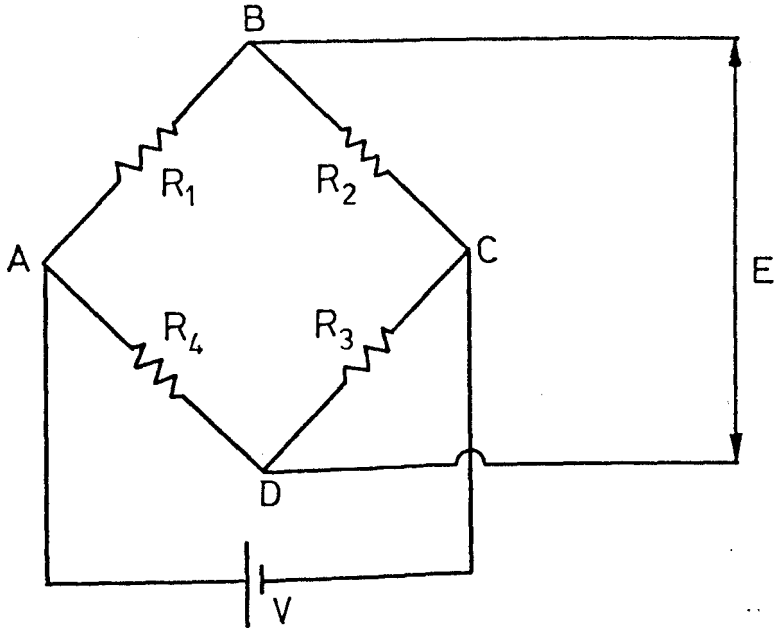

FIG. B·1 (a) Full Bridge Circuit.

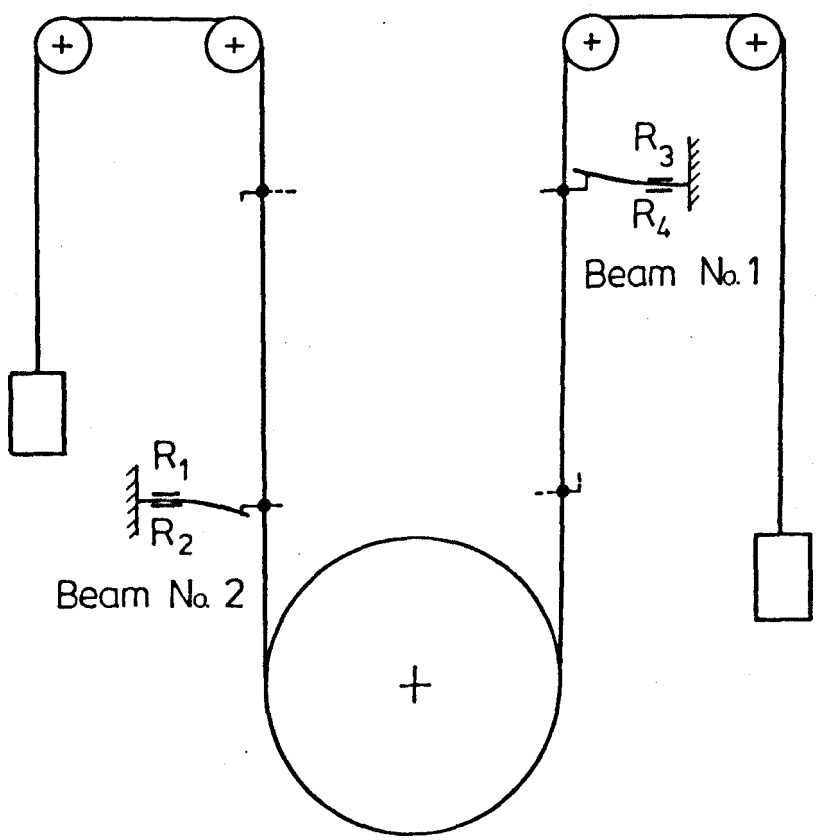

FIG B 1 (b) Configuration of Strain Gauged Displacement Transducers.

Such a configuration is shown in Fig. B.1(b) where beam Nos 1 and 2 are attached with the strain gauges as designated in the bridge circuit in Fig. B.1(a).

On bending the beams, the changes in resistance in the strain gauges are,

$$dR_2 = -dR_3$$

$$dR_1 = -dR_4$$

and dR_2 is not necessarily equal to dR_1. For a strip which is ratchetting dR_2 decreases with the cycle number while dR_1 increases with it. Substituting the above in Eqn. B2 so that it is in terms of dR_1 and dR_2 gives,

$$dE = \frac{V}{4R}\left[2(dR_1 - dR_2)\right] \qquad B3$$

Therefore the output signal dE depends on the difference in the resistance changes in R_1 and R_2 and this in a ratchetting strip increases with the cycle number. The output dE is related to the deflection or extension of the strip by calibration curves which is empirically obtained in Fig. 4.7. From the output dE, the deflection is obtained and this divided by the length of the test section of the strip gives the actual average strain of the strip.

In order to test whether this configuration is susceptible to slippage of the strip or the wheel over or under rotating its limits, let the small amount slippage be S (for Slip). Equal amount of deflection is caused to both beams in the same sense. The increased gauge resistance dR_S due to S is present in both beams and by Equation (B3) dR_S will be eliminated, viz.

$$dE = \frac{V.2}{4R}\left[(dR_1+dR_S) - (dR_2+dR_S)\right]$$

and the output signal remains unchanged. The same reasoning also applies for the effects of temperature on both beams showing that the bridge is self temperature compensating.

APPENDIX C1

PRØGRAM FØR THE BREE BEAM MØDEL SUBJECTED TØ THE BREE LØADING SEQUENCE FØR THE NØN-LINEAR KINEMATIC HARDENING MØDEL, "C" CHARACTERS IN THE FIRST CØLUMN ARE USED TØ SUPPRESS CERTAIN READ AND WRITE STATEMENTS AND CALLS TØ THE GHØST LIBRARY ØF PLØTTING SUBRØUTINES, THE PLØTTING SEGMENT PLØTS THE STRESS AND STRAIN DISTRIBUTIØNS THRØ-UGH BEAM THICKNESS.

```
C-----------------------------------------------------------------------
      DIMENSIØN SN2(50),SN3(50),S(5),SD4(50),SL(50),P(5),RA(5)
      DIMENSIØN ST1(50),ST2(50),ST3(50),SN6(61),ST6(61),F(50)
      DIMENSIØN PØINTS(12,45),PST2(5,50),PSN2(5,50),PS(50),PN(50)
      DIMENSIØN XXX(50)
      CØMMØN/LØØP/M
      CØMMØN/DATA/SN(61),ST(61),E(61)
      INTEGER V,XX,YY,U,RR,SS
C   YØUNGS MØDULUS=E(1),WØRK HARDENING MØDULI=E(2-61),STRAINS=SN
C   STRESSES=ST,PØINTS=P(N),ELEMENTS=K(I),LØAD CYCLE NØ=L(J)
C   UNITS :STRAINS=MICRØSTRAINS,STRESES=MN/M2
C   SN3(I),ST3(I)=PRESENT CYCLE,SN2(I),ST2(I)=PREVIØUS CYCLE
C   RB=RATIØ ØF BENDING TØ YIELD STRESSES
C   RT=RATIØ ØF TENSILE TØ YIELD STRESSES
C   C=STRAIN CHANGE IN BINARY SEARCH PRØCEDURE
C   MF=MRØZ FACTØR
      REAL MF
      MF=2.0
C NUMBER ØF PØINTS ØN FIT M
      M=61
C NUMBER ØF THRØUGH THICKNESS ELEMENTS K
      K=50
C NUMBER ØF HALF CYCLES L
      L=5
C BEAM DIMENSIØNS BXD
      A=0.0254
      B=0.199*A
      D=0.024*A
      READ(5,20)(SN(N),N=1,M)
20    FØRMAT(10F7.1)
      READ(5,30)(SL(N),N=1,M)
30    FØRMAT(15F5.1)
      DØ31 N=1,M
      ST(N)=SL(N)*1.3064*10.0**6
31    CØNTINUE
      E(1)=ST(1)/SN(1)
      DØ 2 N=2,M
      ST6(N)=ST(N)-ST(N-1)
      SN6(N)=SN(N)-SN(N-1)
      E(N)=ST6(N)/SN6(N)
2     CØNTINUE
      WRITE(6,35)
```

```
 35     FORMAT(/2H N,16X,5H E(N),18X,6H SN(N),16X,6H ST(N))
        WRITE(6,40)(N,E(N),SN(N),ST(N),N=1,M)
 40     FORMAT( I3,10X,E14.4,10X,F10.4,8X,E14.7)
C SELECT BENDING LOAD RATIO RB
        RB=2.6
        SB=ST(1)*RB
        RT=SB/E(1)
        R=D*0.5*10.0**6/RT
        ALPHA=ATAN(1.0/R)
C APPLY AXIAL LOAD RATIO RW
        RW=FLOAT(Y*10)*0.1
        T=RW*ST(1)
        W=T*B*D
        CALL STRAIN(T,X)
        SN1=X
        DO 1 I=1,K
        SN2(I)=0.0
        SN3(I)=0.0
        SD4(I)=0.0
        ST2(I)=0.0
        ST3(I)=0.0
 1      CONTINUE
C LOAD CYCLE
        DO 4 J=1,L
        MI=0
        C=500
 49     IF((J/2)*2.EQ.J)GOTO100
        DO 5 I=1,K
        SN3(I)=(D*(FLOAT(I)/FLOAT(K)-0.5))*10.0**6/R+SN1
 5      IF(ABS(SN3(I)).GT.SN(M))GOTO900
        CONTINUE
        GOTO 200
 100    DO 6 I=1,K
        SN3(I)=SN1
 6      CONTINUE
        GOTO 18
 200    IF(J-1)17,17,18
 17     DO12 I=1,K
        YI=SN3(I)
        CALL STRESS(YI,Y)
        SN3(I)=YI
        ST3(I)=Y
 12     CONTINUE
        GOTO 400
 18     CONTINUE
        DO 7 I=1,K
        SD4(I)=SN3(I)-SN2(I)
        IF(SD4(I),GT.0.0)GOTO510
        IF(ABS(SD4(I)).GT.MF*SN(1))GOTO500
        ST3(I)=ST2(I)+E(I)*SD4(I)
        Z=ST3(I)
        GOTO 450
 500    Z1=SN2(I)
        Z2=ST2(I)
        Z3=SN3(I)
```

```
109         CALL REVSTR(Z1,Z2,Z3,Z)
110         ST3(I)=Z
111  450    YI=SN3(I)
112         CALL STRESS(YI,Y)
113         IF(Y.GT.Z)GØTØ83
114         ST3(I)=Y
115         GØTØ 350
116  83     ST3(I)=Z
117         SN3(I)=YI
118         GØTØ350
119  510    YI=SN3(I)
120         CALL STRESS(YI,Y)
121         ST3(I)=Y
122  350    CØNTINUE
123  7      CØNTINUE
124  400    CØNTINUE
125         FT=0.0
126         DØ 9 I=1,K
127         F(I)=ST3(I)*B*D/FLØAT(K)
128         FT=FT+F(I)
129  9      CØNTINUE
130  C BINARY SEARCH FØR EQUILIBRIUM ØF FT AND W
131         IF(FT.LT.W)GØTØ410
132         IF(FT.GT.W)GØTØ420
133  420    IF(MI.EQ.2)GØTØ421
134         IF(MI.EQ.0)GØTØ422
135         C=C/2.0
136         SN1=SN1-C
137         MI=2
138         IF(C.LT.0.5)GØTØ430
139         GØTØ49
140  421    SN1=SN1-C
141         IF(C.LT.0.5)GØTØ430
142         GØTØ49
143  422    SN1=SN1-C
144         MI=2
145         IF(C.LT.0.5)GØTØ430
146         GØTØ49
147  410    IF(MI.EQ.1)GØTØ411
148         IF(MI.EQ.0)GØTØ412
149         C=C/2.0
150         SN1=SN1+C
151         MI=1
152         IF(C.LT.0.5)GØTØ430
153         GØTØ49
154  411    SN1=SN1+C
155         IF(C.LT.0.5)GØTØ430
156         GØTØ49
157  412    SN1=SN1+C
158         MI=1
159         IF(C.LT.0.5)GØTØ430
160         GØTØ49
161  430    DØ11I=1,K
162         SN2(I)=SN3(I)
163         ST2(I)=ST3(I)
```

```
      PSN2(J,I)=SN3(I)
      PST2(J,I)=ST3(I)
11    CONTINUE
C S=SURFACE STRAIN,SI=LOOPWIDTH,SC=CYCLIC STRAIN INCREMENT(C,S,I)
      S(J)=SN2(K)
      P(J)=SN2(1)
4     CONTINUE
C     WRITE(6,2003)
C2003 FORMAT(/ 20H ----------)
C     WRITE(6,600)R,W
C600  FORMAT(/ 14H WHEEL RADIUS=,F7.2,5X,18H WEIGHT EACH SIDE=,F10.4)
      SR=S(1)-S(2)
      SI=S(L)-S(L-1)-MF*SN(1)
      SC=S(L)-S(L-2)
C     WRITE(6,609)(S(J),J=1,5)
C609  FORMAT(/ 5(1X,E14.7))
      IF(SC.GT.1.0)GOTO770
      IF(SI.GT.1.0)GOTO750
      IF(S(1).GT.SN(1))GOTO780
      WRITE(6,80)RB,RW
 80   FORMAT(/ 4H RB=,E14.7,5X,4H RW=,E14.7,5X,10H E ELASTIC)
      GOTO635
780   IF(P(1).LE.-SN(1))GOTO790
      WRITE(6,82)RB,RW
 82   FORMAT(/ 4H RB=,E14.7,5X,4H RW=,E14.7,5X,13H S1 SHAKEDOWN)
      GOTO635
790   WRITE(6,83)RB,RW
 83   FORMAT(/ 4H RB=,E14.7,5X,4H RW=,E14.7,5X,13H S2 SHAKEDOWN)
      GOTO635
750   WRITE(6,84)RB,RW,SI
 84   FORMAT(/ 4H RB=,E14.7,5X,4H RW=,E14.7,5X,14H P PLASTIC,SI=,E14.7)
      GOTO635
770   IF((P(4)-P(2)).GT.1.0)GOTO730
      WRITE(6,85)RB,RW,SC
 85   FORMAT(/ 4H RB=,E14.7,5X,4H RW=,E14.7,5X,15H R1 RATCHET,SC=,E14.7)
      GOTO635
730   WRITE(6,86)RB,RW,SC
 86   FORMAT(/ 4H RB=,E14.7,5X,4H RW=,E14.7,5X,15H R2 RATCHET,SC=,E14.7)
      GOTO635
900   WRITE(6,902)
902   FORMAT(/ 20H ----------)
      WRITE(6,903)RB,RW
903   FORMAT(/ 4H RB=,E14.7,5X,4H RW=,E14.7,5X,14H DATA EXCEEDED)
      GOTO800
635   CONTINUE
800   CONTINUE
      WRITE(6,3000)
3000  FORMAT(1H1)
      WRITE(6,3002)
3002  FORMAT(/ 21H BREE DIAGRAM DETAILS)
      WRITE(6,3004)M
3004  FORMAT(/ 23H NUMBER OF DATA POINTS=,I3)
      WRITE(6,3005)L
3005  FORMAT(/ 22H MAXIMUN CYCLE NUMBER=,I1)
      WRITE(6,3006)K
```

```
 3006  FORMAT(/ 20H NUMBER OF ELEMENTS=,I3)
       WRITE(6,3007)B,D
 3007  FORMAT(/ 7H WIDTH=,F10.4,2H M,5X,11H THICKNESS=,F10.4,2H M)
       WRITE(6,3008)E(1),E(2)
 3008  FORMAT(/ 6H E(1)=,E14.7,5X,6H E(2)=,E14.7)
C  SUBROUTINE TO PLOT STRESS AND STRAIN DISTRIDUTION THROUGH BREE BEAM
       TST=PST2(1,100)/1000000.0
       BST=PST2(1,1)/1000000.0
       TSN=PSN2(1,100)/100.0
       BSN=PSN2(1,1)/100.0
       DO 4000 LM=1,L
       DO5000 LL=1,K
       XXX(LL)=FLOAT(LL)
       PS(LL)=PST2(LM,LL)/1000000.0
       PN(LL)=PSN2(LM,LL)/100.0
       WRITE(6,3009)XXX(LL),PS(LL),PN(LL)
 3009  FORMAT(10X,F10.4,10X,E14.7,10X,F10.4)
       IF(PS(LL).GE.TST)TST=PS(LL)
       IF(PS(LL).LE.BST)BST=PS(LL)
       IF(PN(LL).GE.TSN)TSN=PN(LL)
       IF(PN(LL).LE.BSN)BSN=PN(LL)
 5000  CONTINUE
 4000  CONTINUE
C      WRITE(6,4089)TST,BST,TSN,BSN
C4089 FORMAT(10X,2(E14.7,10X),2(F10.4,10X))
C      TSTS=TST+0.00001
C      BSTS=BST-0.00001
C      TSNN=TSN+0.1
C      BSNN=BSN-0.1
C      CALL PAPER(1)
C      CALL PSPACE(0.1,0.4,0.1,0.9)
C      CALL MAP(0.0,100.0,BSTS,TSTS)
C      DO89 IJ=1,L
C      DO29 LL=1,K
C      PS(LL)=PST2(IJ,LL)/1000000.0
C29    CONTINUE
C      CALL NSCURV(XXX,PS,1,K)
C89    CONTINUE
C      CALL BOX(0.0,100.0,BSTS,TSTS)
C      CALL PSPACE(0.6,0.9,0.1,0.9)
C      CALL MAP(0.0,100.0,BSNN,TSNN)
C      DO43 NJ=1,L
C      DO42 NN=1,K
C      PN(NN)=PSN2(NJ,NN)/100.0
C42    CONTINUE
C      CALL NSCURV(XXX,PN,1,K)
C43    CONTINUE
C      CALL BOX(0.0,100.0,BSNN,TSNN)
C      CALL GREND
       STOP
       END
C SUBROUTINE TO CALCULATE STRAINS GIVEN STRESS-STRAIN DATA
       SUBROUTINE STRAIN(T,X)
       COMMON/DATA/SN(61),ST(61),E(61)
       COMMON/LOOP/M
```

```
      IF(T.GE.ST(1))GØTØ1
      X=T/E(1)
      GØTØ4
1     CØNTINUE
      DØ1Ø N=2,M
      IF((T.GE.ST(N-1)).AND.(T.LE.ST(N)))GØTØ5
      GØTØ12
5     X=SN(N-1)+(T-ST(N-1))/E(N)
      GØTØ4
12    CØNTINUE
1Ø    CØNTINUE
4     RETURN
      END
C SUBRØUTINE TØ CALCULATE STRESS FRØM STRAIN
      SUBRØUTINE STRESS (YI,Y)
      CØMMØN/DATA/SN(61),ST(61),E(61)
      CØMMØN/LØØP/M
      IF(ABS(YI).GE.SN(1))GØTØ2
      Y=ABS(YI)*E(1)
      GØTØ5
2     DØ2Ø N=2,M
      IF((ABS(YI).GE.SN(N-1)).AND.(ABS(YI).LE.SN(N)))GØTØ11
      GØTØ12
11    Y=ST(N-1)+(ABS(YI)-SN(N-1))*E(N)
      GØTØ5
12    CØNTINUE
2Ø    CØNTINUE
5     IF(YI.GT.Ø.Ø)GØTØ4
      Y=-Y
4     RETURN
      END
C SUBRØUTINE TØ CALCULATE REVERSED STRESS
      SUBRØUTINE REVSTR(Z1,Z2,Z3,Z)
      CØMMØN/DATA/SN(61),ST(61),E(61)
      CØMMØN/LØØP/M
      DIMENSIØN SNI(61),STI(61)
      IF(Z3.GT.Z1)GØTØ2Ø
      DØ 8 N=1,M
      SNI(N)=Z1-SN(N)*MF
      STI(N)=Z2-ST(N)*MF
      IF(N.EQ.1)GØTØ6Ø
      IF((Z3.GE.SNI(N)).AND.(Z3.LE.SNI(N-1)))GØTØ31
      GØTØ4Ø
31    Z=STI(N)-(SNI(N)-Z3)*E(N)
      GØTØ3Ø
4Ø    CØNTINUE
8     CØNTINUE
      GØTØ3Ø
6Ø    IF(Z3.LT.SNI(1))GØTØ4Ø
      Z=STI(1)-(SNI(1)-Z3)*E(1)
      GØTØ3Ø
2Ø    DØ1Ø N=1,M
      SNI(N)=Z1+SN(N)*MF
      STI(N)=Z2+ST(N)*MF
      IF(N.EQ.1)GØTØ7Ø
```

```
      IF((Z3.GE.SNI(N-1)).AND.(Z3.LE.SNI(N)))GØT032
      GØTØ45
32    Z=STI(N)-(SNI(N)-Z3)*E(N)
      GØTØ30
45    CØNTINUE
10    CØNTINUE
      GØTØ30
70    IF(Z3.GT.SNI(1))GØTØ45
      Z=STI(1)-(SNI(1)-Z3)*E(1)
30    RETURN
      END
      FINISH
```

****

APPENDIX C2

PROGRAM FOR THE BREE BEAM MODEL SUBJECTED TO IN-PHASE SEQUENCE ON AN ELASTIC/PERFECTLY PLASTIC MATERIAL MODEL, MATERIAL MODEL IS FULLY INTEGRATED INTO PROGRAM.

```
      REAL K,K1,MZ
      DIMENSION E2(50),E3(50),E4(50),S2(50),S3(50),F(50),E7(5),E9(5)
      DIMENSION ER(6,20)
C BEAM DIMENSIONS AND MATERIAL PROPERTIES
      N=50
      A=0.0254
      EB=0.2
      ED=0.024
      B=EB*A
      D=ED*A
      MF=2.0
      TOL=1.0
      YSI=265.779*10.0**6.0
      YEI=1542.0
      E=YSI/YEI
      YS=202.740*10.0**6.0
      YE=YS/E
      IL=5
      WRITE(6,903)EB,ED,TOL,E,YS,YE,IL
903   FORMAT(1X,4H EB=,F5.3,2X,4H ED=,F5.3,2X,5H TOL=,F4.1,2X,3H E=,E14.
     17,2X,4H YS=,E14.7,2X,4H YE=,E14.7,2X,4H IL=,I2,2X,12H NEWMATERIAL)
      DO 12 IC=1,1
      RB=FLOAT(IC)*0.1+2.5
      R=E*D*10.0**6.0/(RB*YS*2.0)
      RI=R/A
C INITIAL STRESSES,STRAINS AND FORCES
      DO 5 I=1,N
      E2(I)=0.0
      E3(I)=0.0
      E4(I)=0.0
      S2(I)=0.0
      S3(I)=0.0
      F(I)=0.0
5     CONTINUE
      E8=0.0
      E10=0.0
      E11=0.0
      DO 15 L=1,1
      RW=FLOAT(L)*0.9
      ED=RW*YS/E
      WI=ED*B*D*E
      AP =WI/4.448
      WP=AP-3.652
      I=0
```

```
      MZ=2.0
C APPLY CYCLIC LOADS
      DO 10 J=1,IL
      M=0
      C=500.0
      E1=ED
49    IF((J/2)*2.EQ.J)GOTO100
C J IS ODD NUMBERED=HALF CYCLE UNDER BENDING AND AXIAL LOADS
      F2=WI
      DO 20 I=1,N
      E3(I)=D*(FLOAT(I)/FLOAT(N)-1.0)*10.0**6/R+E1
20    CONTINUE
      GOTO 200
C J IS EVEN NUMBERED=HALF CYCLE UNDER NO LOADS
100   F2=0.0
      DO 30 I=1,N
      E3(I)=E1
30    CONTINUE
200   CONTINUE
C STRESS AND STRAIN DISTRIBUTION
C     S2 STRESS ON PREVIOUS HALF CYCLE
C     E2 STRAIN ON PREVIOUS HALF CYCLE
C     E3 STRAIN ON PRESENT HALF CYCLE
C     E4 CHANGE IN STRAIN
      IF (J.NE.1) GOTO 300
      DO 40 I=1,N
      IF(ABS(E3(I)).GT.YE) GOTO 50
      S3(I)=E*E3(I)
      GOTO 60
50    IF (E3(I).LT.0.0) GOTO 55
      S3(I)=YS
      GOTO 60
55    S3(I)=-YS
60    CONTINUE
40    CONTINUE
      GOTO 400
300   DO 70 I=1,N
      E4(I)=E3(I)-E2(I)
      S3(I)=S2(I)+E*E4(I)
330   CONTINUE
      IF(ABS(S3(I)).LT.YS) GOTO 340
      IF (S3(I).GT.0.0) GOTO 335
      S3(I)=-YS
      GOTO 340
335   S3(I)=YS
340   CONTINUE
70    CONTINUE
C FORCES SUMMATION
400   DO 80 I=1,N
      F(I)=S3(I)*B*D/FLOAT(N)
80    CONTINUE
      F1=0.0
      DO 90 I=1,N
      F1=F1+F(I)
90    CONTINUE
```

```
      MZ=2.0
C APPLY CYCLIC LOADS
      DO 10 J=1,IL
      M=0
      C=500.0
      E1=ED
49    IF((J/2)*2.EQ.J)GOTO100
C J IS ODD NUMBERED=HALF CYCLE UNDER BENDING AND AXIAL LOADS
      F2=WI
      DO 20 I=1,N
      E3(I)=D*(FLOAT(I)/FLOAT(N)-1.0)*10.0**6/R+E1
   20 CONTINUE
      GOTO 200
C J IS EVEN NUMBERED=HALF CYCLE UNDER NO LOADS
  100 F2=0.0
      DO 30 I=1,N
      E3(I)=E1
   30 CONTINUE
  200 CONTINUE
C STRESS AND STRAIN DISTRIBUTION
C     S2 STRESS ON PREVIOUS HALF CYCLE
C     E2 STRAIN ON PREVIOUS HALF CYCLE
C     E3 STRAIN ON PRESENT HALF CYCLE
C     E4 CHANGE IN STRAIN
      IF (J.NE.1) GOTO 300
      DO 40 I=1,N
      IF(ABS(E3(I)).GT.YE) GOTO 50
      S3(I)=E*E3(I)
      GOTO 60
50    IF (E3(I).LT.0.0) GOTO 55
      S3(I)=YS
      GOTO 60
   55 S3(I)=-YS
   60 CONTINUE
   40 CONTINUE
      GOTO 400
  300 DO 70 I=1,N
      E4(I)=E3(I)-E2(I)
      S3(I)=S2(I)+E*E4(I)
  330 CONTINUE
      IF(ABS(S3(I)).LT.YS) GOTO 340
      IF (S3(I).GT.0.0) GOTO 335
      S3(I)=-YS
      GOTO 340
  335 S3(I)=YS
  340 CONTINUE
   70 CONTINUE
C FORCES SUMMATION
  400 DO 80 I=1,N
      F(I)=S3(I)*B*D/FLOAT(N)
   80 CONTINUE
      F1=0.0
      DO 90 I=1,N
      F1=F1+F(I)
   90 CONTINUE
```

```
109         IF(F1,LT,F2) GØTØ 410
110 C    BINARY  SEARCH  FØR CØMPATIBILITY AND EQUILIBRIUM
111         IF (M,EQ,2) GØTØ 421
112         IF (M,EQ,0) GØTØ 422
113         C=C/2,0
114         E1=E1-C
115         M=2
116         IF(C,LT,TØL)GØTØ430
117         GØTØ 49
118      421 E1=E1-C
119         IF(C,LT,TØL)GØTØ430
120         GØTØ 49
121      422 E1=E1-C
122         M=2
123         IF(C,LT,TØL)GØTØ430
124         GØTØ 49
125      410 IF (M,EQ,1) GØTØ 411
126         IF (M,EQ,0) GØTØ 412
127         C=C/2,0
128         E1=E1+C
129         M=1
130         IF(C,LT,TØL)GØTØ430
131         GØTØ 49
132      411 E1=E1+C
133         IF(C,LT,TØL)GØTØ430
134         GØTØ 49
135      412 E1=E1+C
136         M=1
137         IF(C,LT,TØL)GØTØ430
138         GØTØ 49
139      430 DØ 95 I=1,N
140         E2(I)=E3(I)
141         S2(I)=S3(I)
142         DI=FLØAT(I)
143       95 CØNTINUE
144         E7(J)=E3(N)
145         E9(J)=E3(1)
146 C       WRITE(6,607)(E3(I),S3(I),I=1,N,10)
147 10      CØNTINUE
148         E8=E7(IL)-E7(IL-1)-HZ*YE
149         E10=ABS(E9(1))-YE
150         E11=E7(IL)-E7(IL-2)
151         WRITE(6,609)(E7(J),J=1,IL)
152         WRITE(6,608)E8,E10,E11
153      608 FØRMAT(1X,4H HW=,E14,7,2X,4H BR=,E14,7,2X,4H TR=,E14,7)
154      609 FØRMAT (1H ,5(E14,7,2X))
155 C    607 FØRMAT (10X,E14,7,2X,E14,7)
156 C     CRITERIA FØR DIFFERENTIATING BEHAVIØUR ØF BEAM
157         IF(E11,GT,1,0) GØTØ770
158         IF(E8,GT,1,0)GØTØ750
159         IF(E7(1),GE,YE)GØTØ760
160         WRITE (6,610)RI,AP,RB,RW
161      610 FØRMAT (1X,3HRI=,F7,3,3HIN ,3HWP=,F7,3,4HLBF ,3HRB=,F6,3,4H RW=,F6
162        1,3,14H ELASTIC    E )
```

```
163         G0T0635
164      760 IF(E10,GT,1,0)G0T0614
165         WRITE (6,615)RI,AP,RB,RW
166      615 F0RMAT (1X,3HRI=,F7,3,3HIN ,3HWP=,F7,3,4HLBF ,3HRB=,F6,3,4H RW=,F6
167        1,3,14H SHAKED0WN  S1)
168         G0T0 635
169      614 WRITE (6,616)RI,AP,RB,RW
170      616 F0RMAT (1X,3HRI=,F7,3,3HIN ,3HWP=,F7,3,4HLBF ,3HRB=,F6,3,4H RW=,F6
171        1,3,14H SHAKED0WN  S2)
172         G0T0635
173      750 WRITE (6,620)RI,AP,RB,RW
174      620 F0RMAT (1X,3HRI=,F7,3,3HIN ,3HWP=,F7,3,4HLBF ,3HRB=,F6,3,4H RW=,F6
175        1,3,14H PLASTICITY P )
176         G0T0 635
177      770 IF(E10,GT,1,0)G0T0777
178         WRITE (6,625)RI,AP,RB,RW,RINC
179      625 F0RMAT (1X,3HRI=,F7,3,3HIN ,3HWP=,F7,3,4HLBF ,3HRB=,F6,3,4H RW=,F6
180        1,3,15H RATCHETTING R1,2X,6H RINC=,F9,3)
181         G0T0635
182      777 WRITE (6,778)RI,AP,RB,RW,RINC
183      778 F0RMAT (1X,3HRI=,F7,3,3HIN ,3HWP=,F7,3,4HLBF ,3HRB=,F6,3,4H RW=,F6
184        1,3,15H RATCHETTING R2,2X,6H RINC=,F9,3)
185      635 C0NTINUE
186       15 C0NTINUE
187       12 C0NTINUE
188         ST0P
189         END
190         FINISH
191  ****
```

****

APPENDIX C3

```
C
C
C       PRØGRAM FØR THE BREE SEQUENCE ØF LØADING BASED ØN  THE
C       MØDEL ØF MØRETØN ET AL,(93), SUBRØUTINE STRESS CØNTAIN
C       SUBRØUTINE REVSTR  WHILE  SUBRØUTINE  STRAIN HAVE BEEN
C       INTEGRATED INTØ THE MAIN PRØGRAM,USES ØSGØØD & RAMBERG
C       PØWER LAW, "C"  CHARACTERS ØN THE FIRST CØLUMN ARE FØR
C       SUPPRESSING READ AND WRITE CØMMANDS AND CALLING "GHØST"
C       PLØTTING SUBRØUTINES,  THE PLØTTING SEGMENT PLØTS  THE
C       STRAIN ACCUMULATIØN AGAINST CYCLE NUMBER,
C
C
C-----------------------------------------------------------------------
C
      DIMENSIØN SN2(50),SN3(50),SN(3),SD4(50),PSTR(2,2),CSS(2,2),ST2(50)
      DIMENSIØN ST3(50),F(50),PSTR1(3,50),CM2(2),SN4(2),ST1(50),XX(50)
      DIMENSIØN PST2(5,50),PSN2(5,50),PS(50),PN(50),ER(50),ZZ(50),CY(50)
      DIMENSIØN ZZZ(50),SF2(2,50)
      REAL MF,N,K1,M1,N1
      CØMMØN/DATA/E,YS,YE,MF
      CØMMØN/DATA1/YS1,YS2,YS3,YS4,YE1,YE2,YE3,E1,E2,E3,E4,ITER2,ITER4
      MF=2,0
      FM=1,0
      TØLP=0,001
      FY=0,89
      ND=2
C READ IN EXPERIMENTAL DATA FØR CØMPARISIØN WITH CALCULATIØNS
C IN PLØTTING SEGMENT
C     READ(5,214)(ZZ(I),ER(I),I=1,ND)
214   FØRMAT(2F8,3)
C     D04000LL=1,ND
C     ER(LL)=ER(LL)*287,39/2,0
C     ZZZ(LL)=FLØAT(LL-1)*10,0
C4000 CØNTINUE
C     WRITE(6,215)(ZZZ(LI),ER(LI),LI=1,ND)
C215  FØRMAT(2(E14,7,2X))
C INPUT BEAM DIMENSIØNS,CYCLE LIMITS,STRESS-STRAIN PARAMETERS
      ID=1
      JD=1
      K=50
C NUMBER ØF HALF CYCLES L
      L=21
      A=0,0254
      B=0,199*A
      D=0,016*A
      CF=4,448/(B*D)
      TC=1,0
      YS=34,7*CF
      YS1=0,0
      YS2=72,5*CF
      YS3=79,0*CF
      YS4=86,0*CF
```

```
      YE=400.0
      YE1=890.0
      YE2=3080.0
      YE3=4600.0
      E=YS/YE
      E1=E
      E2=13.0*CF/(YE2-YE1)
      E3=6.25*CF/(YE3-YE2)
      E4=15.0*CF/5600.00
      M1=0.9195552
      K1=(1.0-M1)/M1
      S1=47.81474*CF
      N=6.040963
      C=K1/(S1**(N-1.0)*E)
C WRITING SEGMENT
      WRITE(6,331)
331   FORMAT(27H TYPE 316,     MORETON MODEL)
      WRITE(6,332)M1,S1,N,YE
332   FORMAT(5H M1 =,E14.7,5H S1 =,E14.7,5H N  =,E14.7,5H YE =,E14.7)
      WRITE(6,335)YE1,YE2,YE3,E
335   FORMAT(5H YE1=,E14.7,5H YE2=,E14.7,5H YE3=,E14.7,5H E  =,E14.7)
      WRITE(6,333)E1,E2,E3,E4
333   FORMAT(5H E1 =,E14.7,5H E2 =,E14.7,5H E3 =,E14.7,5H E4 =,E14.7)
      WRITE(6,336)YS,YS1,N1,YS2,YS3
336   FORMAT(5H YS =,E14.7,5H YS1=,F4.1,5H CH =,F5.2,5H YS2=,E14.7,5H YS
     13=,E14.7)
      WRITE(6,337)YS4,MF,FM,K,L,HF
337   FORMAT(5H YS4=,E14.7,5H MF =,F4.2,5H FM =,F4.2,1X,5H K  =,I3,2X,5H
     1 L  =,I6,1X,5H HF =,E14.7)
      WRITE(6,338)FY
338   FORMAT(5H FY =,F7.5)
C APPLYING THE BENDING LOAD
      DO24IC=1,1
      RB=FLOAT(IC-1)*1.0+8.0
      RWS=1.0-RB/4.0
      RWP=1.0/RB
      SB=YS*RB
      RT=SB/E
      R=D*0.5*10.0**6/RT
      DO16II=1,1
      RW=FLOAT(II-1)*1.0+30.0/34.7
C APPLYING THE AXIAL LOAD
      T=RW*YS
      W=T*B*D
      TCYCLE=0.0
      PACCM=0.0
      IF(T.GE.YS)GOTO4007
      X=T/E
      GOTO2044
4007  X=T/E+C*T**N
2044  SN1=X
      WRITE(6,334)RB,R,RW,T
334   FORMAT(5H RB =,E14.7,5H R  =,E14.7,5H RW =,E14.7,5H T  =,E14.7)
C INITIALISING STRESSES,STRAINS,FORCES AND OTHER SETTINGS
      DO1I=1,K
```

```
      SN2(I)=0.0
      SN3(I)=0.0
      SD4(I)=0.0
      ST2(I)=0.0
      ST3(I)=0.0
      SF2(1,I)=2.0
      SF2(2,I)=2.0
      IF(I.GT.2)GØTØ1
      PSTR(1,I)=0.0
      PSTR(2,I)=0.0
      CSS(1,I)=20.0*10.0**6.0
      CSS(2,I)=20.0*10.0**6.0
1     CØNTINUE
      Z4=0.0
      ITER1=0
      ITER2=0
      DØ4J=1,L
      CM=100.0
      ITER3=0
      MI=0
      IF(((J/2)*2.NE.J).AND.(J.GT.4))GØTØ159
      IF(J.LT.5)GØTØ49
      M=2
      SN1=SN4(M)
      CM=CM2(M)
      GØTØ49
159   M=1
      SN1=SN4(M)
      CM=CM2(M)
49    ITER4=0
      ITER1=ITER1+1
C     WRITE(6,114)SN1,C
114   FØRMAT(2(E14.7,2X))
      ITER3=ITER3+1
      IF(ITER3.GT.100)GØTØ16
      IF((J/2)*2.NE.J)GØTØ100
C J IS EVEN NUMBERED=HALF CYCLE UNDER AXIAL AND BENDING LØADS
      M=2
      MF=2.0
      DØ5I=1,K
5     SN3(I)=(D*(FLØAT(I)/FLØAT(K)-0.5))*10.0**6/R+SN1
      GØTØ 18
C J IS ØDD NUMBERED=HALF CYCLE UNDER AXIAL LØAD ØNLY
100   M=1
      DØ6I=1,K
      SN3(I)=SN1
6     CØNTINUE
      IF(J-1)17,17,18
17    DØ12I=1,K
12    ST3(I)=T
      GØTØ 400
18    CØNTINUE
      DØ7I=1,K
      ITER4=0
      Z1=SN2(I)
```

```
      Z2=ST2(I)
      Z3=SN3(I)
      IF(I.GE.3)GØT0134
      CS=20.0*10.0**6.0
      Z4=PSTR(M,I)
      GØT0135
134   CS=10.0*10.0**6.0
      Z4=ABS(ST3(I-1)+ST3(I-1)-ST3(I-2))
135   CØNTINUE
      CD=CS/MF
      ZD=ABS(((Z3-Z1)/MF-YE)/FM+YE)
      ZS=ABS(Z2-Z4)/MF
      CALL STRESS(ZD,ZS,C,N,CD,Y)
      IF(Z3.GE.Z1)GØT02067
      Z=Z2-Y*SF2(M,I)
      GØT02057
2067  Z=Z2+Y*SF2(M,I)
1111  FØRMAT(I3)
2057  CALL STRESS(Z3,Z4,C,N,CS,Y)
      IF(Y.GE.Z)GØT083
      ST3(I)=Y
      GØT0 7
83    ST3(I)=Z
7     CØNTINUE
400   CØNTINUE
C FØRCES SUMMATIØN
      FT=0.0
      DØ9I=1,K
      F(I)=ST3(I)*B*D/FLØAT(K)
      FT=FT+F(I)
9     CØNTINUE
C BINARY SEARCH FØR EQUILIBRIUM AND CØMPATIBILITY
      IF((FT-W).GT.TØLP*W)GØT0420
      IF((FT-W).LT.-TØLP*W)GØT0410
      GØT0430
420   IF(MI.EQ.2)GØT0421
      IF(MI.EQ.0)GØT0422
      CM=CM/2.0
      SN1=SN1-CM
      MI=2
      GØT049
421   SN1=SN1-CM
      GØT049
422   SN1=SN1-CM
      MI=2
      GØT049
410   IF(MI.EQ.1)GØT0411
      IF(MI.EQ.0)GØT0412
      CM=CM/2.0
      SN1=SN1+CM
      MI=1
      GØT049
411   SN1=SN1+CM
      GØT049
412   SN1=SN1+CM
```

```
      MI=1
      GØT049
430   CØNTINUE
      DØ11I=1,K
      SN2(I)=SN3(I)
      ST2(I)=ST3(I)
C     PST2(J,I)=ST2(I)
C     PSN2(J,I)=SN2(I)
      PSTR1(3,I)=PSTR1(2,I)
      PSTR1(2,I)=PSTR1(1,I)
      PSTR1(1,I)=ST3(I)
      IF((J/2)*2.NE.J)GØT02090
      CY(I)=FY*(ABS(ST3(I))-YS)
      SF2(M,I)=(CY(I)-ABS(ST3(I))+3.0*YS)/YS
      GØT02091
2090  SF2(M,I)=MF
2091  IF(I.GT.2)GØT011
      IF((J.LT.3).ØR.(PSTR1(1,I).EQ.PSTR1(3,I)))GØT011
      PSTR(M,I)=ABS(ST3(I)+(PSTR1(1,I)-PSTR1(3,I))*0.1)
      CSS(M,I)=ABS(PSTR1(1,I)-PSTR1(3,I))
C     PSTR2(J+2,I)=PSTR(M,I)
C     PSTR4(J+2,I)=CSS(M,I)
11    CØNTINUE
C     WRITE(6,1112)(SF2(M,I),I=1,K)
1112  FØRMAT(5(F5.2,1X))
      IF(J.EQ.2)S=SN2(K/2)
      SN(3)=SN(2)
      SN(2)=SN(1)
      SN(1)=SN2(K/2)
      STMS=ST3(K/2)
      WRITE(6,2078)SN(1),STMS
      IF(J.LT.3)GØT044
      IF(SN(1).EQ.SN(3))GØT02077
      SN4(M)=SN(1)+(SN(1)-SN(3))*0.2
      CM2(M)=ABS(SN(1)-SN(3))*2.0
C     PSTR3(J+2)=SN4(M)
C     PSTR5(J+2)=CM2(M)
2078  FØRMAT(3(2X,E14.7))
44    IF((J/2)*2.NE.J)GØT04
2077  RATS=(SN(1)-SN(3))*TC
      IF(RATS.LT.1.0)GØT02004
      NCYCLE=J/2
C     TCYCLE=FLØAT(NCYCLE-1)
C     XN(NCYCLE)=FLØAT(NCYCLE-1)
      ACCM=(SN(1)-S)*TC
C     IF(ACCM(NCYCLE).GT.PACCM)PACCM=ACCM(NCYCLE)
C     PACCM=PACCM+50.0
      WRITE(6,2089)RATS,ACCM,ITER3,NCYCLE,S1
2089  FØRMAT(2(E14.7,2X),I7,2X,I4,2X,E14.7)
4     CØNTINUE
C2004 WRITE(6,2005)RB,RW,NCYCLE,ITER1,ITER2,MACCM
C2005 FØRMAT(2(2X,E14.7),2X,I4,2X,2(I7,2X),E14.7)
2004  CØNTINUE
16    CØNTINUE
24    CØNTINUE
```

```
C PLØTTING SEGMENT NØT IN USE
C      CALL PAPER(1)
C      CALL ERRØRS(0)
C      CALL PSPACE(0.0,1.0,0.0,0.0,0.702)
C      CALL MAP(0.0,1.0,0.0,0.0,1.0)
C      CALL BØRDER
C      CALL CTRØRI(90,0)
C      CALL PLØTCS(0.1,0.35,21HACCUMULATED STRAIN    ,21)
C      CALL FSPACE(-1)
C      CALL SUPFIX
C      CALL TYPECS(1H2,1)
C      CALL NØRMAL
C      CALL FSPACE(-2)
C      CALL CTRSET(4)
C      CALL TYPENC(23)
C      CALL CTRSET(-1)
C      IF(PACCM.LT.ER(ND))PACCM=ER(ND)
C      CALL CTRØRI(0,0)
C      CALL PLØTCS(0.65,0.05,12HCYCLE NUMBER,12)
C      CALL PSPACE(0.1,0.9,0.1,0.65)
C      CALL MAP(0.0,TCYCLE,0.0,PACCM)
C      CALL PTPLØT(ZZZ,ER,1,ND,233)
C      CALL PØSITN(0.0,0.0)
C      CALL PTJØIN(XN,ACCM,1,NCYCLE,1)
C      CALL AXES
C      CALL BØX(0.0,TCYCLE,0.0,PACCM)
C      CALL FRAME
C      TST=PST2(1,50)/1000000.0
C      BST=PST2(1,1)/1000000.0
C      TSN=PSN2(1,50)/100.0
C      BSN=PSN2(1,1)/100.0
C      DØ4000LM=1,L
C      DØ5000LL=1,K
C      XX(LL)=FLØAT(LL)
C      PS(LL)=PST2(LM,LL)/1000000.0
C      PN(LL)=PSN2(LM,LL)/100.0
C      IF(PS(LL).GE.TST)TST=PS(LL)
C      IF(PS(LL).LE.BST)BST=PS(LL)
C      IF(PN(LL).GE.TSN)TSN=PN(LL)
C      IF(PN(LL).LE.BSN)BSN=PN(LL)
C5000 CØNTINUE
C4000 CØNTINUE
C      TSTS=TST+0.00001
C      BSTS=BST-0.00001
C      TSNN=TSN+0.1
C      BSNN=BSN-0.1
C      CALL PSPACE(0.0,0.702,0.0,1.0)
C      CALL MAP(0.0,1.0,0.0,1.0)
C      CALL BØRDER
C      CALL PSPACE(0.15,0.35,0.2,0.9)
C      CALL MAP(0.0,50,0,BSTS,TSTS)
C      DØ89IJ=1,L
C      DØ29LL=1,K
C      PS(LL)=PST2(IJ,LL)/1000000.0
C29    CØNTINUE
```

```
329 C      CALL PTJØIN(XX,PS,1,K,1)
330 C89    CØNTINUE
331 C      CALL AXES
332 C      CALL BØX(0.0,50.0,BSTS,TSTS)
333 C      CALL PSPACE(0.4,0.6,0.2,0.9)
334 C      CALL MAP(0.0,50.0,BSNN,TSNN)
335 C      DØ43NJ=1,L
336 C      DØ42NN=1,K
337 C      PN(NN)=PSN2(NJ,NN)/100.0
338 C42    CØNTINUE
339 C      CALL PTJØIN(XX,PN,1,K,1)
340 C43    CØNTINUE
341 C      CALL AXES
342 C      CALL BØX(0.0,50.0,BSNN,TSNN)
343 C      CALL GREND
344 C END ØF PLØTTING SEGMENT
345        STØP
346        END
347 C SUBRØUTINE TØ CALCULATE STRESSES AT FØRWARD AND REVERSED LØADING
348        SUBRØUTINE STRESS (YI,Z4,C,N,CS,Y)
349        REAL N,MF
350        CØMMØN/DATA/E,YS,YE,MF
351        CØMMØN/DATA1/YS1,YS2,YS3,YS4,YE1,YE2,YE3,E1,E2,E3,E4,ITER2,ITER4
352        MI=0
353        YX=ABS(YI)
354        TØL=0.05*10.0**6.0
355        IF(Z4.NE.0.0)GØTØ51
356        IF(YX.GE.YE3)GØTØ46
357        IF(YX.GE.YE2)GØTØ47
358        IF(YX.GE.YE1)GØTØ48
359        IF(YX.GE.YE)GØTØ50
360 45     Y=YX*E
361        GØTØ440
362 46     YQ=YS4+YX*E4
363        GØTØ52
364 47     YQ=YS3+YX*E3
365        GØTØ52
366 48     YQ=YS2+YX*E2
367        GØTØ52
368 50     YQ=YS1+YX*E1
369        GØTØ52
370 51     IF(YX.LT.YE)GØTØ45
371        YQ=Z4
372        ITER4=ITER4+1
373 52     TØLS=TØL*(1.0/E+N*C*YQ**(N-1.0))
374 C      WRITE(6,111)TØLS,YX
375 C111   FØRMAT(3X,2(E14.7,2X))
376 49     ITER2=ITER2+1
377 C      ITER4=ITER4+1
378        YN=YQ/E+C*YQ**N
379 C      WRITE(6,115)YX,YN,YQ,CS
380 C115   FØRMAT(4X,4(E14.7,2X))
381        IF((YN-YX).LT.-TØLS)GØTØ410
382        IF((YN-YX).GT.TØLS)GØTØ420
383        GØTØ430
```

```
384 420   IF(MI.EQ.2)GØTØ421
385       IF(MI.EQ.Ø)GØTØ422
386       CS=CS/2.Ø
387       YQ=YQ-CS
388       MI=2
389       GØTØ49
390 421   YQ=YQ-CS
391       GØTØ49
392 422   YQ=YQ-CS
393       MI=2
394       GØTØ49
395 410   IF(MI.EQ.1)GØTØ411
396       IF(MI.EQ.Ø)GØTØ412
397       CS=CS/2.Ø
398       YQ=YQ+CS
399       MI=1
400       GØTØ49
401 411   YQ=YQ+CS
402       GØTØ49
403 412   YQ=YQ+CS
404       MI=1
405       GØTØ49
406 430   Y=YQ
407 440   IF(YI.GT.Ø.Ø)GØTØ4
408       Y=-Y
409 4     RETURN
410       END
```